Dilepton spectra in $p + p$ and Au + Au collisions at RHIC

A Dissertation Presented

by

Torsten Dahms

to

The Graduate School

in Partial Fulfillment of the Requirements

for the Degree of

Doctor of Philosophy

in

Physics

Stony Brook University

December 2008

Stony Brook University

The Graduate School

Torsten Dahms

We, the dissertation committee for the above candidate for the Doctor of Philosophy degree, hereby recommend acceptance of this dissertation.

Axel Drees – Dissertation Advisor
Professor, Department of Physics and Astronomy

Edward Shuryak – Chairperson of Defense
Professor, Department of Physics and Astronomy

Thomas C. Weinacht
Professor, Department of Physics and Astronomy

Yasuyuki Akiba
Vice Chief Scientist
Radiation Laboratory, RIKEN Nishina Research Center, Wako, Japan

This dissertation is accepted by the Graduate School.

Lawrence Martin
Dean of the Graduate School

Abstract of the Dissertation

Dilepton spectra in $p + p$ and Au + Au collisions at RHIC

by

Torsten Dahms

Doctor of Philosophy

in

Physics

Stony Brook University

2008

Recent experimental results show that a strongly coupled quark-gluon plasma (sQGP) is created in heavy ion collisions at the Relativistic Heavy Ion Collider (RHIC) at Brookhaven National Laboratory (BNL). Electromagnetic radiation, *i. e.*, photons and lepton pairs, are penetrating probes that allow investigating the full time evolution and dynamics of the matter produced, as they do not undergo strong interaction in the final state.

This work presents measurements of electron-positron pairs from $p + p$ collisions at $\sqrt{s} = 200$ GeV collected during the 2005 RHIC run and compares them to results from Au+Au collisions at $\sqrt{s_{NN}}$ = 200 GeV taken in 2004 with the PHENIX detector. The invariant mass distribution of e^+e^- pairs in $p + p$ is consistent with the expected contributions from Dalitz decays of light hadrons, dielectron decays of vector mesons and correlated charm production, which have been measured in the same experiment. The charm and bottom cross section extracted from the measured dielectron yield are $\sigma_{c\bar{c}} = 544 \pm 39(\text{stat.}) \pm 142(\text{syst.}) \pm 200(\text{model})$ μb and

$\sigma_{b\bar{b}} = 3.9 \pm 2.4(\text{stat.})^{+3}_{-2}(\text{syst.})\ \mu\text{b}$, respectively. The dielectron continuum measurement in $p + p$ provides a crucial baseline for the modification of the dielectron continuum observed in Au + Au.

In min. bias Au + Au collisions the yield of dielectrons in the low mass region ($150 < m_{ee} < 750$ MeV/c^2) is enhanced by a factor of $4.0 \pm 0.3(\text{stat.}) \pm 1.5(\text{syst.}) \pm 0.8(\text{model})$ compared to the known hadronic sources. The centrality dependence of this enhancement suggests emission from in-medium scattering processes. The excess dominates the yield in the transverse momentum region below 1 GeV/c and shows significantly lower $\langle p_T \rangle$ than the expected sources. The low p_T enhancement is currently not understood by any theoretical model of heavy ion collisions. The enhancement extends to larger transverse momenta ($p_T > 1$ GeV/c) where it is also observed in $p + p$ and explained by virtual direct photons. The $p + p$ measurement serves as an important test to pQCD calculations of direct photon production from hard scattering processes in this momentum range. An excess with an inverse slope of $T_{\text{eff}} = 221 \pm 23(\text{stat.}) \pm 18(\text{syst.})$ MeV is observed in central Au + Au collisions above the binary scaled direct photon yield in $p + p$. This can be qualitatively explained by hydrodynamical models including thermal photon radiation with initial temperatures of $300 \leq T_{\text{init}} \leq 600$ MeV and formation times of $0.12 \leq \tau_0 \leq 0.6$ fm/c.

To my family.

Contents

List of Figures ix

List of Tables xiii

Acknowledgements xiv

1 Introduction 1

1.1 Quantum Chromodynamics . . . 7

1.1.1 Chiral Symmetry . . . 10

1.2 Dileptons . . . 15

1.2.1 Drell-Yan . . . 16

1.2.2 Open Charm and Bottom . . . 16

1.2.3 Direct Photons . . . 20

1.2.4 Medium Modifications of Vector Mesons . . . 26

1.3 Previous Experimental Results . . . 28

1.3.1 HADES . . . 28

1.3.2 NA45/CERES . . . 30

1.3.3 NA60 . . . 30

1.3.4 WA98 . . . 34

1.4 RHIC . . . 37

2 The PHENIX Experiment 38

2.1 Global Detectors . . . 41

2.1.1 Beam-Beam Counters . . . 41

2.1.2 Zero Degree Calorimeter . . . 41

2.2 Central Arm Detectors . . . 45

2.2.1 Central Magnet . . . 45

2.2.2 Drift Chambers . . . 45

2.2.3 Pad Chambers . . . 48

2.2.4 Ring Imaging Cherenkov Counter . . . 51

2.2.5 Electromagnetic Calorimeter . . . 52

2.2.6 Charged Particle Acceptance 55

3 Analysis **58**
3.1 Data Set and Event Selection 58
3.1.1 $p + p$ Collisions 58
3.1.2 Au + Au Collisions 61
3.2 Charged Particle Tracking 63
3.3 Electron Identification 67
3.4 Pair Analysis 70
3.4.1 Pair Cuts 71
3.4.2 Photon Conversions 73
3.4.3 Event Mixing 76
3.4.4 Correlated Background 79
3.4.5 Like-sign Subtraction 83
3.4.6 Background Subtraction in Au + Au 86
3.5 Efficiency Correction 94
3.5.1 Tracking and Electron Identification Efficiency 94
3.5.2 ERT Efficiency 99
3.5.3 Occupancy Correction in Au + Au 105
3.5.4 Acceptance 108
3.5.5 Bin Shift Correction 110
3.6 Systematic Uncertainties 111
3.7 EXODUS Simulation of Hadron Decays 113

4 Results **119**
4.1 The Dielectron Continuum in $p + p$ Collisions 119
4.1.1 Charm Cross Section 121
4.1.2 ω and ϕ Cross Sections 132
4.1.3 Low Mass p_T Spectra 135
4.1.4 High p_T Direct Photons 135
4.2 Comparison to Au + Au Collisions 144
4.2.1 The Intermediate Mass Region 144
4.2.2 The Low Mass Enhancement 147
4.2.3 Direct Photons 149
4.2.4 p_T of the Low Mass Enhancement 157
4.3 Model Comparisons 163
4.3.1 Thermal Photons 163
4.3.2 Low mass dileptons 163

5 Summary and Outlook **168**

Bibliography **171**

A Background Normalization **185**
A.1 Pairing of electrons and positrons 185

B Beam Pipe Conversions **190**
B.1 Introduction 190
B.2 Analysis 190
B.2.1 Photon Conversions 191
B.2.2 Tagging of Decay Photons 192
B.2.3 Simulations 194
B.3 Conclusions 195

C Data Tables **197**

List of Figures

1.1 QCD Phase Diagram 2
1.2 Expected sources of dilepton production in heavy ion collisions 5
1.3 Expected sources of dilepton production in $p + p$ collisions . . 6
1.4 Feynman diagram of the electromagnetic interaction 7
1.5 Higher order processes of the electromagnetic interaction . . . 8
1.6 Feynman diagram for the strong interaction between quarks . 8
1.7 Higher order processes of the strong interaction 9
1.8 Mexican Hat Potential 13
1.9 Mexican Hat Potentials at $\pi = 0$ 14
1.10 Expectation Value of the Chiral Condensate 15
1.11 Drell-Yan process 16
1.12 LO processes of heavy quark production 17
1.13 Examples of NLO processes of $Q\overline{Q}$ production 18
1.14 Differential cross section of electrons from heavy flavor decays in $p + p$ collisions at $\sqrt{s} = 200$GeV 19
1.15 R_{AA} and v_2 of single electrons from heavy flavor decays 20
1.16 Feynman diagrams for LO direct photon production 21
1.17 Direct photons in $p + p$ collisions at $\sqrt{s} = 200$ GeV 22
1.18 R_{AA} of direct photons 23
1.19 Prediction of thermal photons at RHIC 24
1.20 Vector Dominance 26
1.21 Medium Modifications to Light Vector Mesons 27
1.22 Dielectron continuum in C-C collisions at 1 and 2 AGeV . . . 29
1.23 Dielectron continuum in p-Be and S-Au collisions at SPS energies 31
1.24 Dielectron continuum in Pb-Au collisions at 158 AGeV 32
1.25 IMR dimuon continuum in In-In collisions at 158 AGeV 33
1.26 LMR dimuon continuum in In-In collisions at 158 AGeV . . . 34
1.27 Dimuon m_T spectra in In-In collisions 35
1.28 Direct photons in Pb-Pb collisions 36

2.1 The PHENIX Detector 39

2.2 BBC Components 42
2.3 ZDC Layout 43
2.4 Centrality 44
2.5 Central Magnet 46
2.6 Drift Chamber Frame 47
2.7 Drift Chamber Wire Layout 49
2.8 Drift Chamber Drift Lines 50
2.9 Pad Chamber Pixel Design 51
2.10 RICH Detector 52
2.11 PbSc Module 53
2.12 PbGl Super Module 54
2.13 Energy spectrum of mip's 55
2.14 Single electron acceptance parameterization 57

3.1 Distribution of the Collision Vertex 59
3.2 Ratio of triggered events in the ERT and MB samples 61
3.3 Overlap of two gold nuclei for different impact parameters $\vec{b}$. . 62
3.4 Timing Distribution of DC Hits 66
3.5 Definition of Track Reconstruction Coordinates 66
3.6 RICH ring mask 67
3.7 Energy-Momentum matching 69
3.8 RICH ring overlap 72
3.9 RICH ring distance 73
3.10 Ghost Pairs 74
3.11 Opening angle of conversion pairs 75
3.12 Invariant mass distribution of conversions 75
3.13 Background subtracted like-sign distribution in m_{ee} and p_T . . 78
3.14 $\Delta\phi$ of PYTHIA like-sign pairs 78
3.15 Invariant mass distribution of like-sign pairs 80
3.16 Invariant mass spectra of like- and unlike-sign pair in $p+p$. . 84
3.17 Comparison of background subtraction methods. 86
3.18 Comparison of background subtraction methods. 87
3.19 RMS of all methods as function of m_{ee}. 87
3.20 Invariant mass spectra of like-sign pairs in real and mixed events in MB Au + Au. 88
3.21 Like-sign pairs in real and mixed events for various Au + Au centrality bins. 90
3.22 Invariant mass spectra of like-sign pairs in real and mixed events in MB Au + Au for various p_T bins. 91
3.23 Invariant mass spectra of like- and unlike-sign pair in Au + Au. 93
3.24 Single electron acceptance parameterization 95

3.25 Single electron identification efficiency in $p+p$ an $\mathrm{Au}+\mathrm{Au}$ . . 96
3.26 Pair efficiency in $p+p$ and $\mathrm{Au}+\mathrm{Au}$ 98
3.27 ϕ_V distributions in data and Monte Carlo 99
3.28 p_T distribution of ERT triggered electrons 100
3.29 Single electron ERT trigger efficiency 101
3.30 ERT trigger efficiency for different eID cuts 104
3.31 Comparison of ERT trigger efficiency with different eID cuts . 104
3.32 ERT trigger efficiency for e^+e^- pairs 105
3.33 ERT trigger efficiency for e^+e^- pairs in mass and p_T 106
3.34 Comparison of dielectron spectra in $p+p$ from MB and ERT triggered events 107
3.35 Geometric acceptance of e^+e^- pairs 109
3.36 Bin shift correction for ω and ϕ yields 111
3.37 Signal-to-Background Ratio in $p+p$ and $\mathrm{Au}+\mathrm{Au}$ collisions . 112
3.38 Meson cross sections in $p+p$ collisions at $\sqrt{s}=200$ GeV . . . 115
3.39 Meson cross sections in $\mathrm{Au}+\mathrm{Au}$ collisions at $\sqrt{s_{NN}}=200$ GeV 116
3.40 Cocktail of e^+e^- pairs in $p+p$ collisions at $\sqrt{s}=200$ GeV . . 118
3.41 Cocktail of e^+e^- pairs in $\mathrm{Au}+\mathrm{Au}$ collisions at $\sqrt{s_{NN}}=200$ GeV 118

4.1 Invariant mass spectrum of e^+e^- pairs in $p+p$ collisions . . . 120
4.2 PYTHIA e^+e^- pairs from open charm for different k_T values . . 124
4.3 PYTHIA e^+e^- pairs from open charm for different PDFs 124
4.4 e^+e^- pairs from Drell-Yan from PYTHIA and NLO pQCD . . . 125
4.5 e^+e^- pairs from semi-leptonic heavy flavor decays 127
4.6 Total Charm Cross Section vs. $\sqrt{s}$ 128
4.7 Total Bottom Cross Section vs. $\sqrt{s}$ 129
4.8 p_T spectrum of e^+e^- pairs in the IMR 130
4.9 PYTHIA parton showers 131
4.10 p_T spectrum of e^+e^- pairs in the IMR 132
4.11 Invariant. mass spectrum of e^+e^- pairs around the ω and ϕ . 134
4.12 Invariant ω cross section 136
4.13 Invariant ϕ cross section 137
4.14 Invariant ω cross section in comparison to measurement of hadronic decay channels 138
4.15 Invariant ϕ cross section in comparison to measurement of hadronic decay channels 138
4.16 Invariant mass for different p_T ranges in $p+p$ 139
4.17 Invariant Yield as function of p_T for e^+e^- pairs in different mass ranges in $p+p$ collisions 140
4.18 Invariant mass for different p_T ranges in $p+p$ 141
4.19 Fit of internal conversion shape to data in $p+p$ 142

4.20 Invariant mass spectrum of e^+e^- pairs in min. bias Au + Au collisions . . . 145
4.21 Invariant mass spectrum of e^+e^- pairs in $p + p$ and various centrality bins of Au + Au collisions . . . 146
4.22 IMR yield per N_{coll} as function of N_{part} . . . 147
4.23 LMR yield per $N_{\text{part}}/2$ as function of N_{part} . . . 148
4.24 Invariant mass for different p_T ranges in Au + Au . . . 150
4.25 Invariant mass for different p_T ranges in Au + Au . . . 151
4.26 Invariant mass at low p_T in Au + Au . . . 152
4.27 Fit of internal conversion shape to data in Au + Au . . . 153
4.28 Fraction of direct photons r in $p + p$ and Au + Au . . . 154
4.29 Direct Photon Spectrum in Au + Au and $p + p$ collisions . . . 156
4.30 Invariant Yield as function of p_T for e^+e^- pairs in different mass ranges in min. bias Au + Au collisions . . . 158
4.31 Invariant Yield as function of p_T for e^+e^- pairs in different mass ranges for $p + p$ and min. bias Au + Au collisions . . . 159
4.32 Fits of m_T spectra of e^+e^- pairs in $0.3 < m_{ee} < 0.75$ GeV/c^2 . 162
4.33 Comparison of direct photon yield Au + Au to theoretical predictions . . . 164
4.34 Comparison of direct photon yield Au + Au to theoretical predictions . . . 165
4.35 Comparison of low mass enhancement in Au + Au to theoretical predictions . . . 167

B.1 Invariant mass of e^+e^- pairs from beam pipe conversion . . . 192
B.2 Invariant mass of γe^+e^- triplets . . . 193
B.3 Comparison of direct photon excess in different methode . . . 195

List of Tables

2.1 PHENIX Detector Subsystems 40

3.1 Glauber Monte Carlo Simulation 63
3.2 Electron Identification Cuts 69
3.3 Fit to ratios of like-sign real and mixed events in MB Au + Au 89
3.4 Fiducial Cuts 96
3.5 Electron identification efficiency 97
3.6 Single Electron ERT Efficiency 102
3.7 ERT efficiency as function of mass 103
3.8 Embedding Efficiency 108
3.9 Systematic Uncertainties 113
3.10 Hadron rapidity densities in $p + p$ 114
3.11 Hadron rapidity densities in Au + Au 117

4.1 Pythia Drell-Yan fits to NLO pQCD 126
4.2 Fits to direct photon spectra in Au + Au 155
4.3 Initial conditions of thermal photon predictions 163

C.1 ω and ϕ yields 197
C.2 Fit results of ω yield extraction 198
C.3 Fit results of ϕ yield extraction 200
C.4 Invariant Cross Section of ω 202
C.5 Invariant Cross Section of ϕ 202

Acknowledgements

I would like to gratefully acknowledge my advisor Axel Drees for his support and guidance over the past years. He introduced me to this exciting field of physics and the PHENIX experiment when I came to Stony Brook as an exchange student from Würzburg. Axel was always helpful and encouraging and has been an excellent advisor and a good friend.

I would like to extend my thanks to Alberica Toia with whom I had the pleasure to work closely for over three years. Working with her was inspirational and fun. In her I found another strong supporter of my work.

It has been a wonderful experience to work within the PHENIX collaboration. In particular, I am grateful to Yasuyuki Akiba at BNL for his help and inspiring discussions. I thank Barbara Jacak, Tom Hemmick, Ralf Averbeck and everybody else in the Relativistic Heavy Ion Group at Stony Brook. I also want to thank all my fellow graduate students and friends that provided welcome distraction from work and made life in Stony Brook enjoyable.

Last, I would like to thank my parents for their unconditional love, support, encouragement, and trust. It is impossible to put into words what I owe to them.

Chapter 1

Introduction

Relativistic heavy ion collisions, *i. e.*, collisions in which the projectile energies are much larger than their rest masses, have been an excellent tool to study nuclear matter under extreme conditions and explore the phase diagram of strongly interacting matter for new states of matter. At the Relativistic Heavy Ion Collider (RHIC) at Brookhaven National Laboratory (BNL) gold ions are brought to collisions at center of mass energies of up to $\sqrt{s_{NN}} = 200$ GeV. Before RHIC, the Alternating Gradient Synchrotron (AGS) at BNL and the Super Proton Synchrotron (SPS) have been colliding heavy ions at energies up to $\sqrt{s_{NN}} \approx 5$ GeV (AGS) and $\sqrt{s_{NN}} \approx 17$ GeV and therefore studying nuclear matter at lower temperatures and higher net baryon densities. With even lower energies the heavy ion synchrotron "SchwerIonen Synchrotron" (SIS) provides heavy ion collisions at beam energies up to 2 AGeV. The Large Hadron Collider (LHC) will achieve even higher temperatures in lead on lead collisions at $\sqrt{s_{NN}} = 5.5$ TeV.

At energy densities of $\varepsilon \approx 1$ GeV/fm^3 a phase transition from hadronic matter to deconfined quarks and gluons, the so called quark-gluon plasma (QGP), is predicted [1]. Calculations of lattice quantum chromodynamics (lQCD) predict that such an energy density is reached at a temperature of $T \approx 170$ MeV[1] $\approx 10^{12}$ K [2]. This state may have existed in the early universe a few tens of microseconds after the big-bang and may still exist in the core of neutron stars at densities of 10^{18} kg/m^3 = 0.6 fm^{-3} which exceeds normal nuclear matter density by more than a factor of four. The same calculations also show that, at vanishing net baryon density, with the transition into the deconfined phase, chiral symmetry, which is spontaneously broken in vacuum due to non-vanishing effective quark masses, is restored [2].

[1]Natural units $\hbar = c = k_B = 1$ are employed throughout this thesis except where noted otherwise

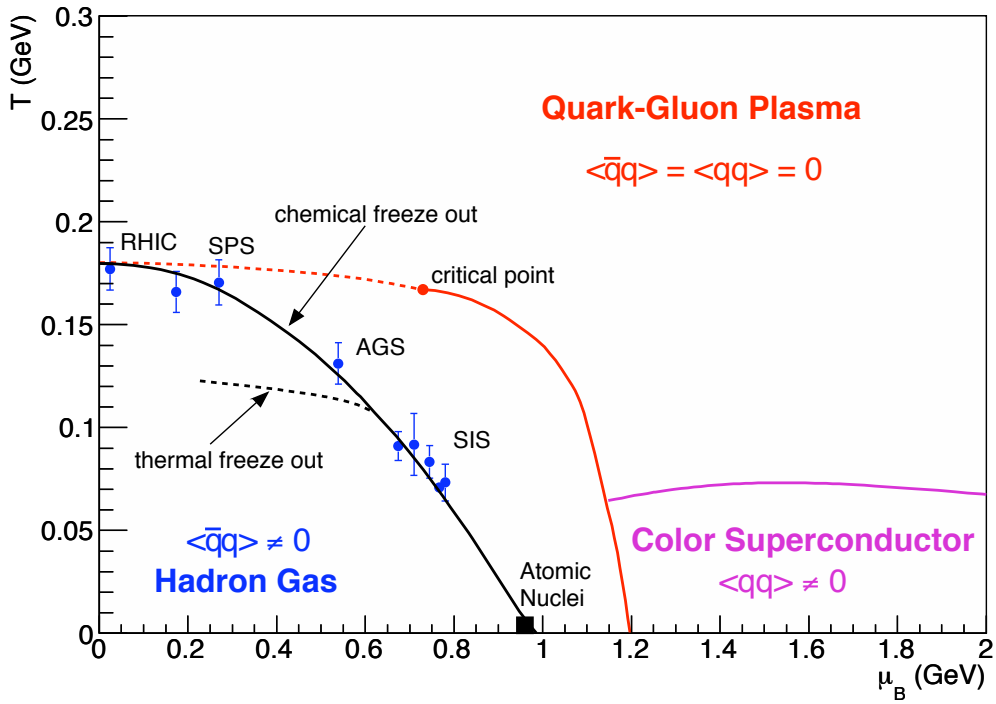

Figure 1.1: Schematic phase diagram of QCD matter as function of temperature T and baryonic chemical potential μ_B. The measured chemical freeze out points for SIS, AGS, SPS, and RHIC energies are shown as points [5]. The *dashed* line denotes the thermal freeze out. The existence and exact location of a critical point are unknown.

In Fig. 1.1 a schematic phase diagram of QCD matter [3–5] is shown as function of temperature T and baryon chemical potential μ_B. Below the phase boundary quarks and gluons are confined to hadrons which form a interacting hadron gas. Above the phase transition, matter of asymptotically free quarks and gluons with partonic degrees of freedom is created. The exact details such as the order of the phase transition are unknown. Lattice QCD calculations indicate a cross over at vanishing net baryon density, while at large net baryon densities a first order phase transition is expected. If such a scenario is realized, a critical point, below which the transition becomes a cross over, would terminate the first order phase transition.

Also shown are for different collision energies, the points at which the fireball created in the collision, reaches its chemical freeze out, *i. e.* the end of inelastic collisions and therefore the production of new particles has stopped. The thermal freeze out refers to the end of elastic collision, *i. e.* the end of momentum transfer between particles, as the mean free path of the particles has become larger than the size of the system. The experimental points of

chemical freeze out are calculated based on the final multiplicities of particle species [6, 7].

Experimental results from all four RHIC experiments (BRAHMS, PHENIX, PHOBOS, and STAR) give clear evidence that a new state of matter has been created in Au+Au collisions at $\sqrt{s_{NN}} = 200$ GeV [8–11]. These results include that a very high energy density $\langle\varepsilon\rangle \approx 15$ GeV/fm^3 is achieved, as indicated by the large energy loss of light hadrons [12, 13], and heavy quarks [14–16]. Furthermore, a large elliptic flow is developed on a partonic level including heavy quarks which is evidence for an early thermalization of the medium[14, 17–19].

Colorless, electromagnetic probes such as photons and dileptons (electron-positron or muon pairs) are particular useful probes to study the the quark-gluon plasma, as they, once emitted, do not undergo strong final state interactions with the hadronic medium. Dileptons are created via various processes during all stages of the collision. There is an approximate time ordering in the invariant mass of the lepton pair; the earlier produced the larger its mass. In the earliest stage, Drell-Yan annihilation between incoming $q\overline{q}$ pairs creates dileptons dominating the invariant mass region well above 3 GeV/c^2. As the formed hot and dense medium rapidly thermalizes, a significant contribution of dileptons from $q\overline{q}$ annihilation is expected, but in contrast to the DY pairs, these pairs should follow a thermal distribution in the intermediate mass region (IMR) $1 < m_{ll} < 3$ GeV/c^2. The major background source for the thermal radiation in the IMR comes from semi-leptonic decays of open charm. Pairs of $c\overline{c}$ quarks created in the initial hard scattering independently hadronize to $D\overline{D}$ mesons, which consist of one charm and one light quark, therefore often referred to as "open charm" mesons. These mesons inherit the strong initial back-to-back correlation of the charm quarks. Their individual weak decay $D \rightarrow Kl\nu_l$ leads to a continuum of lepton pairs dominating the IMR. Medium modifications of charm quarks, which leads to a significant flow and suppression at large transverse momenta of single electrons from open charm decays [15], may also be reflected in the invariant mass distribution of dileptons from open charm decays. After hadronization the main contribution is expected from annihilation of pions and other hadrons. Of particular interest are the two body annihilation of pions through the light vector mesons ρ, ω, and ϕ, as they decay directly into lepton pairs, whose invariant mass reflects the mass of the vector meson at the time of the decay. With the short life time of the ρ of $\tau_\rho = 1.3$ fm and a life time of the hadronic medium of ≈ 10 fm, this channel provides an excellent probe to the effects of chiral symmetry restoration [20]. Once the chemical freeze out is reached, the hadronic resonances and Dalitz decays of light pseudo-scalar mesons as π^0, η contribute to the low mass region (LMR) below 1 GeV/c^2.

A schematic view of all contributions is shown in Fig. 1.2 and is supplemented with a realistic "cocktail" of hadron decays as expected to be measured with PHENIX in $p+p$ collisions shown in Fig. 1.3. This cocktail includes the effects of detector resolution and acceptance.

This thesis is about the analysis of the dielectron continuum in the low and intermediate mass region in $p+p$ collisions at $\sqrt{s} = 200$ GeV recorded in 2005 with the PHENIX detector and the comparison to the dielectron continuum measured in Au + Au collisions taken in 2004. As part of this effort the cross sections of the ω and ϕ in $p+p$ collisions mesons have been measured. The e^+e^- pairs in the intermediate mass region allowed the extraction of the total charm cross section in $p+p$ [21], which is in very good agreement with previous measurements via single electrons [16]. The high mass region (HMR) $m_{ee} > 3$ GeV gave access to the first measurement of the bottom cross section in $p+p$ collisions at $\sqrt{s} = 200$ GeV.

In the continuum of the low mass region a contribution from internal conversions of direct virtual photons has been extracted and provided an important reference for the measurement of direct virtual photons in Au + Au collisions [22]. Furthermore, the measurement of the full dielectron continuum over a wide range in mass ($0 < m_{ee} < 8$ GeV/c^2) and p_T ($0 < p_T < 5$GeV/c) in $p+p$ provides an important baseline for the interpretation of the Au + Au result [23].

This thesis is structured in the following way: In Chapter 1 an introduction into the physics of the dielectron continuum is given. After a brief discussion of the theoretical background in Section 1.1 and the different dilepton sources 1.2 an overview over recent results at other dilepton experiments is given in Section 1.3. In Chapter 2 a description of the PHENIX detector is given. The analysis details are presented in Chapter 3. The various results of this analysis are shown and discussed in Chapter 4. The thesis ends with a summary and an outlook for further analyses of the dielectron continuum in Chapter 5.

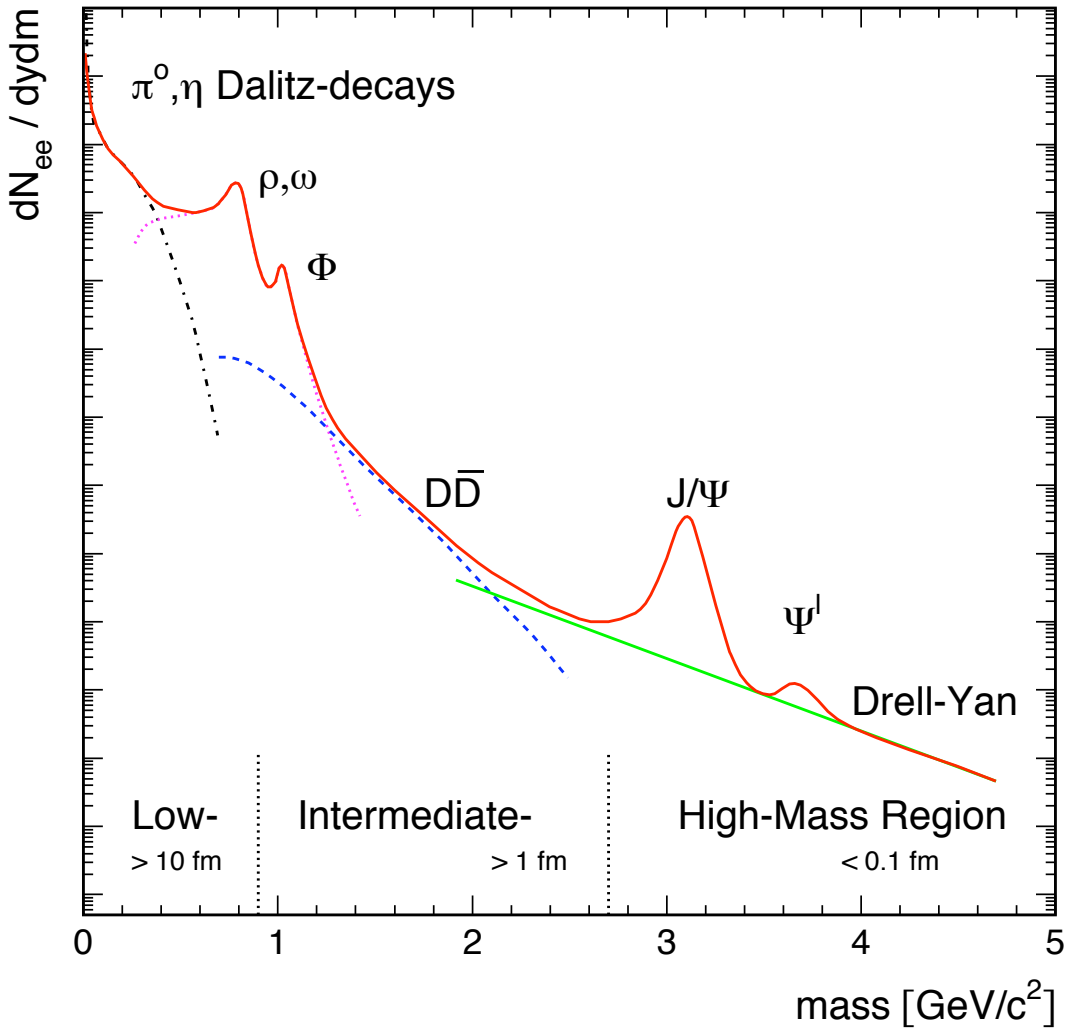

Figure 1.2: Expected sources of dilepton production as function of invariant mass in ultra-relativistic heavy ion collisions.

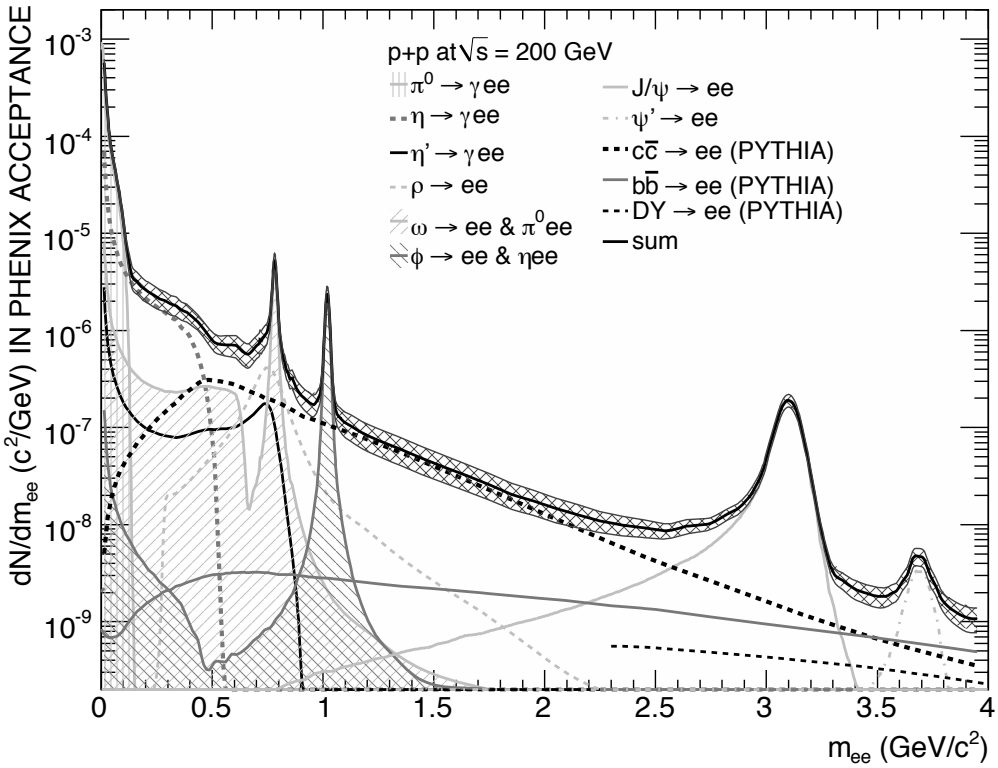

Figure 1.3: Expected sources of dilepton production as function of invariant mass in $p + p$ collisions at $\sqrt{s} = 200$ GeV.

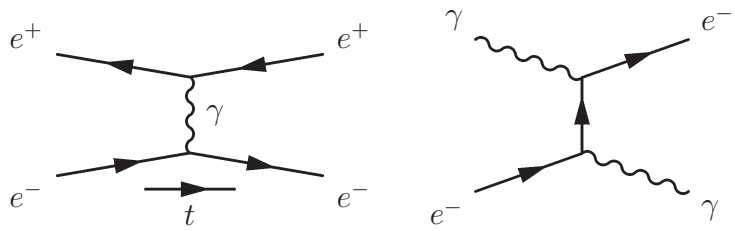

Figure 1.4: Examples of Feynman diagrams for the interaction between two charged particles, and the Compton scattering of a photon on an electron. Time is advancing from the left to the right.

1.1 Quantum Chromodynamics

The theory of quantum electrodynamics (QED) is probably the best understood and tested theory in the field of physics. On very short time scales, which can be estimated by the uncertainty principle ($\Delta E \Delta t \approx \hbar$), electrons are allowed to emit and absorb a virtual photon with non-zero rest mass. The electromagnetic interaction between two charged particles is described by the exchange of such virtual photons. As the photon is charge neutral it does not interact with itself. The strength of the electromagnetic interaction is given by the coupling constant $g_e = \sqrt{4\pi\alpha}$ which depends on the fine structure constant $\alpha = e^2/(\hbar c 4\pi\varepsilon_0) \approx 1/137$. QED predicts a logarithmic increase of the interaction strength with increasing momentum transfers. The interaction between two charged particles, annihilation or scattering, can be represented by the Feynman diagram shown in Fig. 1.4. Also shown are the two diagrams for the Compton scattering of a photon from an electron.

Higher order processes are responsible for changes in the strength of the electromagnetic interaction. As shown in Fig. 1.5 the virtual photon exchanged between two charges can create an e^+e^- pair which subsequently annihilate each other. This virtual e^+e^- pair acts as an electric dipole, effectively screening the two interacting charges. Such vacuum polarization at short distances (large momenta) reduces the effective charge of the electron as well as the fine structure constant:

$$\alpha(|q^2|) = \left(\frac{1}{\alpha(0)} - \frac{1}{3\pi}\ln\frac{|q^2|}{m^2}\right)^{-1} \tag{1.1}$$

$|q^2|$ is the square of the momentum transfer, m the mass of the charged particle and Eq. (1.1) an approximation for large $|q^2|/m$. Other higher order processes are responsible for the electron's self energy and its anomalous magnetic moment $(g_s - 2) \neq 1$ and are shown in Fig. 1.5.

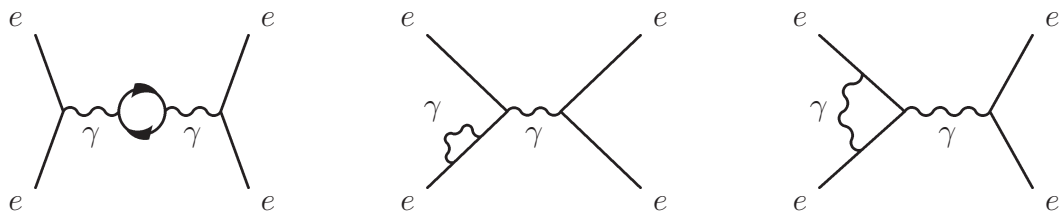

Figure 1.5: Higher order processes of the electromagnetic interaction

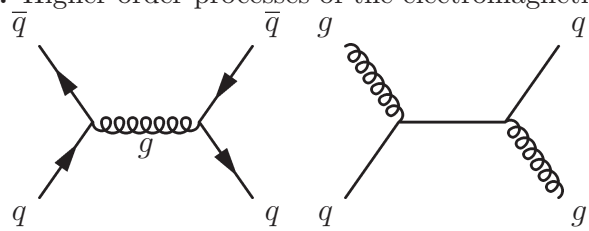

Figure 1.6: Exemplary Feynman diagram for the strong interaction between quarks

In an analog way, in the Standard Model quantum chromodynamics (QCD) describes the strong interaction between quarks via the exchange of color charges[2] carried by gluons. Fig. 1.6 shows the the lowest order Feynman diagrams for quark-antiquark annihilation and quark-gluon scattering.

As gluons themselves carry a non-zero color charge, they can interact with themselves. This allows gluons not only to split into virtual quark-antiquark pairs, but also to split in pairs of gluon as shown in Fig. 1.7. This leads to an important difference from the electromagnetic interaction. The coupling strength of the strong interaction α_s increases with increasing distance of two quarks.

The momentum transfer dependence of the coupling strength can be written in analogy to Eq. (1.1) as:

$$\alpha_{\mathrm{s}}(|q^2|) = \left(\frac{1}{\alpha_{\mathrm{s}}(\mu^2)} + \frac{1}{12\pi}(11N_c - 2N_f) \ln \frac{|q^2|}{\mu^2} \right)^{-1} \tag{1.2}$$

for ($|q^2| \gg \mu^2$) with the number of colors $N_c = 3$ and the number of flavors

[2]The necessity of color charges arises experimentally from the existence of baryons with three quarks of identical flavor, *e. g.* the Δ^{++} consists of three u quarks. The Pauli exclusion principle demands an extra quantum number to allow such a configuration, as any two fermions must not occupy the same state but must at least differ in one quantum number. The introduction of *color* charges "red", "blue" and "green" lifts the degeneracy of the three quarks.

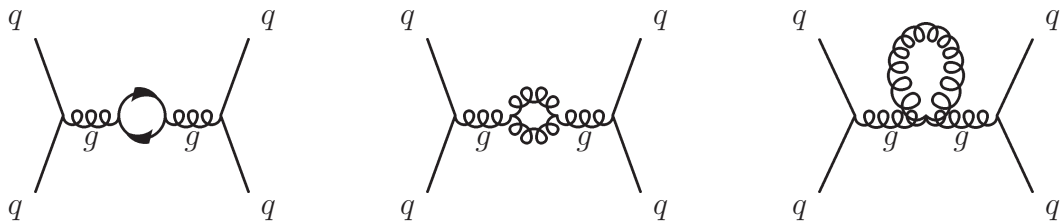

Figure 1.7: Higher order processes of the strong interaction

$N_f = 6$ (in the Standard Model). As for large distances or small momentum transfers the the coupling increases, known as anti-screening, α_s cannot be expanded around $|q^2| = 0$, quite in contrast to α. With increasing momentum transfer the coupling decreases leading to quasi-free quarks and gluons, known as *asymptotic freedom* [24–27]. This allows an expansion of α_s around large momentum transfers and therefore a perturbative treatment as long as $\alpha_\mathrm{s} \leq 1$. However, for small momentum transfers on the order of $q \simeq 1$ GeV/c the perturbative treatment breaks down and both the effective coupling and the relevant degrees of freedom change rapidly with scale — at large distances the degrees of freedom are colorless objects of two (mesons) or three (baryons) confined quarks. This regime of "strong QCD" poses the biggest challenge to the theory of the strong interaction.

The QCD Lagrangian which describes the dynamics of the strong interaction can be expressed as:

$$\mathcal{L}_\mathrm{QCD} = \overline{\psi}(i\hbar\gamma^\mu \mathbf{D}_\mu - \mathbf{M})\psi_- \frac{1}{4}\mathbf{G}^i_{\mu\nu}\mathbf{G}^{\mu\nu\, i} \tag{1.3}$$

where ψ is a vector of Dirac spinors[3] representing the wave function of a spin-1/2 quark-fields. γ^μ are the Dirac matrices and $\mathbf{M} = \mathrm{diag}(m_u, m_d, m_s, \ldots, m_t)$ is composed of the bare quark masses $m_u \simeq 3$, $m_d \simeq 7$, $m_s \simeq 100$ MeV/c^2 and $m_c \simeq 1.25$, $m_b \simeq 4.1$, $m_t \simeq 175$ GeV/c^2. $\mathbf{D}_\mu = \partial_\mu + ig\frac{\lambda^i}{2}\mathbf{A}^i_\mu$ is the covariant derivative with the Gell-Mann matrices λ^i and the spin-1 gauge fields $\mathbf{A}^i_\mu$ with color index $i = 1, \ldots 8$. This term describes the interaction of quarks with gluons, to which the eight gauge fields correspond to. The field strength tensor

$$\mathbf{G}^i_{\mu\nu} = \partial_\mu \mathbf{A}^i_\nu - \partial_\nu \mathbf{A}^i_\mu + igf_{ijk}\mathbf{A}^j_\mu \mathbf{A}^k_\nu \tag{1.4}$$

[3]Each quark can carry one of three colors, red, blue or green. Therefore the vector of Dirac spinors reads: $\psi = \begin{pmatrix} \psi_r \\ \psi_b \\ \psi_g \end{pmatrix}$.

describes the interaction of gluons with other gluons, where $g = \sqrt{4\pi\alpha_\mathrm{s}}$ is the coupling constant of the strong interaction and f_{ijk}'s denote the structure constants of the $SU(3)$ group [28].

1.1.1 Chiral Symmetry

The Lagrangian is invariant under local $SU(3)$ gauge transformations, *i. e.*, it is invariant under arbitrary rotations in color space. In addition, the Lagrangian exhibits a global symmetry $U(1)$ that corresponds to the baryon number conservation. In the limit of vanishing quark masses (which for momentum transfers of $q \simeq 1$ GeV/c is a good approximation for the light quarks u and d, and to a lesser extent also for the strange quark) the Lagrangian reveals another symmetry under global vector and axial vector transformations in the $SU(3)$ flavor space which are defined as:

$$\psi \to \mathrm{e}^{-i\alpha_V^i \frac{\lambda^i}{2}}\psi \quad \text{and} \quad \psi \to \mathrm{e}^{-i\alpha_A^i \frac{\lambda^i}{2}}\gamma_5\psi. \tag{1.5}$$

The conserved Noether currents associated with these symmetries are

$$j^\mu_{V,i} = \overline{\psi}\gamma^\mu \frac{\lambda^i}{2}\psi \quad \text{and} \quad j^\mu_{A,i} = \overline{\psi}\gamma^\mu \frac{\lambda^i}{2}\gamma_5\psi. \tag{1.6}$$

The quark-spinors in Eq. (1.3) can be decomposed into a left- and a right-handed component

$$\psi_{L,R} = \frac{1}{2}(1 \mp \gamma_5)\psi \tag{1.7}$$

which transform under the rotations defined in Eq. (1.5) as:

$$\psi_L \to \mathrm{e}^{-i\alpha_L^i \frac{\lambda^i}{2}}\psi_L \quad \text{and} \quad \psi_R \to \psi_R \tag{1.8}$$

$$\psi_R \to \mathrm{e}^{-i\alpha_R^i \frac{\lambda^i}{2}}\psi_R \quad \text{and} \quad \psi_L \to \psi_L, \tag{1.9}$$

which constitutes a global $SU(3)_L \otimes SU(3)_R$ chiral symmetry in flavor space. This symmetry conserves the handedness, *i. e.*, the projection of the spin on the momentum direction, of a quark. Therefore the two kinds of quarks, left- and right-handed, do not mix dynamically.

Spontaneous Breaking of Chiral Symmetry

The observation of the mass splitting of chiral partners, *e. g.*, the ρ and a_1 mesons have a mass difference of $\simeq 550$ MeV/c^2 ($m_\rho = 776$ MeV/c^2 and $m_{a_1} = 1230$ MeV/c^2 [29]), implies a spontaneous breaking of chiral symmetry

due to a non-vanishing vacuum expectation value of the quark condensate $\langle\overline{\psi}\psi\rangle \neq 0$. While the vector current $j_V = j_L + j_R$ is still conserved the axial-vector symmetry ($j_A = j_L - j_R$) is spontaneously broken, which means that the axial-vector charge $Q_A^k = \int d^3x\, \psi^\dagger \frac{\lambda_k}{2}\gamma_5\psi$ still commutes with the Hamiltonian but the ground state has a non-zero expectation value: $Q_A^k|0\rangle \neq 0$. An often used analogy is a ferromagnet below the Curie temperature, in which the ground state of aligned spins breaks the rotational symmetry. The choice of a particular ground state leads to a spontaneous breaking of chiral symmetry which according to the Goldstone theorem [30] results in the appearance of eight massless Goldstone bosons ($\pi^\pm$, π^0, $K^\pm$, K^0, $\overline{K^0}$, and η)

Such a system can be visualized by the following potential

$$V = -\frac{1}{2}\mu^2(\sigma^\dagger\sigma + \pi^\dagger\pi) + \frac{1}{4}\nu^2(\sigma^\dagger\sigma + \pi^\dagger\pi)^2 \tag{1.10}$$

which is shown for $\mu^2 > 0$ and $\mu^2 < 0$ in Fig. 1.8 [31]. For $\mu^2 > 0$ the potential has a rotational symmetric ground state at $\sigma = \pi = 0$. For $\mu^2 < 0$, the state $\sigma = \pi = 0$ is a local maximum and therefore unstable. An infinite number of degenerate ground states lie on the circle $\sigma^2 + \pi^2 = \mu^2/\nu^2$, which are not rotational symmetric. Therefore, picking a ground state spontaneously breaks the symmetry. However, effects of the symmetry are still present, as excitations around the symmetry axis, *i. e.* axial-vector rotations, do not cost energy. With the identification of the fields $\vec{\pi} \equiv i\overline{\psi}\vec{\lambda}\gamma_5\psi$ and $\sigma \equiv \overline{\psi}\psi$ these rotations correspond to the massless Goldstone bosons. In contrast, radial excitations along the σ field do cost energy and correspond to massive particles.

The strength of the symmetry breaking is measured by the vacuum expectation value of such Goldstone bosons which is, *e. g.*, for pions:

$$\langle 0|j^\mu_{A,k}(x)|\pi_j(p)\rangle = i\delta_{jk} f_\pi p^\mu \mathrm{e}^{-ipx}. \tag{1.11}$$

with the measured pion decay constant $f_\pi = 93$ MeV, which is the order parameter of the chiral symmetry. A second order parameter is the vacuum expectation value or quark condensate

$$\langle\overline{\psi}\psi\rangle = \langle 0|\overline{\psi}_L\psi_R + \overline{\psi}_R\psi_L|0\rangle = \langle 0|\overline{u}u + \overline{d}d|0\rangle. \tag{1.12}$$

The relation between quark condensate $\langle\overline{\psi}\psi\rangle$ and f_π is given by the Gell-Mann-Oakes-Renner relation (GOR) [32]:

$$\begin{aligned} m_\pi^2 f_\pi^2 &= -\overline{m}\langle\overline{\psi}\psi\rangle \\ &= -2\overline{m}\langle\overline{q}q\rangle \end{aligned} \tag{1.13}$$

where $\overline{m} = \frac{1}{2}(m_u + m_d)$ and $\langle \overline{q}q \rangle = \langle \overline{u}u \rangle = \langle \overline{d}d \rangle$.

Explicit Breaking of Chiral Symmetry

The small but non-vanishing mass of the pseudoscalar mesons is explained by the explicit breaking of the chiral symmetry due the finite quark masses.

The finite quark masses create a contribution $-\overline{m}\langle \overline{\psi}\psi \rangle$ in the QCD Lagrangian in Eq. (1.3). This leads to a Mexican hat potential which is slightly tilted towards the positive σ direction which breaks the symmetry of the potential:

$$V = -\frac{1}{2}\mu^2(\sigma^\dagger\sigma + \pi^\dagger\pi) + \frac{1}{4}\nu^2(\sigma^\dagger\sigma + \pi^\dagger\pi)^2 - f_\pi m_\pi^2 \sigma \tag{1.14}$$

which is illustrated in Fig. 1.9. With the choice of $\mu^2/\nu^2 = f_\pi^2$ the tilting leads to a minimum at $\sigma = f_\pi$ and axial-vector currents are no longer conserved, *i. e.* the pseudoscalar mesons, which were the Goldstone bosons of the spontaneous symmetry breaking, acquire a finite mass which is related to the current quark mass by Eq. (1.13). With $\overline{m} \approx 5$ MeV$/c^2$ the vacuum value for the quark condensate becomes $\langle \overline{q}q \rangle \approx -(254 \text{ MeV})^3$.

In-Medium Quark Condensate

So far only vacuum properties of hadronic matter have been discussed. Of particular interest are the dynamics in the presence of a hot and dense medium as it is expected to be created in relativistic heavy-ion collisions. At high pressure or temperature hadronic matter is expected to undergo a phase transition to deconfined quarks and gluons accompanied by the melting of the quark condensate. Already before reaching deconfinement, chiral symmetry is partially restored.

The expected modifications can be derived in the limit of low temperatures T and density starting from the grand canonical partition function for a hadron gas in volume V in contact with a heat bath

$$\mathcal{Z}(V, T, \mu_q) = \mathrm{Tr}(\mathrm{e}^{-(\mathbf{H} - \mu_q \mathbf{N})/T}) \tag{1.15}$$

with the Hamiltonian of the system $\mathbf{H}$, the quark chemical potential μ_q, and the quark number generator $\mathbf{N}$.

The expectation value of the quark condensate is given by the thermal average

$$\langle\langle \overline{q}q \rangle\rangle = \mathcal{Z}^{-1} \sum_n \langle n|\overline{\psi}\psi|n\rangle \mathrm{e}^{-(E_n - \mu_q)/T}, \tag{1.16}$$

where the sum is carried out over all eigenstates of $\mathbf{H}$ with the corresponding

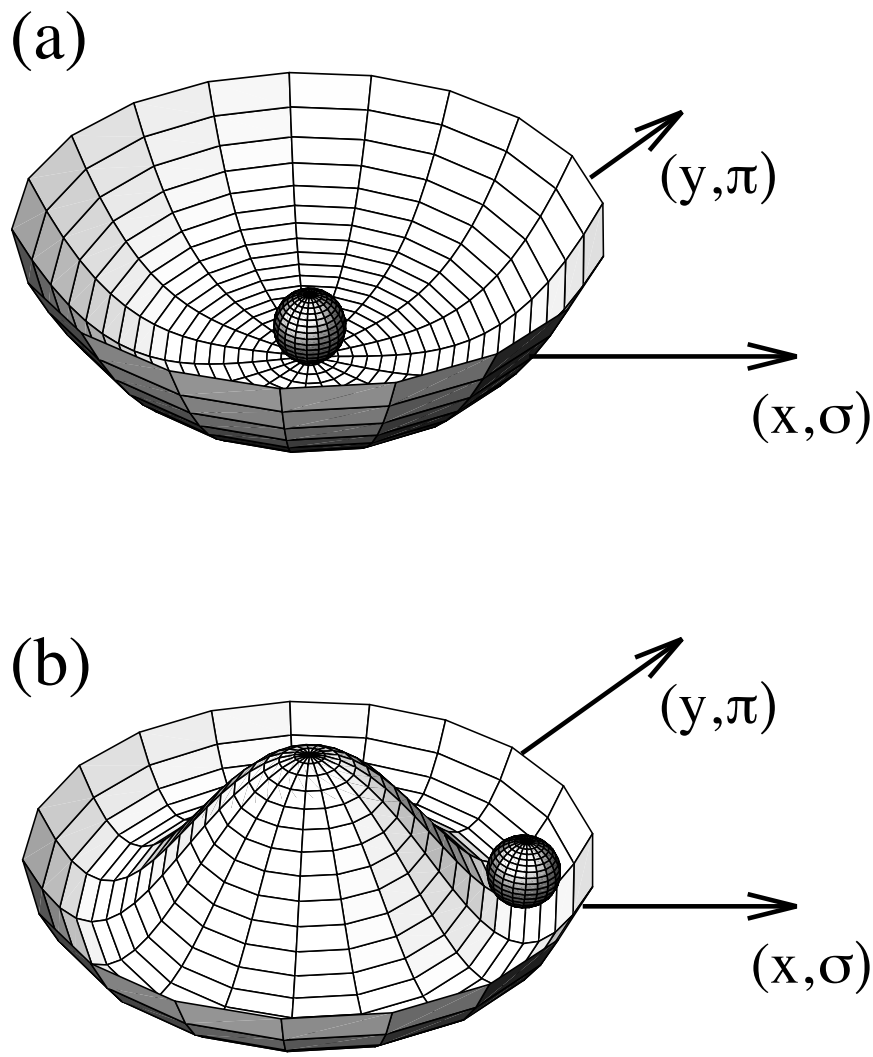

Figure 1.8: Mexican hat potential as defined in Eq. (1.10). The case $\mu^2 > 0$ is shown in (a) has a symmetric ground state at $\sigma = \pi = 0$. For $\mu^2 < 0$ an infinite number of degenerate ground states lie on the circle around $\sigma^2 + \pi^2 = \mu^2/\nu^2$, while $\sigma = \pi = 0$ is a local maximum. The choice of a ground state breaks the symmetry spontaneously.

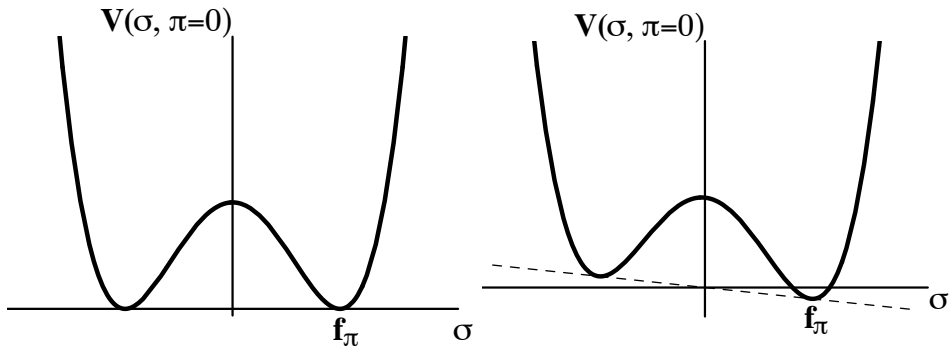

(a) Symmetric Potential **(b)** Tilted Potential

Figure 1.9: Mexican Hat Potential at $\pi = 0$. In case of (b) the potential is tilted along the σ field breaking explicitly the chiral symmetry

eigenvalues E_n. For a non-interacting hadron gas the leading order result to Eq. (1.16) with respect to the vacuum expectation value for low densities is:

$$\frac{\langle\langle\overline{q}q\rangle\rangle}{\langle\overline{q}q\rangle} \simeq 1 - \frac{\Sigma_\pi \rho_\pi^2(T)}{f_\pi^2 m_\pi^2} \tag{1.17}$$

$$= 1 - \frac{(N_f^2-1)}{N_f}\frac{T^2}{12f_\pi^2} + \frac{(N_f^2-1)}{2N_f}\left(\frac{T^2}{12f_\pi^2}\right)^2 - N_f(N_f^2-1)\left(\frac{T^2}{12f_\pi^2}\right)^3 \ln\left(\frac{\Lambda_q}{T}\right) + \mathcal{O}(T^8). \tag{1.18}$$

The scale $\Lambda_q = 470 \pm 110$ MeV is fixed from pion scattering data. To first order the quark condensate at low densities decreases quadratically with the temperature. Analog, the result for finite nuclear densities and low temperatures is a linear decrease with density:

$$\frac{\langle\langle\overline{q}q\rangle\rangle}{\langle\overline{q}q\rangle} \simeq 1 - \frac{\Sigma_N \rho_N^2(\mu_N)}{f_\pi^2 m_\pi^2} \tag{1.19}$$

with baryon density $\mu_N = 3\mu_q$. At nuclear matter densities ($\rho_0 = 0.17$ fm^{-3}) the quark condensate has dropped by 35% with a experimentally determined nucleon σ-term of $\Sigma_N \approx 45$ MeV. Based on these calculations one can derive a prediction of the scalar quark condensate $\langle\overline{q}q\rangle$ as function of temperature and density, which is shown in Fig. 1.10 [33].

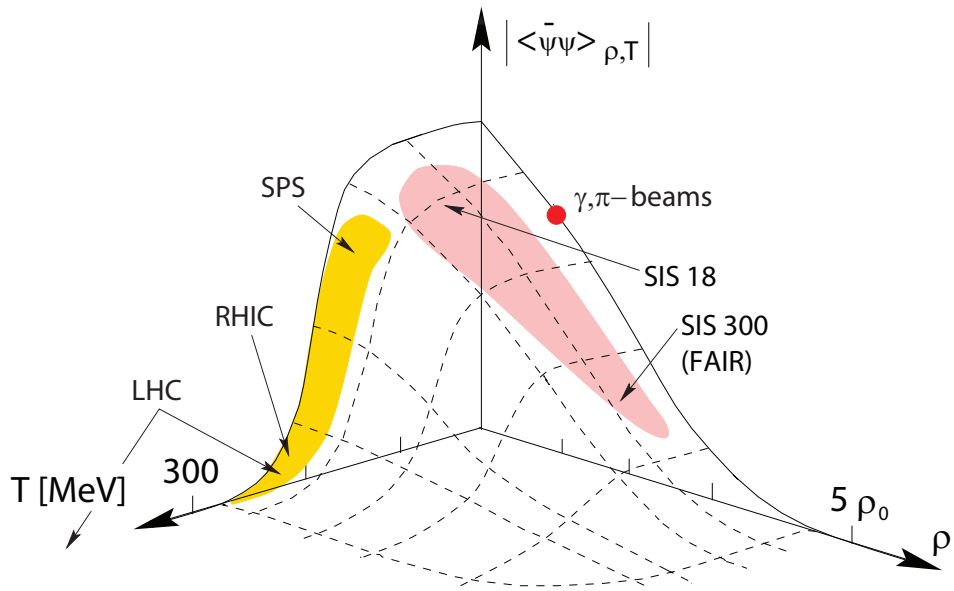

Figure 1.10: The expectation value of the chiral condensate as function of temperature T and nuclear matter density ρ as calculated with the Nambu-Jona-Lasinio model [33]. Figure based on [34].

Based on connections between hadron masses and the quark condensate various scenarios for the change of meson masses with decreasing quark condensates are proposed. Brown and Rho predict in [35] a dropping of the ρ mass by 15–20% at normal nuclear matter densities and a universal Brown-Rho (BR) scaling of the in-medium vector meson masses with the in-medium pion decay constant f_π^*:

$$\frac{\langle\langle\overline{\psi}\psi\rangle\rangle}{\langle\overline{\psi}\psi\rangle} = \left(\frac{f_\pi^*}{f_\pi}\right)^3 \quad \text{and} \quad \frac{f_\pi^*}{f_\pi} = \frac{m_\sigma^*}{m_\sigma} = \frac{m_N^*}{m_N} = \frac{m_\rho^*}{m_\rho} = \frac{m_\omega^*}{m_\omega} \tag{1.20}$$

Other models explain medium modification of vector mesons by interactions with surrounding hadrons in the hot and dense medium. For an excellent review see, *e. g.*, Ref. [3].

1.2 Dileptons

Dileptons are produced during all stages of the collisions and carry a variety of signals. In this Section the various sources are discussed.

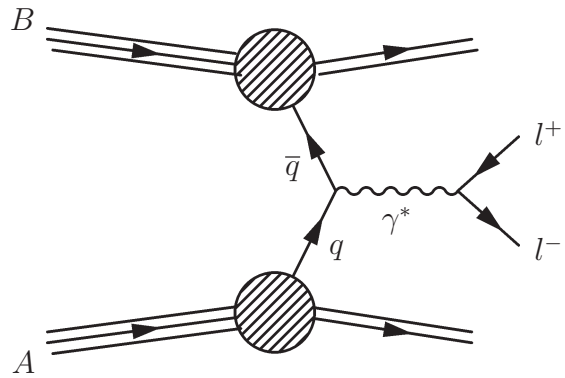

Figure 1.11: Feynman diagram for the production of a dilepton pair via the Drell-Yan process.

1.2.1 Drell-Yan

In a collision of two nuclei, the Drell-Yan process is the annihilation of a quark in one nucleus with a sea antiquark from the other nucleus into a virtual photon which subsequently converts into a lepton pair. This process is shown in Fig. 1.11 for two nuclei A and B and has particular important at large invariant masses ($m_{ll} > 3$ GeV/c^2). At high energies the invariant mass of the lepton pair m_{ll} is given by the product of the quark momenta $x_1\sqrt{s}$ and $x_2\sqrt{2}$:

$$m_{ll}^2 = x_1 x_2 s \tag{1.21}$$

with $\sqrt{s}$ the center of mass energy of the incoming nuclei. The cross section of Drell-Yan dilepton production can be calculated to leading order using parton distribution functions obtained from deep inelastic lepton-nucleon collisions. An additional factor $K \approx 2$ accounts for higher order corrections in α_s is necessary to describe experimental dilepton data.

One can show that in collisions of two equal nuclei with mass number A (*e. g.*, for gold: $A_\mathrm{Au} = 197$), the contribution of dileptons from the Drell-Yan process scales with respect to the nucleon-nucleon case as $A^{4/3}$ [36]. In a thermalized partonic medium the same process, *i. e.*, $q\overline{q} \rightarrow e^+e^-$, is possible between quarks and antiquarks with thermal momentum distributions. Theoretical models predict such a contribution to be dominant in the intermediate mass region.

1.2.2 Open Charm and Bottom

Another contribution to the dilepton continuum are semi-leptonic decays of charm and bottom mesons. Heavy quark pairs ($Q\overline{Q} = c\overline{c}$ or $b\overline{b}$, respectively)

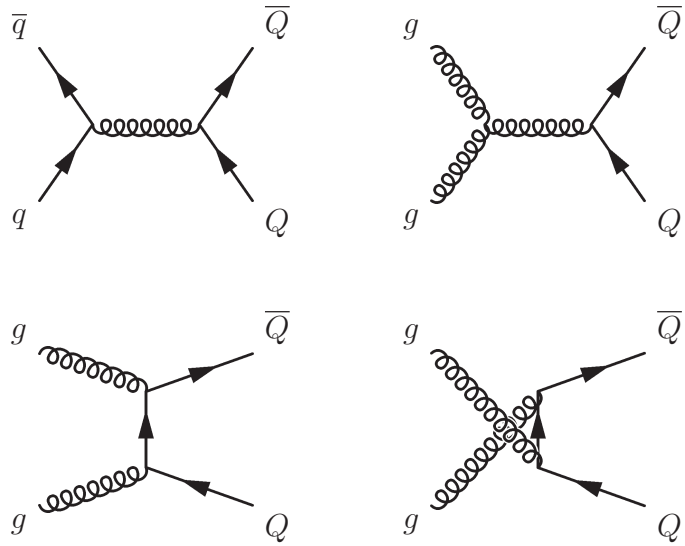

Figure 1.12: Leading order processes of heavy quark production.

are produced in nucleon-nucleon collisions in inelastic hard-scattering processes between constituent quarks of the two nucleons ($q\overline{q} \rightarrow g^* \rightarrow Q\overline{Q}$). The lowest order diagrams for heavy quark production are shown in Fig. 1.12. In addition to the annihilation of two light quarks into a virtual gluon, heavy quarks can be produced by interactions of a gluon of one nucleon with a gluon in the other nucleon ($gg \rightarrow g^* \rightarrow Q\overline{Q}$).

Open charm and bottom mesons are formed out of a heavy quark and a light antiquark ($\overline{u}$, $\overline{d}$, or $\overline{s}$) or a heavy antiquark and a light quark, *e. g.* $D^+ = c\overline{d}$, $B^+ = u\overline{b}$. After production of a heavy quark pair, the quarks undergo fragmentation and can form a D^+D^- pair. Due to the large mass of the c quark, the D^+D^- pair preserves most of the initial correlation of the $Q\overline{Q}$ pair. The charmed (or bottom) mesons then can undergo weak decays into, *e. g.*, $D^+ \rightarrow \overline{K}^0 l^+ \nu_l$. The total branching ratio of semi-leptonic decays of a D meson is on the order of 10%. The semi-leptonic decays of both the D^+ and the D^- results in the creation of a dilepton pair.

Perturbative QCD calculations to leading order are not able to fully describe charm production in nucleon-nucleon collisions. Similar to the Drell-Yan process, a K factor has to be employed to correct for the difference to the measured charm cross section. Higher order calculations such as next-to-leading order (NLO), for which exemplary processes are shown in Fig. 1.13, and fixed-order-plus-next-to-leading order (FONLL) are in agreement with the D meson cross section measured by CDF in $p\overline{p}$ collisions at $\sqrt{s} = 1.96$ TeV [37] as well as with measurements of single electrons [16] and muons [38] from semi-leptonic

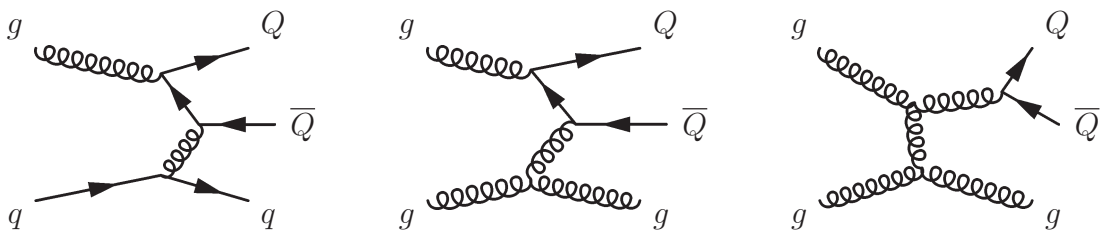

Figure 1.13: Examples of next-to-leading order processes contributing to the production of heavy quark pairs.

charm decays performed by PHENIX in $p+p$ collisions at $\sqrt{s} = 200$ GeV. However, the theoretical uncertainties are large and the data prefer larger cross sections within these uncertainties.

Shown in Fig. 1.14 is the invariant differential cross sections of electrons from heavy flavor decays [16] in comparison to a FONLL calculation [39]. The shape of the FONLL is in good agreement with the data, overall the data are a factor of ≈ 1.7 higher than the calculation, as visible in the bottom panel of the same figure, which shows the ratio of data to FONLL.

In the absence of medium modifications, the production of particles by inelastic hard scattering processes in heavy ion collision is given by the production cross section in $p+p$ collisions scaled by the nuclear overlap factor T_{AB}, which is the integral over the product of the thickness functions of the two colliding nuclei A and B in the geometric overlap region (or T_{AA} in case of two identical nuclei A). There is a simple relation between the nuclear overlap factor, the inelastic $p+p$ cross section and the average number of binary nucleon-nucleon collisions occurring in a nucleus-nucleus collisions: $T_{AA} = \langle N_{\text{coll}} \rangle / \sigma_{pp}$.

In order to quantify the deviation of the yield measured in a nucleus-nucleus collision from the binary scaled $p+p$ expectation the nuclear modification factor R_{AA} is defined as:

$$R_{AA} = \frac{dN_{AA}}{T_{AA}\, d\sigma_{pp}} = \frac{dN_{AA}}{\langle N_{\text{coll}} \rangle\, dN_{pp}} \tag{1.22}$$

were dN_{AA} (dN_{pp}) is the differential particle yield measured in the nucleus-nucleus ($p+p$) collision, and $d\sigma_{pp} = \sigma_{pp}\, dN_{pp}$.

In Au + Au collisions at $\sqrt{s_{NN}} = 200$ GeV the single electron spectra from heavy flavor decays are strongly modified with respect to the expected yield form a hard probe [15]. Their nuclear modification factor is shown in Fig. 1.15. At high p_T single electrons from heavy flavor decays are suppressed with respect the binary scaled yield of electrons in p+p collisions. Furthermore,

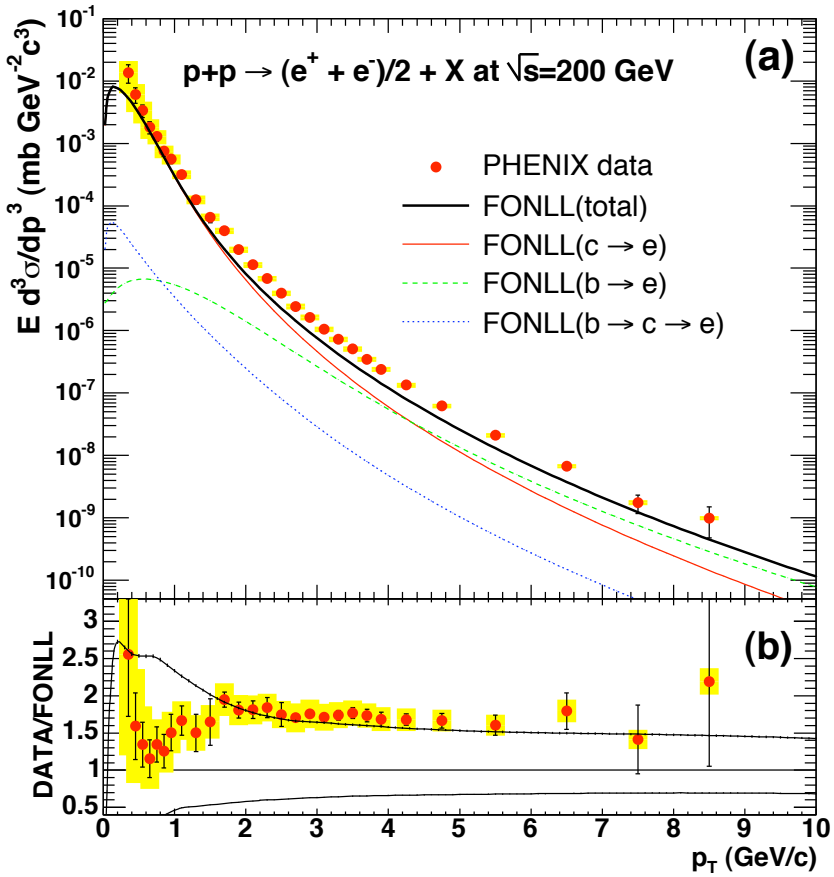

Figure 1.14: (a) Shown is the differential cross section of electrons from heavy flavor decays in $p+p$ collisions at $\sqrt{s} = 200$GeV [16]. The data are compared to the central value of a FONLL calculation [39]. (b) Ratio of data to FONLL calculation. The upper (lower) curve show the upper (lower) theoretical limit of the FONLL calculation.

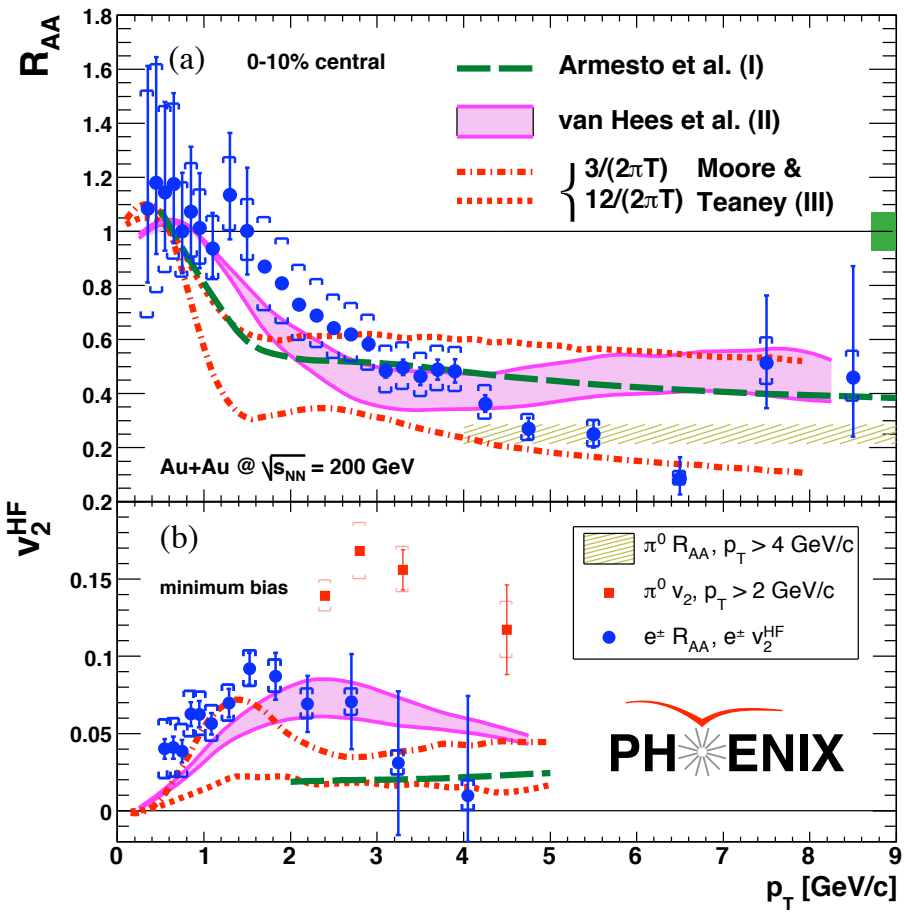

Figure 1.15: (a) Shown is the nuclear modification factor R_{AA} of electrons from heavy flavor decays. (b) Elliptic flow of electrons form heavy flavor decays. A comparison to various models of medium effects is shown [15].

they exhibit significant elliptic flow, measured as the second Fourier coefficient v_2 in the expansion of the azimuthal particle distribution, shown in the bottom panel of Fig. 1.15. Both these effects indicate that charm quarks are subject to significant energy loss and may thermalize in the medium created in $\mathrm{Au}+\mathrm{Au}$ collisions at $\sqrt{s_{NN}} = 200$ GeV. This should leave an imprint also in the e^+e^- pair spectrum in the IMR, where dielectrons from open charm decays are the dominant contribution.

1.2.3 Direct Photons

Direct photons are another important electromagnetic probe of the medium created in heavy ion collisions. As discussed below, direct photons are not

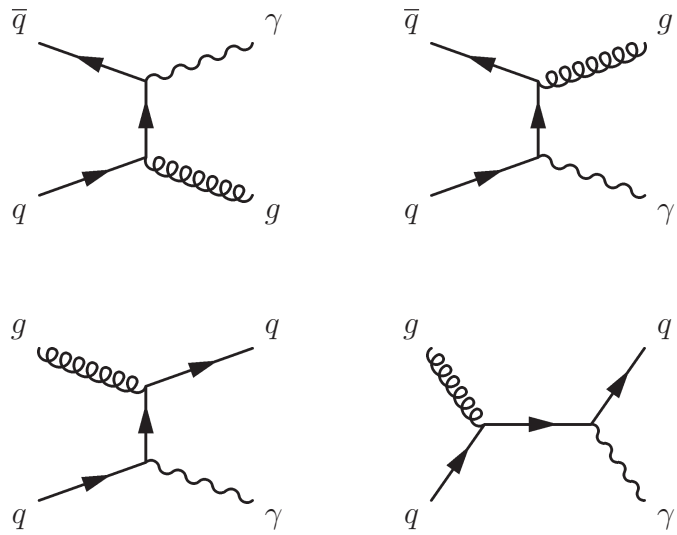

Figure 1.16: Feynman diagrams for direct photon production to leading order. The top row represents the annihilation process, the bottom two graphs the Compton process.

only created as massless real photons, but also as virtual photons with non-zero mass, which internally convert into a dilepton pair.

Direct photons are produced by inelastic scattering processes between the incoming partons. The lowest order processes as shown in Fig. 1.16 are quark-antiquark annihilation into a gluon and a photon and quark-gluon Compton scattering producing a quark and a photon.

The production of direct photons in $p+p$ collisions at $\sqrt{s} = 200$ GeV has been measured by PHENIX [40]. The measured direct photon cross section is in excellent agreement with NLO pQCD calculations [41–44] as shown in Fig. 1.17. The three curves which are shown correspond to three different choices of the momentum scale $\mu = 0.5p_T$, $1.0p_T$, $2.0p_T$. There are actually three different scales involved: the renormalization scale μ_R, the factorization scale μ_F, and the fragmentation scale μ'_F. The fragmentation scale is included, because the calculation includes direct photons from parton fragmentation into photons. All three scales are set to a common value $\mu = \mu_R = \mu_F = \mu'_F$.

In Au+Au collisions, direct photons have been measured at high p_T in various centrality bins [45]. The nuclear modification factor R_{AA} for direct photons with $p_T > 6$ GeV/c is shown in Fig. 1.18 as function of the participating nucleons N_{part}. The production of direct photons is consistent for all centralities T_{AA} scaled direct photons cross section measured in $p+p$, *i. e.*, $R_{AA} = 1$, *i. e.*, the assumption that direct photons with transverse momenta above ≈ 6 GeV/c are produced by inelastic scattering processes between the incoming partons

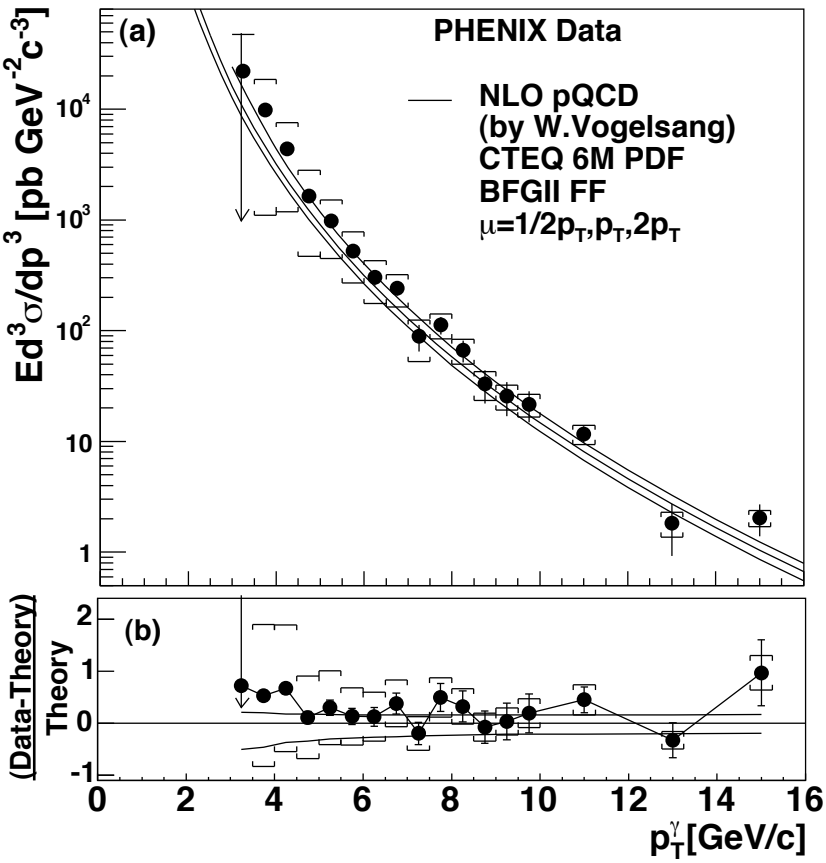

Figure 1.17: Direct photon section measured in $p + p$ collisions at $\sqrt{s}$ = 200GeV [40]. The data are compared with a NLO pQCD calculation [41–44]. The bottom panel shows the ratio of data to theory.

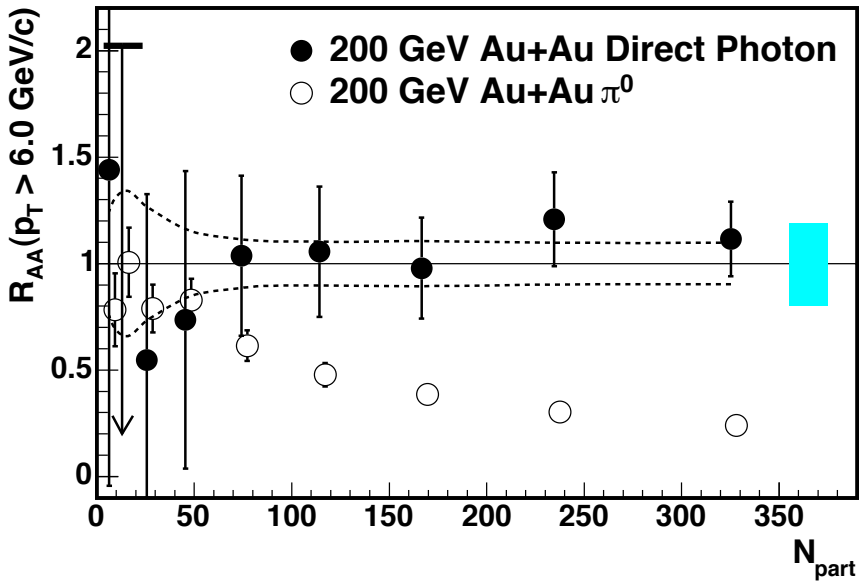

Figure 1.18: Nuclear modification factor of direct photons and π^0's with $p_T > 6.0$ GeV/c as function of N_{part} [45].

and escape the medium unperturbed by final state interactions. This observation is supporting evidence that the observed π^0 suppression [46], also shown in Fig. 1.18, is indeed a final state effect due to energy loss of the partons in the hot and dense medium. At very high p_T a deviation from one is observed which may, while still under investigation and despite large uncertainties, be attributed to isospin differences between the proton and a gold nucleon [47].

As direct photons carry the information about the momentum distribution of the partons involved in their production, the momentum distribution of direct "thermal" photons produced by partons in a thermalized medium directly reflects the temperature of the medium.

In Au + Au collisions at RHIC energies, thermal photons are predicted to be the dominant source of direct photons in $1 < p_T < 3$ GeV/c [48]. This is illustrated in Fig. 1.19 which shows the predicted contributions to the total direct photon spectrum; from the initial hard scattering dominating the direct photon yield for $p_T > 3$ GeV/c, and the relatively soft thermal emission of from the hadron gas being the main contributor at $p_T < 1$ GeV/c, leaving a window for QGP radiation at $1 < p_T < 3$ GeV/c. As initial conditions a formation time of $\tau_0 = 0.33$ fm and a initial temperature $T = 370$ MeV were used.

However, the inclusive photon yield is dominated by a large background of

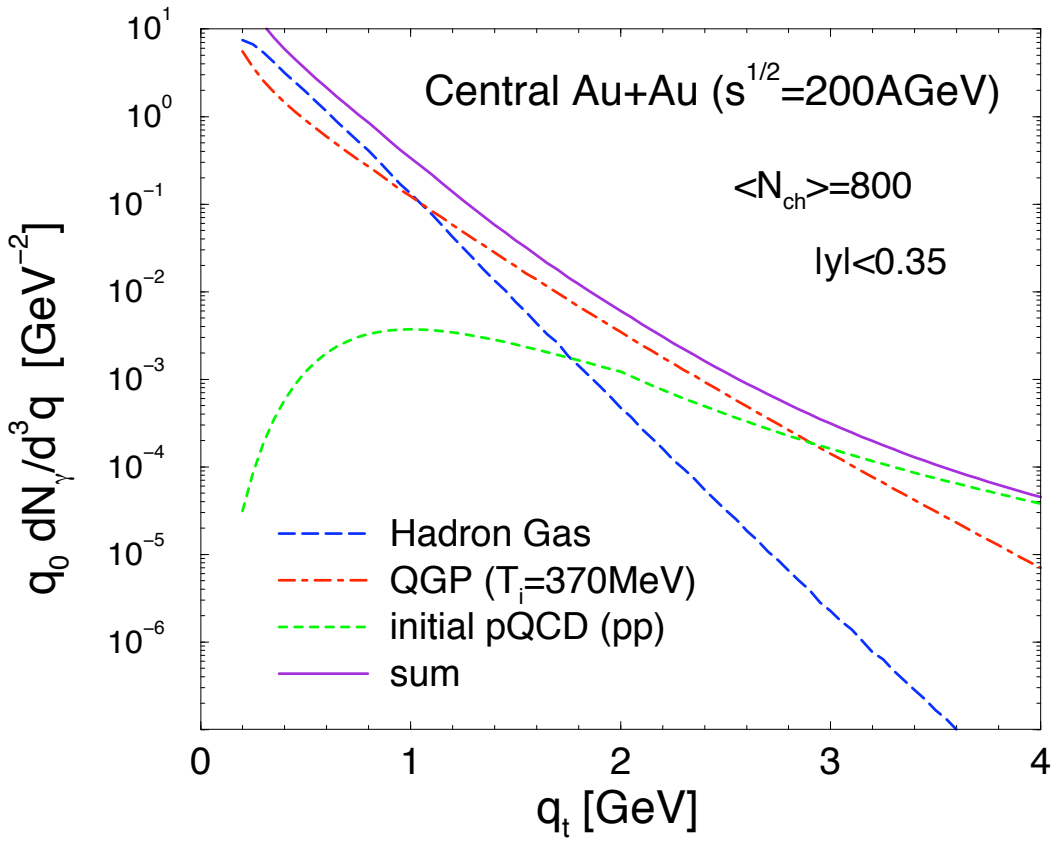

Figure 1.19: Direct photon emission from central Au+Au collisions at $\sqrt{s_{NN}} = 200$ GeV as function of transverse momentum. The *short dashed* line shows the predicted contribution of photons form the initial hard scattering processes, the *dashed-dotted* line thermal radiation from the QGP and the *long-dashed* line emission from the hadron gas.[48].

hadron decays such as $\pi^0 \to \gamma\gamma$ for $p_T \lesssim 5$ GeV/c, limiting the measurement of direct photons at low p_T with the Electromagnetic Calorimeter (EMCal) in PHENIX, which is based on a statistical subtraction of the decay photon background. The uncertainties in the knowledge of the decay background can be reduced by avoiding its explicit measurement, but rather tagging of the decay photons [49]. Furthermore, to circumvent the limitations due to the energy resolution at low photon energies, the excellent capabilities of the PHENIX detector to measure electrons have been utilized by measuring photons via their external conversion into e^+e^- pairs, a method discussed in Appendix B.

In contrast to massless real photons, virtual photons bring an additional observable, their invariant mass, which as discussed in the following brings the advantage of measuring thermal photons in a better signal to background region than real photons. In general any source of real photons, *e. g.* the ones shown in Fig. 1.16, can also create a virtual photon which is emitted as e^+e^- pair. The relation between photon production and the associated e^+e^- pair production can be written as [50]:

$$\frac{d^2n_{ee}}{dm_{ee}} = \frac{2\alpha}{3\pi}\frac{1}{m_{ee}}\sqrt{1-\frac{4m_e^2}{m_{ee}^2}}\left(1+\frac{2m_e^2}{m_{ee}^2}\right)Sdn_\gamma \tag{1.23}$$

with m_{ee} being the invariant mass of the e^+e^- pair and $m_e = 511$ keV/c^2 the mass of the electron. The process dependent factor S aproaches 1 as $m \to 0$ or $m \ll p_T$. For π^0 and η decays, S is given by $S = |F(m_{ee}^2)|^2(1-m_{ee}^2/m_h^2)^3$ [51] where m_h is the hadron mass and $F(m_{ee}^2)$ the form factor. For e^+e^- pair masses approaching m_h, the factor S goes to zero. While the measurement of real thermal photons suffers from a large background of hadron decays (80% of the background comes from π^0 decays), measuring virtual photons allows to select a mass range $m_{ee} > m_{\pi^0} = 135$ MeV/c^2, in which the signal to background ratio is improved by a factor five, thus allowing a 10% signal of direct photons to be observed as a 50% excess of e^+e^- pairs.

For quark-gluon Compton scattering the exact relation between the photon production process and the e^+e^- pair process can be calculated as [52]:

$$\frac{d^3n_{ee}}{dm_{ee}\,dt} = \frac{2\alpha}{3\pi}\frac{1}{m_{ee}}\sqrt{1-\frac{4m_e^2}{m_{ee}^2}}\left(1+\frac{2m_e^2}{m_{ee}^2}\right)(1+\frac{2u}{t^2+s^2}m_{ee}^2)\frac{dn_\gamma}{dt} \tag{1.24}$$

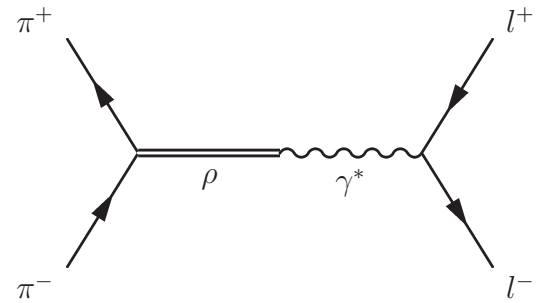

Figure 1.20: Vector dominance model in dilepton production via $\pi^+\pi^-$ annihilation.

in which the Mandelstam variables s, t, and u are defined as:

$$s = (p_q + p_g)^2 \tag{1.25a}$$
$$t = (p_q - p_\gamma)^2 \tag{1.25b}$$
$$u = (p_q - p'_q)^2 \tag{1.25c}$$

with the four-momentum vectors of the incoming quark p_q, incoming gluon p_g, the outgoing real or virtual photon p_g, and the outgoing quark p'_q. Comparing Eq. (1.24) with Eq. (1.23), the process specific S factor for the quark-gluon Compton process can be identified as:

$$\begin{aligned} S &= 1 + \frac{2u}{t^2 + s^2} m_{ee}^2 \\ &= 1 - \frac{2x}{(x + \sqrt{1+x^2})(3x^2 + 1 + 2x\sqrt{1+x^2})} \end{aligned} \tag{1.26}$$

with $x = m_{ee}/p_T$ which for $p_T \gg m_{ee}$ simplifies to $S \approx 1$.

1.2.4 Medium Modifications of Vector Mesons

At later stages of the collision, after the medium has expanded and cooled down below the critical temperature, quarks and gluons are confined to hadrons in a hadron gas. The dominant dilepton production during this stage is expected from pion and kaon annihilation and scattering between other hadrons. The cross section for $\pi\pi$ scattering is dynamically enhanced through the formation of light vector mesons ρ, ω, and ϕ. As these vector mesons carry the same quantum numbers as a photon, they couple according to the vector dominance model (VDM) directly to a lepton pair: $\pi^+\pi^- \to \rho \to \gamma^* \to l^+l^-$ [53]. Thus the invariant mass of the lepton pair directly reflects the mass distribution

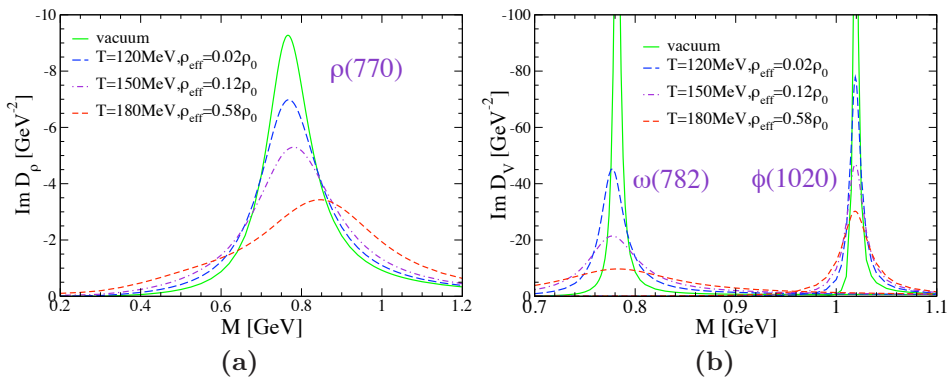

Figure 1.21: In-medium spectral function of the vector mesons for different temperatures and densities [54, 55].

of the vector meson at the time of its decay. As the lifetime of the ρ meson ($\tau \approx 1.3$ fm) is shorter than the lifetime of the hadron gas ≈ 10 fm, most of the ρ mesons will decay in-medium imprinting any medium effect on the lepton pair. The invariant mass distribution of e^+e^- pairs from ρ decays is given by the ρ spectral function (modulo a thermal Bose factor f_B). Schematically ρ spectral function as function of its energy ω and 3-momentum $\vec{q}$, defined as the imaginary part of the propagator, can be presented in the form of:

$$D_\rho(\omega, \vec{q}) = \frac{\mathrm{Im}\,\Sigma_\rho(\omega, \vec{q})}{|\omega^2 - q^2 - m_\rho^2 + \mathrm{Re}\,\Sigma_\rho(\omega, \vec{q})|^2 + |\,\mathrm{Im}\,\Sigma_\rho(\omega, \vec{q})|^2}, \tag{1.27}$$

with the ρ the pole mass m_ρ. The ρ self-energy Σ_ρ includes the summation of all scattering amplitudes which includes in-medium interactions with baryons and mesons which broaden the spectral function.

As an example, a prediction of the spectral functions of ρ, ω, and ϕ at RHIC energies by R. Rapp [54, 55] is shown in Fig. 1.21. Recent reviews of the role of the ρ meson in dilepton emission can be found, *e. g.*, in Refs. [3, 56–59]. In this calculation the ρ and ω spectral function shows the strong broadening towards higher temperatures and densities, *i. e.*, towards the phase boundary. The slight upward shift in mass is due to repulsive parts in the self energy, *e. g.*, from baryonic particle-hole excitations. The ϕ does not show such strong modifications, but at the highest temperatures the width is significantly increased by a factor of ≈ 7.

This explains the special role of the light vector mesons, and their in-medium modifications, in dilepton measurements. In contrast, heavier vector mesons such as the J/ψ or the Υ have a substantially longer lifetime and decay predominantly after freeze out. Also they carry information of modifications

to heavy quarks, *e. g.*, suppression, but it is in the magnitude of their signal rather than their spectral shape, see *e. g.* Ref. [60].

After the thermal freeze out temperature is reached, the dominant sources of lepton pairs are resonance and Dalitz decays of light mesons with their vacuum properties, such as π^0, η, η'. ω, and ϕ.

1.3 Previous Experimental Results

A number of experiments have measured the dilepton continuum in heavy ion collisions under a variety of conditions. The chapter gives a brief summary of their results, but is by no means meant to be complete. Section 1.3.1 summarizes the recent results of the HADES experiment at the SIS accelerator at GSI. Section 1.3.2 presents the result of the NA45/CERES collaboration at the SPS accelerator at CERN. The measurement of the dimuon continuum by the NA60 collaboration is summarized in Section 1.3.3. The section concludes with the direct photon measurement of the WA98 collaboration in Section 1.3.4.

1.3.1 HADES

The High Acceptance DiElectron Spectrometer (HADES) is a fixed target experiment at SIS accelerator at GSI. It has measured the dielectron continuum up to $m_{ee} = 1$ GeV/c^2 in low energy collisions of light ions, such as C-C at 1 and 2 AGeV [61, 62] as shown in Fig. 1.22. The yield of e^+e^- pairs is compared to a cocktail of decays of $\pi^0 \to \gamma e^+e^-$, $\eta \to \gamma e^+e^-$, $\omega \to \pi^0 e^+e^-$, and $\omega \to e^+e^-$. While the mass region below 150 MeV/c^2 is well explained by the cocktail, an enhanced yield of e^+e^- pairs in the mass region of 0.15–0.50 GeV/c^2 above the cocktail is observed. Also including in addition ρ and Δ resonance decays does not fully explain the measured yield. HADES also compared the yield of e^+e^- pairs to the results of the DLS experiment [63] and finds them in good agreement [61, 64] challenging current theoretical descriptions of the dielectron production at these energies. The excess yield scales as the π^0 yield with increasing beam energy, rather than the η yield [61]. From preliminary results [65] from elementary reactions ($p - p$, $n - p$) it has been shown that a isospin dependent Bremsstrahlung contribution, increased by a factor of ≈ 4 with respect to early theoretical calculations, can almost entirely explain the excess observed in C-C collisions at the same energy [66, 67]. This clearly shows the importance of a baseline measurement in elementary collisions at the same energy as the heavy-ion collisions.

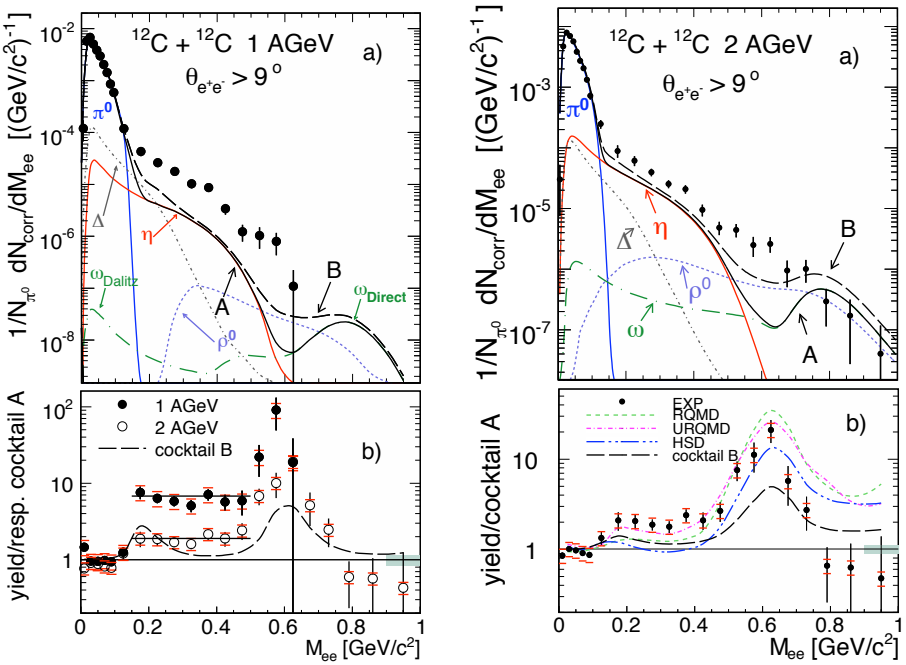

(a) C-C at 1 AGeV [61] **(b)** C-C at 2 AGeV [62]

Figure 1.22: Invariant mass spectrum of e^+e^- pairs measured by HADES in C-C collisions at 1 AGeV (a) and 2 AGeV (b), respectively. The measured yields are compared to a cocktail of e^+e^- pairs from decays of π^0, η and ω (cocktail A, *solid line*). A second cocktail, including Δ and ρ resonance decays is shown as *dashed line* (cocktail B). The bottom panels show the ratios of data and cocktail A.

1.3.2 NA45/CERES

The NA45 experiment[4] better known as ChErenkov Ring Electron Spectrometer (CERES) was a fixed target experiment at the Super Proton Synchrotron (SPS) at CERN. It has measured the dielectron continuum in heavy-ion reactions at kinetic beam energies of 40–200 AGeV [68–70].

While the e^+e^- pair yield in proton induced collisions such as p-Be (as shown in Fig. 1.23a) and p-Au at 450 AGeV is fully reproduced by a cocktail of hadron decays, an enhanced yield for $m_{ee} \geq 200$ MeV/c^2 has been observed in S-Au collisions at 200 AGeV which is shown in Fig. 1.23b [68]. CERES has also measured a low mass enhancement of e^+e^- pairs in Pb-Au collisions at 40 and 158 AGeV. At the latter energy the p_T and centrality dependence of the enhancement have been studied, which was found to be localized at low p_T and to increase stronger than linear with the charged particle density [70] suggesting binary annihilation processes such as $\pi^+\pi^- \to \rho \to \gamma^* \to e^+e^-$. Their results are compared to model calculations of three scenarios, (i) free $\pi\pi$ annihilation in vacuum, (ii) assuming Brown-Rho scaling of the in medium ρ meson [71], and (iii) a modified in-medium ρ spectral function [3]. The models have employed a thermal fireball model to include the full time evolution of the system which includes the experimentally determined freeze out conditions $(T, \rho_B)_{\text{fo}} = (115\text{ MeV}, 0.33\rho_0)$ and initial conditions of $(T, \rho_B)_{\text{init}} = (190\text{ MeV}, 2.55\rho_0)$, as well as a finite pion chemical potential. For the dropping mass scenario a in-medium mass of:

$$m_\rho^* = m_\rho \left(1 - C\frac{\rho_B}{\rho_0}\right)\left(1 - \frac{T}{T_c^\chi}\right)^\alpha \tag{1.28}$$

with $C = 0.15$, $T_c^\chi = 200$ MeV and $\alpha = 0.3$ has been assumed. Clearly, the in vacuum $\pi\pi$ annihilation fails to describe the data, it gives too much yield at the ω resonance peak and too little in the mass range $0.2 < m_{ee} < 0.7$ MeV/c^2, which leads to the conclusion that in-medium modifications must play a role. Within the experimental uncertainties both the dropping mass as the in-medium collisional broadening scenarios give a reasonable description of the enhanced dielectron yield.

1.3.3 NA60

The NA60 experiment at SPS was created out of the NA50 experiment[5] [73] upgraded with a silicon-vertex tracker. NA50 had measured $\mu^+\mu^-$ pairs, rather

[4] named after its location in the North Area of the SPS, in contrast to the West Area
[5] itself an upgrade of the NA38 experiment [72] to study Pb-Pb collisions

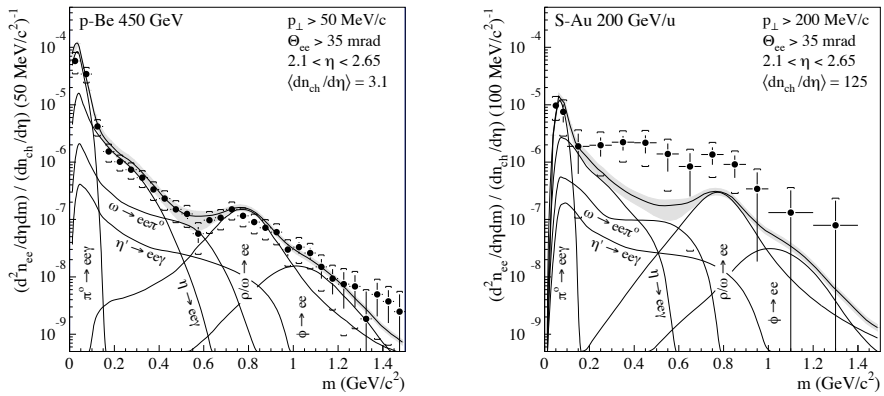

(a) p-Be at 450 AGeV **(b)** S-Au at 200 AGeV

Figure 1.23: Invariant mass spectrum of e^+e^- pairs measured by CERES in p-Be collisions at 450 AGeV (a) and S-Au collisions at 200 AGeV (b), respectively. The measured yields are compared to a cocktail of e^+e^- pairs from hadron decays; the various sources are shown individually. While the cocktail agrees with the measured yield of e^+e^- pairs in p-Be collisions, an enhancement above the cocktail is observed in Pb-Au collisions [68].

than e^+e^- pairs eliminating the major background source of π^0 Dalitz decays due to the larger muon mass ($m_\mu = 105.66$ MeV/c^2). For Pb-Pb collisions at 158 AGeV, they reported an enhanced dimuon yield in the intermediate mass region of $1.15 < m_{\mu\mu} < 2.56$ GeV/c^2 of up to a factor of ≈ 1.65 above the expected sources from open charm decays and Drell-Yan [74]. They were able to rule out an enhanced Drell-Yan production, as the mass shape of the enhancement was much steeper then expected for Drell-Yan and concluded the enhancement was consistent with a charm production enhanced with respect to the one observed in p-A collisions, but did not excluded the contribution of thermal radiation.

The upgrade with a silicon-vertex tracker allowed NA60 to determine the distance between the muon tracks and the collision vertex. Due to the long life-time of D mesons, their decays vertex would be offset from the collision vertex in contrast to a prompt source of $\mu^+\mu^-$ pairs [75]. Fig. 1.25a shows the invariant mass spectrum of excess $\mu^+\mu^-$ pairs compared to the expected shapes from open charm decays and Drell-Yan [76]. The shape is compatible with semi-leptonic decays of charmed mesons. Fig. 1.25b shows the weighted offset distribution of all $\mu^+\mu^-$ pairs. The weight in the $\mu^+\mu^-$ pair offset from the vertex considers the momentum dependent resolution of the vertex measurement of a muon. The distribution of $\mu^+\mu^-$ pairs is fitted with the expected shapes from open charm and prompt decays. The result is compatible with

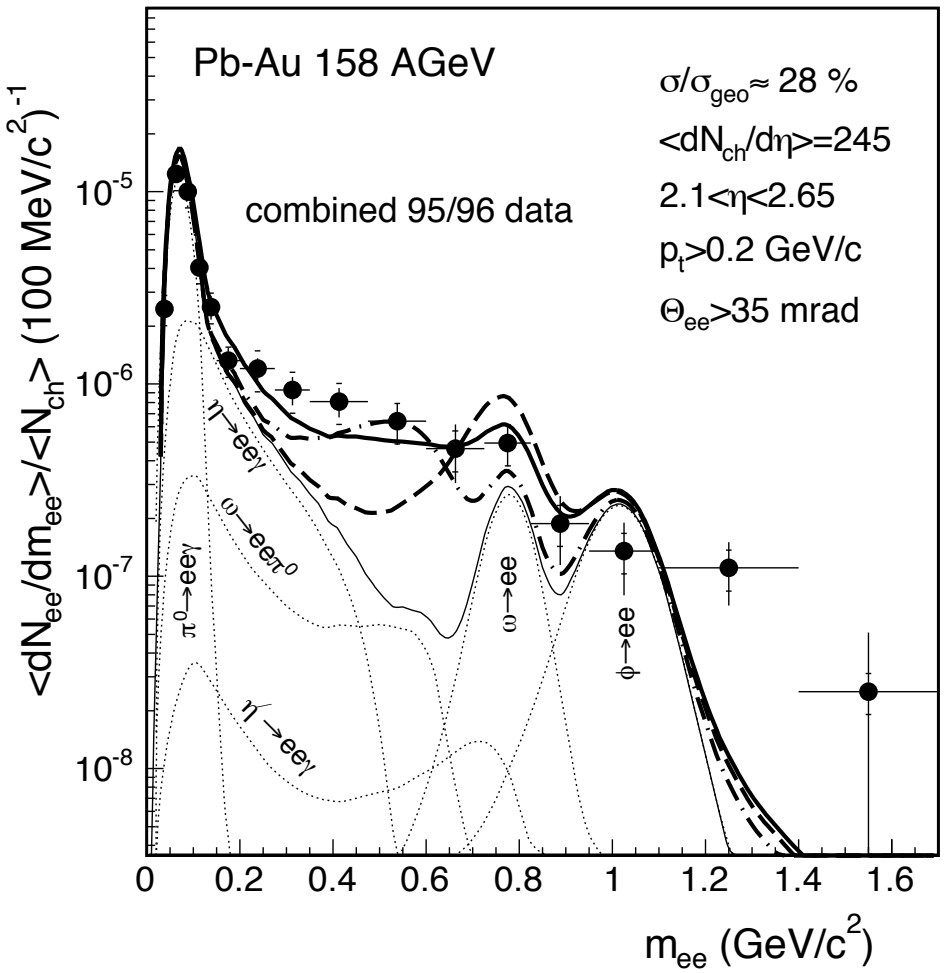

Figure 1.24: Invariant mass spectrum of e^+e^- pairs measured by CERES in Pb-Au collisions at 158 AGeV. The measured yield is compared to a cocktail of e^+e^- pairs from free hadron decays and (i) without ρ decays (*thin line*), (ii) a vacuum ρ spectral function (*thick dashed line*) [71], (iii) a dropping in-medium ρ mass (*thick dashed-dotted line*) [3], (iv) a medium-modified ρ spectral function (*thick solid line*) [70].

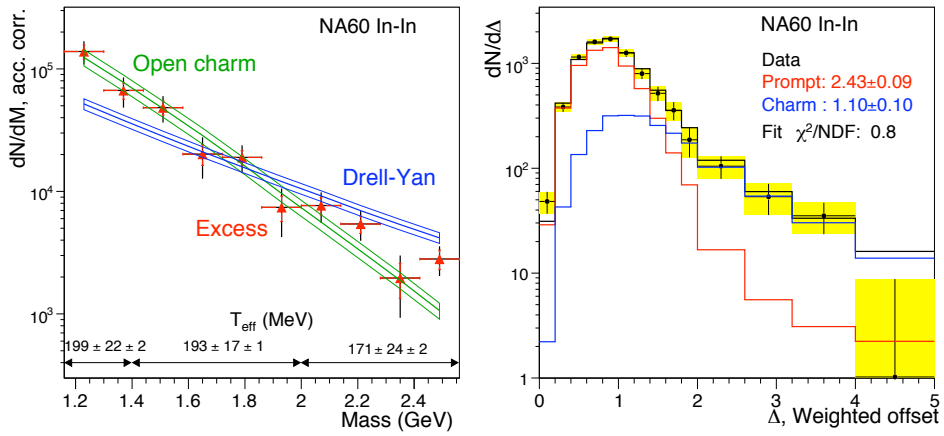

(a) (b)

Figure 1.25: Shown in (a) is the mass distribution of the acceptance corrected excess yield compared to the expected shapes from open charm and Drell-Yan decays. A fit of prompt and charm decays to the weighted offset distribution of $\mu^+\mu^-$ pairs in the intermediate mass region is shown in (b) [76].

an open charm yield as extrapolated from the NA50 p-A result and a prompt excess with an enhancement factor of 2.4 over the Drell-Yan contribution.

Furthermore, NA60 has observed an enhancement in the low mass dimuon continuum in In-In collisions at 158 AGeV shown in Fig. 1.26a [76–78]. The high precision of the data allowed them to subtract all sources of hadron decays (besides the contribution of ρ decays) and extract the enhancement. The two scenarios which were in reasonable agreement with the CERES data as shown in the previous chapter, an in-medium broadened ρ spectral function [3] and the dropping mass [71] are compared to the excess yield in Fig. 1.26b. While the broadening scenario is in good agreement, the Brown-Rho scaling does not explain the observed enhancement.

The m_T spectra of the excess yield is shown in Fig. 1.27a for four slices in mass and the ϕ. They are fitted to an exponential and the inverse slope parameter T_{eff} is shown in Fig. 1.27b together with the results of the same fitting procedure of the excess yield observed in the intermediate mass region. The inverse slope of the low mass enhancement follows closely the trend observed for the hadrons η, ω and ϕ which is consistent with the expected linear increase due to radial flow indicated by the solid line $T_{\text{eff}} = T_{\text{fo}} + m\langle\beta_T\rangle$. The effective temperature of the vacuum ρ is much higher, which is interpreted as a later decoupling of the ρ from the medium and therefore obtaining a larger radial flow. Above the ϕ meson the effective temperature suddenly drops and stays constant with mass. This behaviour is consistent with an thermal emission from

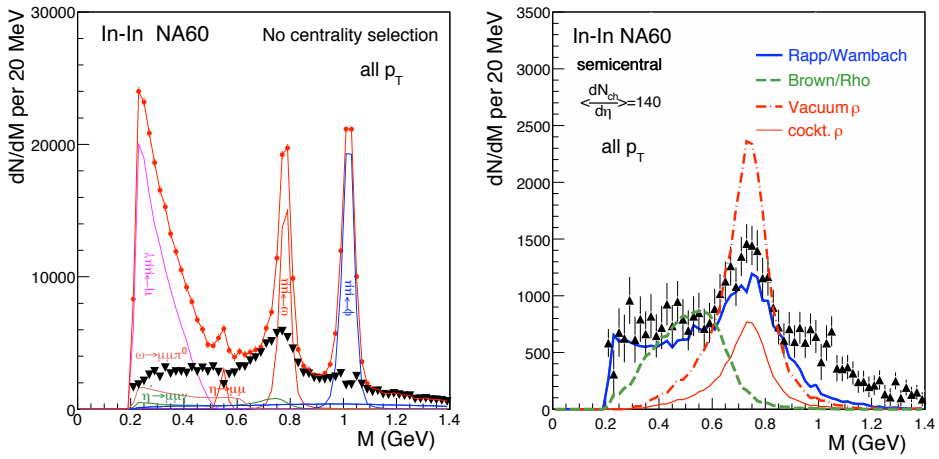

(a) (b)

Figure 1.26: Shown in (a) is the invariant mass spectrum of $\mu^+\mu^-$ pairs measured by NA60 in In-In collisions at 158 AGeV. The measured yield (*open circles*) is compared to individual sources of $\mu^+\mu^-$ pairs from hadron decays without any ρ contribution. Their contributions are subtracted from the data, and the difference (*solid triangles*) attributed to ρ decays [76, 78]. In (b) the excess yield is compared to a number of theoretical predictions in [76].

the early partonic phase, before significant radial flow has developed [79], but hadronic scenarios are not excluded [80].

At very low m_T ($m_T - M < 0.2$ GeV/c^2) a steepening of the m_T spectra shown in Fig. 1.27a is observed for all four mass windows of the excess yield. This trend is opposite to the expectation for radial flow and is not seen for the ϕ meson.

1.3.4 WA98

The WA98 Collaboration has measured direct photons in Pb-Pb collisions [6] [81] based on a statistical subtraction of decay photons, which show an excess above the yield expected from the direct photon measurements in proton induced reaction. The result is shown in Fig. 1.28 in comparison to a prediction of direct photons [48], which includes a contribution of thermal emission from a QGP phase; $\approx 30\%$ of the total thermal photon yield. This prediction is based on the same fireball model which successfully describes the low mass enhancement observed in the dilepton continuum in CERES and NA60 with

[6] with an array of lead glass calorimeter which is now installed in PHENIX

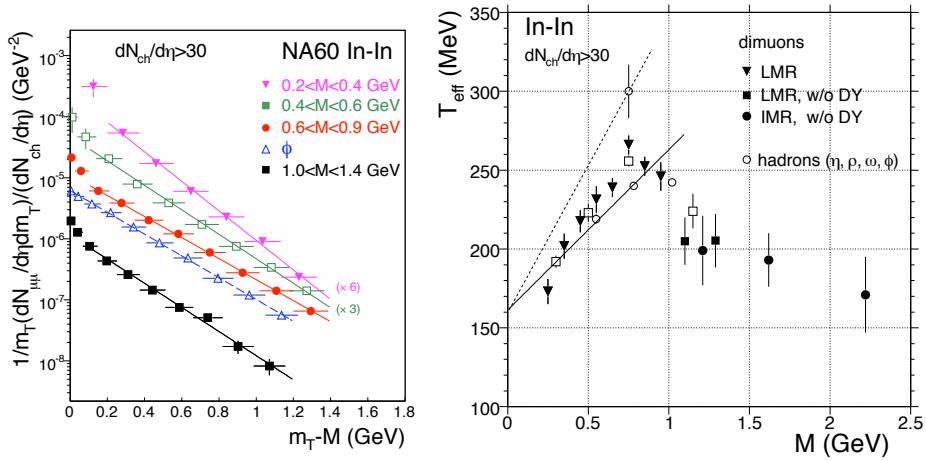

(a) (b)

Figure 1.27: Shown in (a) are the m_T spectra of the excess yield of $\mu^+\mu^-$ pairs in four mass windows in comparison to the ϕ summed over all centralities excluding the most peripheral bin. In (b) the inverse slopes T_{eff} are shown as function of the invariant mass. The inverse slopes are extracted from a fit of the m_T spectra in (a) (*open symbols*) and of narrower mass windows (*filled triangles*). The inverse slopes are compared to the slopes of hadrons (*open circles*) [76, 78].

a formation time of $\tau_0 = 1$ fm and an initial temperature of $T_i \simeq 210$ MeV. The two recently published low p_T data points [82], extracted via photon HBT (Hanbury Brown and Twiss Effect [83, 84]) interferometry, are not described by current theoretical models which attribute this yield to the hadronic stage of the fireball [48, 85]. But the inclusion of soft Bremsstrahlung off $\pi\pi$ and πK scattering improves the situation [86].

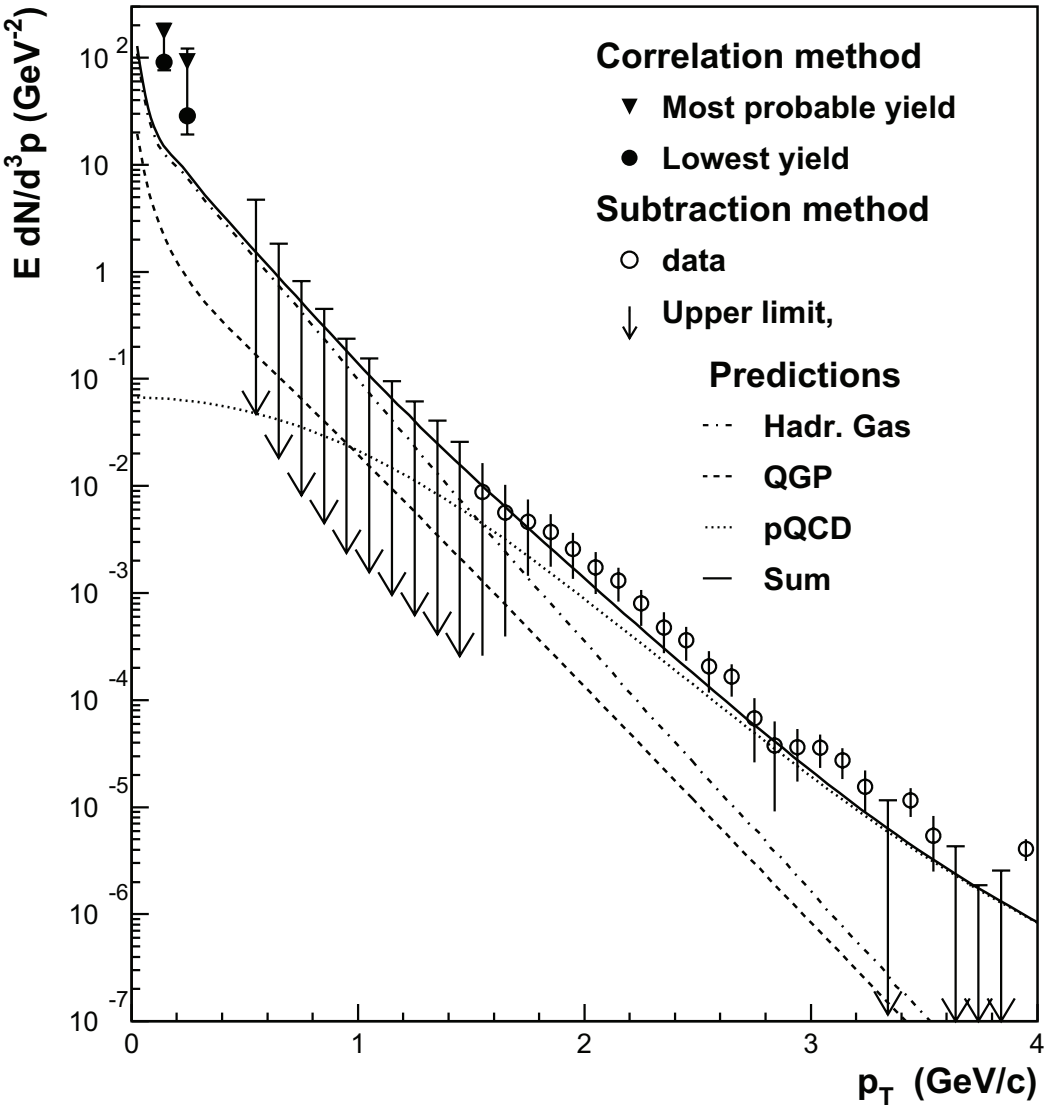

Figure 1.28: Yield of direct photons in Pb-Pb collisions at 158 AGeV measured by WA98. The lowest to points are extracted from the strength of the two-photon correlation [82], the other points with a statistical subtraction method [81].

1.4 RHIC

The Relativistic Heavy Ion Collider (RHIC) at Brookhaven National Laboratory (BNL) provides heavy-ion collisions at the highest energies currently available. It provides collisions of $p + p$, d + Au, Cu + Cu, and Au + Au with energies up to $\sqrt{s_{NN}} = 200$ GeV, but can also vary the collision energies to close the gap to SPS energies on the search for a critical point in the QCD phase diagram. Besides the study of the quark-gluon plasma, the polarized $p + p$ collisions are of particular interest for the study of the proton spin structure and allows to measure the gluon's contribution to the spin of the proton [87]. For the near future RHIC plans to provide polarized $p + p$ collisions at $\sqrt{s} = 500$ GeV, energetic enough to produce W bosons, which will allow to probe $\overline{u}$ and $\overline{d}$ quarks independently.

The ions are accelerated in two intersecting rings, one clockwise, the other counter-clockwise and brought to collisions at the six ring intersections. Four of the intersections have been equipped with experiments. The BRAHMS experiment was designed to measure charged hadrons over a wide range of rapidity and transverse momentum. It completed its data taking program in 2006. PHOBOS was equipped with subsystems to measure charge particle multiplicities over almost the entire solid angle, and in addition with two magnetic spectrometers providing particle identification in a narrow aperture. Phobos completed its running time at RHIC in 2005. The Solenoid Tracker At RHIC (STAR) with its large acceptance Time Projection Chamber (TPC) covering the full azimuth and $|y| < 1.5$ is a multipurpose detector with focus on global event analyses, particle correlations and particle identification.

Reviews of the results of the first three years of RHIC operation by all four collaborations can be found in their "white papers" [8–11].

Chapter 2

The PHENIX Experiment

The PHENIX experiment[1] is a detector system which consists of four spectrometer arms and two sets of global detectors. Of the four spectrometer arms, two, the so called central arms, are located at mid-rapidity covering each $\eta < 0.35$ in pseudo-rapidity and $\pi/2$ in azimuth. The two arms at forward rapidity, the muon arms, cover both 2π in azimuth. The north arm covers the pseudo-rapidity range of $1.15 < \eta < 2.44$ while the south arms extends over the pseudo-rapidity range $-1.15 > \eta > -2.25$.

The detector setup is shown in Fig. 2.1; the upper panel shows the two central arms in a cut-away view perpendicular to the beam direction, while a view along the beam direction is displayed in the lower panel. The latter one also shows the two Muon Arms at forward rapidity. The azimuthal and rapidity coverage of each subsystem is summarized in Tab. 2.1.

Two global detectors, the beam-beam counters (BBCs) and the zero-degree calorimeters (ZDCs), serve as event trigger and are responsible to measure global event parameters like the collision time, vertex and centrality. They are described in Section 2.1.

The two central arms provide tracking and momentum measurements of charged particles over a large range in p_T from 0.2 GeV/c to 20 GeV/c, as well as particle identification; electrons are identified via the Ring Imaging Cherenkov Counter (RICH) and the energy-momentum matching measured in the Electromagnetic Calorimeter (EMCal) and the Drift Chamber (DC), respectively, photons via their electromagnetic showers in the EMCal and hadrons via their time of flight. All detector subsystem that have been used for the measurements presented in this thesis are described in Section 2.2.

[1] A variety of explanations for the name PHENIX exist, from the a posteriori definition as Pioneering High-Energy Nuclear Interaction eXperiment to the experiment which rose from the ashes of the original proposals for the RHIC experiments TALES, SPARC, OASIS, and DIMUON.

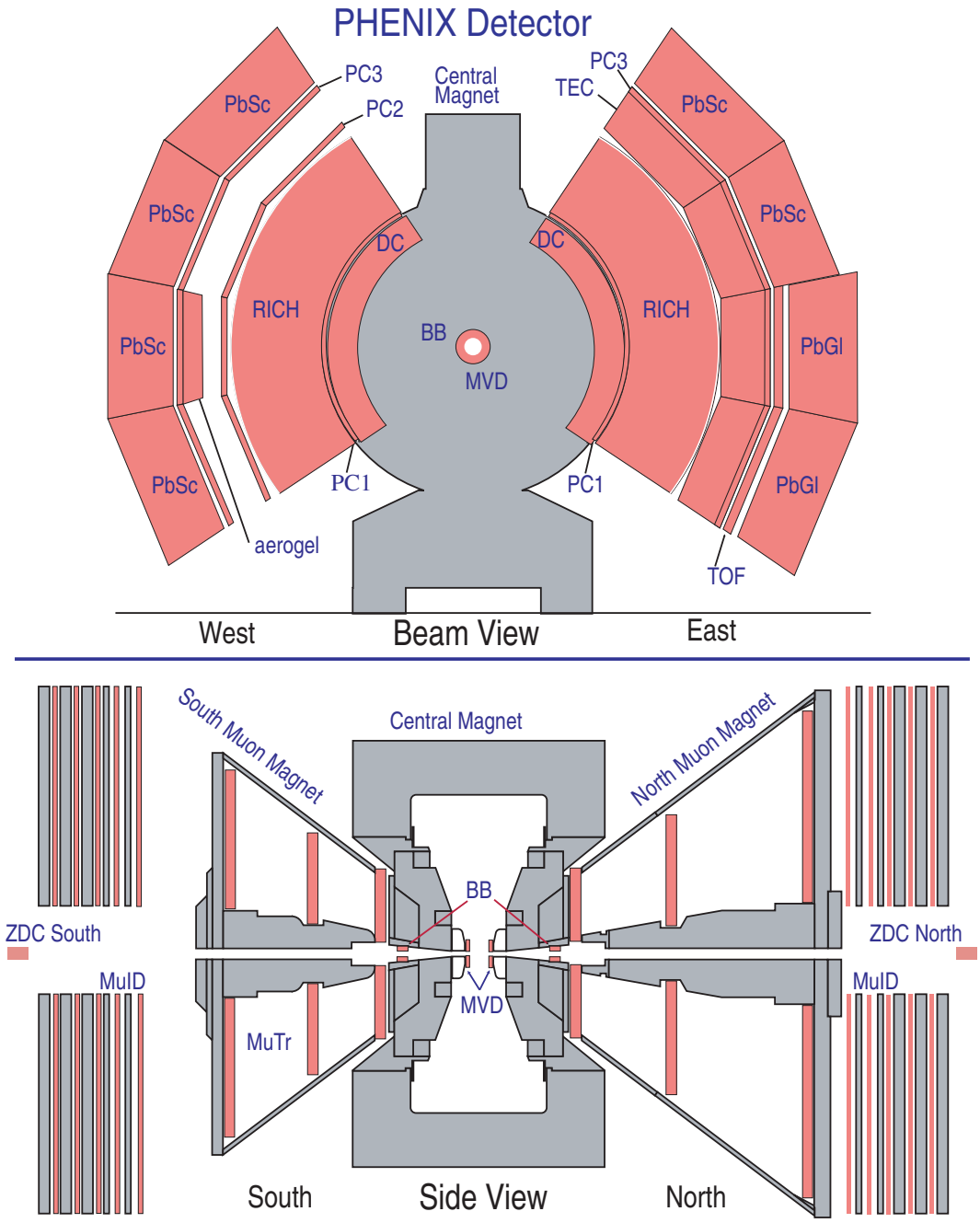

Figure 2.1: The PHENIX Detector configuration as of 2004. The upper figure shows the two central arms in a view perpendicular to the beam axis. The lower one shows a cut away view along the direction of the beam.

Table 2.1: Summary of the PHENIX detector subsystems [88].

Element	$\Delta\eta$	$\Delta\phi$	Purpose and special features
Magnet			
Central (CM)	± 0.35	2π	Up to 1.15 Tm
Muon (MMS)	-1.1 to -2.2	2π	0.72 Tm for $\eta = 2$
Muon (MMN)	1.1 to 2.4	2π	0.72 Tm for $\eta = 2$
Beam-beam Counters (BBC)	$\pm$ (3.1 to 3.9)	2π	Start timing, fast vertex
Zero-degree Calorimeter (ZDC)	± 2 mrad	2π	Minimum bias trigger
Drift Chambers (DC)	± 0.35	$2 \times \pi/2$	Good momentum and mass resolution $\sigma_m/m = 1\%$ at $m = 1$ GeV
Pad Chambers (PC)	± 0.35	$2 \times \pi/2$	Pattern recognition, tracking for non-bend direction
Time Expansion Chambers (TEC)	± 0.35	$\pi/2$	Pattern recognition, dE/dx
Ring Imaging Cherenkov Counter (RICH)	± 0.35	$2 \times \pi/2$	Electron identification
Time of Flight (ToF)	± 0.35	$\pi/4$	Hadron identification, $\sigma < 100$ ps
EMCal			
Lead-Scintillator (PbSc)	± 0.35	$\pi/2 + \pi/4$	Electron and photon identification and energy measurement
Lead-Glass (PbGl)	± 0.35	$\pi/4$	$e^{\pm}/\pi^{\pm}$ separation at $p > 1$ GeV/c by EM shower and $p < 0.35$ GeV/c by ToF $K^{\pm}/\pi^{\pm}$ separation up to 1 GeV/c by ToF
Muon Tracker (MuTr)			Tracking for muons
MuTr South	-1.15 to -2.25	2π	
MuTr North	1.15 to 2.44	2π	
Muon Identifier (MuID)			Steel absorber and Iarocci tubes for μ/hadron separation
MuID South	-1.15 to -2.25	2π	
MuID North	1.15 to 2.44	2π	

For a description of the other central arm detectors, *i. e.* the Time Expansion Chamber (TEC), the Time of Flight detector (ToF), as well as the muon arms, in which two detectors (MuTr and MuID) allow tracking and identification of muons at forward rapidity, one is referred to Refs. [89–91].

2.1 Global Detectors

Global detectors are used to measure the event topology, *i. e.*, the vertex position, the orientation of the reaction plane, and the centrality of the collision. Furthermore they measure the time at which a collision occurs. There are two pairs of detector systems installed on either side of the interaction point which are responsible for event selection and characterization in heavy ion collisions: two sets of beam beam counters cover $3.1 < |\eta| < 3.9$ and two sets of zero degree calorimeters are installed at $\eta \approx \pm 6.9$.

2.1.1 Beam-Beam Counters

The major tasks of the Beam-Beam Counters (BBC) [92, 93] are to serve as a trigger for collisions at the interaction point and to provide time and vertex information of the collision. The BBC comprises of two identical sets of 64 hexagonal shaped Cherenkov counters as shown in Fig. 2.2, which are installed around the beam pipe at a distance of ±144 cm on the north and south side of the interaction point.

Measuring the time difference between the BBC North and the BBC South, allows for the determination of the collision time as well as collision vertex:

$$t_0 = \frac{1}{2}(t_{\mathrm{BBCS}} + t_{\mathrm{BBCN}}) \tag{2.1a}$$

$$z_{\mathrm{vertex}} = \frac{c}{2}(t_{\mathrm{BBCS}} - t_{\mathrm{BBCN}}) \tag{2.1b}$$

where t_{BBCS} and t_{BBCN} are the average arrival time of particles in the BBC South and BBC North, respectively. The time resolution of the BBC is 52±4 ps (rms). This corresponds to a vertex position resolution of 1.1 cm.

2.1.2 Zero Degree Calorimeter

All four RHIC experiments are equipped with a pair of Zero Degree Calorimeters (ZDC) [94] located at a distance of 18 m downstream of each interaction point behind the first accelerator "DX" dipole magnet as shown in Fig. 2.3.

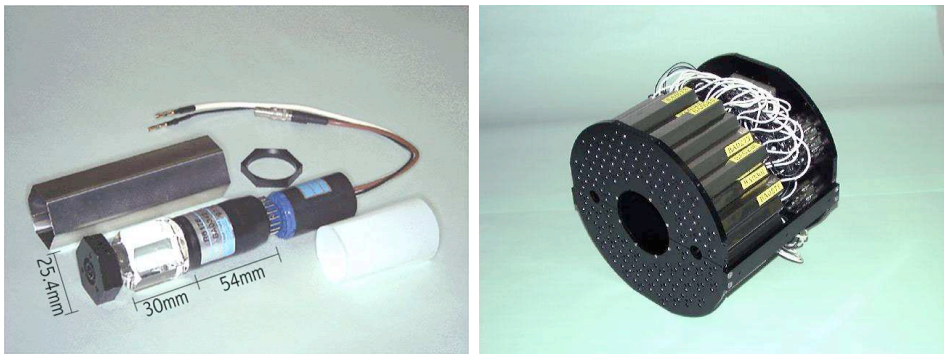

(a) **(b)**

Figure 2.2: Components of the BBC. (a) shows a photomultiplier tube (PMT) with a diameter of 25.4 mm and a 30 mm thick Quartz window mounted in front of it. (b) shows 64 PMTs assembled to one unit.

Their task is to measure the energy of spectator neutrons, which did not participate in the collision and therefore carry still a large fraction of the beam momentum. While charged particles like spectator protons are deflected by the "DX" dipole magnet in front, neutrons hit the ZDC and create a hadronic shower. Neutral particles created within the heavy ion collision moving in forward direction have typically a much smaller energy. The ZDC consist of Cherenkov sampling hadronic calorimeter made of a tungsten alloy with a conical coverage of 21 mrad around the beam direction. The energy resolution of the ZDC is $\sigma_E/E = 85\%/\sqrt{E} \oplus 9.1\%$.

The total energy deposited by spectator neutrons can be used in anti-correlation with the total charge deposited in the BBC to determine the centrality of the collision as shown in Fig. 2.4. The centrality is a measure for how much the two colliding ions overlap. In addition to the centrality determination the ZDC also serves as part of the minimum bias trigger in heavy ion collisions and provides timing information, but with a resolution of ≈ 200 ps it is less accurate than the BBC.

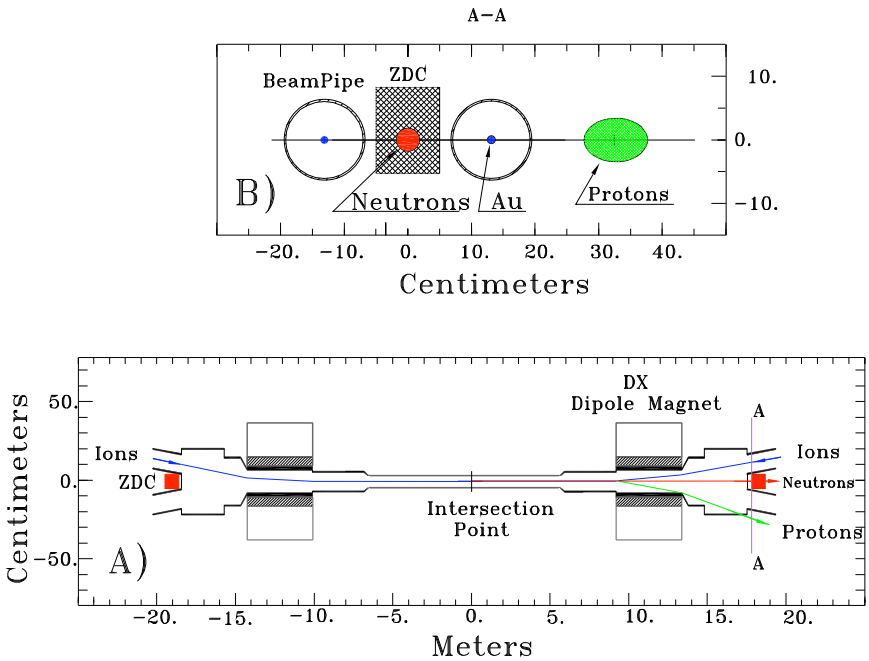

Figure 2.3: Top: Cut-away view of the ZDC in the plane perpendicular to the beam axis indicating deflection of protons and neutrons downstream of the "DX" Dipole magnet. Bottom: Plan view of the collision region [94].

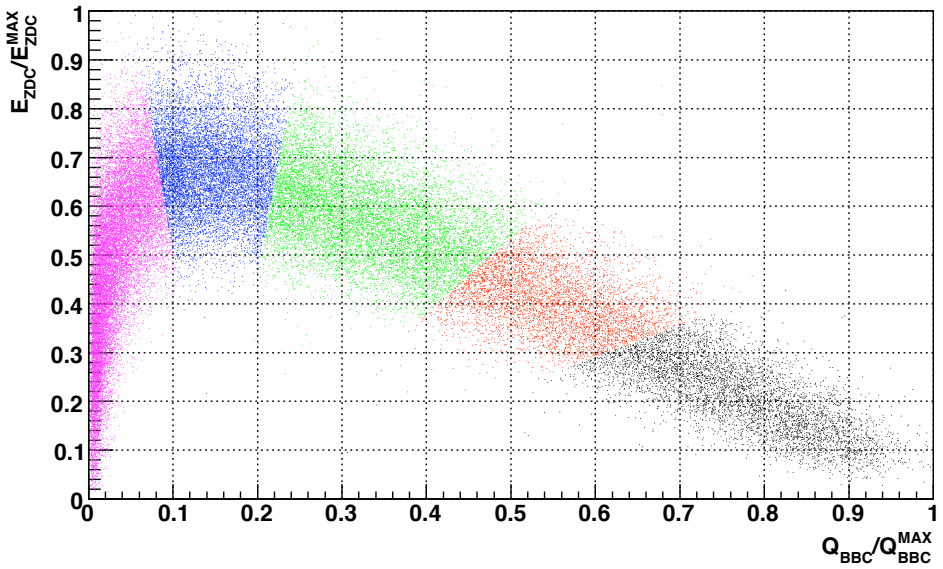

Figure 2.4: Correlation between the total energy deposited in the ZDC and the total charge measured in the BBC for Au + Au collisions at $\sqrt{s_{NN}} = 200$ GeV. The colored regions show the definition of centrality classes based on this correlation (black: 0–10%, red: 10–20%, green: 20–40%, blue: 40–60%, and magenta: 60–92%). Their boundaries are perpendicular to the centroid of the distribution.

2.2 Central Arm Detectors

The two Central Arms consist out of several subsystems for charged particle tracking, momentum measurement and particle identification. Each arm covers $|\eta| < 0.35$ in pseudo-rapidity and $|\phi| < \pi/2$ in azimuth. The central arm coordinate system is chosen with its origin at the nominal interaction point such that the $\hat{z}$-axis is aligned with the beam direction pointing north, the $\hat{x}$-axis pointing west and the $\hat{y}$-axis upwards perpendicular to the two other axis. In this coordinate system the west arm covers $-\frac{3}{16}\pi < \phi < \frac{5}{16}\pi$ and the east arm $\frac{11}{16}\pi < \phi < \frac{19}{16}\pi$.

2.2.1 Central Magnet

The transverse momentum of charged particles is determined by their bending in the magnetic field provided by the Central Magnet (CM) [95]. It consists out of an inner and an outer pair of concentric Helmholtz coils inside a steel yoke which provide a axially-symmetric magnetic field around the interaction point that is parallel to the beam direction as shown in Fig. 2.5. They cover a polar angle range of $70° < \theta < 110°$ which corresponds to a pseudo-rapidity range of $|\eta| < 0.35$.

The two pairs of Helmholtz coils can be run with the same (++) or opposite (+−) polarity. In the ++ configuration a total field integral of $\int Bdl = 1.5$ Tm is achieved over the first 2 m from the interaction point, while the magnetic field in the region of the tracking devices ($R > 2$ m) is nearly zero in order to allow a tracking model which assumes straight tracks and to minimize the smearing of Cherenkov rings in the Ring Imaging Cherenkov Counter.

The +− configuration leads to a cancellation of the field in the first 50 cm around the vertex to approximately zero field integral, which is used in combination with the Hadron-Blind Detector (HBD) [96, 97], which was installed for the first time in 2007 inside this field free region and will be briefly discussed in Chapter 5.

2.2.2 Drift Chambers

A charged particle which traverses a gas-filled detector randomly ionizes the gas. The electrons from the primary ionization process are drifted in an electrical field towards an anode (sense) wire after a time proportional to the distance of the the track to the wire. Hits in subsequent anodes can be reconstructed to a track as described Section 3.2.

Two Drift Chambers (DC) are installed in both Central Arms as the main tracking device for charged particles in PHENIX. They each consist out of a

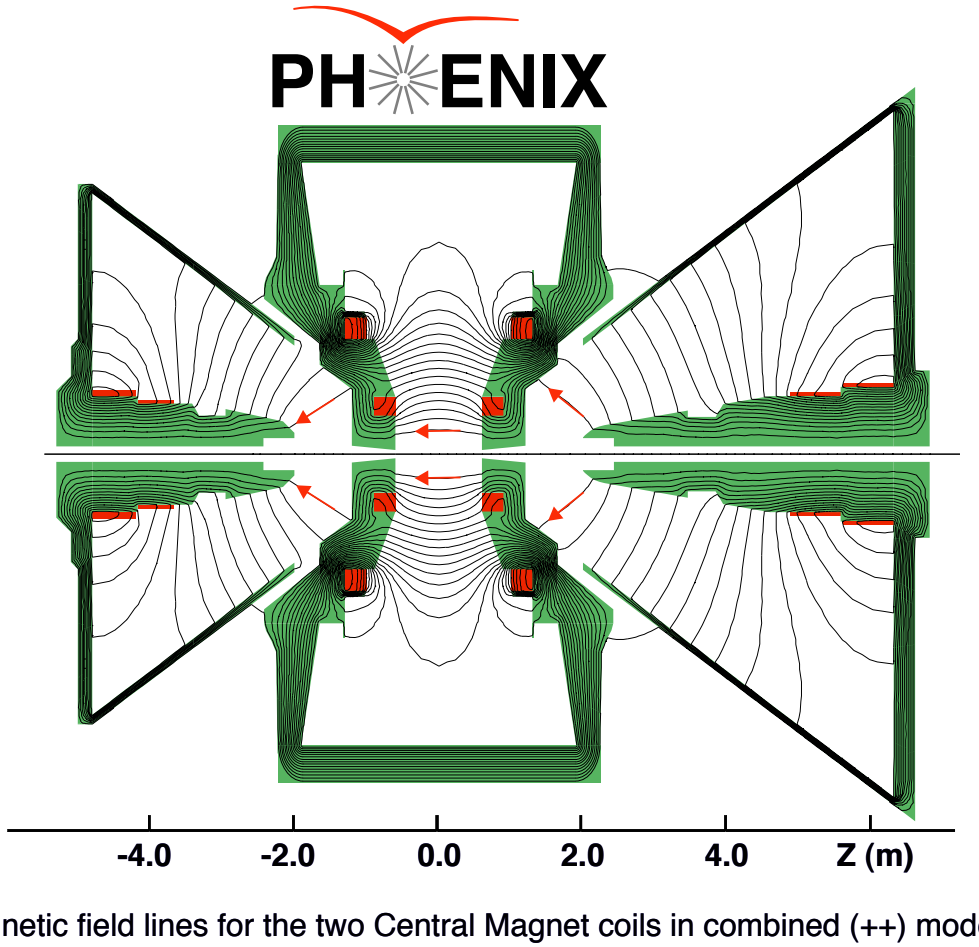

Figure 2.5: The PHENIX Central and Muon Magnets and their field lines shown in a cut-away view for adding (++) configuration [95]. Also shown are the two magnets in the Muon Tracker arms on either side of the Central Magnet.

multiwire gas chamber located at a distance of 2.02 m to 2.40 m from the interaction point outside the magnetic field of the Central Magnet. The DC reconstructs the trajectory of charged particles in the $r - \phi$ plane in order to determine their transverse momentum p_T.

Both chambers extend over 2 m along the beam direction corresponding to $\Delta\eta = \pm 0.35$ in pseudo-rapidity; while the Drift Chamber installed in the Central Arm West covers $-\frac{3}{16}\pi < \phi < \frac{5}{16}\pi$ in azimuth, the one in the East Arm covers $\frac{11}{16}\pi < \phi < \frac{19}{16}\pi$. Their active volume is confined by Mylar windows and supported by a cylindrical shaped titanium frame as shown in Fig. 2.6. The detectors are filled with a gas mixture of 50% Argon and 50% Ethane.

A design goal of the drift chamber was to measure the mass of the ϕ meson

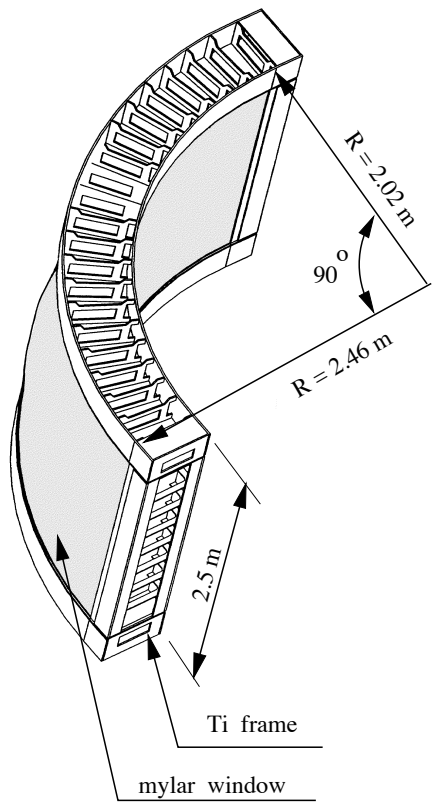

Figure 2.6: The PHENIX Drift Chamber Frame [89].

in the $\phi \rightarrow e^+e^-$ decay channel with a resolution better than its natural width of 4.4 MeV/c^2. In conjunction with the necessity to perform in a high particle multiplicity environment (as many as two hundred tracks in the central Au+Au collisions) this imposes the following requirements on the DC:

- Single wire resolution better than 150 μm in $r - \phi$.
- Single wire two track separation better than 1.5 mm.
- Single wire efficiency better than 99%.
- Spacial resolution in $\hat{z}$-direction better than 2 mm.

Each Drift Chamber consists of 20 identical sectors covering 4.5°. As illustrated in Fig. 2.7, each sector contains six different types of wire modules, X1, U1, V1, X2, U2, and V2 stacked in radial direction. Every module contains, alternating in azimuth direction, four anode (sense) and four cathode planes.

The X1 and X2 wires run parallel to the beam direction to track particles in the $r - \phi$ plane. Behind each X wire module two smaller U and V modules follow whose wires have a small stereo angle of 6° with respect to the X wires in order to measure the $\hat{z}$-coordinate of the track.

Each X module contains twelve sense wires separated by Potential (P) wires and surrounded by Back (B) and Gate (G) wires as shown in the left panel of Fig. 2.7 to shape the electrical field lines such that every sense wire is alternating sensitive to drift charges from only one side therefore limiting the left-right ambiguity to a region of ±2 mm. A calculation of the nominal drift field configuration due to this wire layout is shown in Fig. 2.8. The layout of the U,V-stereo modules is identical, but they contain only four sense wires. The stereo wires start in one sector and end on the other side of the Drift Chamber in the neighboring sector, as illustrated in the right panel of Fig. 2.7.

For the pattern recognition to work with up to 500 tracks, each sense wire is separated in two halves at the center. Each half is read out independently. To electrically isolate the two halves, they are connected by a 100 μm thick Kapton strip. In total the Drift Chamber contains 6500 wires and therefore 13000 read out channels.

2.2.3 Pad Chambers

The Pad Chambers are multiwire proportional chambers with a cathode pad readout that determine space points along the straight trajectory of charged particles to determine the polar angle θ which allows to reconstruct the $\hat{z}$-component of the momentum vector.

The Central Arms are equipped with three layers of Pad Chambers in the West Arm and two layers in the East Arm, respectively. The first layer of Pad Chambers (PC1) is installed just behind the Drift Chambers, while the third layer (PC3) is situated right in front of the Electromagnetic Calorimeter. The second layer of Pad Chambers (PC2) is only present in the West Arm following the Ring Imaging Cherenkov Counter.

Each PC contains a single layer of wires within a gas volume that is confined by two cathode planes. One cathode plane is solid copper, while the the other one is segmented into a fine array of pixels as shown in Fig. 2.9. The basic unit is a pad formed by nine non-neighboring pixels, which are read out by a common channel. Three pixels within a pad form a cell. For a valid hit, three neighboring pads must sense the avalanche. The interleaved design allows a fine position resolution of 1.7 mm in $\hat{z}$ direction and 2.5 mm in $\hat{x}$ and $\hat{y}$ and reduces at the same time the number of electronic channels by a factor of nine.

Associating hits in PC1 with tracks reconstructed in the DC is essential to determine the three dimensional momentum of a particle.

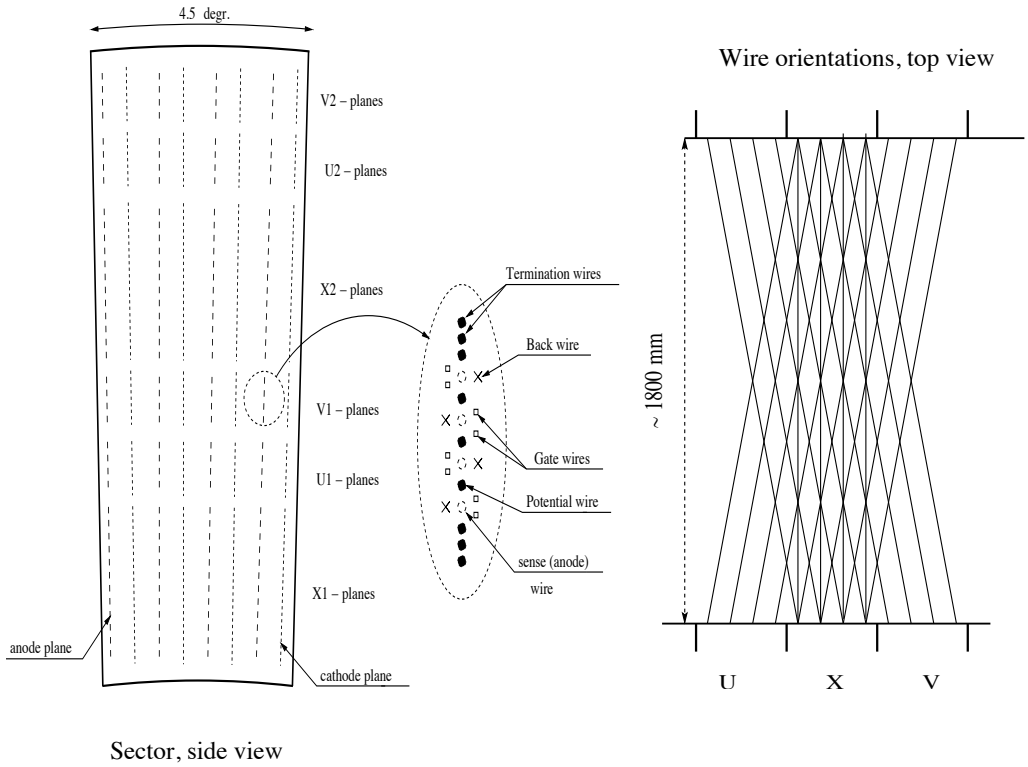

Figure 2.7: Left: Cut-away view of the wire layout within one keystone of the Drift Chamber. Right: Plan view of the stereo wire orientation [89].

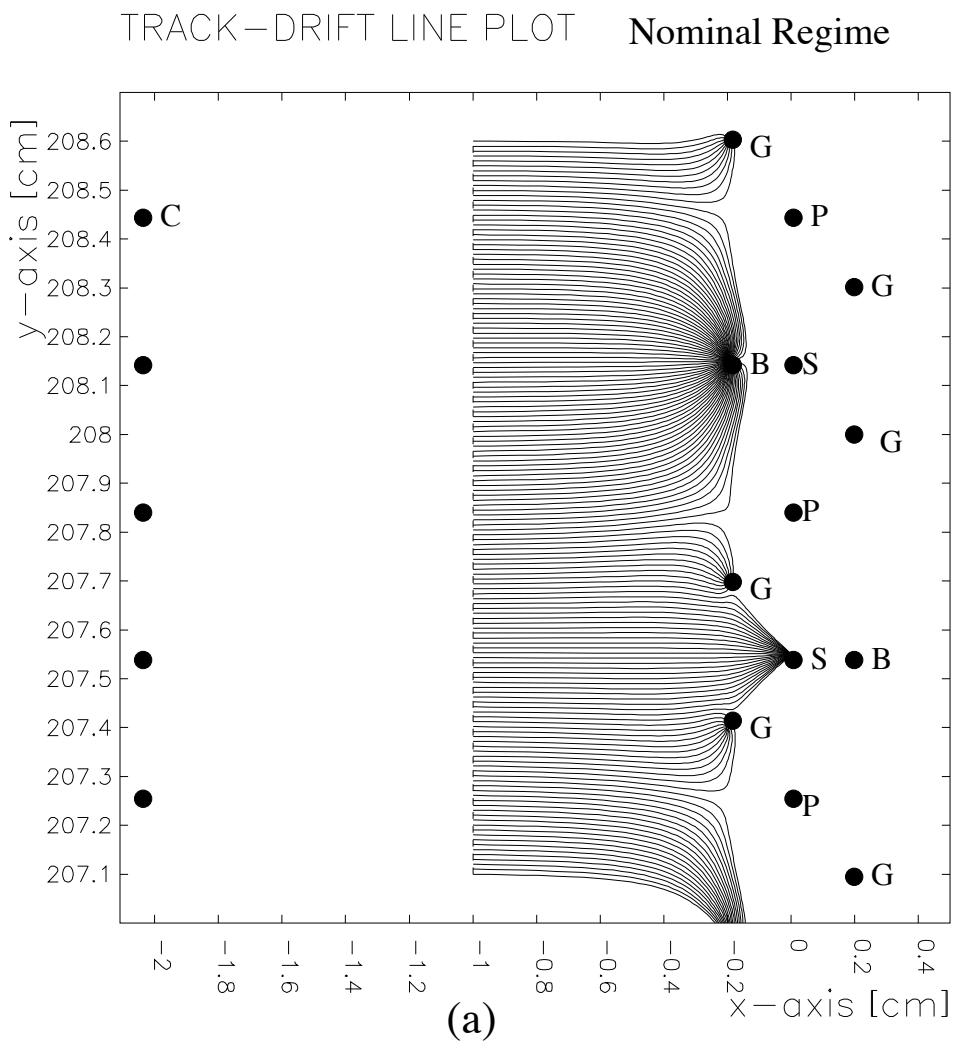

Figure 2.8: Calculation of the drift lines for the nominal electrostatic field configuration. Different wires are marked by letters: Back (B), Gate (G), Potential (P), and Sense (S) wires [89].

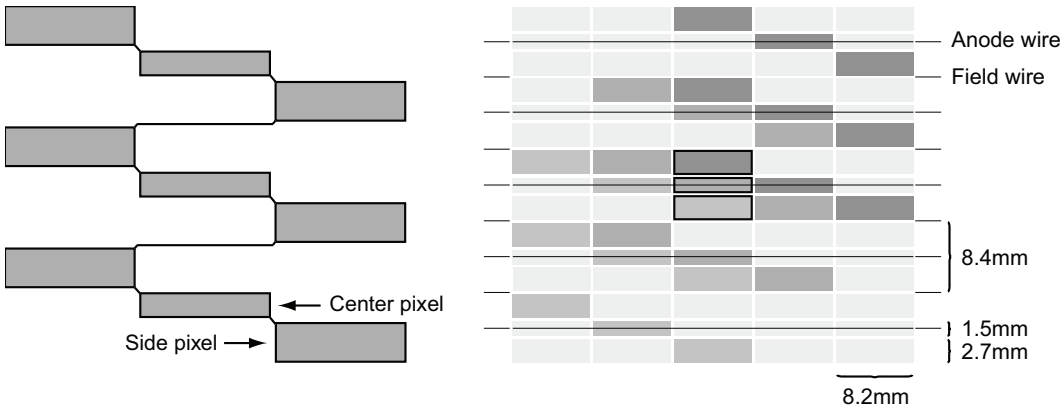

Figure 2.9: Left: the pad and pixel geometry. Right: Interleaved pad design. [89].

2.2.4 Ring Imaging Cherenkov Counter

A charged particle travelling in a medium with a velocity βc that is greater than the speed of light in this medium, $c_n = c/n$ for a medium with refractive index n, emits Cherenkov radiation under angle $\cos\theta_C = 1/(n\beta)$.

In each of the two central arms a Ring Imaging Cherenkov Counter (RICH) is installed between the inner and outer tracking detectors following the first layer of Pad Chambers [90]. Its main purpose is the separation of electrons from the large background of charged pions produced in heavy-ion collisions. In combination with the Electromagnetic Calorimeter it also provides information for an electron trigger in $p+p$ collisions. Behind the entrance window with an area of 8.9 m^2 a volume of 40 m^3 is filled with CO_2 as radiator gas, which has a refractive index of $n-1 = 410\times10^{-6}$ [29], corresponding to a threshold velocity $\beta_t = 1/n = 0.99590168$ and a γ-factor of $\gamma_t = 1/\sqrt{1-\beta_t^2} = 34.932$. This leads to a Cherenkov threshold of $p_t = m_\pi\gamma_t\beta_t = 4.87$ GeV/c for charged pions ($m_\pi = 139.570$ MeV/c^2), while electrons ($m_e = 0.511$ MeV/c^2) exceed the Cherenkov threshold already with a momentum of $p_t = 0.018$ GeV/c. Below the pion threshold the RICH has a hadron rejection of 10^4 to 1.

A cut-away view of the RICH detector is shown in Fig. 2.10. The Cherenkov light is focused by two intersecting spherical mirrors with a total area of 20 m^2 onto two arrays of 1280 photo-multiplier tubes (PMT) each which are located on either side of the entrance window. An average number of 10 photons per $\beta \approx 1$ particle are emitted under the angle of $\theta_C \approx 9$ mrad. They are focused to a ring on the PMT array with an asymptotic radius of ≈ 11.8 cm. The glass in front of the photo tube absorbs light with wave lengths below 200 nm. The mirror reflectivity is 83% at this wave length and rises to 90% at 250 nm.

In $p+p$ collisions the RICH also serves as Level-1 trigger on rare events

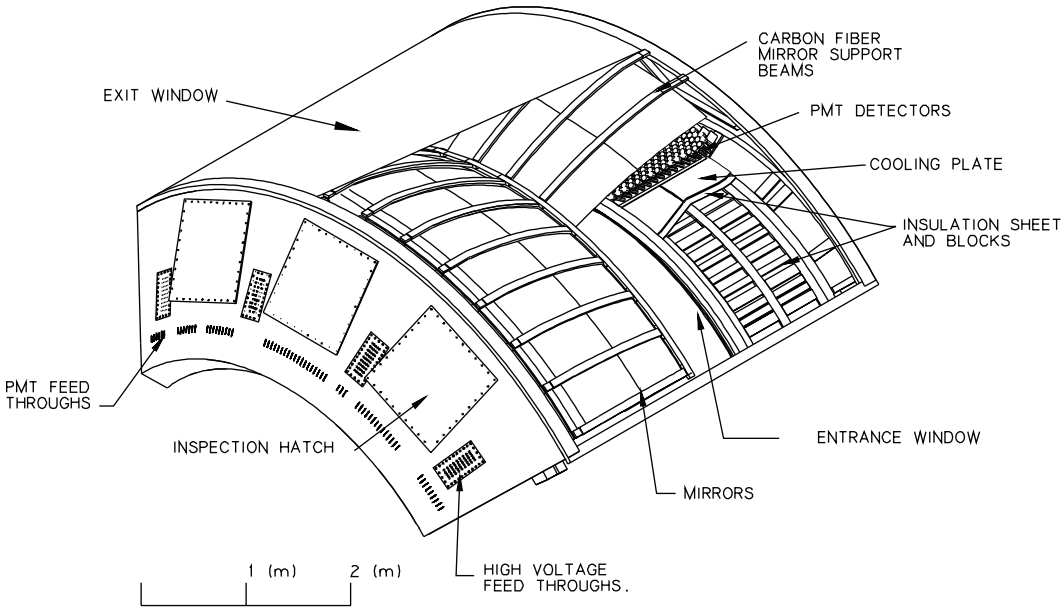

Figure 2.10: A cut-away view of one arm of the PHENIX RICH detector [90].

with electrons. The trigger is comprised of 64 non overlapping trigger tiles in each PMT array. Each trigger tile consists of $4(\phi) \times 5(z)$ PMTs, an area which approximately corresponds to the size of a Cherenkov ring of a $\beta \approx 1$ particle.

2.2.5 Electromagnetic Calorimeter

High-energy electrons and photons lose energy in matter predominantly via Bremsstrahlung and e^+e^- pair production, respectively. The amount of energy they lose is defined by the radiation length X_0, which is both (a) the mean length of traversed matter after which an electron has lost all but $1/e$ of its energy and (b) 7/9 of the mean free path for e^+e^- pair production by a photon.

The Electromagnetic Calorimeter (EMCal) measures the energy and position photons and electrons. Furthermore, it serves as trigger on rare events with high momentum photons. It comprises of eight sectors covering each 22.5° in azimuth and $\Delta\eta = \pm 0.35$ in pseudo-rapidity. All four sectors of the West Arm and the two top sectors in the East Arm are shashlik type lead-scintillator (PbSc) sampling calorimeter. The two bottom sectors are lead-glass (PbGl) Cherenkov calorimeters, which had been used previously in the CERN experiment WA98 at the SPS.

The PbSc calorimeter contains a total of 15,552 individual towers which are made of 66 sampling cells with alternating layers of 1.5 mm Pb and 4 mm scintillator (1.5%PT/0.01%POPOP) [98]. A module as shown in Fig. 2.11

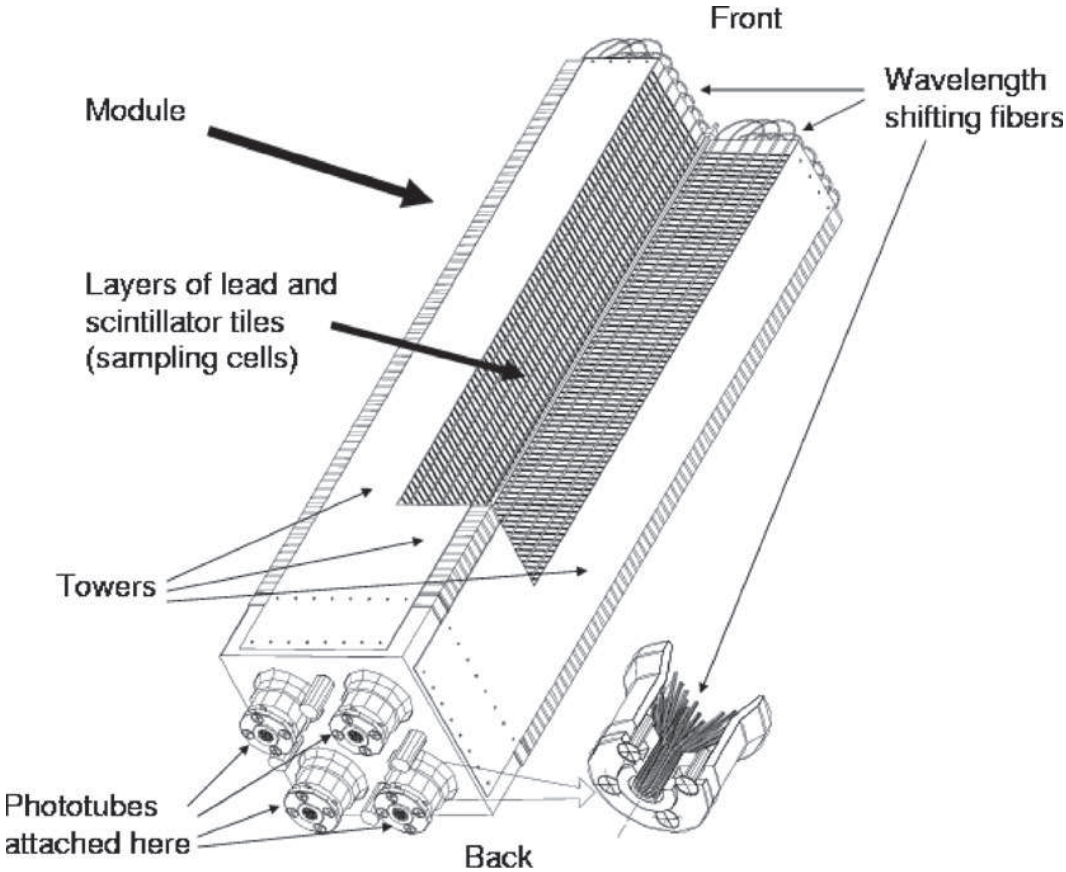

Figure 2.11: View of a PbSc module showing the layers of Pb and scintillator, the wavelength shifting fibers and the phototubes attached to the back.

comprises of four optically isolated towers which are read out individually. Each tower has measures 5.535×5.535 cm^2 across and has a length of 37.5 cm, which corresponds to 18 X_0. 36 modules are held by a common support structure called super module. 18 super modules form a sector. The energy resolution of the PbSc Calorimeter is

$$\frac{\sigma_E}{E} = \frac{8.1\%}{\sqrt{E}} \oplus 2.1\%. \tag{2.2}$$

Each sector of the PbGl calorimeter comprises of 192 super modules (SM) which contain each 24 modules as shown in Fig. 2.12. Each module measures 4×4 cm^2 across, is 40 cm long (14.3 X_0), and read out with a photomultiplier

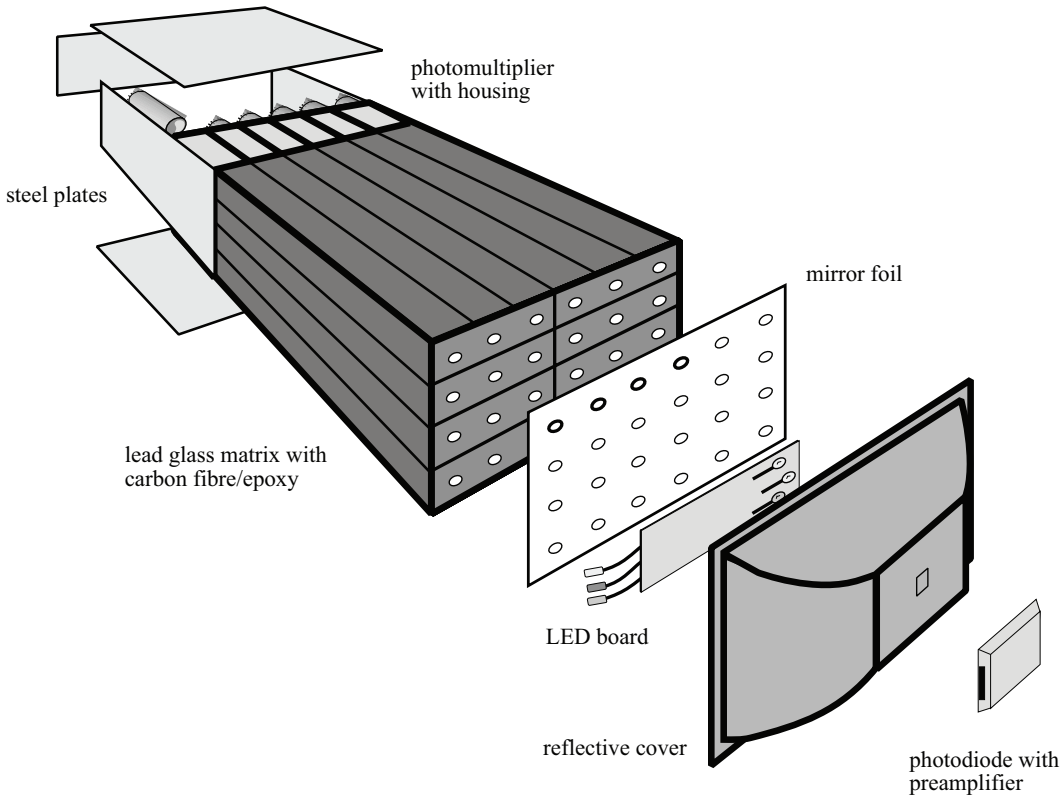

Figure 2.12: View of a PbGl super module.

at its end. The energy resolution of the PbGl Calorimeter is

$$\frac{\sigma_E}{E} = \frac{5.9\%}{\sqrt{E}} \oplus 0.76\%. \tag{2.3}$$

With a thickness of 18 X_0 in the PbSc and 14.3 X_0 in the PbGl, respectively, electrons and photons will deposit their energy within the calorimeter as electromagnetic shower of subsequent Bremsstrahlung and e^+e^- pair creation. In the PbSc the electrons within the electromagnetic shower created in the Pb-layer produces scintillation light in the scintillator layers. The scintillation light is guided by wavelength shifting fibers to the phototubes located at the back of each tower. In the PbGl, which has a refractive index of $n = 1.648$, the electromagnetic showers is detected by Cherenkov light radiated by electrons in the shower. The Cherenkov light is read out at the end of the Calorimeter by photomultiplier tubes.

In contrast to electrons and photons, the energy loss of hadrons in matter

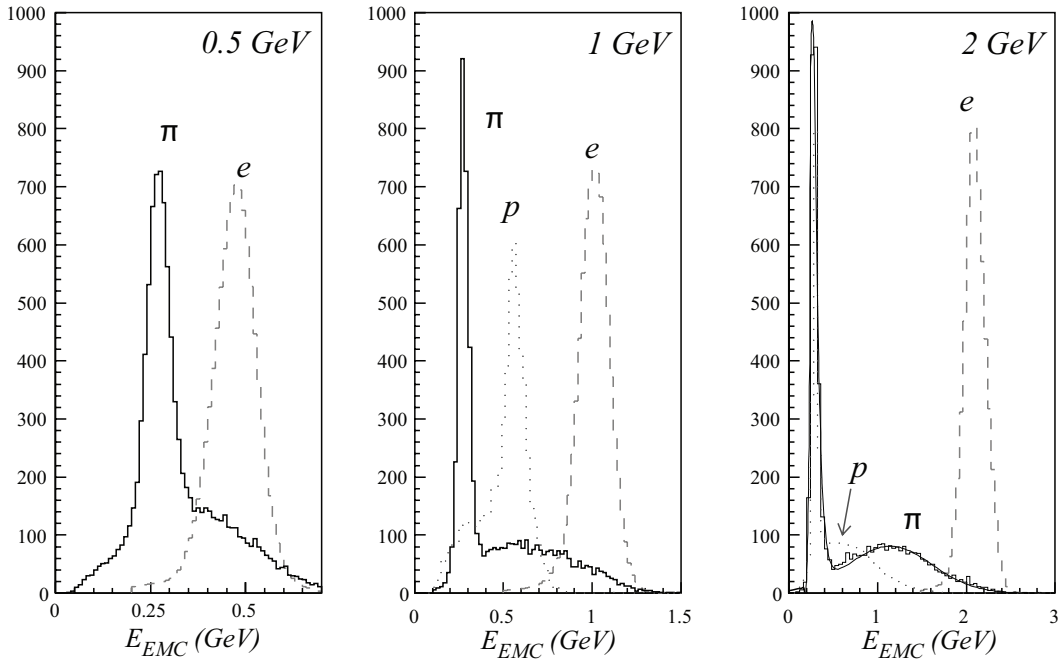

Figure 2.13: Energy spectrum measured with the PbSc calorimeter, when exposed to pions, protons and electrons for incident energies of 0.5, 1, and 2 GeV [98]. The y-axis shows counts in arbitrary units.

occurs primarily through ionization and atomic excitations. For typical hadron energies ($0.1 \leq E \leq 10$ GeV) the energy deposited in matter is nearly independent of the particle's energy, therefore these particles are called minimum ionizing particles, or mip's. Furthermore, PbSc has a nuclear interaction length $\lambda_I = 0.85$ and PbGl $\lambda_I = 1.05$, respectively. Therefore, only few hadrons will interact strongly and deposit a significant fraction of their energy. This leads to mip peaks in the energy spectrum as shown in Fig. 2.13 for charged pions and protons along with electrons for comparison.

The EMCal serves as Level-1 trigger for events with high momentum photons, triggering when the energy deposited in an area of 4×4 overlapping towers surpasses a defined threshold. In addition the energy in a area of 2×2 overlapping towers can be used in coincidence with the RICH trigger to trigger on events with electron candidates.

2.2.6 Charged Particle Acceptance

The central arm acceptance of charged tracks depends on their charge sign q, their transverse momentum and their azimuthal angle. The magnetic field of the central magnets will bend a particle emitted under ϕ_0 and momentum

p_T; its azimuthal angle measured at a distance r from the vertex increases inverse proportional to p_T. Therefore the relation between azimuthal angle at the vertex and at the DC (RICH) is given by:

$$\phi_{\mathrm{DC}} = \phi_0 + q\frac{k_{\mathrm{DC}}}{p_T} \tag{2.4a}$$

$$\phi_{\mathrm{RICH}} = \phi_0 + q\frac{k_{\mathrm{RICH}}}{p_T} \tag{2.4b}$$

An electron is accepted if its azimuthal angle is within the coverage of DC and RICH in one of the two central arms, *i. e.*:

$$\phi_{\mathrm{min}} < \phi_{\mathrm{DC}} \leq \phi_{\mathrm{max}} \quad \&\& \quad \phi_{\mathrm{min}} < \phi_{\mathrm{RICH}} \leq \phi_{\mathrm{max}}$$

Fig. 2.14 shows the distribution of single electrons measured in $p+p$ collisions in q/p_T vs. ϕ_0. The west arm coverage extends around $\phi \approx 0$ and the the east arm around $\phi \approx \pi$. The shapes can be described by the low p_T cut of 0.2 GeV/c limits the distribution within $|q/p_T| < 5$ c/GeV shown as horizontal dashed black lines and the conditions defined in Eq. (2.5), with $k_{\mathrm{DC}} = 0.206$ rad GeV/c, $k_{\mathrm{RICH}} = 0.309$ rad GeV/c, $\phi_{\mathrm{min}} = -\frac{3}{16}\pi$ rad and $\phi_{\mathrm{max}} = \frac{5}{16}\pi$ rad for the west arm and $\phi_{\mathrm{min}} = \frac{11}{16}\pi$ rad, and $\phi_{\mathrm{max}} = \frac{19}{16}\pi$ rad for the east arm, respectively, whose boundaries are shown as solid black lines.

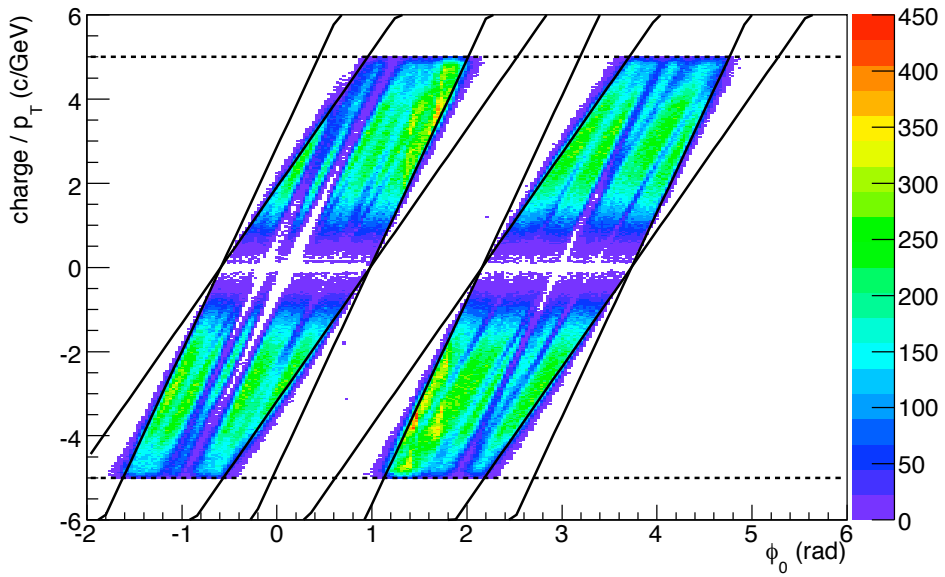

Figure 2.14: Single electron acceptance. The diagonal line represent the acceptance limits due to RICH and DC as defined in Eq. (2.5). The dashed lines indicate the low p_T cut off at 200 MeV/c.

Chapter 3

Analysis

In this chapter the analysis of the dielectron continuum in $p + p$ as well as Au + Au collisions at a $\sqrt{s_{NN}} = 200$GeV is presented. The analysis procedure of both data sets has large overlap so they are discussed in parallel, but emphasizing differences where they are present.

The major steps of the analysis are outlined briefly here. The analysis begins with the event selection in Section 3.1, which is discussed for $p + p$ in Section 3.1.1 and in Section 3.1.2 for Au + Au based on trigger and vertex information. This is followed by a single electron analysis, including the tracking discussed in Section 3.2 and electron identification in Section 3.3.

Single electrons are paired to electron-positron pairs as explained in Section 3.4. The subtraction of combinatorial and correlated background is discussed in the Sections 3.4.3–3.4.5. The resulting invariant mass and p_T spectra of e^+e^- pairs are corrected for reconstruction and electron identification efficiencies as well as trigger efficiencies as presented in Section 3.5. The p_T spectra of e^+e^- pairs require an additional correction for the detector acceptance which is discussed in Section 3.5.4.

Section 3.7 presents a calculation *(Cocktail)* of the expected e^+e^- pair yield from hadronic decays. The results will be compared to the experimental data in Chapter 4.

3.1 Data Set and Event Selection

3.1.1 $p + p$ Collisions

The analysis is based on the data set of $p + p$ collisions at $\sqrt{s} = 200$ GeV which was collected during the run period in 2005.

Two data samples are used for the measurement of the dielectron contin-

uum: a reference sample of events which were selected by the minimum bias trigger (MB) and a data set recorded with the single electron trigger (ERT). The MB trigger for $p+p$ collisions requires that the BBC has registered hits in at least two photo tubes and an online determined collision vertex within 30 cm:

$$\mathrm{MB} \equiv (\mathrm{BBC} \geq 2) \cap (|z_{\mathrm{vertex}}| < 30 \text{ cm}) \tag{3.1}$$

The MB trigger cross section is $\sigma_{\mathrm{BBC}} = 23.0 \pm 2.2$ mb corresponding to $54.5 \pm 6\%$ of the inelastic $p+p$ cross section $\sigma_{pp} = 42.2$ mb. Simulations, and data collected without requiring the BBC trigger, indicate that the triggered events include $79 \pm 2\%$ of events with particles in the central arm acceptance. This number coincides with the fraction of non-diffractive events triggered by the BBC from which it is concluded that for non-diffractive collisions the BBC trigger can have only little bias towards events with particles produced in the central arms.

Events with a collision vertex far from the origin have a higher chance to create particles that hit the nose cones of the central magnet. This creates additional particles, *e. g.*, from photon conversions which are reconstructed in the central arm detectors that do not originate from the actual collision. The z_{vertex} distribution of events is shown in Fig. 3.1a. While this distribution is centered around $z_{\mathrm{vertex}} = 0$ cm and has a full width at half maximum of ≈ 30 cm, the number of electrons in the central arm peaks strongly for $|z_{\mathrm{vertex}}| > 25$ cm, as shown in Fig. 3.1b. Therefore, an vertex cut of $z_{\mathrm{vertex}} < 25$ cm, with the vertex position determined offline by the BBC with better accuracy, is applied to avoid such contamination. Although with ~ 4 kHz the

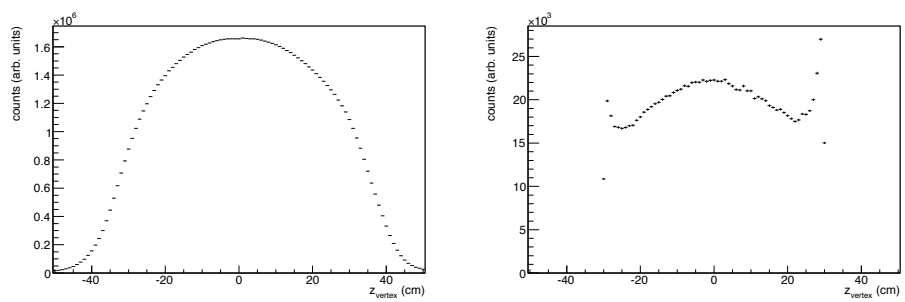

(a) **(b)**

Figure 3.1: z_{vertex} distribution of events (a) and of electrons (b) in $p+p$ collisions at $\sqrt{s} = 200$ GeV.

rate at which PHENIX can record data exceeds the capability of any other RHIC experiments, it would not be useful to only record events based on

the MB trigger if one wants to study rare events, containing, *e. g.*, electrons. Therefore, PHENIX has a variety of Level-1 triggers to select particularly interesting events, *e. g.*, events with a high p_T particle in the central arm or an electron candidate. They are called ERT (EMCal RICH triggers), as they are based on the energy measurement in the EMCal, which in case of the electron trigger is matched to hits in the RICH.

The high p_T photon trigger is based on the energy measured within a 4×4 neighboring EMCal towers. If this energy exceeds a set threshold, the trigger is fired. During the $p + p$ run in 2005 there were three triggers with different energy thresholds:

- ERTLL1_4x4a: $E > 2.1$ GeV
- ERTLL1_4x4b: $E > 2.8$ GeV
- ERTLL1_4x4c: $E > 1.4$ GeV

In addition to the high p_T photon trigger an electron trigger (ERTLL1_E) was active. This trigger requires a minimum deposited energy of 400 MeV in an overlapping tile of 2x2 EMCal towers matched to a hit in the RICH. The RICH hit is required within a trigger tile of 4x5 photo tubes. The location of the RICH trigger depends on the momentum of the trigger particle and is determined from a look-up table, assuming an electron to be the trigger particle, *i. e.* the momentum being equal to the energy deposited within the 2x2 EMCal towers. Only events which are triggered in coincidence with the MB trigger (ERTLL1_E&BBCLL1) are considered for the analysis so that a cross section for MB collisions can be extracted. The efficiency of the ERT trigger is discussed in Section 3.5.2. When in the following the term "ERT trigger" is used, it refers to the ERTLL1_E&BBCLL1 trigger unless stated otherwise.

The downscale factors on the MB trigger changes frequently to adjust for changing beam conditions. These downscale factors are recorded in a database and have to be considered when determining the total luminosity recorded.

This analysis uses a MB data sample of 1.5 billion events and an ERT triggered sample of 270 million events. As the ERT trigger requires the coincidence of the MB trigger one can calculate the number of sampled MB events that the ERT data set of a given run corresponds to by as:

$$N_{\mathrm{MB}}^{\mathrm{sampled}} = N_{\mathrm{MB}} \cdot f_{\mathrm{scale-down}} \cdot N_{\mathrm{ERT}}^{\mathrm{MB}} / N_{\mathrm{MB}}^{\mathrm{ERT}} \tag{3.2}$$

Where N_{MB} is the number of events recorded with the MB trigger in this run and $f_{\mathrm{scale-down}}$ is the scale-down factor for the MB trigger. The correction factor $N_{\mathrm{ERT}}^{\mathrm{MB}} / N_{\mathrm{MB}}^{\mathrm{ERT}}$ is necessary in occasions when during the data reconstruction

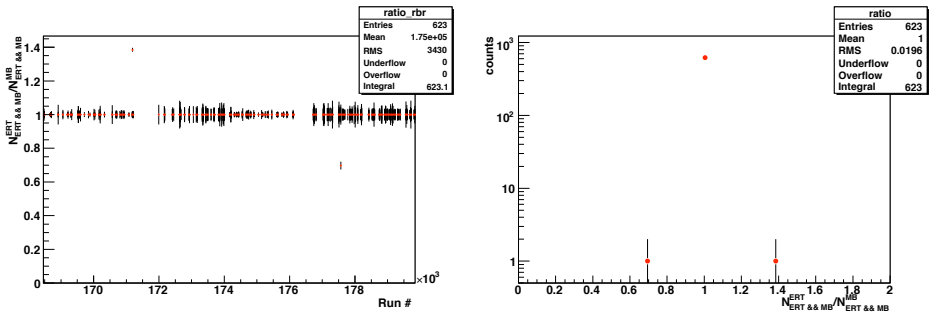

(a) $N_{\mathrm{ERT}}^{\mathrm{MB}}/N_{\mathrm{MB}}^{\mathrm{ERT}}$ as function of run # **(b)** $N_{\mathrm{ERT}}^{\mathrm{MB}}/N_{\mathrm{MB}}^{\mathrm{ERT}}$

Figure 3.2: Ratio of triggered events in the ERT and MB samples

a file segment of either the MB sample or the ERT sample is lost. In this case the number of ERT triggered events in the MB sample ($N_{\mathrm{MB}}^{\mathrm{ERT}}$) does not equal the number of MB triggered events in the ERT sample ($N_{\mathrm{ERT}}^{\mathrm{MB}}$). This ratio is shown in Fig. 3.2a for all run numbers. Runs for which this ratio is > 2 or < 0.5 are rejected (5 runs), all others which are not equal to 1 are corrected (2 runs).

The total number of MB events sampled by the ERT trigger is the sum of Eq. (3.2) over all runs:

$$N_{\mathrm{MB}}^{\mathrm{sampled}} = 5.18558 \times 10^{10}$$

3.1.2 Au + Au Collisions

The analysis of the dielectron continuum in Au + Au at $\sqrt{s_{NN}} = 200$ GeV is performed on the data set recorded during the RHIC running time in 2004. Collisions were selected based on a minimum bias trigger, requiring at least two hits in each of the BBC and a coincident hit in one of the ZDCs. In addition the collision vertex had to be within 38 cm:

$$\mathrm{MB} \equiv (\mathrm{BBCN} \geq 2) \cap (\mathrm{BBCS} \geq 2) \cap (\mathrm{ZDCS} \geq 1 \cup \mathrm{ZDCN} \geq 1) \cap (|z_{\mathrm{vertex}}| < 38\,\mathrm{cm}) \tag{3.3}$$

$92^{+2.5}_{-3.0}\%$ of the inelastic Au + Au cross section are selected by this trigger. For the same reason as in $p + p$ a vertex cut is applied at $z_{\mathrm{vertex}} < 25$ cm in the offline analysis.

In contrast to protons, gold ions cannot be treated as point-like particles. They consist of 197 nucleons, 79 protons an 119 neutrons. When accelerated to an energy of 200 GeV per nucleon they are Lorentz contracted in longitudinal

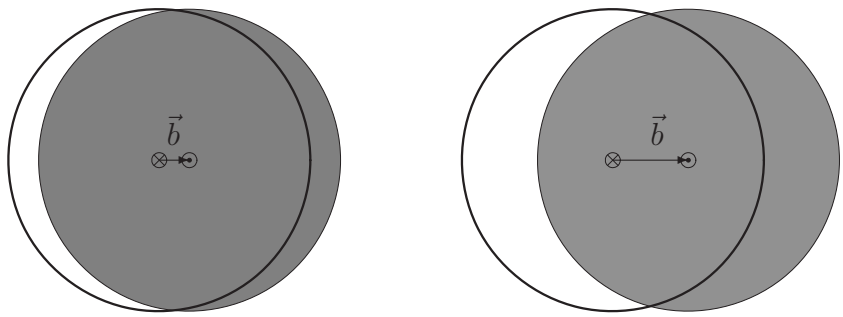

Figure 3.3: Overlap of two gold nuclei for different impact parameters $\vec{b}$.

directions and look much like pan cakes with a radius of ≈ 7 fm in the lab frame. Not every collision of two gold ions is head on, but their centers are shifted by a distance called the impact parameter $\vec{b}$ as illustrated in Fig. 3.3.

The number of nucleons participating in a collision N_{part}, depends on the impact parameter. Every nucleon that participates in a collision can undergo a number of binary collisions N_{coll} with other nucleons. Both numbers can be calculated with a Glauber Monte Carlo simulation, which is a simple geometric model of the nuclei in which the nucleons are distributed following a Wood-Saxon potential. For the centrality classes used in this analysis the results of such a Glauber Monte Carlo simulations [99] are tabulated in Tab. 3.1.

Table 3.1: Average values of N_{part}, N_{coll}, and $\vec{b}$ for different centrality classes of Au + Au and $p + p$ collisions at $\sqrt{s_{NN}} = 200$ GeV [99]. Quoted errors are systematic uncertainties. Also listed are the number of events and the number of signal e^+e^- pairs for each centrality class.

Centrality	$\langle N_{\text{part}} \rangle$	$\langle N_{\text{coll}} \rangle$	$\langle \vec{b} \rangle$	N_{evt}	Signal Pairs
			Au + Au		
0–10%	325.2 ± 3.3	955 ± 94	3.2 ± 0.2	8.6×10^7	9.2×10^4
10–20%	234.6 ± 4.7	603 ± 59	5.7 ± 0.3	8.6×10^7	6.6×10^4
20–40%	140.4 ± 4.9	297 ± 31	8.1 ± 0.3	1.7×10^8	8.1×10^4
40–60%	59.95 ± 3.6	91 ± 12	10.4 ± 0.4	1.7×10^8	3.3×10^4
60–92%	14.5 ± 2.5	14.5 ± 4.0	13.0 ± 0.5	2.9×10^8	1.1×10^4
0–92%	109.1 ± 4.1	258 ± 25	9.5 ± 0.4	8.1×10^8	28.3×10^4
			$p + p$		
MB	2	1	0	1.5×10^9	1.4×10^4
ERT	2	1	0	2.7×10^8	22.8×10^4

3.2 Charged Particle Tracking

With the help of the Drift and Pad Chambers charged particles are tracked down to momenta of 200 MeV/c with a resolution of

$$\sigma_p/p = 0.7\% \oplus 1\% p/(GeV/c). \tag{3.4}$$

A track is reconstructed in the $r - \phi$ plane with six measurements in the X1 and another six the X2 plane of DC over a radial distance of 20 cm. The drift time after which a hit is registered by the anode wire is measured with respect to the collision time t_0 which is measured by the BBC. The working gas is chosen such that the drift velocity is uniform in the active region. This allows to convert the time after which a hit is measured by a particular wire into a distance at which the track passed this wire:

$$x(t) = v_{\text{drift}} \cdot t. \tag{3.5}$$

The drift velocity is obtained by measuring the time distribution of all hits in a DC arm. A typical distribution is shown in Fig. 3.4. The distribution has a characteristic peak which is about twice as high as the following plateau. This is due to tracks within a distance of 2 mm from the anode wire, the region

in which the back wires do not shield the field and the left-right ambiguity remains and therefore twice as many hits are registered as outside that region. The time interval between leading edge and trailing edge corresponds to a drift distance of 2 cm, which is the separation between the cathode and anode wires. The drift velocity is calibrated based on these time distributions for every run. The expected value for the DC working gas is: $v_{\text{drift}} = 50\ \mu\text{m/ns}$. Further calibrations are necessary to consider effects due to the signal width dependence of the arrival time, edge effects in the drift field, geometrical shifts between wires and the global alignment with respect to the collision vertex.

Once the hit times are converted into distances a track candidate is reconstructed with a combinatorial Hough transformation over all possible hit combinations [100]. This is done for in a 2-dimensional space of the coordinates ϕ and α. The angle ϕ is the azimuthal angle of a track candidate at the DC reference radius of 223 cm, as shown in Fig. 3.5. The inclination α of the track candidate with respect to an infinite momentum (*i. e.*, straight) track at angle ϕ is inverse proportional to the momentum and its sign depends on the charge of the particle. Any combination of hits that have a local maximum and surpass the threshold criterion are considered a track candidate. After this Hough transformation further steps are performed to remove background tracks. First, hits are tested on their association to a track. A fit is performed that weights hits according to their distance from the track, such that the weight goes to zero for hits far away from the track. Then it is required that each hit can only belong to one track. Any track with less than eight hits is rejected.

In addition the hits are measured in the UV wires as well as PC1 hits are matched to track candidates to reconstruct the polar angle of the track candidate. If there are more than one PC1 hit that can be associated to a track, the hit associated with the most UV hits is used. The following bits are used to determine the track quality:

```
0 (1)   X1 used
1 (2)   X2 used
2 (4)   UV found
3 (8)   UV unique
4 (16)  PC1 found
5 (32)  PC1 unique

Valid patterns include:

49,50,51  1 1 0 0 x x PC1 found/unique, no UV
61,62,63  1 1 1 1 x x PC1 found/unique, UV found/unique
```

```
17,18,19  0 1 0 0 x x PC1 found/ambiguous, no UVs
21,22,23  0 1 0 1 x x PC1 found/ambiguous, UV found but tied
29,30,31  0 1 1 1 x x PC1 found/ambiguous, UV found w/ one best choice
```

The highest quality tracks can have is 63, *i. e.*, it is reconstructed based on hits in the X1 and X2 planes, has a unique PC1 and UV hit. In addition to these, tracks with quality 31, *i. e.*, requiring hits in X1 and X2 plane and a unique UV hit, but only a ambiguous PC1 hit, as well as with quality 51, *i. e.*, demanding hits in X1 and X2 plane and a unique PC1 hit, but without a matching UV hit, are considered in this analysis.

The measurement of α allows to reconstruct the transverse momentum of charged particles. There is a close relationship between α and the magnetic field integral along the trajectory of a particle:

$$\alpha \simeq \frac{K}{p_T} \tag{3.6}$$

where $K = 206$ mrad GeV/c is the total magnetic field integral. With the measurements of α and ϕ at the DC reference radius, one can determine the initial azimuthal angle at the collision vertex $\phi_0 = \phi - \alpha + \Delta\phi$, with $\Delta\phi = 0.3$ GeV/c $\frac{\int B\,dl}{p_T}$.

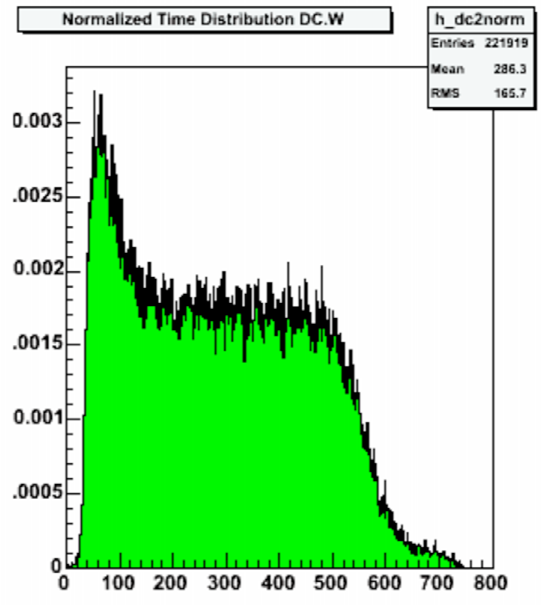

Figure 3.4: Example of a time distribution of hits in the Drift Chamber West arm summed over all wires (collected over $\approx 15,000$ $p+p$ events). The x-axis displays time in units of ns.

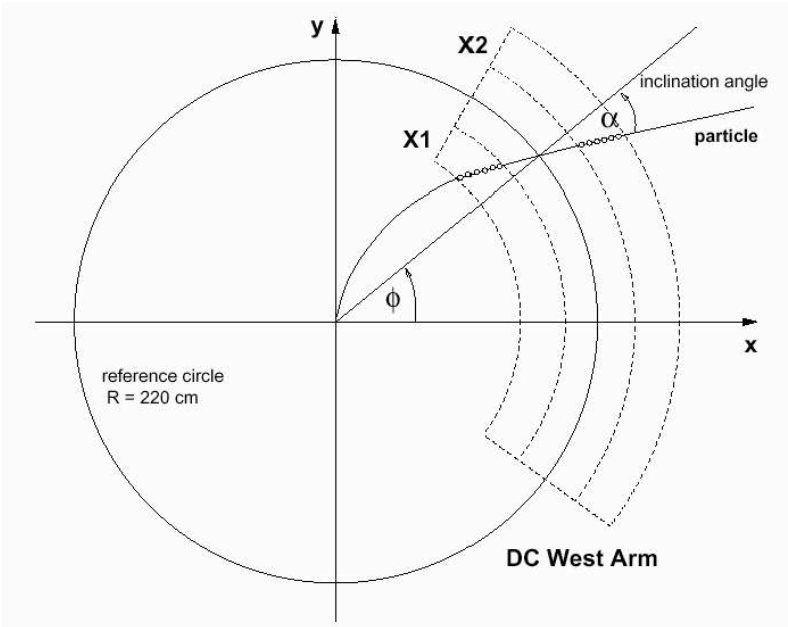

Figure 3.5: Definition of the coordinates ϕ and α used in the Drift Chamber track reconstruction.

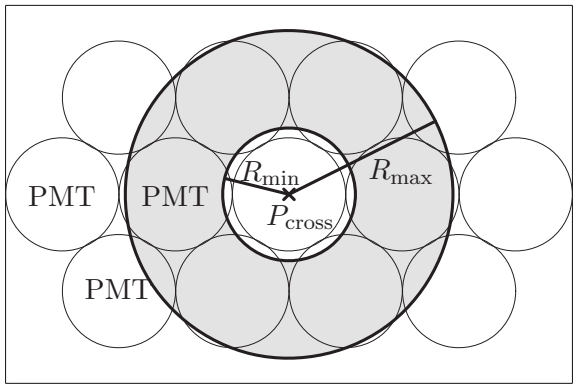

Figure 3.6: Ring mask on the RICH PMT array. P_{cross} is the coordinate of the track projection around which the ring mask (shaded) is applied. The ring mask is limited by $R_{\text{min}} < r < R_{\text{max}}$

3.3 Electron Identification

Electrons emit an average number of 10 Cherenkov photons in the RHIC under an angle of $cos(\theta) = 1/(n\beta)$, which are focused to rings in the PMT plane with an asymptotic radius of ≈ 5.4 cm.

Based on the tracking information from Drift and Pad Chambers, a projection of the track onto the PMT plane is calculated and stored in coordinates of the PMT plane: $P_{\text{cross}} = (z_{\text{cross}}, \phi_{\text{cross}})$. As illustrated in Fig. 3.6, around this point the number of PMT hits n_0 with a distance between $R_{\text{min}} = 3.3$ cm and $R_{\text{max}} = 8.4$ cm are counted. Based on the pulse height measured in a PMT the number of photo electrons (npe_i) is determined. The ring center is reconstructed with n_0, the location R_i of the hit PMT, and the number of photo-electrons in this area ($\text{npe}_0 = \sum_i \text{npe}_i$) as:

$$R_{\text{center}} = \frac{\sum_i \text{npe}_i \cdot R_i}{\sum_i \text{npe}_i} \tag{3.7}$$

with coordinates $R_{\text{center}} = (z_{\text{center}}, \phi_{\text{center}})$. The distance to the track projection (*displacement*) is calculated as:

$$\text{disp} = \sqrt{(z_{\text{cross}} - z_{\text{center}})^2 - (\phi_{\text{cross}} - \phi_{\text{center}})^2}. \tag{3.8}$$

In addition the quality of the measured ring shape is expressed in terms of the difference to the expected ring shape:

$$\chi^2/\text{npe}_0 = \frac{\sum_i (R_i - R_0)^2 \cdot \text{npe}_i}{\sum_i \text{npe}_i} \tag{3.9}$$

with $R_0 = 5.9$ cm.

The distance between the track projection onto the EMCal and the position of the associated EMCal cluster is calculated in azimuthal and $\hat{z}$ direction, emcdphi_e and emcdz_e, respectively. These matching variables in units of radians and cm are converted into units of one standard deviation σ by fitting the distribution to a Gaussian and stored as emcsdphi_e and emcsdz_e. As the cluster position in the EMCal is particle species dependent due to the different shower shapes, this calibration is done for electron candidates. A circular 5 σ cut on the distance is applied in $p + p$ while in Au + Au a 3 σ matching is required.

In comparison to their momentum of $p > 200$ MeV/c, electrons have a negligible mass ($m_e = 511$ keV/c^2). Therefore the energy they deposit in the EMCal must match the momentum ($E = \sqrt{p^2 + m_e^2} \simeq p$). In contrast, hadrons only deposit a fraction of their energy in the EMCal which leads to a measured energies which are smaller than their momenta.

Fig. 3.7a shows the E/p distribution of charged tracks in min. bias $p + p$ collisions in comparison with electron candidates, *i. e.*, charged tracks fulfilling all but the E/p eID cut. While the distribution of all charged tracks shows no clear peak due to electrons at $E/p = 1$, requiring the eID cut greatly improves the signal to background ratio. The width of the peak of $\approx 14\%$ is dominated by the energy resolution of the EMCal given in Eqs. (2.2, 2.3).

The reconstructed energy does not match the momentum for all electrons, as in some cases their shower overlaps with a photon shower which leads to a larger energy and causes the tail at $E/p > 1$. Electrons from off-vertex decays or late conversions have a misreconstructed momentum, as the tracking algorithm assumes all tracks to originate from the collision vertex. Off-vertex decays traverse less magnetic field integral and are therefore bent less, which leads to a larger reconstructed momentum and $E/p < 1$. In the momentum range of $p \lesssim 4$ GeV/c, relevant for this analysis, the momentum resolution of the drift chamber Eq. (3.4) is better than the energy resolution of the EMCal Eqs. (2.2, 2.3). Therefore, in the e^+e^- pair analysis the invariant mass and p_T of the e^+e^- pair is calculated using the momentum information rather than the energy Eq. (3.10). As a consequence, electrons with a mismeasured energy can be kept, while electrons with misreconstructed momenta are removed with a cut on $E/p > 0.5$ in $p + p$. In Au + Au the momentum dependence of the E/p distribution is corrected and the matching is stored in units of a standard deviation dep $= (E/p - 1)/\sigma_{E/p}$. This parameterization is determined by a Gaussian fit of the E/p distribution of electron candidates as function of p_T. A value of dep > -2 is required for tracks to pass the electron identification cut.

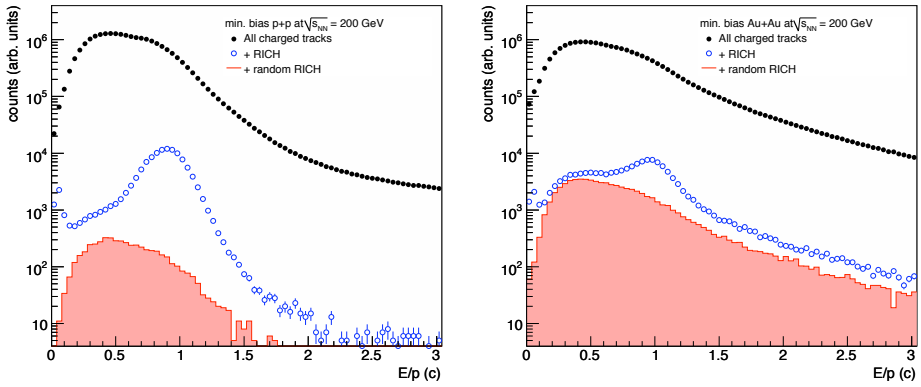

(a) $p+p$ **(b)** $\mathrm{Au}+\mathrm{Au}$

Figure 3.7: E/p distribution in min. bias $p+p$ (a) and min. bias $\mathrm{Au}+\mathrm{Au}$ (b) for charged tracks (black), tracks after applying the RICH cuts (blue) and contribution of hadrons randomly associated to hits in the RICH (red).

Table 3.2: Electron identification cuts for $p+p$ and $\mathrm{Au}+\mathrm{Au}$.

eID cut	$p+p$	$\mathrm{Au}+\mathrm{Au}$
quality	63||31||51	
n_0	≥ 1	≥ 2
disp	< 10 cm	< 5 cm
χ^2/npe_0	< 15 cm^2	< 10 cm^2
E/p	> 0.5	–
dep	–	$> -2\ \sigma$
$\sqrt{\mathrm{emcsdphi_e}^2 + \mathrm{emcsdz_e}^2}$	$< 5\ \sigma$	$< 3\ \sigma$

In addition, some background remains underneath the peak which is attributed to random associations of RICH hits to hadrons. This contribution can be estimated by matching tracks in the north side of the drift chamber to hits in the south side of the RICH and vice versa. This is done by swapping the RICH sides during the track reconstruction. In contrast to a single electron analysis, this hadron contamination is unreducable in the pair analysis. Fig. 3.7b shows the same distributions for min. bias $\mathrm{Au}+\mathrm{Au}$ collisions, in which the hadron contamination is much larger. In the region $0.7 < E/p < 1.2$ the contribution to the sample of electron candidates is about 1.6% in $p+p$ and 16% in $\mathrm{Au}+\mathrm{Au}$ collisions All electron identification cuts are summarized in Tab. 3.2.

3.4 Pair Analysis

In an event the source of any electron or positron is unknown and therefore all electrons and positrons are combined to *foreground* pairs, like sign FG_{++}, FG_{--} and unlike sign FG_{+-}. In the $p+p$ data set it is checked that at least one of the tracks in each pair is associated to a hit of the ERT trigger. From the single track information, the invariant mass m_{ee} and the transverse momentum p_T of the e^+e^- pair are calculated as:

$$\begin{aligned} m_{ee}^2 &= (p_+ + p_-)^2 \\ &= (E_+ + E_-)^2 - (\vec{p}_+ + \vec{p}_-)^2 \qquad (3.10) \\ p_T^2 &= (p_{x,+} + p_{x,-})^2 + (p_{y,+} + p_{y,-})^2 \qquad (3.11) \end{aligned}$$

with $E_\pm = \sqrt{\vec{p}_\pm^2 + m_e^2}$, $m_e = 511$ keV/c^2, and the 3-momentum vector $\vec{p}_\pm$ as measured with the drift chamber.

The *foreground* pairs can be generally separated into *physical* and *unphysical* pairs. With *physical* pairs it is referred to an e^+e^- pair which originates from the same parent, which can be either a hadron, *e. g.*, $\omega \to e^+e^-$ or a photon. The photon can either be virtual and convert internally (such a virtual photon appears for instance in the π^0 Dalitz decay: $\pi^0 \to \gamma\gamma^* \to \gamma e^+e^-$), or real and convert in detector material (*e. g.*, the two photon decay of a π^0: $\pi^0 \to \gamma\gamma \to \gamma e^+e^-$). The latter type of photon conversions, also referred to as external conversion, are for reasons that will be explained in Section 3.4.2 not reconstructed with their real mass $m = 0$ but contaminate the invariant mass spectrum of e^+e^- pairs up to $m_{ee} \approx 0.3$ GeV and need to be removed from the sample of *physical* pairs in order to extract the physics signal of hadron decays and internal photon conversions. By definition, *physical* pairs can only exist as unlike sign pairs. However, the chance to reconstruct both the electron and the positron of such pairs is very much reduced by the limited azimuthal acceptance and the low momentum cut off at $p < 200$ MeV/c.

The other, much larger contribution to the *foreground*, are *unphysical* pairs, *i. e.*, electrons and positrons that are not from the same hadron, but just a result of combining all electrons in the event. *Unphysical* pairs can either be of unlike- or like-sign charge combinations. Most of these pairs are completely *uncorrelated* combinations of electrons, which can be described with a combinatorial background generated with an event mixing technique. However, some fraction of the *unphysical* pairs is *correlated*, either due to correlations early on in the decay history, *i. e.*, the pair does not share the same parent, but the same "grand parent" particle, in which case they are referred to as *cross* pairs or because they were produced within the same jet, therefore denoted *jet*

pairs. Another source of *correlated* pairs are *ghost* pairs, which appear when tracks share the same detector information.

This classification scheme has ignored one very important source of e^+e^- pairs, *i. e.*, e^+e^- pairs from semi-leptonic open charm and bottom decays correlated through flavor conservation, discussed in Section 1.2.2. They do not originate from the same parent, however, they are considered *physical* pairs.

In this Section all the details of the various background subtractions are discussed. Beforehand, a schematic overview over the various background sources is given as orientation. Noted in parenthesis are the Section number in which the particular background is discussed and a keyword referring to the method with which this background is removed.

All Pairs:

- physical pairs
  - hadron and open charm decays, internal conversions (Signal)
  - external photon conversions (ϕ_V cut, Section 3.4.2)
- unphysical pairs
  - uncorrelated (Mixed Events, Section 3.4.3)
  - correlated
    - Detector Ghosts (Pair Cuts, Section 3.4.1)
    - Jet and Cross Pairs (Simulations, Section 3.4.4)

3.4.1 Pair Cuts

In order to reproduce the shape of the combinatorial background of uncorrelated e^+e^- pairs with mixed events, it needs to be assured that any detector correlations are removed from the sample of e^+e^- pairs in real events. Such correlations can occur, when two electron candidates share detector information, *e. g.* have overlapping rings in the RICH, share the same hit in PC1 or have overlapping cluster in the EMCal. For instance, two electrons which traverse the RICH along parallel trajectories would emit Cherenkov photons which are focused on the same ring, as any two parallel photons are focused by the spherical mirror onto the same focal point. Therefore, a RICH hit due to an electron would be matched also to any charged track crossing the RICH parallel to the electron and therefore fulfill all eID cuts on RICH variables, even if the charged track itself does not emit Cherenkov photons. This effect is illustrated in Fig. 3.8.

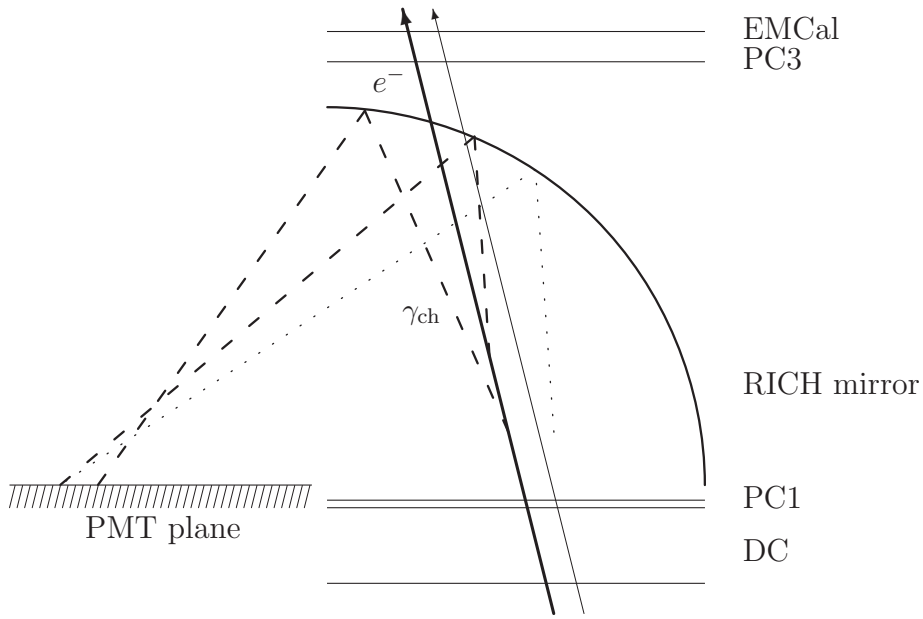

Figure 3.8: Overlapping rings in the RICH PMT plane due to two parallel tracks.

While an uncorrelated hadron contamination would be reproduced by mixed event, such a *ghost* pair is highly correlated in its geometry and therefore in the invariant mass spectrum. They have typical small opening angle and are therefore reconstructed with a small invariant mass. As like-sign tracks are bent by the magnetic field bents in the same direction, in contrast to unlike-sign pars which are bent in opposite directions, they have even smaller masses than unlike-sign pairs.

Naturally, these *ghost* pairs do not exist in mixed events and therefore have to be rejected in real events. They are rejected with an event cut which rejects events (real and mixed) if there are two tracks which overlap in RICH, EMCal, or PC1. On overlaps in the RICH a cut is applied based on the distance between the ring centers associated to the two electron candidates of a pair. The distance between two tracks i and j is calculated as:

$$\Delta_{\rm center} = \sqrt{(z^i_{\rm center} - z^j_{\rm center})^2/\sigma^2_{z_{\rm center}} + (\phi^i_{\rm center} - \phi^j_{\rm center})^2/\sigma^2_{\phi_{\rm center}}} \qquad (3.12)$$

with $\sigma_{z_{\rm center}} = 3.6$ cm and $\sigma_{\phi_{\rm center}} = 10$ mrad being the rms of the distributions of ring distances (without any pair cut) in $\hat{z}$ and $\hat{\phi}$ directions, respectively, as shown in Fig. 3.9. A cut of $\Delta_{\rm center} > 10$ (equivalent to 36 cm) is applied, which corresponds to twice the expected ring diameter ($\sim$16.8 cm). One may consider to cut only on one ring diameter as this would be enough to remove

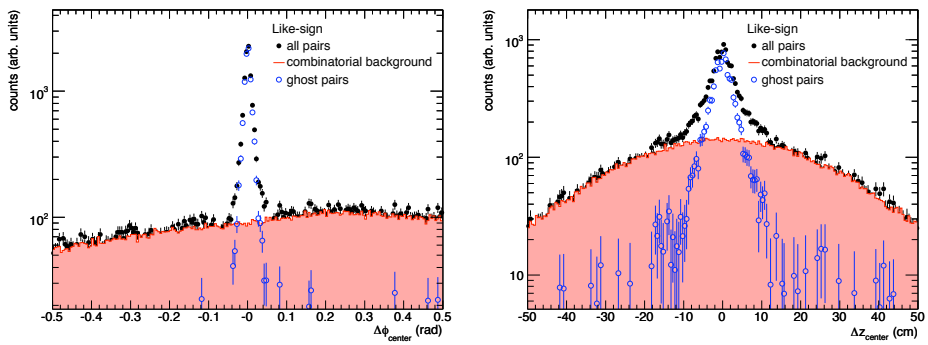

(a) (b)

Figure 3.9: Distance of the ring centers associated to two tracks in $\Delta\phi_{\text{center}}$ (a) and Δz_{center} (b).

false positive ring association to charged hadrons, but in addition one observes a reduction in the reconstruction efficiency of two electrons which have close rings, as their rings may overlap and distort their shape, which increases, *e. g.*, χ^2/npe_0. This effect only vanishes once the two ring are clearly separated by more than one ring diameter, *i. e.* their centers by more than two ring diameters. In the EMCal events are rejected if two electron candidates are associated to two clusters within a 3×3 tower region (which is the average size of an electromagnetic shower). In the PC1 the cut is applied at $\Delta z \leq 0.5$ cm and $\Delta\phi \leq 20$ mrad, which is the size of a cell. The pair cut on RICH variables has the largest effect and the combined cuts remove $\sim 0.08\%$ of all events in $\text{Au} + \text{Au}$ collisions and a fraction of pairs which varies from 4% in the most central to 2% in the most peripheral collisions. In $p + p$ this cut removes only 0.1% of all pairs.

The effect of ghost pairs on the e^+e^- pair distribution can be studied with the invariant mass distribution of like-sign pairs, *i. e.*, e^+e^+ and e^-e^- pairs, which do not contain any physics signal. The real and mixed event distributions of like-sign pairs in MB $\text{Au} + \text{Au}$ collisions is shown in black and red, respectively, in Fig. 3.10a. The mixed events clearly deviate in shape from the real event distribution. In the invariant mass distribution of e^+e^- pair the ghosts are also clearly visible at $m \approx 500$ MeV/c^2 as shown in Fig. 3.10b, where the mixed events deviate from the real events.

3.4.2 Photon Conversions

Photon conversions contribute to the final spectrum of e^+e^- pairs and should be rejected. Electrons from conversions that are created off vertex in detector

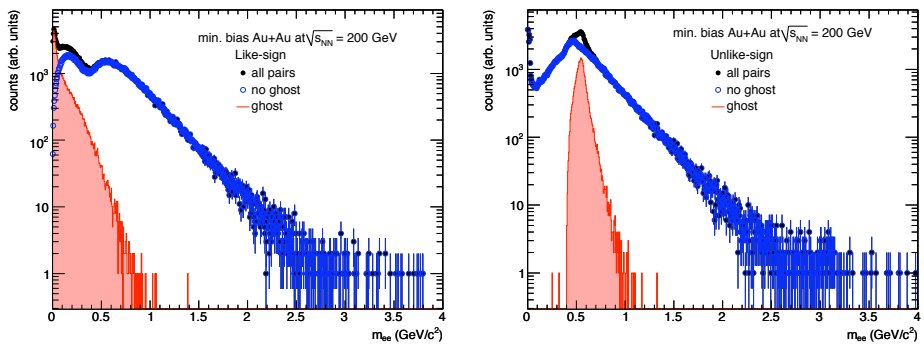

(a) like-sign pairs **(b)** unlike-sign pairs

Figure 3.10: Invariant mass distribution of like-sign (a) and unlike-sign pairs(b). All pairs are shown in black, ghost pairs in blue and all others in red.

material, *e. g.*, the beam pipe made of Beryllium (0.3 X_0), pass through less magnetic field integral than the PHENIX tracking algorithm assumes, which leads to a misreconstructed momentum. In addition the opening angle of the e^+e^- pair is misreconstructed, as it is tracked back to the collision vertex, rather than to the conversion vertex, as illustrated in Fig. 3.11. Therefore, conversion pairs have an apparent mass that increases with the distance from the collision vertex and therefore with the misreconstructed opening angle.

Photon conversions occur in the beam pipe at a radius of 4 cm which corresponds to the peak at $m_{ee} \approx 20$ MeV/c^2 in the invariant mass spectrum shown in Fig. 3.12, in detector support structures ($m_{ee} \approx 80$MeV/c^2 and $m_{ee} \approx 125$ MeV/c^2) as well as in the air before, and much reduced within, the installed Helium bag which contributes as a continuum out to $m_{ee} \leq 300$ MeV/c^2, corresponding to the DC entrance window, beyond which electrons do not bend anymore because the region is field-free. Therefore, electrons from photon conversions within the DC are straight and rejected with the high-p_T cut of 20 GeV/c. As photons are massless, conversion pairs do not have an intrinsic opening angle, but are aligned perpendicular to the axial magnetic field. A cut on the orientation of e^+e^- pairs is used to remove those conversion photons. To measure the orientation of the e^+e^- pair plane with respect to the $\hat{z}$ direction,

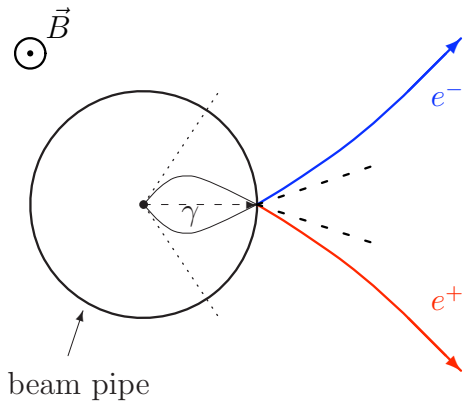

Figure 3.11: Misreconstruction of the opening of a conversion pair. Shown are the photon and the conversion pair which is created in the beam pipe. The real opening angle between the original trajectories (dashed lines) is much smaller than the reconstructed opening angle, artificially created by tracking the particles back to the collision vertex (dotted lines).

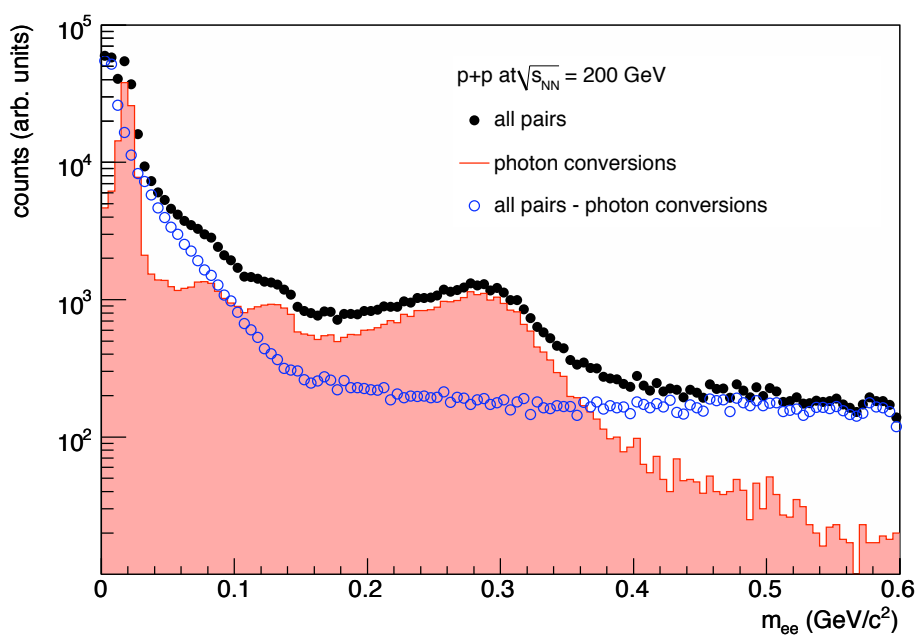

Figure 3.12: Invariant mass distribution of all e^+e^- pairs in real events (black), photon conversions (red) and remaining pairs (blue). The peak at 20 MeV/c^2 is caused by photon conversions in the beam pipe. The remaining shape is due to other detector support structures (see text).

i. e., the magnetic field, the angle ϕ_V is defined [101]:

$$\vec{u} = \frac{\vec{p}_1 + \vec{p}_2}{|\vec{p}_1 + \vec{p}_2|} \tag{3.13a}$$

$$\vec{v} = \vec{p}_1 \times \vec{p}_2 \tag{3.13b}$$

$$\vec{w} = \vec{u} \times \vec{v} \tag{3.13c}$$

$$\vec{u}_a = \frac{\vec{u} \times \hat{z}}{|\vec{u} \times \hat{z}|} \tag{3.13d}$$

$$\phi_V = \arccos\left(\frac{\vec{w} \cdot \vec{u}_a}{|\vec{w}||\vec{u}_a|}\right). \tag{3.14}$$

Here $\vec{p}_1$ is the 3-momentum vector of the electron and $\vec{p}_2$ the 3-momentum vector of the positron. The following cuts are applied:

- $m < 0.60$ && $\phi_V > 0.1$ rad
- $m < 0.03$ && $\phi_V > 0.25$ rad

To remove beam pipe conversions a harder cut has to be applied, because the multiple scattering within Beryllium smears the orientation with respect to the magnetic field more than in air. In addition the resolution of the ϕ_V measurement improves with increasing conversion radius. This cut removes $> 98\%$ of all conversion pairs.

3.4.3 Event Mixing

As mentioned in the introduction to this Section, most of the e^+e^- pairs are of uncorrelated origin. While the unlike-sign spectrum contains both physics signal and background pairs, the like-sign spectrum does not contain any physics signal and therefore is a direct measure of the background. It can be shown (see Appendix A) that, as long as electrons and positrons are produced in pairs, the unlike-sign combinatorial background is the geometrical mean of the like-sign backgrounds, independent of efficiency and acceptance differences, *i. e.*:

$$\langle BG_{+-} \rangle = 2\sqrt{\langle BG_{++} \rangle \langle BG_{--} \rangle}. \tag{3.15}$$

In experiments with equal acceptance for like- and unlike-sign pairs, the distribution of like-sign pairs in real events can be directly related to the unlike-sign background through their geometrical mean $BG_{+-} = 2\sqrt{FG_{++}FG_{--}}$ and subtracted from the unlike-sign pair spectrum to obtain the physics signal.

Because of a different acceptance for like- and unlike-sign pairs a correction needs to be applied to use this method in PHENIX.

Another possibility, which leads to a higher statistical accuracy, is the event mixing. Electrons from events with similar topology are combined to pairs to statistically approximate the combinatorial background. To ensure the same topology, events are categorized in pools according to their centrality, z-vertex and reaction plane. In Au+Au, mixed events were generated in ten centrality, six z-vertex and one reaction plane pools[1], while five z-vertex pools were used for $p+p$.

The ERT trigger used in the $p+p$ analysis biases the single electron distribution towards higher p_T. Therefore, to generate the correct combinatorial background shape of e^+e^- pairs, the mixed events must be generated from the minimum bias sample, but as in real events it is required that in every pair at least one of the electrons must fulfill the ERT trigger condition.

The shape of the like-sign background from mixed events can be compared to the like-sign distribution in real events to determine in which region and how well the background shape is reproduced in the event mixing. The absolute normalization of unlike-sign combinatorial background is given by the geometrical mean of the observed positive and negative like-sign pairs $2\sqrt{BG_{++}BG_{--}}$ where BG_{++} and BG_{--} are determined by integrating the mixed event distributions after they have been normalized in a region where the mixed events reproduce the distribution from real events, which means it is enforced that:

$$\frac{\int_A BG_{++} + BG_{--}}{\int_A FG_{++} + FG_{--}} \equiv 1 \tag{3.16}$$

where A denotes the normalization region.

Background Normalization

The like-sign spectra as function of mass and p_T after mixed event subtraction are shown in the left panel of Fig. 3.13. The figure clearly shows that mixed and real events do not have the same distribution like-sign pairs, which is an indication of correlated pairs. However, in the region $m_{ee} \sim p_T$ the distributions are very similar. Since for a pair with opening angle δ it is $m_{ee} = p_1 p_2 (1 - \cos\delta)$, the condition $m_{ee} \sim p_T$ roughly corresponds to an azimuthal opening angle of $\Delta\phi \sim \pi/2$. This was checked with a PYTHIA simulation of minimum bias events which is described in Section 3.4.4. The

[1] One reaction plane pool means no separation by reaction plane. However, it was tested that the reaction plane pooling has no effect on the mixed event distribution and can be neglected

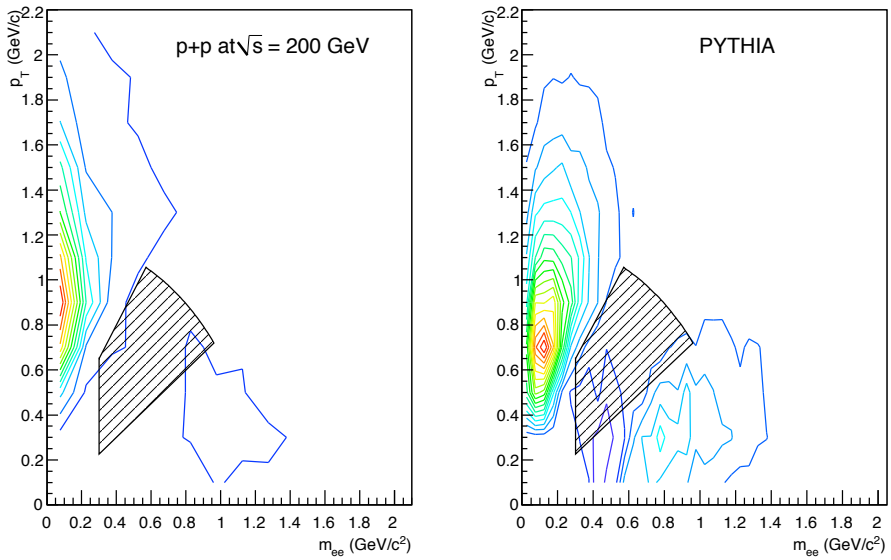

Figure 3.13: Mixed event subtracted like-sign spectrum in data (left) and as calculated with PYTHIA (right) as function of invariant mass and p_T. The dashed region outlines the normalization area as defined in Eq. (3.17).

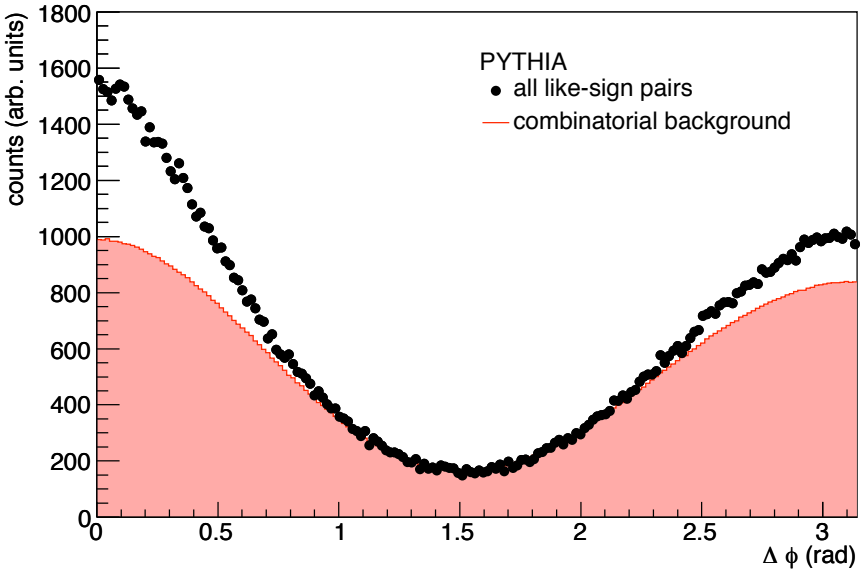

Figure 3.14: $\Delta\phi$ distribution of PYTHIA like-sign pairs in same (*black*) and mixed (*red*) events.

$\Delta\phi$ distribution of like-sign pairs from these simulated events is shown in Fig. 3.14. This distribution is compared to the mixed event distribution also generated from the PYTHIA simulation. The mixed events agree well with the real events around $\Delta\phi \sim \pi/2$. Thus, the mixed event distribution in PYTHIA is normalized in the region defined by:

$$m_{ee} > 300 \text{ MeV}/c^2 \quad \&\& \tag{3.17a}$$
$$m_T < 1.2 \text{ MeV}/c^2 \quad \&\& \tag{3.17b}$$
$$p_T/c - 1.5m_{ee} \leq 200 \text{ MeV}/c^2 \quad \&\& \tag{3.17c}$$
$$p_T/c - 0.75m_{ee} \geq 0 \text{ MeV}/c^2. \tag{3.17d}$$

which is shown as the dashed contour in Fig. 3.13. The yield remaining after the subtraction such normalized mixed event is considered correlated and discussed in Section 3.4.4. The same region is used to normalize the mixed events to the real events in data. The normalization to this region has a statistical accuracy of 2.8%.

3.4.4 Correlated Background

Fig. 3.15 shows the invariant mass distribution of like-sign pair of real and mixed events in $p+p$ collisions. The pairs from mixed events do not reproduce the shape of like-sign pairs in real events which is an indication for correlated background whose two sources are discussed in the following.

Cross Pairs

The first correlation of like-sign pairs stems from hadron decays with two e^+e^- pairs in the final state, *e. g.*, for a π^0 these are the double Dalitz decay ($\pi^0 \to e^+e^-e^+e^-$), the Dalitz decay ($\pi^0 \to \gamma e^+e^-$) in which the photon converts into an e^+e^- pair in detector material, and the two photon decay ($\pi^0 \to \gamma\gamma$) in which both photons convert into two e^+e^- pairs[2]:

$$\begin{aligned} \pi^0 &\to \gamma_1\gamma_2 \\ &\to e_1^+e_1^-e_2^+e_2^- \end{aligned} \tag{3.18}$$

The e^+e^- pair with the same parent photon is considered physics signal (*i. e.*, $e_1^+e_1^-$ and $e_2^+e_2^-$), and in case of a real photon conversion in detector material removed with a cut (see Section 3.4.2). The *"cross"* combinations into two

[2]All these decays are in principle two photon decays, but with two, one or zero virtual photons

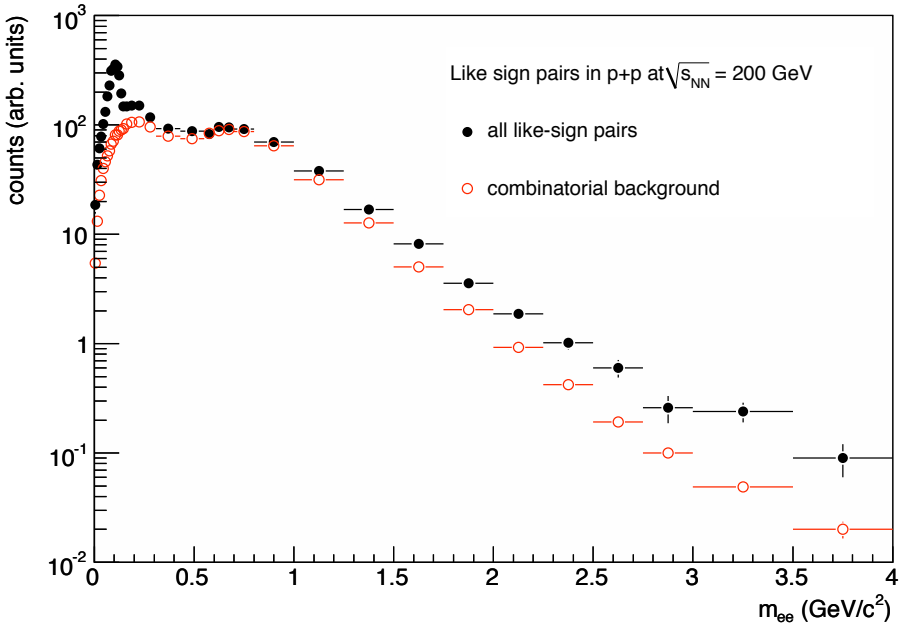

Figure 3.15: Invariant mass distribution of all like-sign pairs in real events (black) and mixed events (red). The normalization is discussed in Section 3.4.3. A clear shape difference is observed at small and at large masses, indicating a source of correlated background.

unlike-sign pairs ($e_1^+e_2^-$ and $e_2^+e_1^-$) as well as into two like-sign pairs ($e_1^+e_2^+$ and $e_1^-e_2^-$) are not purely combinatorial, but correlated via the π^0 mass ($m_{ee} < m_{\pi^0}$). Therefore, their contribution is present in the real event spectra of both unlike- and like-sign pairs, but not in mixed events. Fig. 3.15 shows the invariant mass distribution of like sign pairs in real (black) and mixed events (red). The peak visible in the real event distribution of like-sign pairs at a mass of $m_{ee} \approx 100$ MeV/c^2 is due to cross pairs. The same cross combinations are possible for η decays, with the additional decay channel of $\eta \to \pi^0\pi^0\pi^0$. Therefore these correlated pairs extend up to a mass of $m_\eta \approx 550$ MeV/c^2.

For every decay, contributions to unlike-sign signal U, unlike-sign cross C and like-sign cross pairs L can be calculated in terms of branching ratios ($BR_{\gamma\gamma} = 98.8\%$, $BR_{\text{Dalitz}} = 1.2\%$, and $BR_{\text{dbl.Dalitz}} = 3.14 \times 10^{-5}$ [29]) and conversion probability ($P_{\text{conv}} = 0.3\%$) relative to the π^0 multiplicity:

- $\pi^0 \to \gamma\gamma \to e^+e^-e^+e^-$:
  - $U = 0$
  - $C = 2 \cdot BR_{\gamma\gamma} \cdot P_{\text{conv}}^2 = 2 \cdot 98.8\% \cdot 0.3\%^2 = 1.76 \times 10^{-5}$
  - $L = 2 \cdot BR_{\gamma\gamma} \cdot P_{\text{conv}}^2 = 2 \cdot 98.8\% \cdot 0.3\%^2 = 1.76 \times 10^{-5}$
- $\pi^0 \to \gamma\gamma^* \to e^+e^-e^+e^-$:
  - $U = BR_{\text{Dalitz}} = 1.2\%$
  - $C = 2 \cdot BR_{\text{Dalitz}} \cdot P_{\text{conv}} = 2 \cdot 1.2\% \cdot 0.3\% = 7.2 \times 10^{-5}$
  - $L = 2 \cdot BR_{\text{Dalitz}} \cdot P_{\text{conv}} = 2 \cdot 1.2\% \cdot 0.3\% = 7.2 \times 10^{-5}$
- $\pi^0 \to \gamma\gamma^* \to e^+e^-e^+e^-$:
  - $U = 2 \cdot BR_{\text{dbl. Dalitz}} = 2 \cdot 3.14 \times 10^{-5} = 6.28 \times 10^{-5}$
  - $C = 2 \cdot BR_{\text{dbl. Dalitz}} = 2 \cdot 3.14 \times 10^{-5} = 6.28 \times 10^{-5}$
  - $L = 2 \cdot BR_{\text{dbl. Dalitz}} = 2 \cdot 3.14 \times 10^{-5} = 6.28 \times 10^{-5}$

which gives a total of $U = 1.2 \times 10^{-2}$ unlike-sign signal pairs, $C = 1.5 \times 10^{-4}$ unlike-sign cross pairs, and $L = 1.5 \times 10^{-4}$ like-sign cross pairs per π^0.

The same calculation for the η yields a total of $U = 6 \times 10^{-3}$ unlike-sign signal pairs, $C = 6.7 \times 10^{-4}$ unlike-sign cross pairs, and $L = 6.7 \times 10^{-4}$ like-sign cross pairs per η. Here the branching ratios ($BR_{\gamma\gamma} = 39.38\%$, $BR_{\text{Dalitz}} = 0.6\%$ [29]) have been used and the unknown double Dalitz branching ratio of the has been assumed to be the square of the single Dalitz: $BR_{\text{dbl. Dalitz}} = BR_{\text{Dalitz}}^2 = 1.23 \times 10^{-5}$. The three π^0 decay of the *eta* contribute with an additional $C = L = 6.09 \times 10^{-4}$ to the unlike- an like-sign cross pairs.

All these contribution are simulated with a fast Monte Carlo (EXODUS) of π^0 and η double Dalitz decay as well as $\eta \to \pi^0\pi^0\pi^0$ decays and filtered into the PHENIX acceptance. The resulting unlike- and like-sign cross pairs are shown Fig. 3.16.

Jet Pairs

Besides cross pairs another source contributes to correlated background pairs. This contribution can be reproduced with minimum bias events from PYTHIA simulations [102–104]. PYTHIA is a computer program widely used as Monte Carlo simulation of high-energy elementary particle collisions, *e. g.* $e + p$ or $p + p$. The particle interactions are calculated using leading order matrix elements and the Lund string fragmentation model [105]. PYTHIA 6.319 with CTEQ5L parton distribution function [106] has been used. The following hard QCD processes have been activated:

MSUB 11: $f_i f_j \to f_i f_j$

MSUB 12: $f_i \overline{f}_i \to f_k \overline{f}_k$

MSUB 13: $f_i \overline{f}_j \to gg$

MSUB 28: $f_i g \to f_i g$

MSUB 53: $gg \to f_k \overline{f}_k$

MSUB 68: $gg \to gg$

Here g denotes a gluon and f_i a fermion with flavor i, *i. e.*, u, d, s, b, t, e^-, ν_e, μ^-, ν_μ, τ^-, or ν_τ, and their corresponding antiparticles $\overline{f}_i$. Flavors appearing in the initial carry indices i or j, while flavors created only in the final state are denoted k. A Gaussian width of 1.5 GeV for the primordial k_T distribution is used (PARP(91)=1.5), and the minimum parton p_T has been set to 2 GeV (CKIN(3)=2.0).

In this simulation the branching ratio of the π^0 Dalitz decay was set to 100% to increase the sample of e^+e^- pairs. The resulting $\Delta\phi$ distribution of like sign pairs from real (black) and mixed events (red) in PYTHIA is shown in Fig. 3.14. The mixed event like-sign pairs have been normalized to the like-sign pairs in real events in the range $70° < \Delta\phi < 110°$, in which the distributions of like-sign pairs in real and mixed events agree well. The deviation in shape at $\Delta\phi \approx 0$ can be attributed to electrons which originate from two π^0 decays which occurred within the same jet, while the correlation at $\Delta\phi \approx \pi$ comes from electrons that are decay products of π^0's in back-to-back jets. π^0's within

the same jet are close in ϕ which leads to a small opening angle of the e^+e^- pair, which also causes these pairs to have a rather small mass and at the same time a large p_T as their momentum vectors add constructively. e^+e^- pairs correlated via back-to-back jet have large opening angles and therefore larger invariant masses, while their p_T is smaller than the one of pairs in the same jet, as their momentum vectors cancel mostly. These correlations in m_{ee} and p_T are shown in Fig. 3.13 for like-sign pairs from PYTHIA after the subtraction of mixed events.

Fig. 3.16 shows invariant mass spectra of like sign pairs (top) and unlike-sign pairs (bottom) in real events, the mixed event distribution normalized according to Eq. (3.17) and the distributions after mixed event subtraction. The remaining like-sign correlated pairs are fitted with the distribution of cross and jet pairs in the two mass regions $0.06 < m_{ee} < 0.12$ GeV/c^2 and $0.80 < m_{ee} < 2.00$ GeV/c^2:

$$\int_{0.06}^{0.12} \left(\frac{dN}{dm}\right)_{\text{like}} dm = A \int_{0.06}^{0.12} \left(\frac{dN}{dm}\right)_{\text{cross}} dm + B \int_{0.06}^{0.12} \left(\frac{dN}{dm}\right)_{\text{jet}} dm \tag{3.19a}$$

$$\int_{0.8}^{2} \left(\frac{dN}{dm}\right)_{\text{like}} dm = B \int_{0.8}^{2} \left(\frac{dN}{dm}\right)_{\text{jet}} dm \tag{3.19b}$$

The resulting normalization factors are applied to the unlike-sign distributions of cross and jet pairs which are shown in Fig. 3.16. The unlike-sign signal results from subtracting the correlated background from all correlated pairs.

3.4.5 Like-sign Subtraction

As a systematic check of the subtraction of combinatorial and correlated background an independent, completely data driven method has been developed, that does not make any assumption about the background contributions. As stated at the beginning of the chapter, the like-sign spectrum is free of physics signal and therefore a measure of the background, whether correlated or uncorrelated. But the different acceptance of unlike- and like-sign pairs in PHENIX, needs to be considered before they can be subtracted from the real event spectrum of e^+e^- pairs.

The acceptance difference between unlike- and like-sign pairs is preserved in mixed events, therefore the ratio of $BG_{+-}/(BG_{++} + BG_{--})$ is the proper correction to convert the distribution of like-sign pairs in real events into the background distribution of e^+e^- pairs. The signal of e^+e^- pairs is calculated

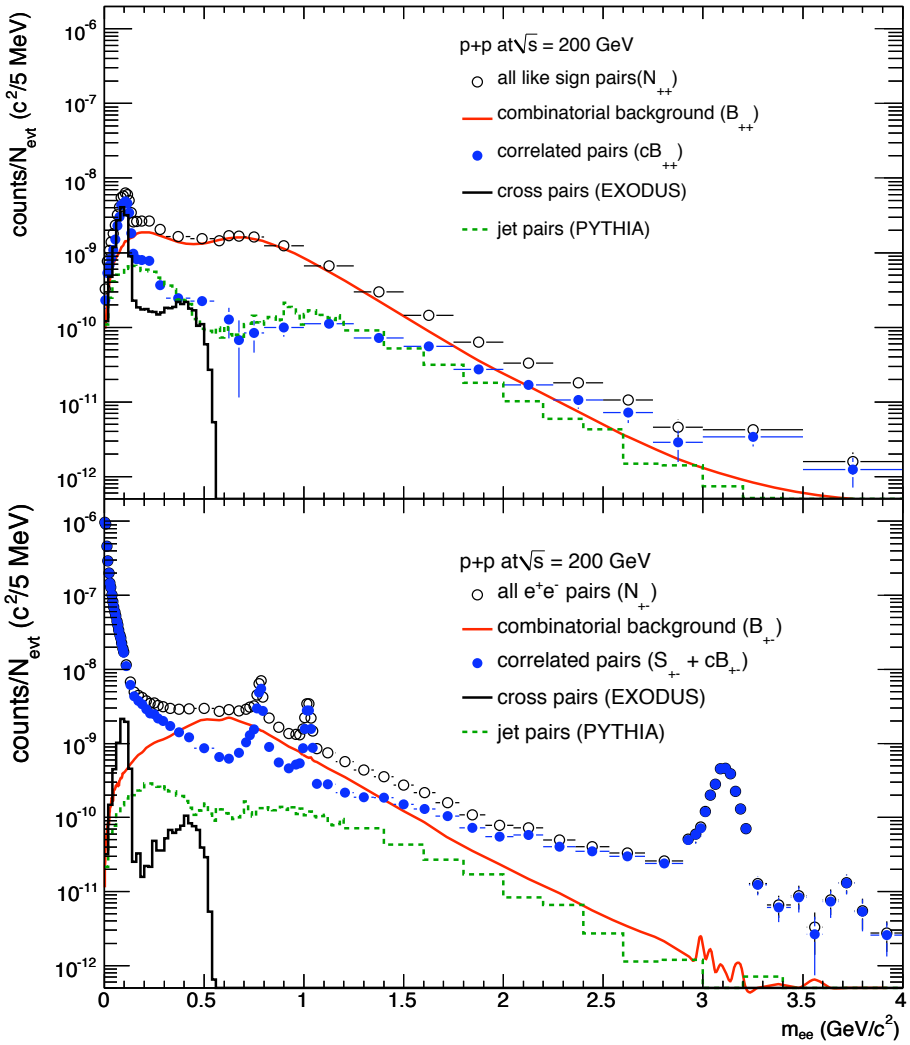

Figure 3.16: Raw dielectron spectra. The top panel shows like-sign pairs as measured in the experiment, the combinatorial background from mixed events, the correlated pair background obtained by subtracting the combinatorial background, and the individual contributions from cross and jet pairs to the correlated background (see text). The bottom panel shows the same distributions for unlike-sign pairs. The correlated background in both panels is normalized to the measured like-sign pairs remaining after subtracting the combinatorial background.

in m_{ee} and p_T as follows:

$$S_{+-} = FG_{+-} - (FG_{++} + FG_{--})\frac{BG_{+-}}{(BG_{++}BG_{--})}. \tag{3.20}$$

In the special case that the real event like-sign spectrum is perfectly described by the mixed events, this expression reduces to $S = FG_{+-} - BG_{+-}$.

The background distributions of like- and unlike-sign pairs are shown in Fig. 3.4.5 together with the relative acceptance.

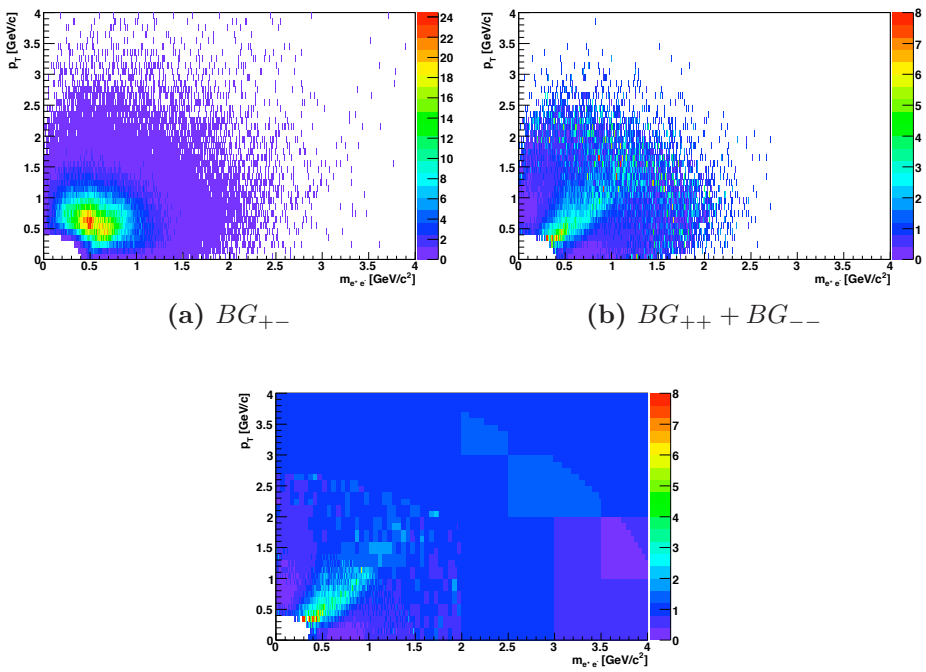

(a) BG_{+-} **(b)** $BG_{++} + BG_{--}$

(c) Relative Acceptance

Alternatively to using the like sign foreground, one can first subtract the mixed events (normalized as discussed in Section 3.4.3) and then subtract the mixed event subtracted like sign signal, corrected for the relative acceptance, from the mixed event subtracted unlike-sign spectrum everywhere but in the normalization region[3]. To increase statistics at high p_T and large invariant mass, the Au + Au mixed events have been used as an alternative description of the relative acceptance. The relative acceptance for correlated and uncorrelated pairs may differ. This effect has been studied its effect by

[3]Note that a subtraction including this region would be arithmetically identical to the previous method, which skips the mixed event subtraction.

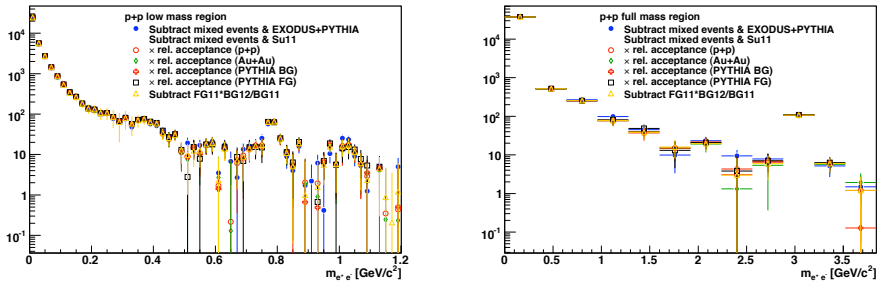

(a) LMR **(b)** IMR

Figure 3.17: Comparison of background subtraction methods.

using PYTHIA foreground spectra to determine the relative acceptance, *i. e.*, $FG_{+-}/(FG_{++} + FG_{--})$. In addition the mixed events from PYTHIA have been used to describe the relative acceptance. Fig. 3.17 shows a comparison of the subtracted unlike-sign spectra with the presented methods.

There are two systematic uncertainties in the background subtraction, one due to the statistics available in the normalization region for the various background sources:

- mixed events: 2.43%
- cross pairs: 2.49%
- jet pairs: 6.86%

The systematic uncertainty on the measured signal is shown in Fig. 3.18. The other systematic uncertainty is in the shape of the subtracted correlated background, which is estimated from the RMS of the various subtraction methods described above, which is shown in Fig. 3.19. For $m_{ee} < 2$ GeV a systematic uncertainty of 5% (10% above) has been assigned.

3.4.6 Background Subtraction in Au + Au

The like-sign distribution of real and mixed events in minimum bias Au + Au collisions are compared in Fig. 3.20. Their shapes agree not only in the region defined in Eq. (3.17), but for all masses above 550 MeV/c^2. Qualitatively, this can be explained with the suppression of away-side jets observed in Au + Au collisions [107]. At small masses, below 200 MeV/c^2 a like-signal from cross pairs is observed. The ratio of mixed event subtracted to mixed events is fitted above 550 MeV/c^2 to a constant, which gives a result of -0.000259 ± 0.000633

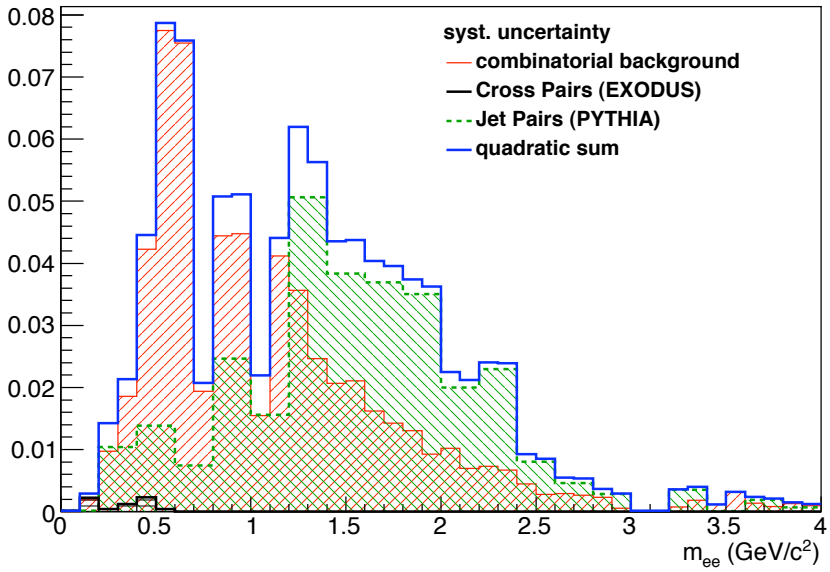

Figure 3.18: Comparison of background subtraction methods.

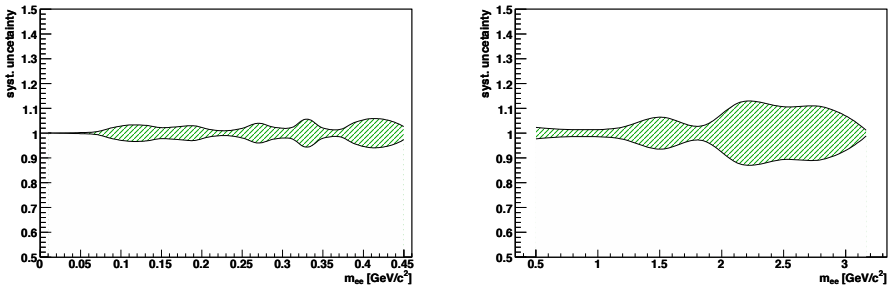

(a) LMR (b) IMR

Figure 3.19: RMS of all methods as function of m_{ee}.

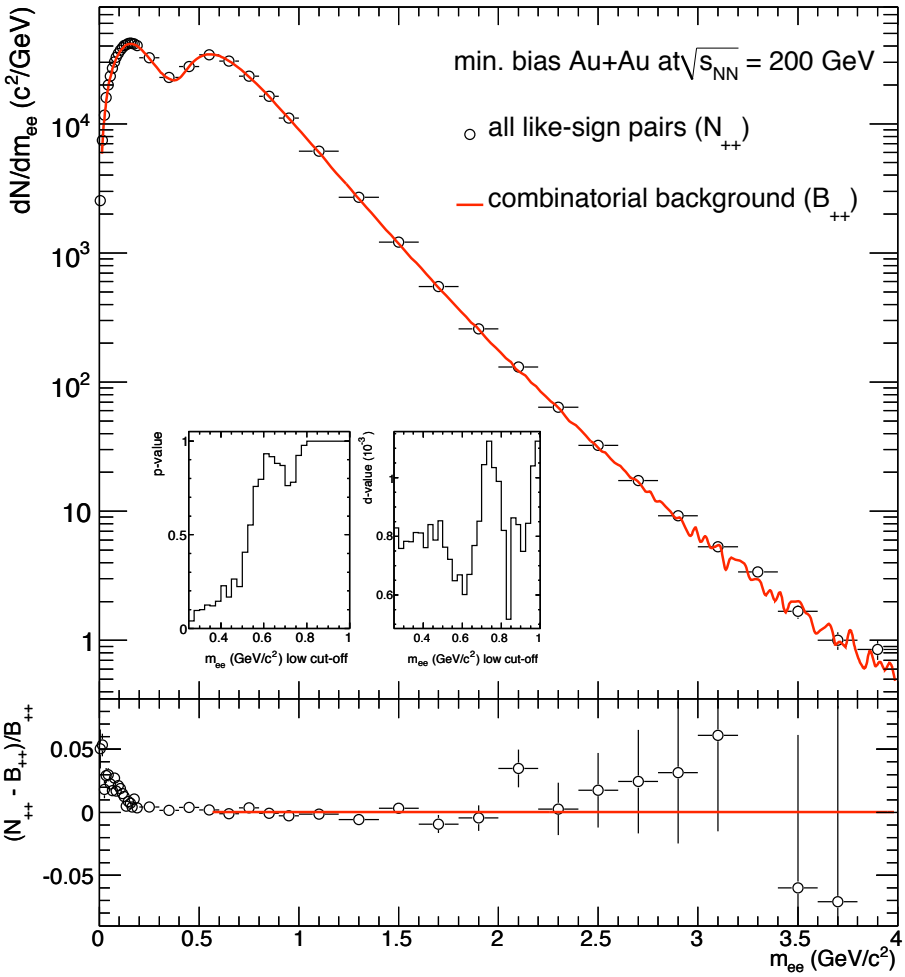

Figure 3.20: Invariant mass distribution of like sign pairs in real events (*open circles*) and mixed events (*red line*). The mixed events to real events are normalized above 700 MeV/c^2. The bottom panel shows the ratio of the mixed event subtracted spectrum and the mixed events.

Table 3.3: Fit parameters to ratios shown in Fig. 3.20 and Fig. 3.21.

Centrality	Constant	χ^2/DOF	χ^2 test	max. dist
0–10%	0.00063 ± 0.00088	1.25	0.58	0.0013
10–20%	−0.0009 ± 0.0014	1.42	0.54	0.0018
20–40%	−0.0024 ± 0.0018	1.12	0.56	0.0037
40–60%	−0.0085 ± 0.0050	1.42	0.69	0.0099
60–92%	−0.018 ± 0.016	1.56	1.02	0.042
00–92%	−0.00026 ± 0.00063	1.45	0.51	0.0011

well in agreement with zero and a $\chi^2/DOF = 1.45$. Fig. 3.21 shows the like-sign mass spectra of real and mixed events divided in centrality bins of 0–10%, 10–20%, 20–40%, 40–60% and 60–90%. The same fits as for the MB spectra are performed and summarized in Tab. 3.3, which also includes the results of a statistical χ^2 test and the maximum deviation of a Kolmogorov-Smirnov test (also see inserts to Fig. 3.20). The maximum deviations of Kolmogorov-Smirnov test are small compared to the uncertainties of the absolute normalization of the mixed event background. The p-values corresponding the the χ^2 test, which are greater than 0.999 for all centrality classes, confirm the hypothesis that the two distributions are compatible and can be accepted for any commonly used significance level.

Finally, Fig. 3.22 shows the invariant mass spectra of like-sign pairs in real and mixed event for different p_T ranges: $p_T < 1$ GeV/c, $1 \leq p_T < 2$GeV/c, and $p_T \geq 2$ GeV/c. Again no deviation of the mixed event shape from the real event distribution is observed for $m_{ee} > 550$ MeV/c^2.

The mixed event are normalized to the like-sign pairs in real events in the mass range $0.7 < m_{ee} < 4$ GeV/c^2:

$$\frac{\int_{0.7}^{4.0} BG_{++} + BG_{--}}{\int_{0.7}^{4.0} FG_{++} + FG_{--}} \equiv 1 \tag{3.21}$$

The lower limit of 0.7 GeV/c^2 is chosen conservatively to avoid any contamination from correlated background observed at low mass and provides at the same time sufficient statistical accuracy of 0.12%. The absolute normalization of the unlike-sign background is given by the geometrical mean of the normalized like-sign integrals: $BG_{+-} = \sqrt{BG_{++} + BG_{--}}$. An Additional 0.2% uncertainty, due to a correction of that normalization by 1.004 ± 0.002 for the fact that the applied pair cuts removes a different fraction of like- than unlike-sign pairs, yields to a total systematic uncertainty of 0.25% on the background

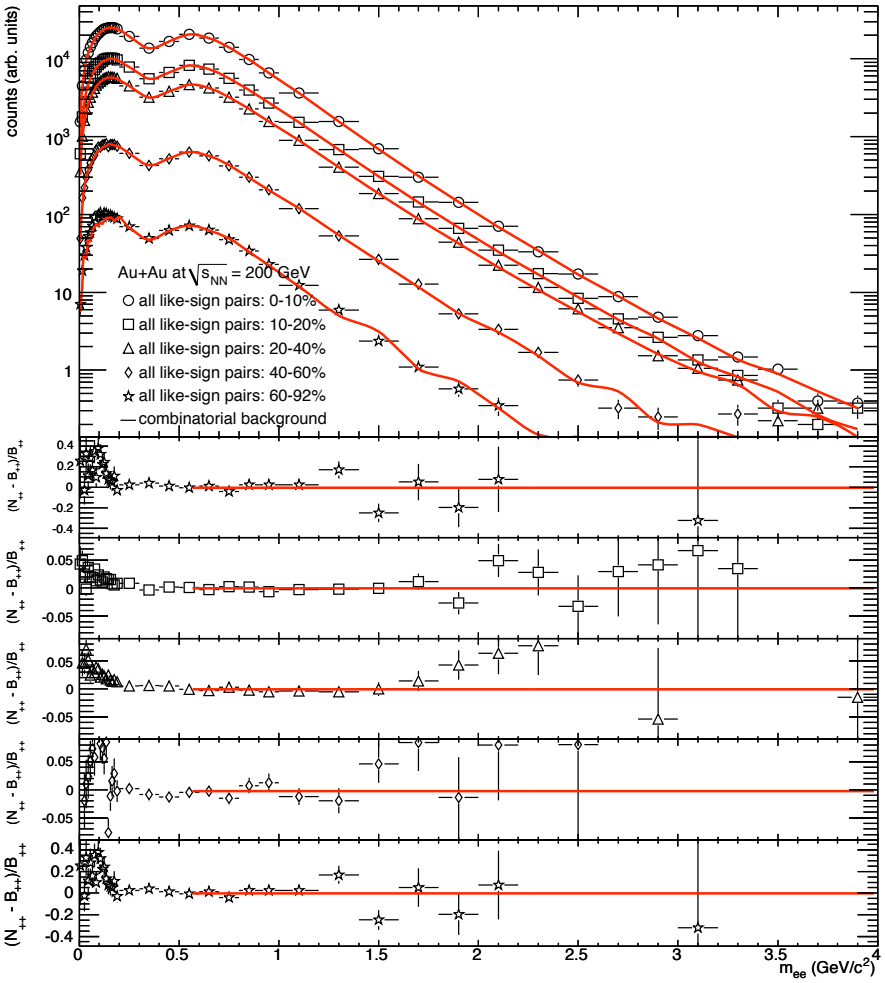

Figure 3.21: Invariant mass distribution of like sign pairs in real events (*open circles*) and mixed events (*red line*) for different centrality bins. The mixed events to real events are normalized above 700 MeV/c^2. The bottom panel shows the ratio of the mixed event subtracted spectrum and the mixed events.

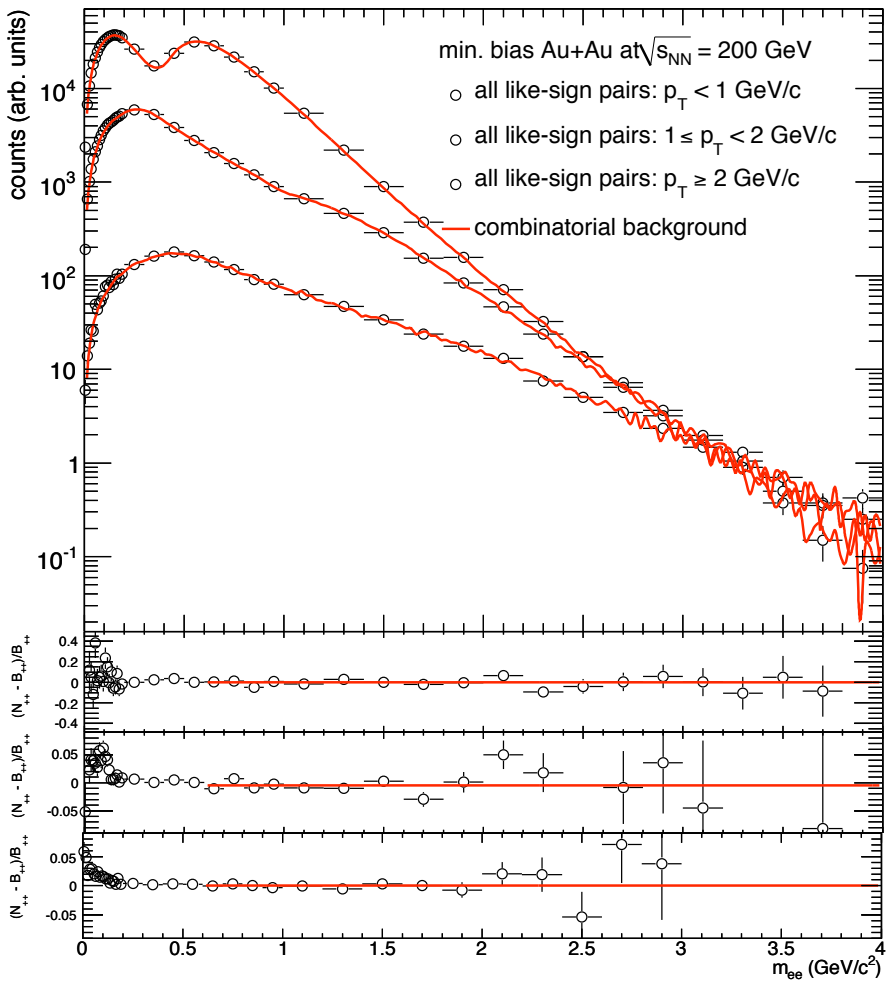

Figure 3.22: Invariant mass distribution of like sign pairs in real events (*open circles*) and mixed events (*red line*) for different p_T bins. The mixed events to real events are normalized above 700 MeV/c^2. The bottom panel shows the ratio of the mixed event subtracted spectrum and the mixed events.

normalization, which is a conservative upper limit of the uncertainty.

The correlated background, remaining after mixed event subtraction, due to cross pairs and a contribution of jet-pairs at small masses is subtracted analog to the $p + p$ analysis. But, in contrast to $p + p$, there is no room for a correlated signal due to away-side jet correlations. Due to the known modifications of the away-side jet, the Au + Au data are indeed expected to differ from the PYTHIA simulation. Therefore, the near-side correlations, *i. e.*, pairs with $\Delta\phi < \pi/2$ are separated from the away-side contribution with $\Delta\phi > \pi/2$ and the three components cross, near-, and aways-side pairs are fitted to the like-sign correlated background distribution:

$$\left(\frac{dN}{dm}\right)_{\text{like}} = A\left(\frac{dN}{dm}\right)_{\text{cross}} + B\left(\frac{dN}{dm}\right)_{\text{near}} + C\left(\frac{dN}{dm}\right)_{\text{away}} \tag{3.22}$$

As the mixed events have been normalized at $m_{ee} > 0.7$ GeV/c^2 it follows that $C = 0$. The different background contributions are illustrated in Fig. 3.23. Here the away-side curve is shown for illustration only and is normalized as the near-side curve. The overall contribution of correlated pairs relative to the unlike-sign signal is small, and comparing different subtraction strategies leads to a systematic uncertainty of 10% on correlated background subtraction in the LMR.

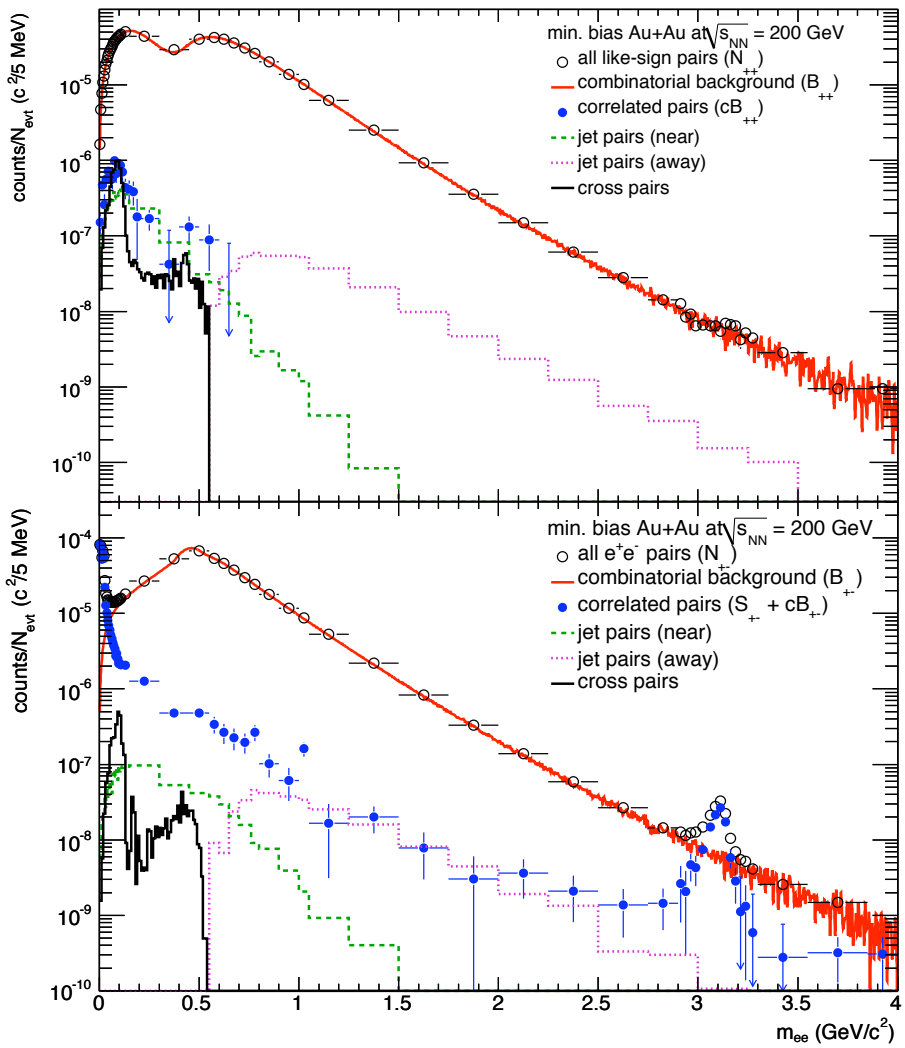

Figure 3.23: Raw dielectron spectra in min. bias Au + Au. The top panel shows like-sign pairs as measured in the experiment, the combinatorial background from mixed events, the correlated pair background obtained by subtracting the combinatorial background, and the individual contributions from cross and near- and away-side jet pairs to the correlated background (see text). The bottom panel shows the same distributions for unlike-sign pairs. The correlated background in both panels is normalized to the measured like-sign pairs remaining after subtracting the combinatorial background.

3.5 Efficiency Correction

The distribution of e^+e^- pairs after subtraction of all background sources needs to be corrected for the pair efficiencies of track reconstruction ($\varepsilon^{\text{pair}}_{\text{reco}}$), electron identification ($\varepsilon^{\text{pair}}_{\text{eID}}$) and (in case of $p+p$) triggering by the ERT ($\varepsilon^{\text{pair}}_{\text{ERT}}$). The pair efficiencies for track reconstruction and electron identification are the product of the single efficiencies, *i. e.*, $\varepsilon^{\text{pair}}_{\text{reco}} = \varepsilon^{+}_{\text{reco}}\varepsilon^{-}_{\text{reco}}$ and $\varepsilon^{\text{pair}}_{\text{eID}} = \varepsilon^{+}_{\text{eID}}\varepsilon^{-}_{\text{eID}}$, while the trigger efficiency for a pair can be expressed in terms of the single trigger efficiency as: $\varepsilon^{\text{pair}}_{\text{ERT}} = (1-\varepsilon^{+}_{\text{ERT}})\varepsilon^{-}_{\text{ERT}} + (1-\varepsilon^{-}_{\text{ERT}})\varepsilon^{+}_{\text{ERT}} + \varepsilon^{+}_{\text{ERT}}\varepsilon^{-}_{\text{ERT}}$. Tracking and electron identification efficiency include effects due to dead areas within the detector acceptance. In addition the efficiency of the pair cuts ($\varepsilon_{\text{pair cuts}}$) needs to be taken into account. The idea is that the invariant mass spectra are corrected "into the PHENIX acceptance" as:

$$\frac{dN}{dm_{ee}} = \frac{1}{N_{\text{evt}}}\frac{1}{\Delta m_{ee}}\frac{N_{ee}}{\varepsilon_{\text{pair}}}\frac{\varepsilon_{\text{BBC}}}{\varepsilon_{\text{bias}}} \tag{3.23}$$

with Δm_{ee} the bin width in GeV/c^2, $\varepsilon_{\text{pair}} = \varepsilon^{\text{pair}}_{\text{reco}}\varepsilon^{\text{pair}}_{\text{eID}}\varepsilon^{\text{pair}}_{\text{ERT}}\varepsilon_{\text{pair cuts}}$ is the pair efficiency, $\varepsilon_{\text{BBC}} = 0.545 \pm 0.06$ is the BBC efficiency and $\varepsilon_{\text{bias}} = 0.79 \pm 0.02$ is the BBC trigger bias.

On the other hand, p_T distributions of e^+e^- pairs are corrected for the limited geometric acceptance ($\varepsilon^{\text{pair}}_{\text{geo}} = \varepsilon^{+}_{\text{geo}}\varepsilon^{-}_{\text{geo}}$) into full azimuth ($0 < \phi \leq 2\pi$) and into one unit of rapidity ($|y| < 0.5$). The spectra are shown as yield invariant under Lorentz transformation:

$$\frac{1}{2\pi\, p_T}\frac{d^2N}{dp_T\, dy} = \frac{1}{2\pi\, p_T}\frac{1}{N_{\text{evt}}\,\Delta p_T}\frac{N_{ee}}{\varepsilon_{\text{pair}}\,\varepsilon^{\text{pair}}_{\text{geo}}}\frac{\varepsilon_{\text{BBC}}}{\varepsilon_{\text{bias}}}. \tag{3.24}$$

This invariant yield can be converted into an invariant cross section by multiplying with the inelastic $p+p$ cross section $\sigma^{\text{inel}}_{pp} = 42.2$ nb.

$$E\frac{d^3\sigma}{dp^3} = \frac{1}{2\pi\, p_T}\frac{d^2N}{dp_T\, dy}\sigma^{\text{inel}}_{pp} \tag{3.25}$$

3.5.1 Tracking and Electron Identification Efficiency

The tracking and electron identification efficiency is calculated for single electrons based on a full Monte Carlo simulation of π^0 decays. 450M events are generated containing π^0's flat in rapidity ($|y| < 0.5$), azimuth ($0 < \phi \leq 2\pi$), vertex distribution ($|z_{\text{vertex}}| < 30$ cm), and in p_T ($0 < p_T < 25$ GeV/c). To enhance statistics the Dalitz decay branching ratio is set to 100%.

These events have been processed through a full GEANT simulation pro-

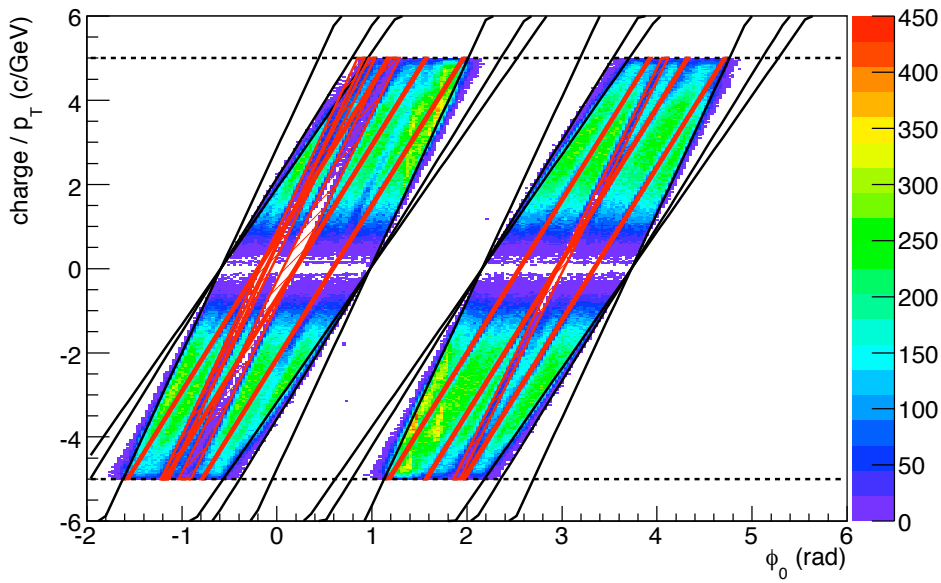

Figure 3.24: Single electron acceptance. The diagonal line represent the acceptance limits due to RICH and DC as defined in Eq. (2.5). The dashed lines indicate the low p_T cut off at 200 MeV/c. Dead areas are removed with fiducial cuts shown as red shaded areas.

gram of the PHENIX detector [108] which includes the details of the detector response. The output is analyzed by the PHENIX event reconstruction chain. The same single electron cuts are applied in simulation as in real data. Every electron is weighted according to a realistic p_T distribution of the parent π^0. The electron identification efficiency is determined as function of the single electron p_T:

$$\varepsilon^{\pm}_{\mathrm{eID}} = \frac{dN^{\pm}_{\mathrm{out}}/dp^{\pm}_T}{dN^{\pm}_{\mathrm{in}}/dp^{\pm}_T} \tag{3.26}$$

$dN^{\pm}_{\mathrm{in}}/dp^{\pm}_T$ is the p_T distribution of generated electrons that fall into active area within the PHENIX acceptance as parameterized in Eq. (2.5). The active area is parameterized from data as function of the single particle charge sign q, p_T and azimuthal angle ϕ_0 as shown in Fig. 3.24. Dead areas are removed with fiducial cuts which are listed in Tab. 3.4 in the simulations. $dN^{\pm}_{\mathrm{out}}/dp^{\pm}_T$ is the number of generated electrons in the same fiducial area that pass the electron identification cuts. Fig. 3.25 shows the single electron (positron) efficiency as function of p_T in $p+p$ collisions.

The correction for e^+e^- pairs is determined with the hadron decay generator EXODUS. The single electron (positron) efficiency is parameterized by a

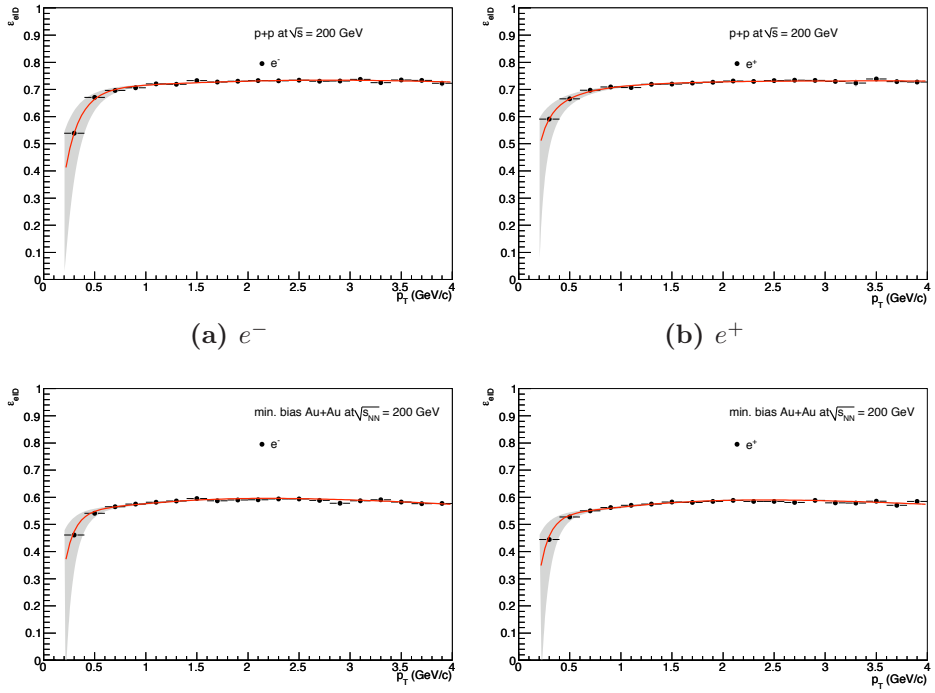

(a) e^- **(b)** e^+

(c) e^- **(d)** e^+

Figure 3.25: Track reconstruction and electron identification efficiency in $p+p$ collisions (a)–(b) and in $\mathrm{Au}+\mathrm{Au}$ (c)–(d) as function of the single electron p_T.

Table 3.4: Fiducial cuts in the PHENIX acceptance.

	Dead Area		
A	$-0.88+4.56\phi_0<q/p_T$ &&	$q/p_T>$	$-0.28+4.56\phi_0$
B	$0.28+4.56\phi_0<q/p_T$ &&	$q/p_T>$	$0.58+4.56\phi_0$
C	$0.52+4.86\phi_0<q/p_T$ &&	$q/p_T>$	$0.88+4.86\phi_0$
D	$-2.68+4.56\phi_0<q/p_T$ &&	$q/p_T>$	$-2.38+4.56\phi_0$
E	$-13.78+4.56\phi_0<q/p_T$ &&	$q/p_T>$	$-13.48+4.56\phi_0$

Table 3.5: Parameterization of the single electron efficiency.

	$p+p$		Au + Au	
	electrons	positrons	electrons	positrons
a	0.991	−0.662	0.824	0.818
b (GeV/c)	−0.244	−0.0400	−0.168	−0.182
c (GeV/c)^2	0.00963	−0.00431	8.12×10^{-4}	8.88×10^{-4}
d (GeV/c)$^{-1}$	−0.0260	−0.00349	−0.0324	−0.0301
e	−0.478	0.417	−0.340	−0.236
f (GeV/c)$^{-1}$	−2.01	5.60×10^{-9}	−3.14	−3.15

fit of the following functional form:

$$f(p_T) = a + b/p_T + c/p_T^2 + dp_T + \mathrm{e}^{(e+fp_T)} \tag{3.27}$$

The fit values for electrons and positrons in $p+p$ and Au + Au collisions, respectively, are tabulated in Tab. 3.5. This parameterization has been implemented in EXODUS and used as a weight to each electron. In addition e^+e^- pairs are rejected if at least one of the electrons falls in one of the dead areas defined in Tab. 3.4. Then the efficiency to reconstruct and identify an e^+e^- pair is determined as function of the pair p_T and the invariant mass.

This method has been cross checked with a full Monte Carlo simulation of e^+e^- pairs. About 1M e^+e^- pairs have been generated, one half of them flat in mass (0–4 GeV/c^2) and p_T (0–4 GeV/c), the other half linearly falling in mass (0–1 GeV/c^2) and p_T (0–1 GeV/c) to enhance the statistics at low mass and p_T where the efficiency varies the most. The pairs have been simulated flat in azimuth ($0 < \phi \leq 2\pi$) and rapidity ($|y| < 0.5$). Only pairs with both electron and positron in the ideal PHENIX acceptance were processed by GEANT, reconstructed and analysed with the same cuts as the data. As with the previous method, the efficiency is calculated as function of the e^+e^- pair p_T and mass.

The efficiency to reconstruct and identify an e^+e^- pair is shown as function of its invariant mass in Fig. 3.26 averaged over all p_T assuming the p_T shape from the hadron decay cocktail. At high masses the pair efficiency of $\approx 45\%$ is the square of the plateau value of the single efficiency which consist out of the efficiency of the track reconstruction (90%), the electron identification (75%) and the dead areas (65%) within the acceptance. Towards smaller masses the shape of the pair efficiency is the result of the convolution of the single electron efficiency which steeply falls towards low p_T and the geometrical acceptance which cuts the single electron spectrum at $p_T < 200$ MeV/c. In

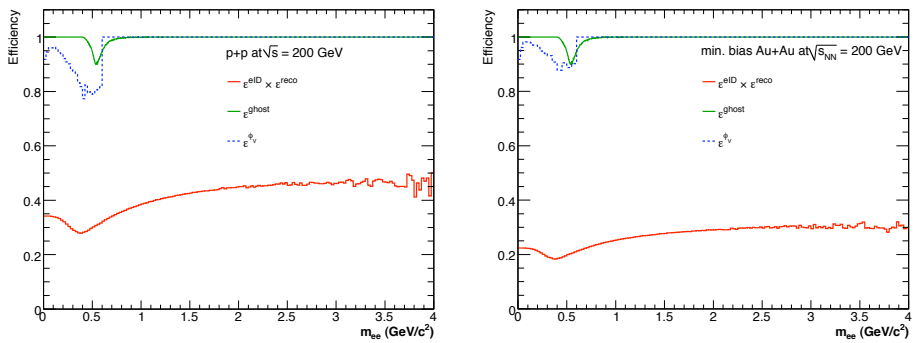

(a) $p + p$ **(b)** $\mathrm{Au} + \mathrm{Au}$

Figure 3.26: Track reconstruction and electron identification efficiency in $p + p$ collisions (a) and in $\mathrm{Au} + \mathrm{Au}$ (b) as function of e^+e^- pair invariant mass.

the mass range $0.4 < m_{ee} \leq 0.8$ GeV/c^2 the pair efficiency drops as a result of the single efficiency decrease at low single electron momenta. But for masses below 0.4 GeV/c^2 the geometrical acceptance removes all pairs with $m_T = \sqrt{p_T^2 + m_{ee}^2} < 0.4$ GeV/c^2, which leads to a higher average p_T for e^+e^- pairs in this mass window and therefore a rise of the efficiency.

The effect of the pair cuts on legitimate signal pairs is shown separately in Fig. 3.26. The efficiency is due to legitimate pairs that accidentally fulfill one of the pair cut criteria, *e. g.*, share the same ring in the RICH and are therefore removed. This efficiency is studied with mixed events in which any detector overlap is accidental by definition. The pair cut efficiency is calculated as:

$$\varepsilon_{\text{pair cuts}} = \frac{d^2 N_{\text{mix}}^{\text{pair cuts}}}{dm_{ee} dp_T} \Bigg/ \frac{d^2 N_{\text{mix}}}{dm_{ee} dp_T} \tag{3.28}$$

where $d^2 N_{\text{mix}}^{\text{pair cuts}}/(dm_{ee} dp_T)$ is the mixed event distribution of e^+e^- pairs with pair cuts and $d^2 N_{\text{mix}}/(dm_{ee} dp_T)$ the one without pair cuts.

The ϕ_V removes not only photon conversions but also signal pairs which happen to be oriented in the magnetic field like conversions. This effect is studied with the full GEANT Monte Carlo simulation of π^0's which was already used for the electron identification efficiency. Above the π^0 mass this is extended with the help of hadron decay simulations with EXODUS. To simulate the detector resolution, an empirical smearing of the magnitude and direction of the 3-momentum vector of the electrons was implemented to reproduce the ϕ_V distribution observed in data and the GEANT simulation. The Gaussian smearing of the azimuthal and polar angle of the 3-momentum vector $\vec{p}$ of a

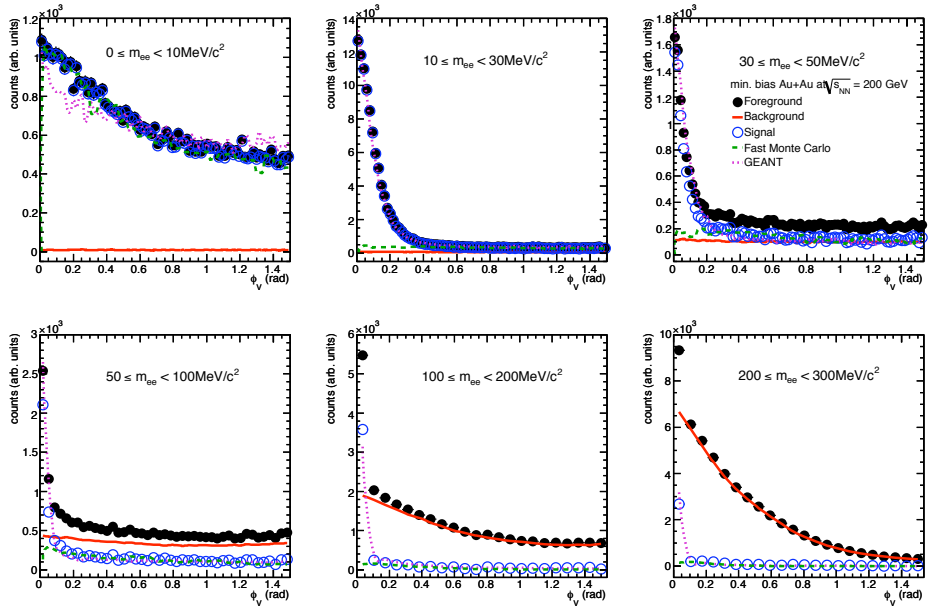

Figure 3.27: Comparison of ϕ_V distributions for various mass regions in data (Au + Au), EXODUS and the GEANT simulation.

track with charge sign $q = \pm 1$ was parameterized as follows:

$$\mu_\phi = q \cdot 0.002 \left(0.021 + \frac{0.16}{|\vec{p}|^2}\right) \tag{3.29a}$$

$$\sigma_\phi = 0.0023 \sqrt{5.1 + \frac{0.46}{|\vec{p}|^3}} \tag{3.29b}$$

$$\mu_\theta = 0.0 \tag{3.29c}$$

$$\sigma_\theta = 0.001 \sqrt{0.54 + \frac{0.36}{|\vec{p}|^3}} \tag{3.29d}$$

The resulting ϕ_V distribution is compared for different mass ranges to data and the full GEANT simulation in Fig. 3.27. The efficiency is calculated from the ratio of e^+e^- pairs with and without applying the ϕ_V cut and is shown together with the other efficiencies in Fig. 3.26.

3.5.2 ERT Efficiency

The dielectron analysis in $p + p$ requires that at least one electron in every event is associated with a hit in the ERT trigger. This biases the distribution

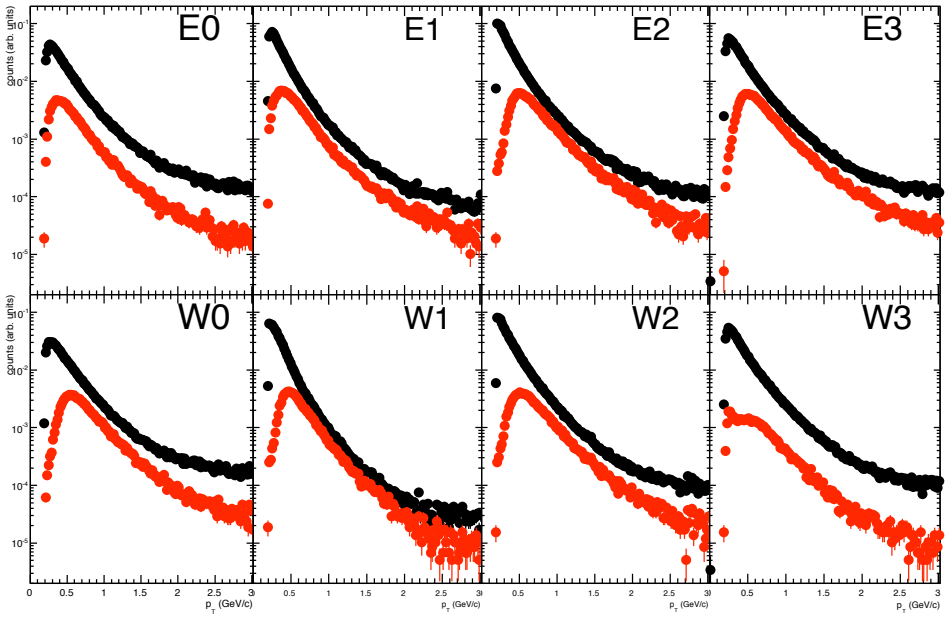

Figure 3.28: p_T distribution of single electrons (*black*) and single electrons which are associated with an ERT trigger hit (*red*).

of e^+e^- pairs and needs to be corrected to allow for a meaningful comparison. The trigger efficiency of a single electron is determined with the MB data sample. The Level-1 trigger decision is recorded also in the MB data set. It is possible that an event is not registered as ERT events, *i. e.*, the Level-1 ERT trigger bit is not set, but contains an electron associated to a hit in the ERT tiles. Such events would lead to a miscounting of electrons which fired the trigger, therefore, only MB events are considered in which the ERT trigger bit is set. Within those the p_T spectrum of electron candidates $dN^{\pm}_{\mathrm{MB\&\&ERT}}/dp^{\pm}_T$, *i. e.*, tracks that fulfill the electron identification cuts, that can be associated to a fired ERT trigger tile is shown in Fig. 3.28. The distribution is compared to the p_T spectrum of all electrons candidates in all MB events $dN^{\pm}_{\mathrm{MB}}/dp^{\pm}_T$ (*i. e.*, the ERT trigger bit is not required).

The trigger efficiency is defined as the ratio of the two as in Eq. (3.30), which is shown in Fig. 3.29 for each EMCal sector individually as function of the single electron p_T

$$\varepsilon^{\pm}_{\mathrm{ERT}} = \frac{dN^{\pm}_{\mathrm{MB\&\&ERT}}/dp^{\pm}_T}{dN^{\pm}_{\mathrm{MB}}/dp^{\pm}_T} \tag{3.30}$$

The trigger efficiency rises steeply above the trigger threshold of 400 MeV

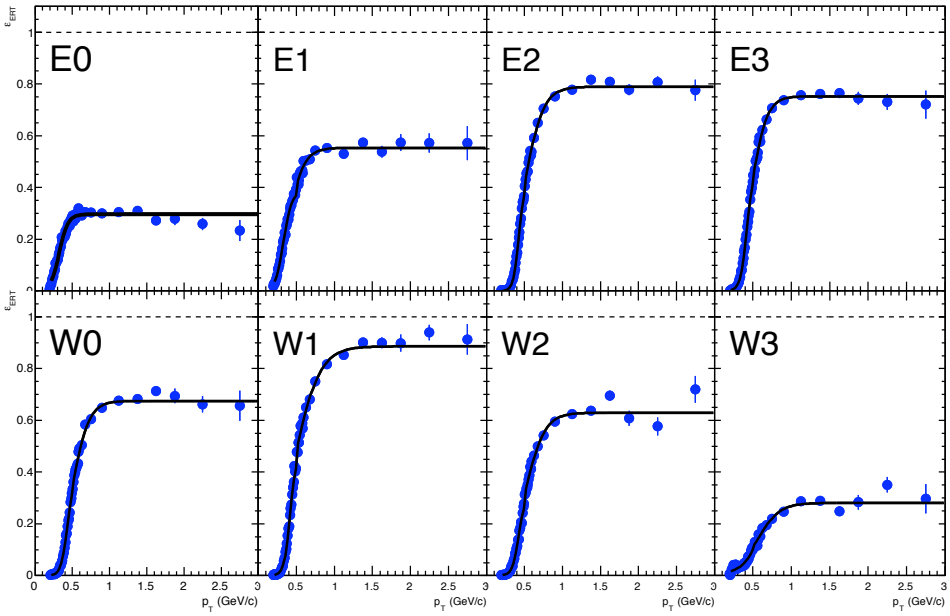

Figure 3.29: Single electron ERT trigger efficiency for all eight EMCal sectors. The fits are summarized in Tab. 3.6.

and reaches half of it's plateau value at $p_T \approx 600$ MeV/c^2. The plateau value itself strongly depends on the EMCal sector, due to the variation in the number of active trigger tiles. The trigger efficiencies are fit to two Fermi functions[4], one below and the other above a single electron p_T of 0.5 GeV/c:

$$f(p_T) = \frac{\varepsilon_0}{\mathrm{e}^{-(p_T-p_0)/k}+1}\theta(p_T-0.5) + \frac{\varepsilon_0'}{\mathrm{e}^{-(p_T-p_0')/k'}+1}\theta(p_T+0.5) \qquad (3.31)$$

The fit results for every sector are tabulated in Tab. 3.6

It is important to note, that to determine the ERT efficiency more stringent electron identification cuts need to be applied to reduce the hadron contamination in the electron sample to a negligible amount. This is necessary as any hadron in the electron sample lowers the apparent single electron trigger efficiency. But the contribution of hadrons to the e^+e^- pair spectrum is subtracted with the combinatorial background, therefore, the hadron contamination in the pair spectrum is much reduced to a negligible fraction. It is the trigger efficiency of the electrons in this background subtracted sample, that are of interest. Therefore, the following eID cuts are applied:

[4]for EMCal sector E0 it was sufficient to fit the ERT efficiency with one Fermi function over the full p_T range

Table 3.6: Parameterization of the ERT efficiency for single electrons.

Sector	ε_0	p_0 (GeV/c)	k (GeV/c)	ε_0'	p_0' (GeV/c)	k' (GeV/c)
E0	0.297	0.326	16.7	—	—	—
E1	0.386	0.331	19.5	0.553	0.394	9.61
E2	0.415	0.425	27.8	0.790	0.493	8.15
E3	0.465	0.418	24.3	0.753	0.470	9.92
W0	0.396	0.439	23.1	0.675	0.499	9.08
W1	0.460	0.413	26.6	0.886	0.471	6.03
W2	0.303	0.422	24.3	0.630	0.505	7.85
W3	66.7	1.53	6.32	0.281	0.562	6.99

- 0.20 GeV $\leq p_T \leq$ 20.0 GeV
- DC track quality == 63 || 51 || 31
- $\mathrm{n}_0 \geq 3$
- disp < 5
- $\chi^2/\mathrm{npe}_0 < 10.0$
- $0.8 < E/p < 1.2$
- $\sqrt{\mathrm{emcsdphi_e}^2 + \mathrm{emcsdz_e}^2} < 2\sigma$

On the other hand, this introduces a bias towards electrons which are more likely to fire the ERT trigger, *e. g.*, the harder n_0 cut prefers electrons that emit more Cherenkov light in the RICH. This effect has been studied, by varying the electron identification cuts. The trigger efficiency is compared for the strong eID cuts listed above, the standard eID cuts used for the pair analysis and a third set of cuts:

- 0.20 GeV $\leq p_T \leq$ 20.0 GeV
- DC track quality == 63 || 51 || 31
- $\mathrm{n}_0 \geq 2$
- disp < 5
- $\chi^2/\mathrm{npe}_0 < 10.0$

- $E/p > 0.8$
- $\sqrt{\text{emcsdphi_e}^2 + \text{emcsdz_e}^2} < 3\sigma$

which in its strength lies in between the two other sets. The resulting trigger efficiencies are shown in Fig. 3.31. The ratio with respect to the last set of eID cuts shows only a small effect for $p_T > 1.5$ GeV/c, but for $p_T < 1.5$ GeV/c differences up to 20% appear, which is assigned as systematic uncertainty on the trigger efficiency.

The efficiency of an e^+e^- pair is determined analog to the calculation of the electron identification efficiency with EXODUS. e^+e^- pairs from hadron decays are generated and the EMCal sector that an electron would hit is determined as function of its p_T and azimuthal emission. Then its probability to fire the ERT trigger is given by the trigger efficiency in this EMCal sector which has been parameterized from the fit results in Tab. 3.6. For an e^+e^- pair to survive, at least one of the two electrons must have fired the ERT trigger.

The ratio of e^+e^- pairs surviving the ERT trigger condition and all pairs is determined in mass and p_T of the pair. For the p_T inclusive mass spectrum a trigger efficiency is applied in mass only as shown in Fig. 3.32. The projection onto the mass axis is weighted by the p_T distribution of e^+e^- pairs from EXODUS. The plateau at large invariant mass corresponds to the average single electron trigger efficiency at high p_T. The shape is similar to the eID efficiency, but has a more pronounced minimum, as the trigger condition needs to be matched by only one of the electrons.

Table 3.7: Parameterization of trigger efficiency as function of mass.

a (c/GeV)	b (c^2/GeV^2)	c (c^3/GeV^3)	d (c^4/GeV^4)
0.349	0.861	−2.47	1.21

ε_0	p_0 (GeV/c)	k (GeV/c)	ε_0'	p_0' (GeV/c)	k' (GeV/c)
0.260	1.14	3.79	0.585	0.408	7.24

The mass range $1 < m_{ee} < 3$ GeV/c^2 has large statistical uncertainties due to the absence of hadron decays in this region. Therefore, and to smoothen other statistical fluctuations the result is parameterized by a fit. For $m_{ee} <$ 400 MeV/c^2 a third order polynomial is fit. Above, the sum of two Fermi functions is fit to the ERT efficiency. The result is summarized in Tab. 3.7.

For the differential analysis in mass and p_T, the two dimensional trigger efficiency distribution is smoothened by fitting the p_T distribution of e^+e^-

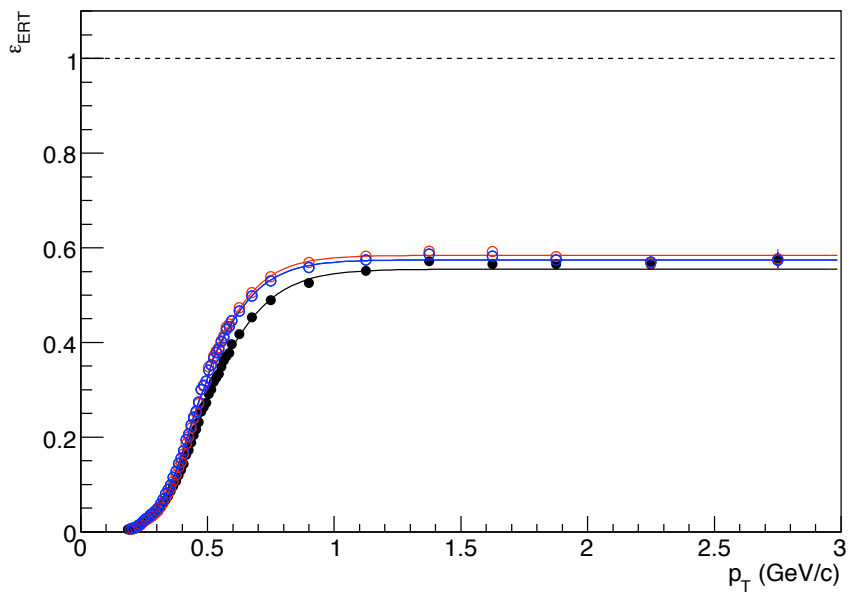

Figure 3.30: ERT trigger efficiency for single electrons with different eID cuts. The trigger efficiency for strong eID cuts is shown in (*red*), for medium eID cuts (*blue*), and for lose eID cuts in (*black*).

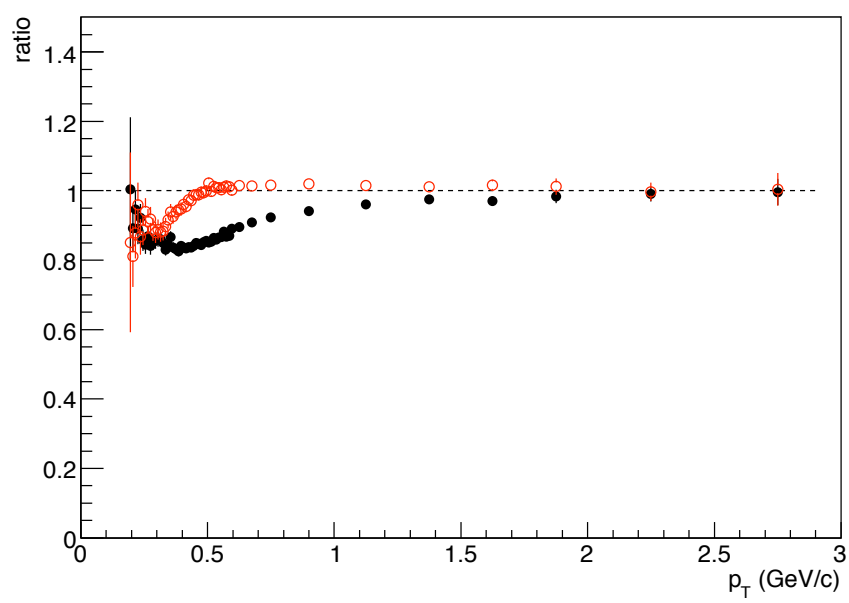

Figure 3.31: Shown are the ratios of ERT trigger efficiencies with different eID cuts. Strong divided by medium is shown in (*red*), lose divided by medium in (*black*).

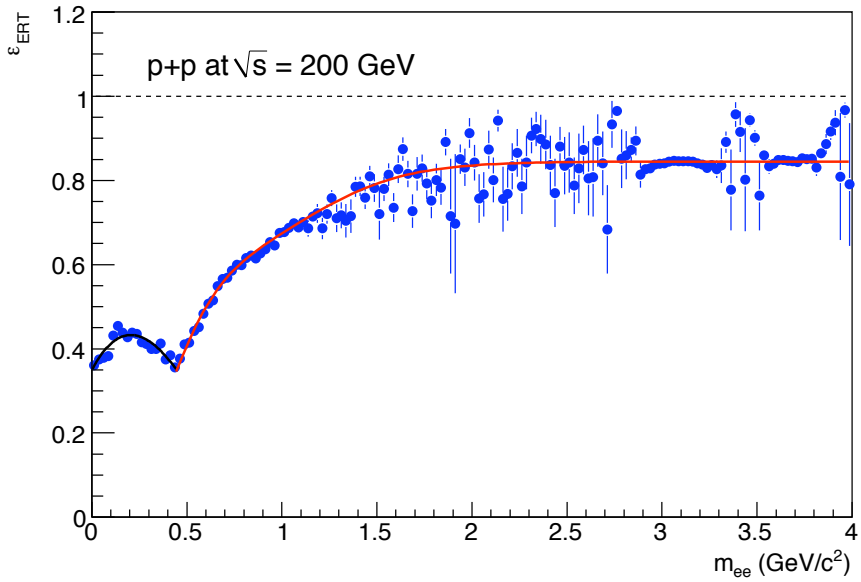

Figure 3.32: ERT trigger efficiency for e^+e^- pairs as function of m_{ee}. The fits are summarized in Tab. 3.7.

pairs in narrow mass slices in the LMR, the J/ψ and ψ'. The IMR is fitted in slices of p_T analog to the p_T inclusive trigger efficiency in Fig. 3.32. The results are combined into a smoothed parameterization of the ERT efficiency as function of mass and p_T which is shown in Fig. 3.33.

The uncertainty in the trigger efficiency due the electron identification cuts of 20% at low p_T affects e^+e^- pairs with $m_T < 1$ GeV/c^2, for which this uncertainty is assigned. Elsewhere a 5% systematic uncertainty is assigned. This includes uncertainties due in the precise location of dead trigger tiles, which has been studied by shuffling EMCal sectors in the simulation of the ERT pair efficiency.

Figure 3.34 compares of the invariant mass spectra for the $p + p$ data obtained with the MB and ERT data sets. The ERT data set has been corrected by ERT trigger efficiency and eID efficiency, while the MB is corrected only for the eID. The agreement between the two data sets confirms the assessed accuracy of the ERT correction.

3.5.3 Occupancy Correction in Au + Au

In Au + Au collisions there is also a finite efficiency loss for particle detection due to the presence of other particles nearby. To get a quantitative un-

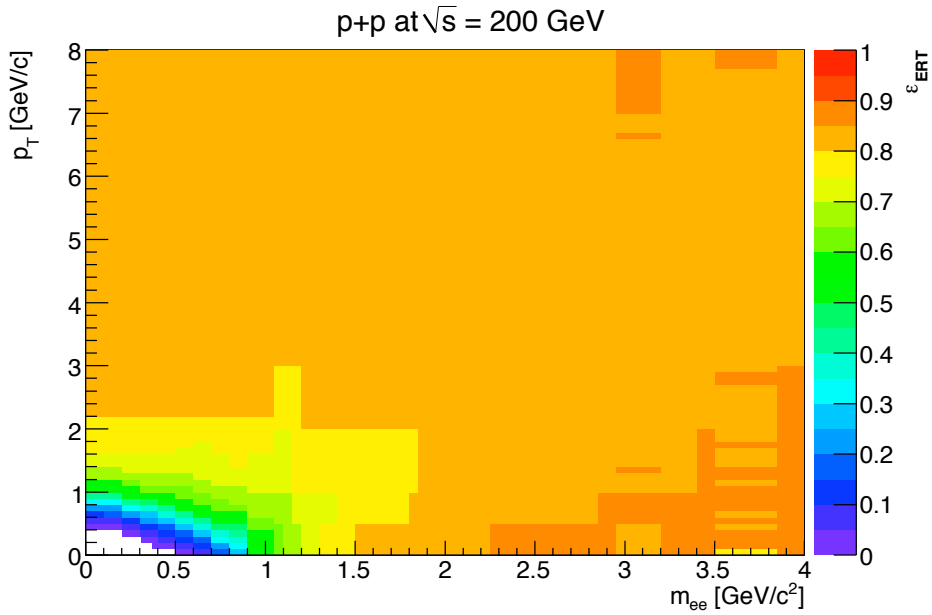

Figure 3.33: ERT trigger efficiency for e^+e^- pairs as function of m_{ee} and p_T.

derstanding of the multiplicity-dependent efficiency loss, single electrons and positrons are generated with a full GEANT Monte Carlo simulation of the PHENIX detector and then embedded into data files containing detector hits from real Au + Au events. Next, these new files containing the embedded $e^{\pm}$ are run through the entire reconstruction software to produce track candidates containing the variables used for the electron identification cuts.

Since all the detectors used in the analysis are located after the pair has been opened by the magnetic field, the pair embedding efficiency is defined as the square of the single electron efficiency

$$\epsilon_{\text{embed}}^{\text{pair}} = \left(\varepsilon_{\text{embed}}^{\pm}\right)^2 \tag{3.32}$$

$$= \left(\frac{\#\text{ reconstructed } e^{\pm} \text{ from embedded data}}{\#\text{ reconstructed } e^{\pm} \text{ from single track data}}\right)^2 \tag{3.33}$$

where a reconstructed particle from embedded data has most of its detector hits associated with hits from the simulated particle.

Tab. 3.8 lists the embedding efficiencies for the centrality classes used in the analysis. For the minimum bias the occupancy correction is weighted by the effective pair signal in each centrality class; since most of the yield is concentrated in the most central classes, the resulting pair efficiency is 0.81 instead of $0.92 = 0.96^2$. A systematic uncertainty of $\approx 3\%$ has been assigned

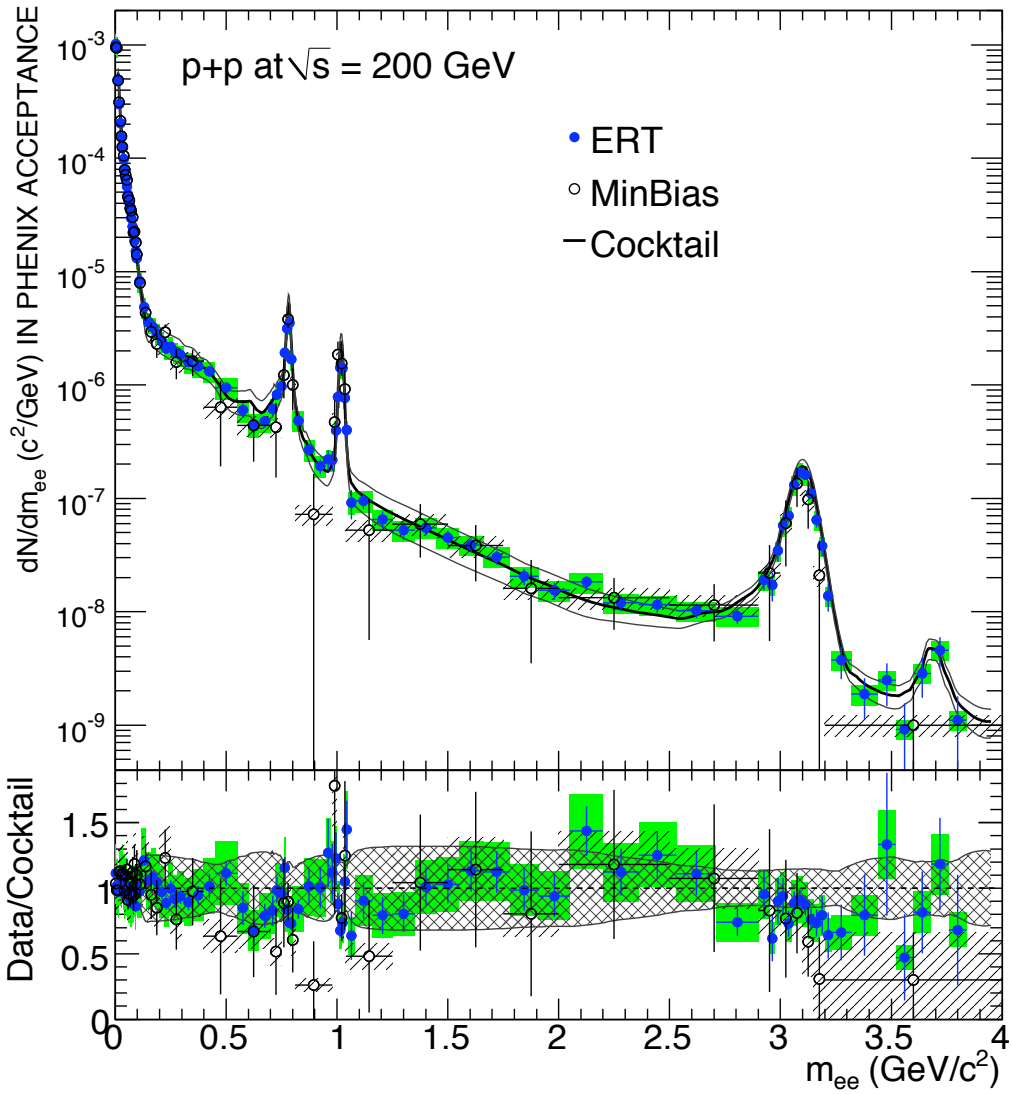

Figure 3.34: Invariant mass spectra for $p+p$ data with the MB (*hollow*) and ERT (*solid*) data sets. The agreement between the two data sets is excellent.

Table 3.8: Embedding efficiency.

Centrality	$\varepsilon^{\pm}_{\text{embed}}$	$\varepsilon^{\text{pair}}_{\text{embed}}$
0–10%	0.86	0.74
10–20%	0.91	0.83
20–40%	0.93	0.87
40–60%	0.97	0.95
60–92%	0.99	0.98
0–92%	0.96	0.81

by calculating the occupancy efficiency with a data-driven method [109].

3.5.4 Acceptance

In addition to corrections for the track reconstruction, electron identification and ERT trigger efficiency, the p_T spectra of e^+e^- pairs are also corrected for the geometrical acceptance of the two central arm detectors $\varepsilon^{\text{pair}}_{\text{geo}}$. It accounts for the fraction of e^+e^- pairs over full azimuth $0 < \phi \leq 2\pi$ and one unit of rapidity ($|y| < 0.5$) of which at least one electron was not within the detector acceptance.

The acceptance correction has been calculated based on a Monte Carlo simulation of Dalitz decays of pseudo-scalar mesons (π^0, η, η') and direct decays of vector mesons (ρ, ω, ϕ, J/ψ, ψ'). The rapidity distribution of all mesons is assumed to be flat, which is well justified by measurements of BRAHMS [110]. The p_T distribution of these mesons is taken from PHENIX measurements (see Section 3.7), their polarization from the PDG book [29]. Vector mesons are assumed to be unpolarized.

The acceptance correction is calculated as all other corrections in mass and p_T by dividing the number of e^+e^- pairs within the detector acceptance, *i. e.*, both tracks fulfill Eq. (2.5), by all pairs in $0 < \phi \leq 2\pi$ and $|y| < 0.5$. The systematic uncertainty on the polarization and due to the p_T parameterization is studied with a simulation of unpolarized pairs with a flat mass and p_T distribution, [5]. The resulting acceptance corrections are compared in Fig. 3.35 for a number of mass ranges as function of p_T. The shapes of the two acceptance corrections are very similar and agrees within 5% for the lowest mass bin, and better at higher masses.

In the intermediate mass region (1–3 GeV/c^2) charmed meson decays dominate the e^+e^- invariant mass spectrum. Their contribution has been simu-

[5] which has already been used as cross check for the eID efficiency

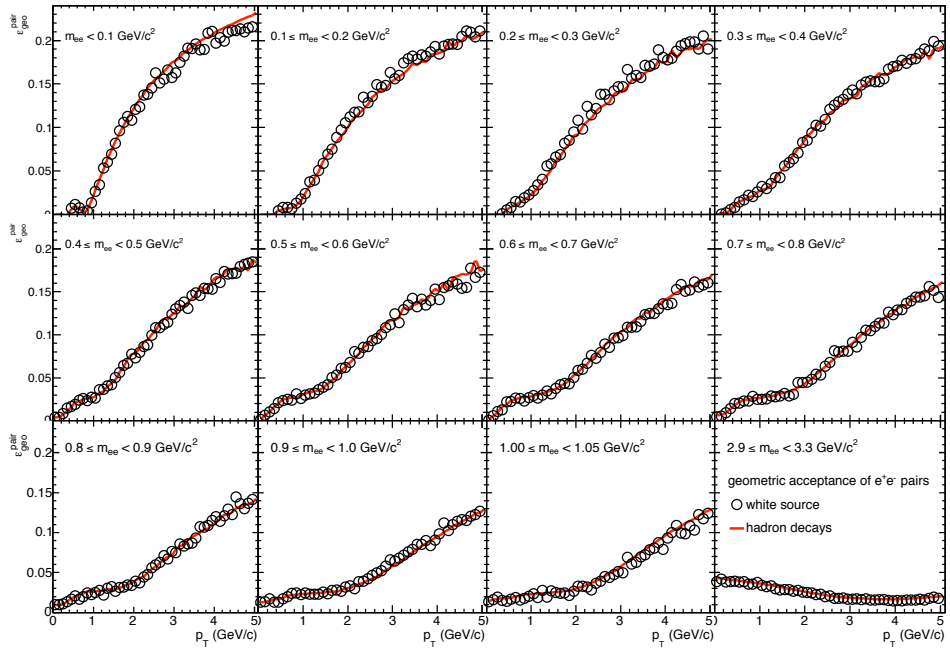

Figure 3.35: Acceptance of e^+e^- pairs as function of p_T for various mass ranges: 0–0.1, 0.1–0.2, 0.2–0.3, 0.3–0.4, 0.4–0.5, 0.5–0.6, 0.6–0.7, 0.7–0.8, 0.8–0.9, 0.9–1.0, 1.0–1.05, and 2.9–3.3 GeV/c^2 (from left to right, top to bottom). The acceptance based on the hadronic cocktail is shown in black, the one based on white pairs in blue.

lated with PYTHIA and normalized to the measured $c\bar{c}$ cross section measured in Ref. [16]. These e^+e^- pairs do not share the same parent, both are produced by semi-leptonic decays of charmed mesons, *e. g.* D, but their parents are correlated as they contain each one of the c quarks which are always produced in pairs. $c\bar{c} \rightarrow D\overline{D} \rightarrow e^+e^-$. For masses $m_{ee} < 0.5$ GeV/c^2 the charm contribution is negligible, above a systematic uncertainty of 5% has been added due to the uncertainty in the charm cross section of 30%.

3.5.5 Bin Shift Correction

For the p_T spectra of e^+e^- pairs a further correction is applied to take into account the difference between the average p_T of e^+e^- pairs within a bin and the bin center due to the finite bin width.

The bin shift correction of the extracted yield is determined by iteratively fitting the dN/dp_T spectra with a power law and shifting the yield in every p_T bin the fits by the relative difference between the yield at the bin center (p_T^{cent}) and at the average p_T of the bin $\langle p_T \rangle$. Three iterations are performed, but already after the first iteration the bin shift correction changes insignificantly. As example, the fit results are shown in Fig. 3.36 for the ω and ϕ mesons yields (also see Section 4.1.2). Instead of correcting the bin center for the bin shift, the yield is adjusted by a factor:

$$\delta(p_T^{\text{cent}}) = \frac{\int_{p_T^{\text{cent}}-\Delta/2}^{p_T^{\text{cent}}+\Delta/2} \frac{dN}{dp_T}\, dp_T}{\frac{dN}{dp_T}\Big|_{p_T=p_T^{\text{cent}}}} \tag{3.34}$$

where Δ is the bin width. The bin shift correction is applied on the final binning and only after this correction is the yield dN/dp_T converted into an invariant yield or cross section $Ed^3\sigma/dp^3$.

The correction for the ω yield in p_T bins of 200 MeV/c is $\sim 3.28\%$ below 3 GeV/c and $\sim 1.8\%$ above. The bin shift correction for the ϕ cross section is $\sim 2.2\%$ in the full range of 0–5 GeV/c.

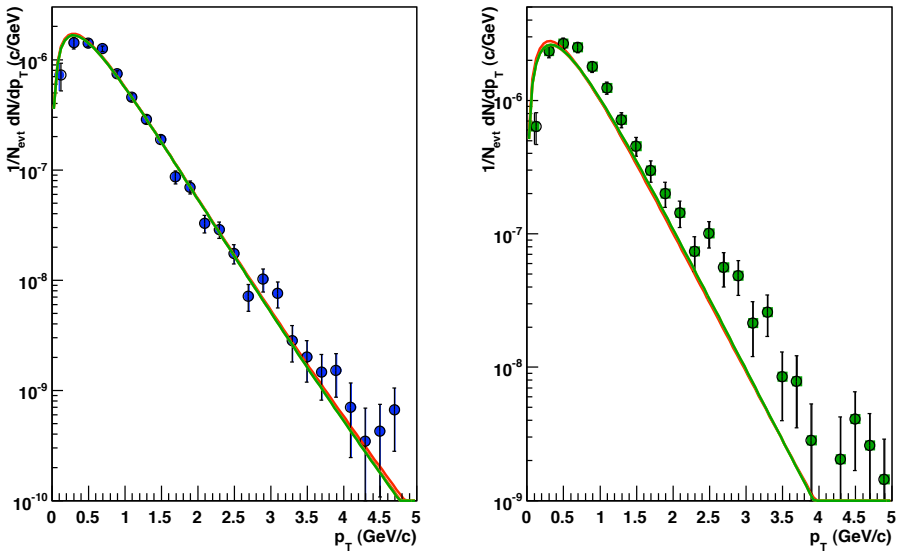

Figure 3.36: Yield of ω (*left*) and ϕ (*right*) before bin shift correction. The data are fit to a power-law to determine the bin sift correction. The first iteration is shown in red, the third iteration in green. Open points show the bin shift corrected bin centers.

3.6 Systematic Uncertainties

The various contribution to the total systematic uncertainty, which are summarized in Tab. 3.9, are described in the following. (i) The uncertainty on the e^+e^- pair reconstruction, which is twice the uncertainty on the single electron reconstruction efficiency[15, 16], includes uncertainties on the efficiency of electron identification cuts, geometrical acceptance, and run-by-run fluctuations; the uncertainty on (ii) the conversion rejection cut, (iii) the ERT and minimum bias trigger efficiencies. These uncertainties are included on the yield of e^+e^- pairs in the invariant mass spectra. The uncertainties on the track reconstruction do not have a strong dependence on the e^+e^- pair p_T, therefore they are assigned independent of p_T. Pair and conversion cuts are localized in mass ($m_{ee} < 600$ MeV/c^2) and also rather p_T independent.

The largest contribution is the systematic uncertainty on the background subtraction. The mixed event normalization enters with $3\% \times B/S$ in $p+p$ and in Au+Au with $0.25 \times B/S$. But the background-to-signal ratio, which is strongly mass and p_T dependent, is two orders of magnitude worse for Au+Au collisions than in $p+p$ as shown in Fig. 3.37. As the signal-to-background ratio shows a p_T dependence, it is assigned for each p_T bin individually.

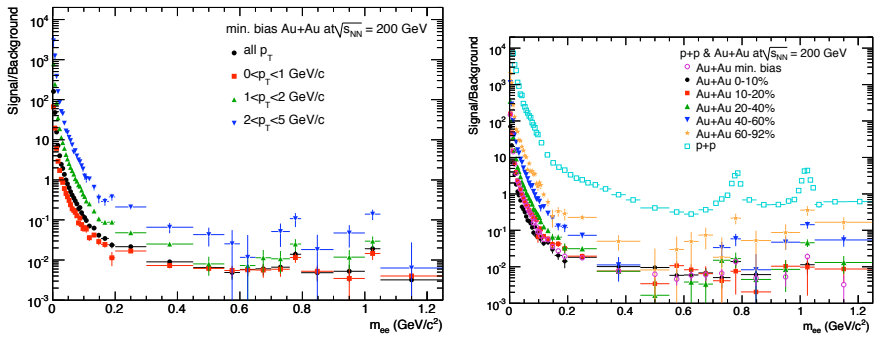

(a) **(b)**

Figure 3.37: Signal-to-Background ratio for e^+e^- pairs in min. bias Au + Au collisions with different p_T ranges (a) and for different centralities (b) which also includes e^+e^- pairs in $p + p$ collisions.

For the p_T spectra the uncertainty on the acceptance correction of 10%, and for $m_{ee} > 0.5$ GeV/c^2 an additional 5% due to the charm contribution, are included in the systematic uncertainty.

Table 3.9: Systematic uncertainties of the dilepton yield due to different sources and indication of mass range where the error is applied.

Syst. Uncert. component	$p+p$	Au + Au	Mass Range (GeV/c^2)
pair reconstruction	14.4%	13.4%	0–4
conversion rejection	6.0%	6.0%	0–0.6
pair cuts	5.0%	5.0%	0.4–0.6
occupancy efficiency	—	3.0%	0–4
ERT efficiency	5.0%	—	$m_T > 1$
	20.0%	—	$m_T \leq 1$
combinatorial background	3.0%$\cdot B/S$	0.25%$\cdot B/S$	0–4
correlated background ("near-side")	3.0%	10.0%	0–0.6
correlated background ("away-side")	11.0%	—	> 1
centrality	—	10.0%	0–4
acceptance correction	10.0%	10.0%	0–4
charm acceptance	5.0%	5.0%	>0.5

3.7 EXODUS Simulation of Hadron Decays

Exodus is a fast Monte Carlo simulation of hadron decays. Key input is the rapidity density dN/dy of neutral and charged pions which is determined by a fit to PHENIX data [87] with a modified Hagedorn function:

$$E\frac{d^3\sigma}{dp^3} = A\left(\mathrm{e}^{-\left(ap_T+bp_T^2\right)} + p_T/p_0\right)^{-n} \tag{3.35}$$

with $A = 377 \pm 60$ mb GeV^{-2}, $a = 0.356 \pm 0.014$ (GeV/c)$^{-1}$, $b = 0.068 \pm 0.019$ (GeV/c)$^{-2}$, $p_0 = 0.7 \pm 0.02$ GeV/c, and $n = 8.25 \pm 0.04$.

PHENIX cross section measurements of π^0, $\pi^\pm$, η, η', ω, ϕ, and J/ψ are shown in Fig. 3.38. The fit of the charged and neutral pion data with Eq. (3.35) is also shown.

To parameterize the other hadron spectra, the modified Hagedorn fit of the pion data is m_T scaled, replacing p_T in Eq. (3.35) by $\sqrt{(p_T/c)^2 - m_{\pi^0}^2 + m_h^2}$, where m_h is the mass of the hadron and fit with a free normalization factor to the hadron spectra. The good description of the data by the fits indicates that meson production in $p+p$ collisions follows m_T scaling. Accordingly, this observation is extended to other mesons for which no data are available.

In order to extract the meson yield per inelastic $p+p$ collision the fits are integrated over all p_T. Results, systematic uncertainties, and references to data

are given in Tab. 3.10. For the ρ meson $\sigma_\rho/\sigma_\omega = 1.15 \pm 0.15$ is assumed, consistent with values found in jet fragmentation [29]. The η' yield is scaled to be consistent with jet fragmentation $\sigma_{\eta'}/\sigma_\eta = 0.15 \pm 0.15$ [29] which is consistent with preliminary measurements by PHENIX [111]. The ψ' is adjusted to the value of $\sigma_{\psi'}/\sigma_{J/\psi} = 0.14 \pm 0.03$ [112] in agreement with preliminary PHENIX results [113]. For the η, ω, ϕ, and J/ψ the quoted uncertainties include those on the data as well as those using different shapes of the p_T distributions. Specifically their spectra have been fitted with the functional form given in Eq. (3.35) with all parameters free and also an exponential distribution in m_T. For the ρ, η', and ψ' the uncertainty is given by the uncertainty assumed for the cross section ratios. It is important to note that the dilepton spectra from meson decays are rather insensitive to the exact shape of the p_T distribution.

Table 3.10: Hadron rapidity densities in $p+p$ collisions at $\sqrt{s} = 200$ GeV used in Exodus.

	$\frac{dN}{dy}\Big\vert_{y=0}$	rel. uncert.	meson/π^0	data used
π^0	1.065 ± 0.11	10%	1.0	PHENIX [87, 114]
η	0.11 ± 0.03	30%	0.1032	PHENIX [115]
ρ	0.089 ± 0.025	28%	0.0834	jet fragmentation [29]
ω	0.078 ± 0.018	23%	0.0732	PHENIX [116–121]
ϕ	0.009 ± 0.002	24%	0.0084	PHENIX [116–118, 120, 122]
η'	0.016 ± 0.005	40%	0.0127	PHENIX [111] and [29]
J/ψ	$(1.77 \pm 0.27)\times 10^{-5}$	15%	0.0000166	PHENIX [123]
ψ'	$(2.5 \pm 0.7)\times 10^{-6}$	27%	0.0000023	world average [112]

Once the meson yields and p_T spectra are known the dilepton spectrum is given by decay kinematics and branching ratios, which are implemented in our decay generator Exodus following earlier work published in [16]. The branching ratios are taken from the compilation of particle properties in [29]. For the Dalitz decays π^0, η, $\eta' \to \gamma e^+e^-$ and the decay $\omega \to \pi^0 e^+e^-$ the Kroll-Wada expression [50] is used with electromagnetic transition form factors measured by the Lepton-G collaboration [51, 126]. For the decays of the vector mesons ρ, ω, $\phi \to e^+e^-$ the expression derived by Gounaris and Sakurai [127] is used, extending it to 2 GeV/c^2, slightly beyond its validity range. For the J/ψ and $\psi' \to e^+e^-$ the same expression modified to include radiative corrections is used as discussed in [123]. All vector mesons are assumed to be unpolarized. For the Dalitz decays of which the third body is a photon, the angular distribution is sampled according to $1 + \lambda \cos^2\theta_{\rm CS}$ distribution, where $\theta_{\rm CS}$ is the polar angle of the electrons in the Collins-Soper frame.

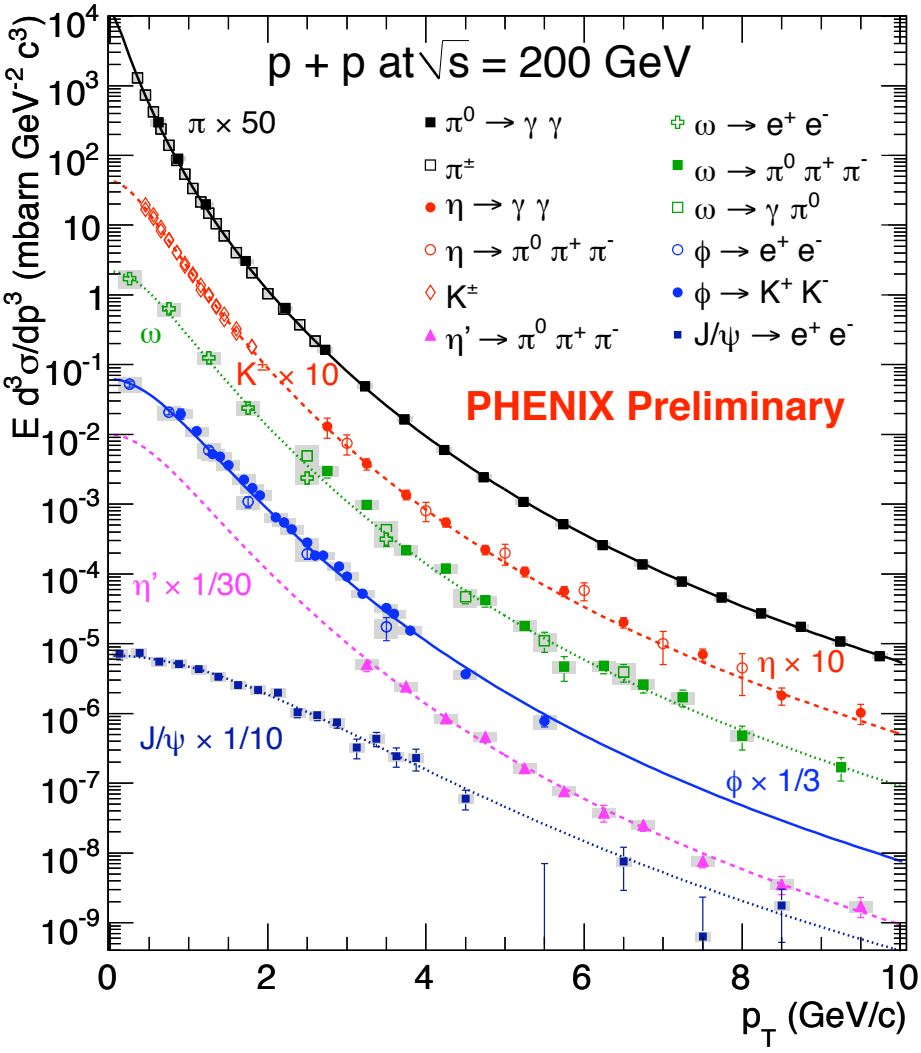

Figure 3.38: Compilation of meson production cross sections in $p+p$ collisions at $\sqrt{s} = 200$ GeV. Shown are data for neutral [87] and charged pions [114], η [115], kaons [114], ω [116–121], ϕ [116–118, 120, 122], η' [111], and J/ψ [123]. The data are compared to the parameterization based on m_T scaling used in our hadron decay generator.

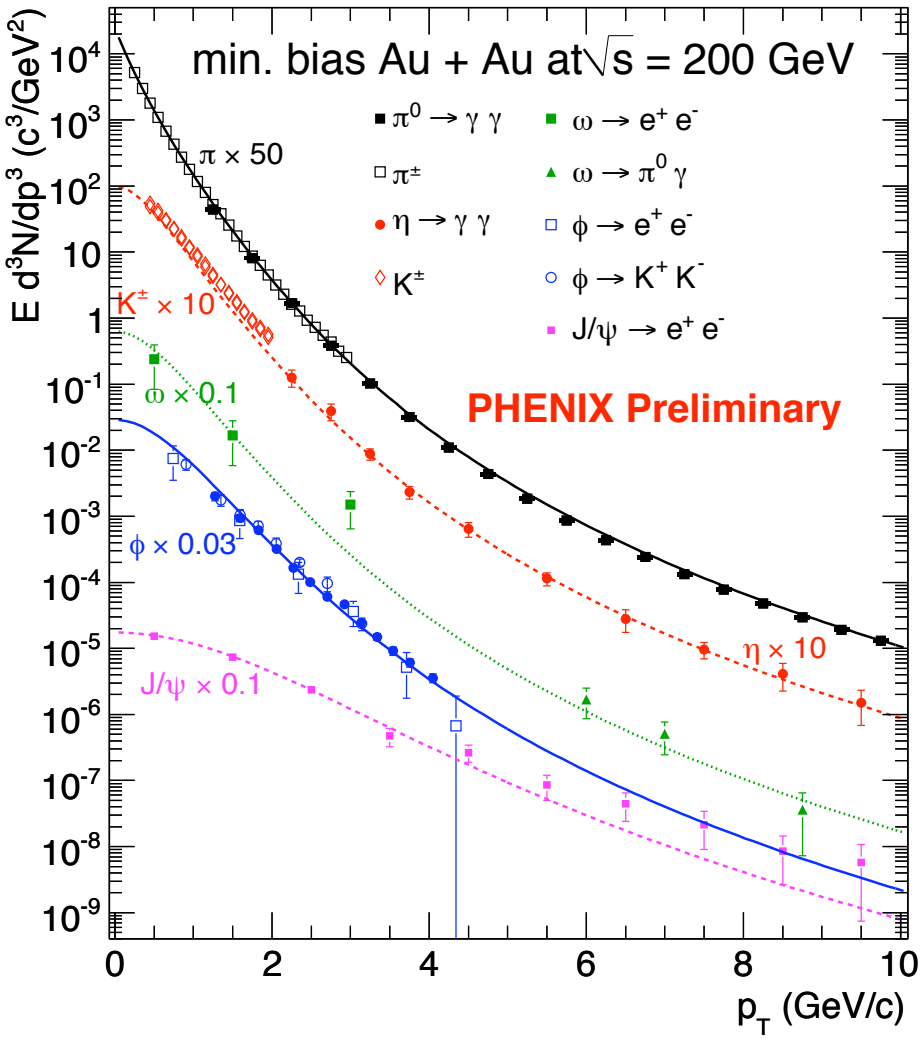

Figure 3.39: Compilation of meson production cross sections in Au + Au collisions at $\sqrt{s_{NN}}$ = 200 GeV. Shown are data for neutral [46] and charged pions [124], η [115], kaons [124], ω [120], ϕ [120, 125] and J/ψ [60]. The data are compared to the parameterization based on m_T scaling used in our hadron decay generator.

Table 3.11: Hadron rapidity densities in Au + Au collisions at $\sqrt{s_{NN}} = 200$ GeV used in EXODUS.

	$\frac{dN}{dy}\Big\vert_{y=0}$	rel. uncert.	meson/π^0	data used
π^0	97.72 ± 9.5	10%	1.0	PHENIX [46, 124]
η	10.77 ± 3.2	30%	0.112	PHENIX [115]
ρ	8.60 ± 2.6	30%	0.08981	jet fragmentation [29]
ω	9.88 ± 3.0	30%	0.1032	PHENIX [120]
ϕ	2.05 ± 0.6	30%	0.0214	PHENIX [120, 125]
η'	2.05 ± 2.05	100%	0.02146	jet fragmentation [29]
J/ψ	$(1.79 \pm 0.26)\times10^{-5}$	15%	0.0000182	PHENIX [60]
ψ'	$(2.6 \pm 0.7)\times10^{-6}$	27%	0.0000027	PHENIX [113] and [112]

The resulting systematic uncertainties depend on mass and range from 10 to 25%. They are combined of the uncertainty of the measured π^0 yield and the meson-to-pion ratios which is the dominant uncertainty. They also include uncertainties on the measured electromagnetic transition form factors, in particular for the $\omega \to \pi^0 e^+e^-$ decay whose contribution, however, is only visible in the mass range around $500 < m_{ee} < 600$ MeV/c^2.

The e^+e^- pairs from hadron decays are filtered into the PHENIX acceptance as defined in Eq. (2.5) and their momenta and angular distributions are smeared to take into account the detector resolution, as defined in Eq. (3.4) and Eq. (3.29). The resulting invariant mass spectra are shown in Fig. 3.40 for $p+p$ collisions and in Fig. 3.41 for Au+Au collisions, respectively. The contribution of the various sources are shown individually and include a contribution from open charm decays which is discussed in Section 4.1.1.

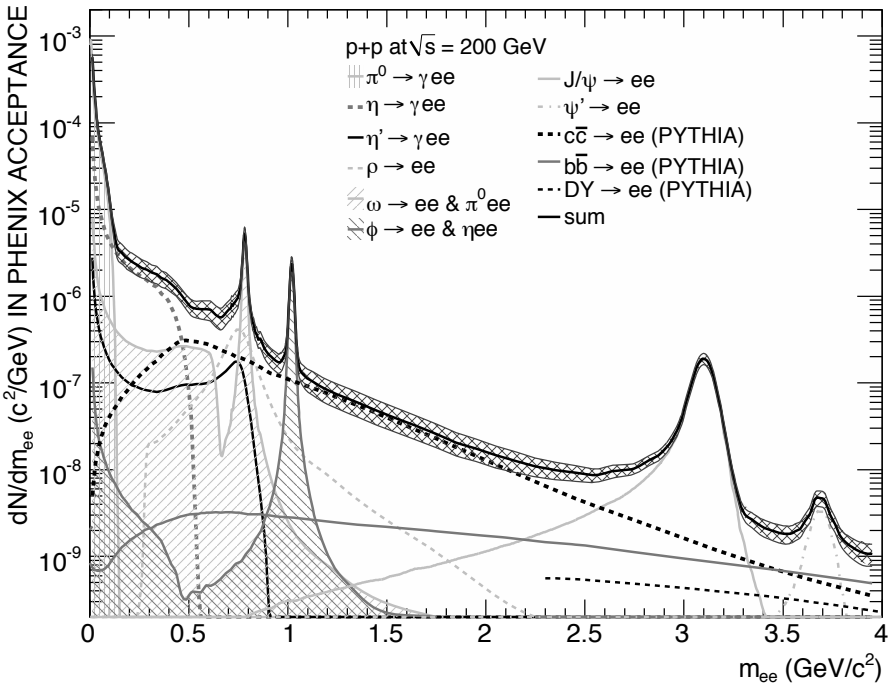

Figure 3.40: Expected invariant mass spectrum of e^+e^- pairs from hadron decays (cocktail) in Au + Au collisions at $\sqrt{s} = 200$ GeV from EXODUS.

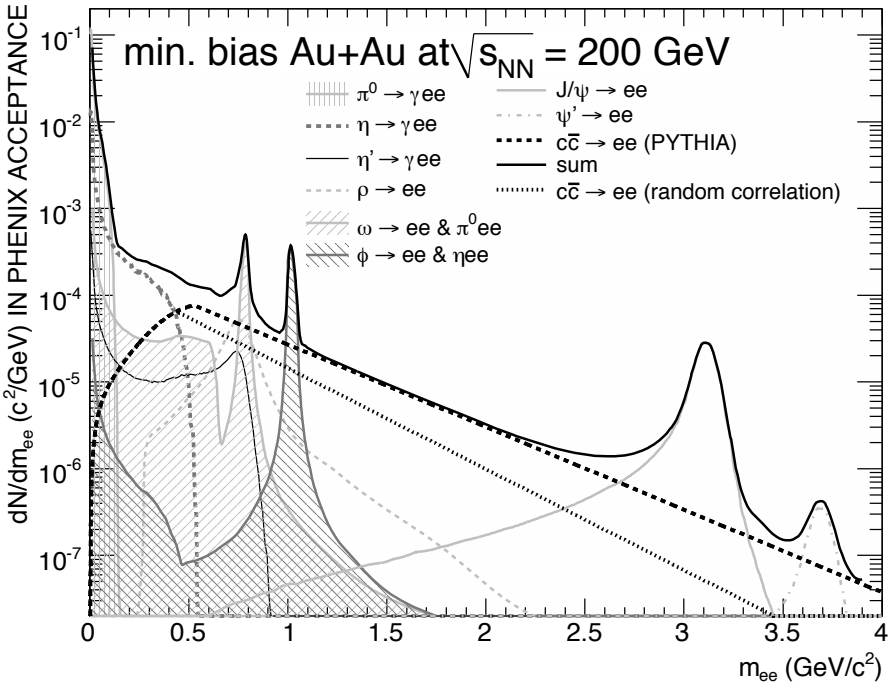

Figure 3.41: Expected invariant mass spectrum of e^+e^- pairs from hadron decays (cocktail) in Au + Au collisions at $\sqrt{s_{NN}} = 200$ GeV from EXODUS.

Chapter 4

Results

This chapter summarizes the various results of the dielectron continuum analysis. At first the invariant mass spectrum of e^+e^- pairs in $p+p$ collisions at $\sqrt{s} = 200$ GeV is shown in Section 4.1 followed by the measurement of the charm cross section via the e^+e^- pair yield in the intermediate mass region in Section 4.1.1. Section 4.1.2 presents the p_T spectra of the ω and ϕ mesons measured via their resonance decays into e^+e^- pairs. The results of the dielectron continuum analysis of $p+p$ collisions are concluded with p_T spectra of the low mass continuum and the contributions of virtual direct photons in Section 4.1.4. While the analysis of $p+p$ collisions is certainly the major achievement of this thesis, a detailed comparison to the dielectron continuum measured in Au+Au collisions is given. The results are presented in Section 4.2 and compared to theoretical models in Section 4.3.

4.1 The Dielectron Continuum in $p+p$ Collisions

The invariant mass distribution of e^+e^- pairs calculated according to Eq. (3.23) is compared to the hadronic cocktail as shown in Fig. 4.1. The contribution from semileptonic heavy quark decays is discussed in the Sec. 4.1.1. The data are well described by the expected contributions from hadron decays and semi-leptonic decays of heavy flavored mesons over the entire mass range. The resonance peaks of ω, ϕ, J/ψ, and the ψ' are well reproduced and their width in good agreement with the expected mass resolution. The ratio of data to cocktail is unity within the quoted uncertainties as shown in the bottom panel of Fig. 4.1.

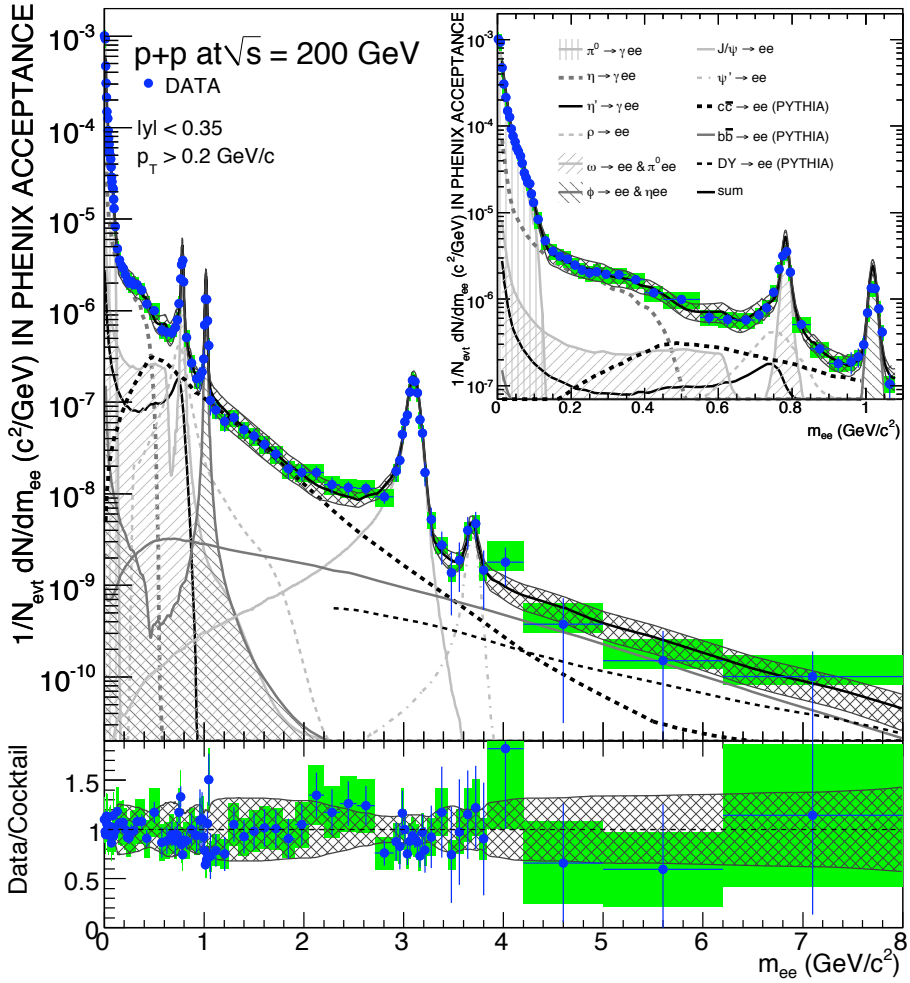

Figure 4.1: Electron-positron pair yield per inelastic $p+p$ collision as function of pair mass. Data show statistical (bars) and systematic (shades) errors separately. The yield per event can be converted to a cross section by multiplying with the inelastic $p+p$ cross section of 42.2 mb. The data are compared to a cocktail of known sources. The contribution from hadron decays is independently normalized based on meson measurements in PHENIX, the systematic uncertainties are given by the error band. The contribution from open charm production is scaled to match the data ($\sigma_{c\bar{c}} = 544 \pm 39$(stat.) $\pm$ 142(syst.) $\pm$ 200(model) μb). The inset shows the same data but focuses on the low mass region. The bottom panel shows the ratio of data to the cocktail of known sources. The systematic uncertainties of the data are shown as boxes, while the uncertainty on the cocktail is shown as band around 1.

4.1.1 Charm Cross Section

Except for the vector meson peaks, the dilepton yield in the mass range above 1.1 GeV/c^2 is dominated by semileptonic decays of D and B mesons correlated through flavor conservation.

In order to extract the charm cross section, first the measured e^+e^- pair yield is integrated in the mass range $1.1 < m_{ee} < 2.5$ GeV/c^2 and compared to the cocktail yield and the yield from semileptonic decays of open heavy quarks (charm and bottom) as well as Drell-Yan calculated with PYTHIA [102, 104]. PYTHIA 6.205 with CTEQ5L parton distribution function [106] has been used. Following earlier analyses [128, 129] a number of modifications to PYTHIA parameters have been made:

- PARP(91) = 1.5 (k_T),
- MSTP(33) = 1 (use common K factor)
- PARP(31) = 3.5 (K factor),
- MSTP(32) = 4 (Q^2 scale)

  in addition for charm production:

- MSEL = 4 ($c\bar{c}$ production)
- PMAS(4,1) = 1.25 (m_c),

  for bottom:

- MSEL = 5 ($b\bar{b}$ production)
- PMAS(5,1) = 4.1 (m_b),

  and for Drell-Yan:

- MSEL = 11 (Z or γ^* production)
- PARP(31) = 1.8 (K factor)
- CKIN(3) = 2.0 (min. parton p_T).

The following cross sections are assumed:

- $\sigma_{c\bar{c}} = 567 \pm 57(\text{stat.}) \pm 193(\text{syst.})$ μb [16]
- $\sigma_{b\bar{b}} = 3.7 \pm 3.7$ μb [130]

- $\sigma_{\mathrm{DY}} = 42 \pm 42$ nb [131]

The integrated yield of e^+e^- pairs in $1.1 < m_{ee} < 2.5$ GeV/c^2 in the PHENIX acceptance are:

- measured: $Y_{\mathrm{data}} = (4.53 \pm 0.28(\mathrm{stat.}) \pm 0.97(\mathrm{syst.})) \times 10^{-8}$
- PYTHIA charm: $Y_{c\bar{c}} = 4.08 \times 10^{-8}$
- PYTHIA bottom: $Y_{b\bar{b}} = 2.62 \times 10^{-9}$
- PYTHIA Drell-Yan: $Y_{\mathrm{DY}} = 2.66 \times 10^{-10}$
- EXODUS cocktail: $Y_{\mathrm{hadr}} = 3.20 \times 10^{-9}$

The contribution from the cocktail is essentially only due to the tail of the ρ, which is not known at this high mass. Therefore, an uncertainty of 100% is assigned. However, since the cocktail contributes only 7% to the data in this mass range, the systematic uncertainty on the measured yield due to the ρ contribution is only 7%. Also the bottom cross section from FONLL has a 100% uncertainty, which for the same reason translates into only a 6% systematic uncertainty on the measured yield.

The ratio of $(Y_{\mathrm{data}} - Y_{\mathrm{hadr}})/(Y_{c\bar{c}} + Y_{b\bar{b}} + Y_{\mathrm{DY}}) = 0.96$ can be used to convert the charm cross section measured in Ref. [16] which is used as input for PYTHIA:

$$\frac{d\sigma_{c\bar{c}}}{dy} = 123 \pm 12(\mathrm{stat.}) \pm 37(\mathrm{syst.})\ \mu\mathrm{b}$$
$$\sigma_{c\bar{c}} = 567 \pm 57(\mathrm{stat.}) \pm 193(\mathrm{syst.})\ \mu\mathrm{b}$$

into what is measured in this analysis:

$$Y_{\mathrm{data}} - Y_{\mathrm{hadr}} = (4.21 \pm 0.28(\mathrm{stat.}) \pm 1.02(\mathrm{syst.})) \times 10^{-9}$$
$$\frac{d\sigma_{c\bar{c}}}{dy} = 118.1 \pm 8.38(\mathrm{stat.}) \pm 30.73(\mathrm{syst.}) \pm 39.5(\mathrm{model})\ \mu\mathrm{b}$$
$$\sigma_{c\bar{c}} = 544 \pm 39(\mathrm{stat.}) \pm 142(\mathrm{syst.}) \pm 200(\mathrm{model})\ \mu\mathrm{b}$$

This measurement is an important confirmation of the result reported in Ref. [16], in particular, as the STAR Collaboration has reported a charm cross section in $p+p$ collisions [132, 133], which is a factor of two larger than observed by PHENIX. Currently, the source for this discrepancy is unknown, but if PHENIX was to overestimate its single electron identification efficiency

by a factor of two, this effect would enter quadratically into the e^+e^- pair measurement and therefore lead to a significant difference between the dielectron and single electron results.

The systematic and model uncertainties on this measurement are due to a number of sources. As the fraction of e^+e^- pairs from correlated heavy quark decays at mid-rapidity depends on the dynamical correlation between the quarks, additional systematic uncertainties beyond the parameterization of the PHENIX acceptance (10%). The momentum of a parton inside the colliding hadrons are expected to have a finite "primordial" component k_T which is perpendicular to the beam direction due to Fermi motion. In PYTHIA the 'primordial k_T' parameter is used to define the width of the Gaussian distribution of the primordial parton k_T. The value of k_T affects the azimuthal correlation between c and $\bar{c}$. While a nominal value of 1.5 GeV/c is used, k_T has been varied between 1 and 3 GeV/c. The resulting e^+e^- pair spectra are shown in Fig. 4.2 and the integrated yields are:

$$
\begin{aligned}
Y_{c\bar{c}}(k_T = 1.0 \text{ GeV}/c) &= 3.74 \times 10^{-4} \\
Y_{c\bar{c}}(k_T = 1.5 \text{ GeV}/c) &= 4.12 \times 10^{-4} \\
Y_{c\bar{c}}(k_T = 2.0 \text{ GeV}/c) &= 4.64 \times 10^{-4} \\
Y_{c\bar{c}}(k_T = 2.5 \text{ GeV}/c) &= 5.10 \times 10^{-4} \\
Y_{c\bar{c}}(k_T = 3.0 \text{ GeV}/c) &= 5.53 \times 10^{-4}
\end{aligned}
$$

Due to the variation in the yield an uncertainty of 20% is assigned.

The uncertainty of the relative abundance of charm quarks and the branching ratios of semileptonic decays is 21% [16]. A total branching ratio of $c \to e$ of $9.5\% \pm 1\%$ was calculated from the the particle ratios $D^+/D^0 = 0.45 \pm 0.1$, $D_s/D^0 = 0.25 \pm 0.1$, and $\Lambda_c/D^0 = 0.1 \pm 0.05$ and the branching ratios according to [29]. The change in the distributions leads to an uncertainty of 15% [16].

Furthermore the systematic uncertainty on the longitudinal correlation of the charm quarks (rapidity gap) has been studied by changing the parton distribution function (PDF). A PDF $f_i^p(x, Q^2)$ describes probability to find a parton with flavor i inside a beam particle p participating in a hard-scattering process with momentum transfer Q^2. As the PDF can not be calculated with pQCD, PDFs are constructed by various groups by fits to experimental data for a fixed momentum transfer Q_0^2 and are then extrapolated in the (x, Q^2) plane.

The resulting spectra for five different PDFs (CTEQ5L [106], CTEQ4L [134], GRV94LO [135], GRV98LO [136], and MRST(c-g)[137]) are shown in Fig. 4.3. The variation in the e^+e^- pair yield in the PHENIX acceptance is 11%.

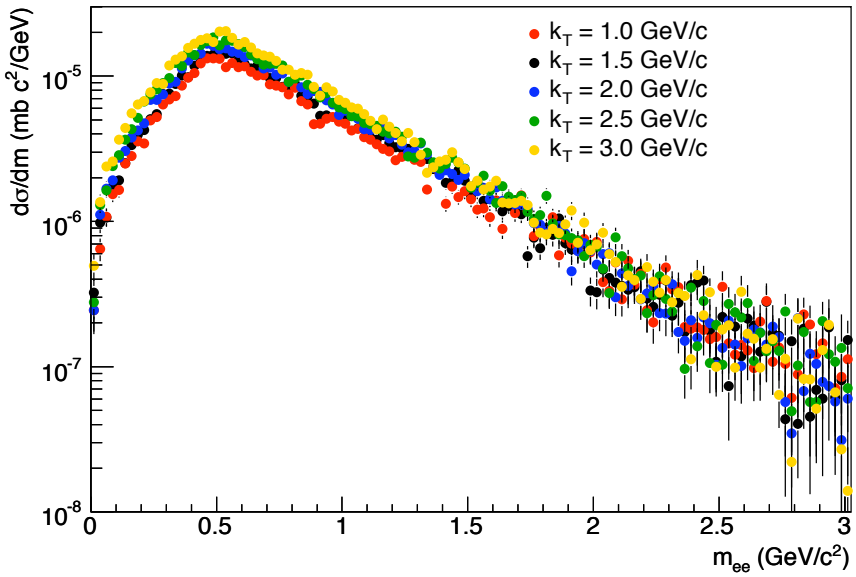

Figure 4.2: e^+e^- pairs from semileptonic open charm decays for different values of k_T: 1.0 GeV/c (*blue*), 1.5 GeV/c (*black*), 2.0 GeV/c (*yellow*), 2.5 GeV/c (*magenta*), and 3.0 GeV/c (*cyan*).

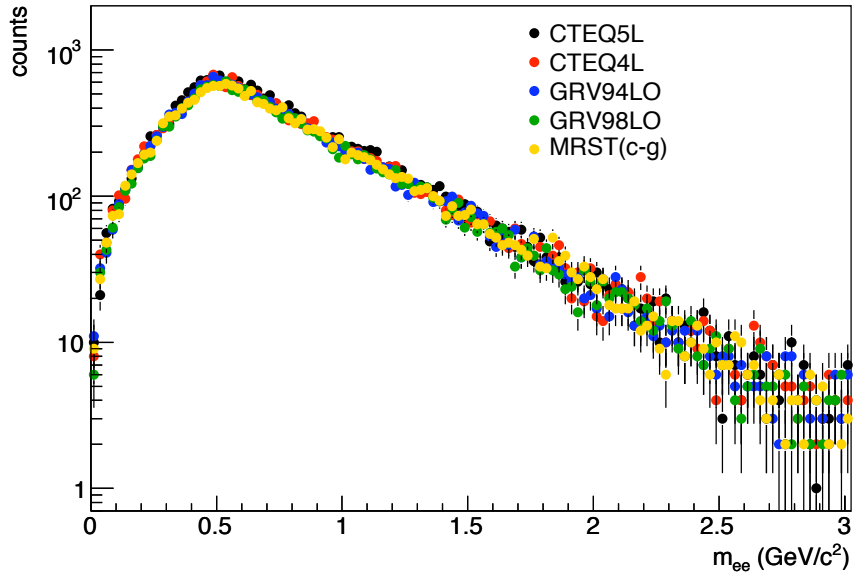

Figure 4.3: e^+e^- pairs from semileptonic open charm decays for different PDFs: CTEQ5L (*black*), CTEQ4L (*blue*), GRV94LO (*red*), GRV98LO (*green*), and MRST(c-g) (*yellow*).

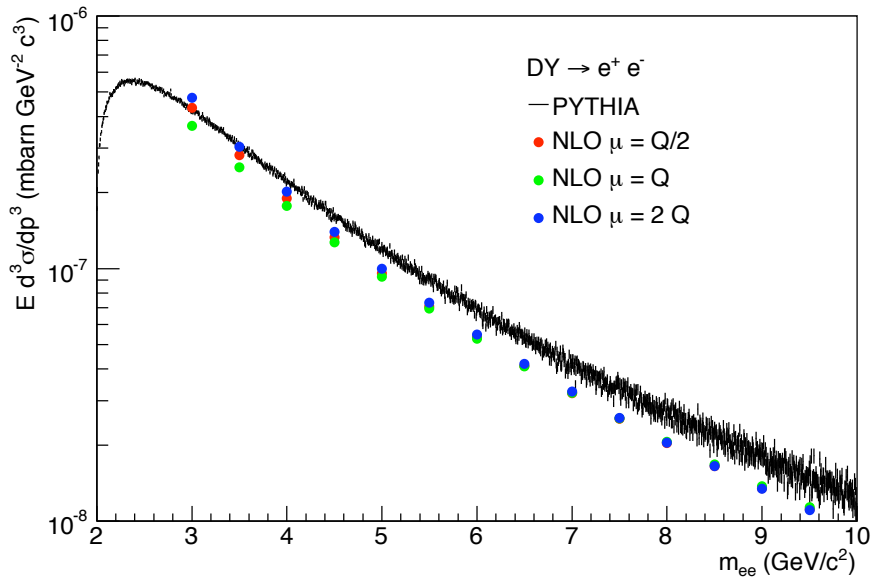

Figure 4.4: e^+e^- pairs from Drell-Yan in $|y_{ee}| < 0.5$ from PYTHIA (black) and a NLO pQCD calculation [138] for three scales: $\mu = q/2$ (*red*), $\mu = q$ (*green*), and $\mu = 2q$ (*blue*).

Drell-Yan

As estimate of the Drell-Yan contribution to the e^+e^- pair spectrum a NLO pQCD calculation by Werner Vogelsang has been used [138]. The invariant mass spectrum of e^+e^- pairs in $|y_{ee}| < 0.5$ is shown in Fig. 4.4 using CTEQ6M PDF [139] with the scales $\mu = q/2$, q, and $2q$.

The result is compared to a PYTHIA calculation which is shown in the same figure. While above 4 GeV/c^2 the two calculations disagree in shape, the integrated yields agree within 20% in the region of interest.

Fitting

In a second approach the charm and bottom cross section have been extracted with a simultaneous fit of the mass shapes from PYTHIA to the cocktail subtracted data shown in Fig. 4.5.

The fit is performed in a mass range $1.1 < m_{ee} < 7.0$ GeV/c^2, but excludes the mass range $2.5 < m_{ee} < 3.9$ GeV/c^2 to avoid influences from imperfections in the subtractions of J/ψ and ψ', with the mass spectra from PYTHIA for e^+e^-

pairs from charm, bottom and Drell-Yan:

$$dN/dm_{ee} = p_0 \cdot dN_{c\bar{c}}/dm_{ee} + p_1 \cdot dN_{b\bar{b}}/dm_{ee} + dN_{\mathrm{DY}}/dm_{ee} \tag{4.1}$$

where p_0 and p_1 denote the two fit parameters and $dN_{c\bar{c}}/dm_{ee}$, $dN_{b\bar{b}}/dm_{ee}$, and dN_{DY}/dm_{ee} are the mass distributions of simulated e^+e^- pairs in the PHENIX acceptance from charm, bottom and Drell-Yan with the cross sections $\sigma_{c\bar{c}} = 567$ μb [16], $\sigma_{b\bar{b}} = 3.7$ μb [130] and $\sigma_{\mathrm{DY}} = 42$nb [131], respectively. The fit result is $p_0 = 0.914 \pm 0.082$ and $p_1 = 1.064 \pm 0.714$. When scaling the PYTHIA Drell-Yan spectrum above 4GeV/c^2 to the NLO pQCD calculation by W. Vogelsang [138] the results are summarized in Tab. 4.1.

Table 4.1: Fit results for scaling the PYTHIA Drell-Yan spectrum to the NLO pQCD calculation [138] above 4 GeV/c^2.

	p_0	p_1
$\mu = q/2$	0.909 ± 0.083	1.15 ± 0.72
$\mu = q$	0.897 ± 0.083	1.25 ± 0.72
$\mu = 2q$	0.910 ± 0.083	1.14 ± 0.72

The resulting charm and bottom cross sections are therefore:

$$\sigma_{c\bar{c}} = 518 \pm 47(\mathrm{stat.}) \pm 135(\mathrm{syst.}) \pm 190(\mathrm{model})\ \mu\mathrm{b}$$
$$\sigma_{b\bar{b}} = 3.9 \pm 2.4(\mathrm{stat.})^{+3}_{-2}(\mathrm{syst.})\ \mu\mathrm{b}$$

The fit result for the charm cross section is in good agreement with yield integration method. Although the significance of the bottom cross section is limited by large uncertainties, it is the first measurement of bottom production at RHIC energies. A preliminary result of the bottom to charm ratio measured via electron-hadron correlations [140] leads to a bottom cross section of $\sigma_{b\bar{b}} = 4.61 \pm 1.31(\mathrm{stat.})^{+2.57}_{-2.22}(\mathrm{syst.})$ μb which is in good agreement with the dielectron result.

Dependence on Collision Energy

The $\sqrt{s}$ dependence of charm production in $p+p$ collisions as predicted by a NLO pQCD calculations [141] is shown in Fig. 4.6. It is compared to experimental data from SPS and FNAL experiments at $\sqrt{s} \approx 20$ GeV, data from PHENIX at $\sqrt{s} = 200$ GeV and results from the UA2 Collaboration at $\sqrt{s} = 630$ GeV. The two data points from PHENIX are the cross sections measured

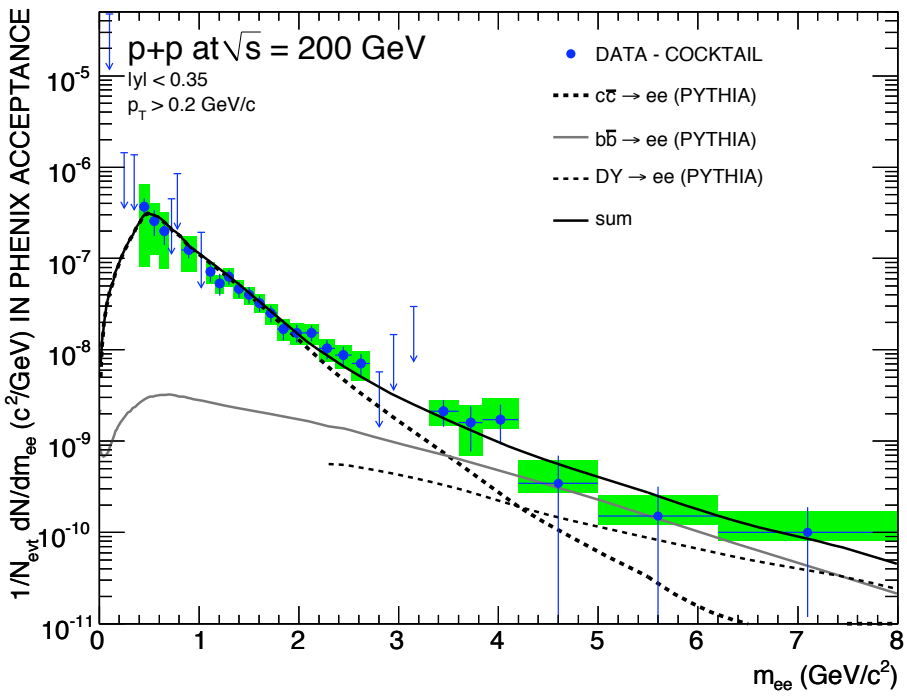

Figure 4.5: Electron-positron mass distributions from semileptonic decays of heavy flavor, obtained by subtracting the contribution from π^0, η, ω, ρ, ϕ, η', J/ψ and ψ' mesons from the inclusive e^+e^- pair yield. The arrows indicate upper limits (95% CL) in the mass regions where the charm contribution is smaller or comparable to the systematic uncertainties. For all data points statistical error bars and systematic uncertainty boxes, including data and model contributions, are shown. Also shown are expected contributions from charm, scaled to data, and bottom as well as Drell-Yan.

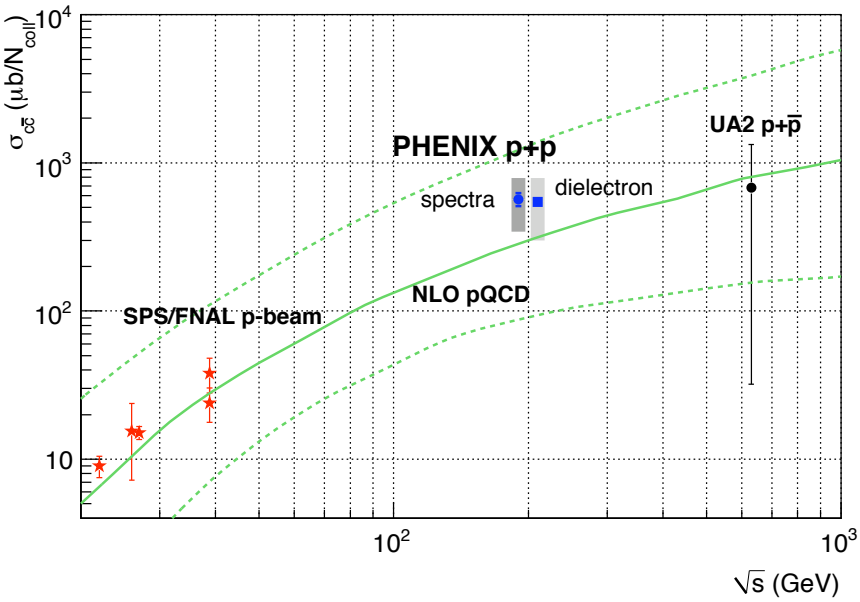

Figure 4.6: Shown is a NLO pQCD calculation of the total charm cross section as function of the collisions energy $\sqrt{s}$. The central value is shown as *solid* line, the upper and lower ends of the uncertainty band are shown as *dashed* lines. The calculation is compared to experimental measurements of the charm cross section including the result of this thesis labeled *dielectron*.

with single electrons from semi-leptonic heavy flavor decays [16] (labeled *spectra*) and the result presented in this thesis (labeled *dielectron*). Within the large theoretical uncertainties, NLO calculations describes the experimental data over the full range of $\sqrt{s}$.

For the same NLO calculation, the bottom cross section is compared to measurements as function of $\sqrt{s}$ in Fig. 4.7. The PHENIX data point labeled *spectra* is the result of the electron-hadron analysis [140] and the point labeled *dielectron* is the result of this thesis. NLO calculation.

Transverse Momentum Dependence

While it is known that PYTHIA simulations as used in this analysis fail to describe the single electron spectra at high p_T [16], it is of little concern here, as the IMR is dominated by e^+e^- pairs from $c\bar{c}$ decays with small p_T but large opening angle. Fig. 4.8 shows the measured yield of e^+e^- pairs in the mass range $1.1 < m_{ee} < 2.5$ GeV/c^2 as function of p_T. The data are corrected for electron identification and ERT trigger efficiency, but not for the

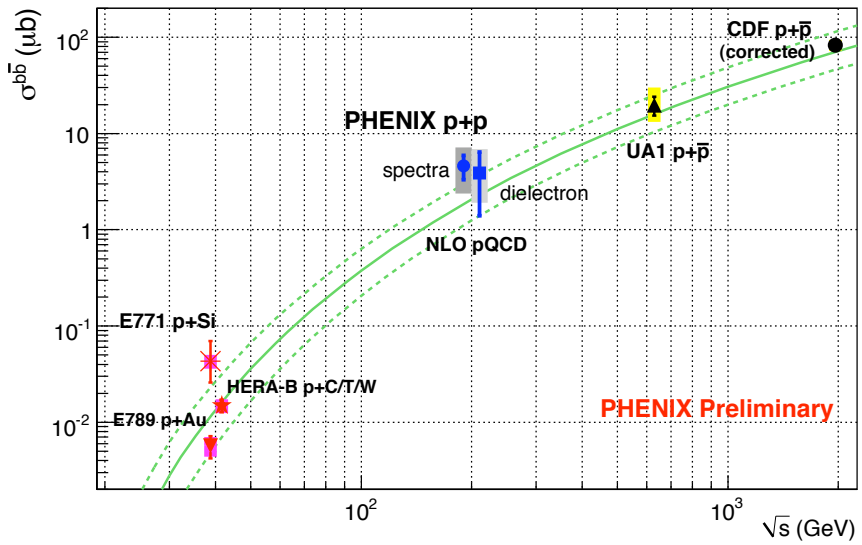

Figure 4.7: Shown is a NLO pQCD calculation of the total bottom cross section as function of the collisions energy $\sqrt{s}$. The central value is shown as *solid* line, the upper and lower ends of the uncertainty band are shown as *dashed* lines. The calculation is compared to experimental measurements of the charm cross section including the result of this thesis labeled *dielectron*.

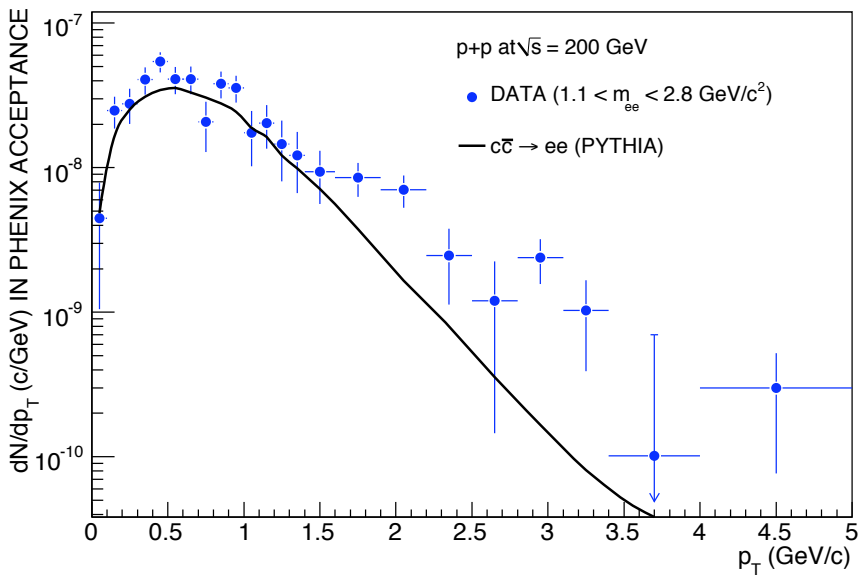

Figure 4.8: Measured p_T distributions of e^+e^- pairs in the mass region $1.1 < m_{ee} < 2.8$ GeV/c^2 in. The data are corrected for eID and ERT efficiency but not for the geometric acceptance. The yield is compared to the expected yield from open charm calculated with PYTHIA filtered into the PHENIX acceptance. No systematic uncertainties are shown.

geometric acceptance. The measured distribution of e^+e^- pairs is compared to a PYTHIA calculation filtered into the PHENIX acceptance. While at high p_T PYTHIA fails to describe the p_T spectrum of e^+e^- pairs, the low p_T region which contains the dominant fraction of the yield is sufficiently well described. Very much analog to the single electron p_T. It will be interesting to study this p_T dependency in more detail and compare to NLO calculations. To leading order heavy quark pairs are produced back-to-back, thus their pair p_T sums to zero. Deviations from this are due to the intrinsic k_T carried by the incoming partons. In contrast, as shown in Fig. 1.13, next-to-leading order processes have three particles in the final state and therefore the distribution of heavy quark pairs should be more isotropic and contribute more at high p_T.

Leading Order vs. Next-to-Leading Order Calculations

In Ref. [142] parton showers in PYTHIA have been used to approximate some of the real corrections to leading order hard scattering processes. For example, a final state heavy quark can radiate a gluon or an initial state gluon can split into a quark-antiquark pair. According to the number of how many heavy

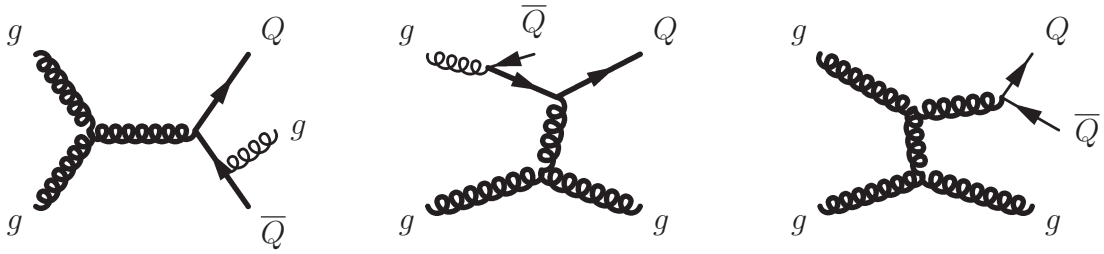

Figure 4.9: Examples of pair creation, flavor excitation, and gluon splitting in PYTHIA. The thick lines correspond to hard scattering processes, the thin ones to parton showers [142].

quarks are produced in the LO hard scattering process the following processes are defined:

pair creation: Two heavy quarks are created in the final state by quark-antiquark or gluon annihilation. These are the LO processes shown in Fig. 1.12

flavor excitation: One heavy quark, which is assumed to come from a gluon splitting process, is put on mass shell by hard scattering off a parton from the opposite hadron.

gluon splitting: No heavy quark is involved in the hard scattering, but a heavy quark pair is created in initial or final state showers from a gluon.

The corresponding Feynman graphs are shown in Fig. 4.9 in which thick lines correspond to the hard scattering process and thin lines to the parton shower.

The results of a PYTHIA calculation including parton showers tuned for charm production in Pb+Pb collisions at $\sqrt{s} = 5.5$ TeV are shown in Fig. 4.10. The total charm cross section has been scaled to a NLO calculation which is shown in comparison. Transverse momentum and rapidity distributions of single charm quarks, as well as the invariant mass, p_T and $\Delta\phi$ of $c\bar{c}$ pair are shown. Besides the fundamental differences in the two calculations, the overall agreement is rather good. However,especially $\Delta\phi$ distributions show significant differences. It is very interesting to note that the p_T distributions of the pair creation, which as the LO processes has two hard scattered quarks in the final state, shows a significantly softer p_T distribution than flavor excitation and gluon splitting which have both a more isotropic distribution of the heavy quark pair. This underlines the importance of higher order processes at high p_T.

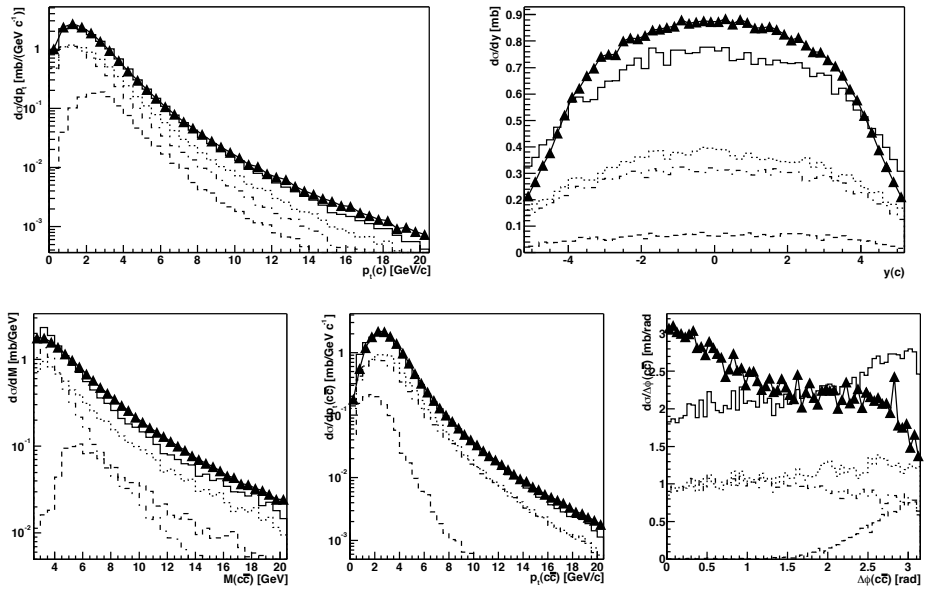

Figure 4.10: Charm production in Pb + Pb collisions at $\sqrt{s} = 5.5$ TeV calculated by PYTHIA including parton showers (*solid line*). The individual components are pair production (*dashed*), flavor excitation (*dotted*), and gluon splitting (*dot-dashed*). The PYTHIA result is compared to a NLO calculation (*triangles*)[142].

4.1.2 ω and ϕ Cross Sections

As discussed in Section 1.2.4 the in-medium resonance decays of the vector mesons ω and ϕ provide information about the hadronic phase of the medium created in heavy ion collisions at the time of decay. To measure potential medium-modifications to the line shape of the resonances, a baseline measurement of the line shapes in $p + p$ collisions is crucial. Furthermore, the study of hadronic versus electromagnetic decays of the ϕ are particularly interesting. As the ϕ mass ($m_\phi = 1019$ MeV/c^2) is very close to twice the kaon mass ($m_K = 493.7$ MeV/c^2), the decay $\phi \to K^+K^-$ is very sensitive to any changes of the ϕ mass due to, *e. g.*, the restoration of chiral symmetry.

To provide this baseline, the cross sections of ω and ϕ have been measured in $p + p$ collisions via their resonance decays into e^+e^- pairs. Fig. 4.11 shows the raw invariant mass spectra of e^+e^- pairs for various slices in p_T of 200 MeV/c up to 2 GeV/c and beyond in two bins from 2–3 GeV/c and 3–5 GeV/c. They are shown together with the the sum of correlated and combinatorial background and the signal after background subtraction. Already before background subtraction the ω and ϕ peaks are very pronounced. The figure also shows a fit to a Gaussian with the mean being fixed to the PDG

value of the ω and ϕ mass ($m_\omega = 782.65$ MeV/c^2, $m_\phi = 1019.460$ MeV/c^2 [29]), respectively.

The ω and ϕ yields (listed in Tab. C.1) are extracted by counting e^+e^- pairs in a mass region which corresponds to a 3σ interval, *i. e.*, 0.740–0.815 GeV/c^2 and 0.965–1.065 GeV/c^2, respectively.

Alternatively, to determine the systematic uncertainty on the peak extraction, the peaks are fitted with a Gaussian + n^{th} order polynomial ($n = 0, 1, 2$) to allow for contributions due to the underlying continuum. The fits for the ω have been performed in the mass range 0.6–0.9 GeV/c^2 while for the ϕ the range 0.9–1.2 GeV/c^2 was chosen. The systematic uncertainties on the peak extraction have been determined out of the variation of the yield with the different fits. For the ω this uncertainty is 14%, while for the ϕ it is 20% for $p_T > 1$ GeV/c and 12% below. This uncertainty is added in quadrature to the ones listed in Tab. 3.9.

Analog to Eq. (3.24) the invariant cross section of ω and ϕ mesons is calculated as

$$E\frac{d^3\sigma_{\omega,\phi}}{dp^3} = \frac{1}{2\pi\, p_T}\frac{1}{N_{\text{evt}}\,\Delta p_T}\frac{N_{\omega,\phi}}{B^{\omega}_{ee}\,\varepsilon_{\text{pair}}\,\varepsilon^{\text{pair}}_{\text{geo}}}\frac{\varepsilon_{\text{BBC}}}{\varepsilon_{\text{bias}}}\sigma^{\text{inel}}_{pp} \tag{4.2}$$

with the branching ratios for the decays $\omega \to e^+e^-$: $B^{\omega}_{ee} = 7.18 \pm 0.12\%$ and $\phi \to e^+e^-$: $B^{\phi}_{ee} = 2.97 \pm 0.04\%$, respectively [29].

The resulting ω cross sections as function of p_T are shown in Fig. 4.12. In Fig. 4.14 it is compared to existing measurements at higher p_T via hadronic decays, *i. e.*, $\omega \to \pi^0\pi^+\pi^-$ and $\omega \to \pi^0\gamma$ [119–121]. In the p_T region in which both measurements exist, they are in good agreement. Also shown is a common fit to a m_T scaled modified Hagedorn parameterization of charged and neutral pions as defined in Eq. (3.35) with only the normalization factor as free parameter, which has been used as parameterization of the ω in the EXODUS cocktail calculation as described in Section 3.7. In addition, alternative fits with a modified Hagedorn and all parameters free and a simple exponential in m_T ($E\frac{d^3\sigma}{dp^3} = A\mathrm{e}^{-(m_T/T_{\text{eff}})}$) are shown.

Fig. 4.13 shows the measured ϕ cross section, which in Fig. 4.15 is compared to the result of the hadronic decay into two kaons [120, 122]. The agreement in the region where both measurements are available is not very good and currently not understood. A further investigation of the problem is ongoing and both results. As for the ω, the data are fit to the m_T scaled modified Hagedorn parameterization of charged and neutral pions, a modified Hagedorn with all parameters left free and an exponential in m_T.

For both, ω and ϕ cross sections, the fits with a modified Hagedorn and all parameters free results in a shape very comparable to the fit of charged and

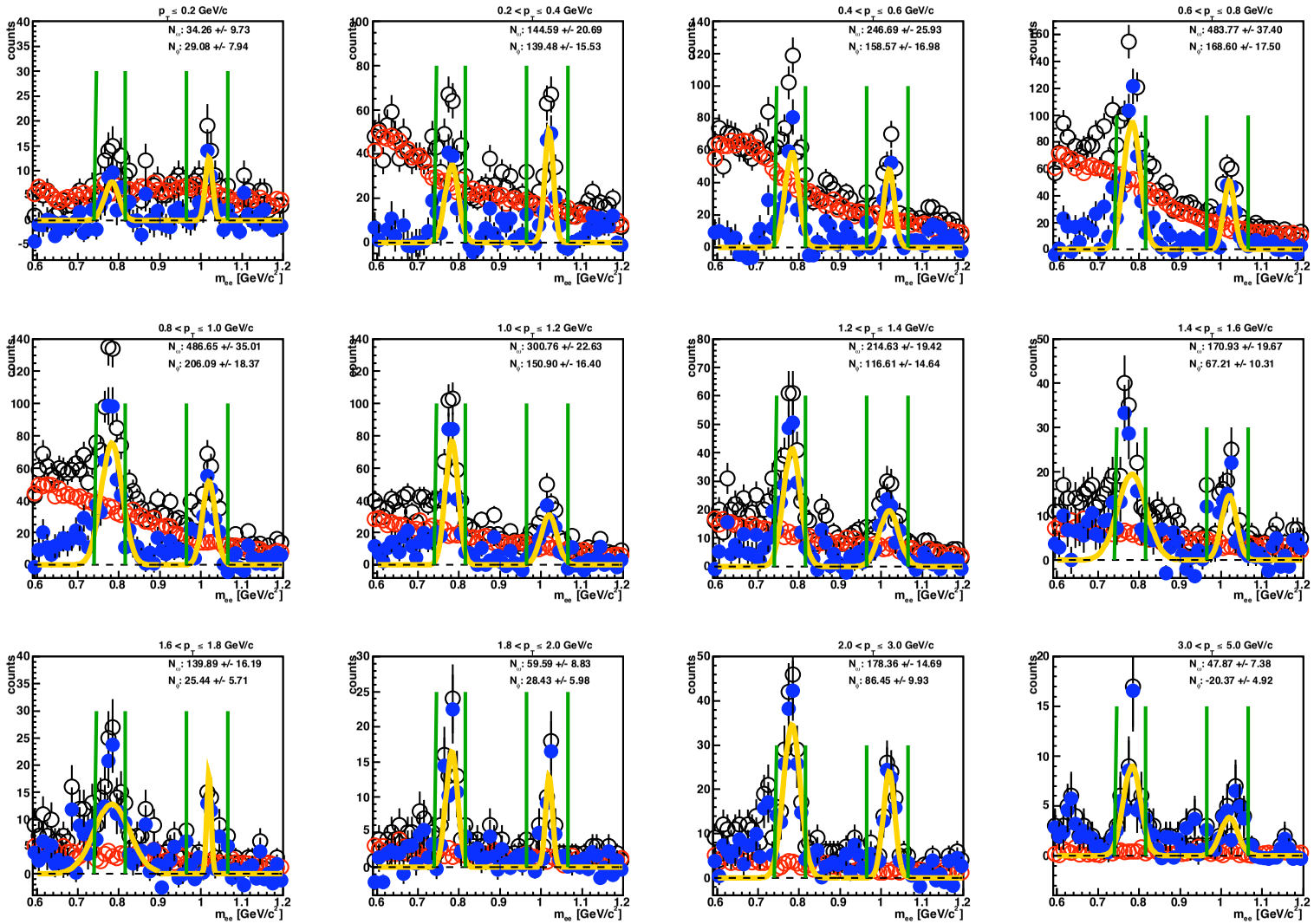

Figure 4.11: Invariant mass spectrum of e^+e^- pairs. Foreground (*black*), combinatorial background (*red*) and Signal (*blue*). Also shown are two Gaussian fits (*orange*) to ω and ϕ, respectively.

neutral pions. The exponential fit in m_T offers only a good description at low p_T but fails for $p_T > 2$ GeV/c.

4.1.3 Low Mass p_T Spectra

To study the p_T dependency of the dielectron continuum the invariant mass spectra for e^+e^- pairs in various p_T ranges is shown in Fig. 4.16. The results are again compared to the cocktail, which has been normalized to the measured e^+e^- pair yield in $m_{ee} < 30$ MeV/c^2. A cocktail with absolute normalization agrees with the data in this region within the systematic uncertainty of 20%. Again, the $p + p$ data are in good agreement with the cocktail over the full mass range and for all p_T bins, except for some small deviations at high p_T which are discussed in Section 4.1.4.

In a next step the yield of e^+e^- pairs in small mass ranges is analyzed as function of p_T. The yield is now corrected for the geometric acceptance of the PHENIX central arm detectors. The invariant yield as function of the e^+e^- pair p_T as defined in Eq. (3.24) is shown in Fig. 4.17 for e^+e^- pairs in different mass ranges and compared to the cocktail. The p_T spectrum of e^+e^- pairs with $m_{ee} < 0.1$ GeV/c^2, dominated by π^0 Dalitz decays, is in excellent agreement with the expectation of hadron decays. Also the p_T spectra of the other mass windows agree within the systematic uncertainties well with the cocktail for $p_T < 2$ GeV/c. Above a small excess, which was also visible in the high p_T mass spectra in Fig. 4.16, is observed. This excess is analyzed in the next Chapter.

4.1.4 High p_T Direct Photons

As discussed in Section 1.2.3 any source of real direct photons can also produce a virtual photon which subsequently converts internally into an e^+e^- pair. The mass distribution is given by Eq. (1.23) and is proportional to $1/m$ for $p_T \gg m_{ee}$.

In this Chapter an attempt is made to analyze the small excess observed at high p_T in the low mass region of the dielectron continuum, which is shown more detailed again in Fig. 4.18, under the assumption that it is solely due to internal conversions of direct virtual photons. While at zero mass e^+e^- pairs from hadron decays have the same shape in mass as internal conversions of direct photons, the suppression due to S when approaching the hadron mass changes the shape of e^+e^- pairs from hadron decays. Therefore, one can fit, after an initial normalization to the mass range 0–30 MeV/c^2, the two expected shapes for e^+e^- pairs from hadronic decays f_{cocktail} (as shown in Fig. 4.17) and from direct photons f_{direct} in the mass range 80–300 MeV/c^2

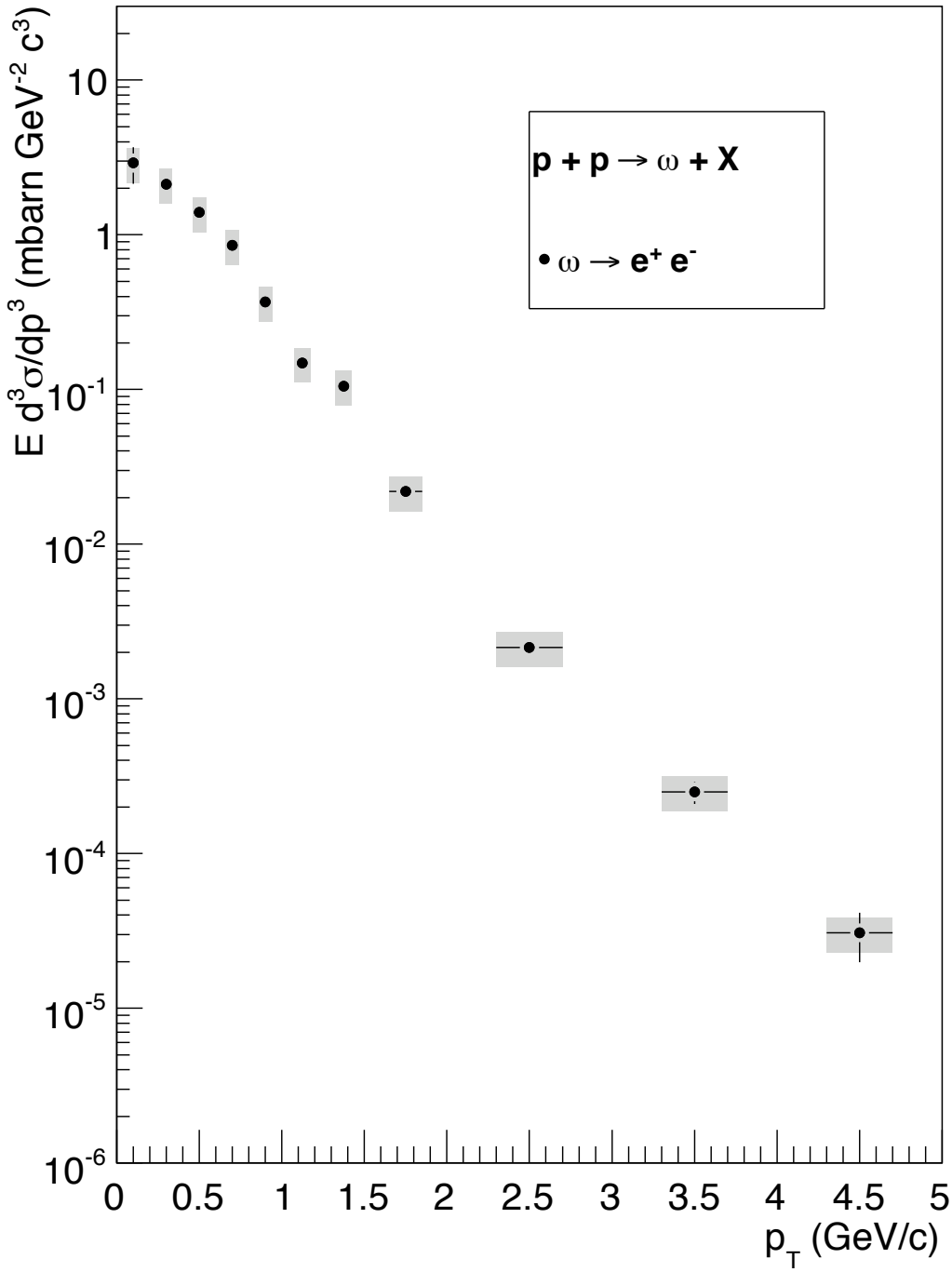

Figure 4.12: Invariant cross section of ω in $p+p$ collisions as function of p_T. The stat. errors are drawn as bars, the syst. uncertainties are represented with the gray boxes.

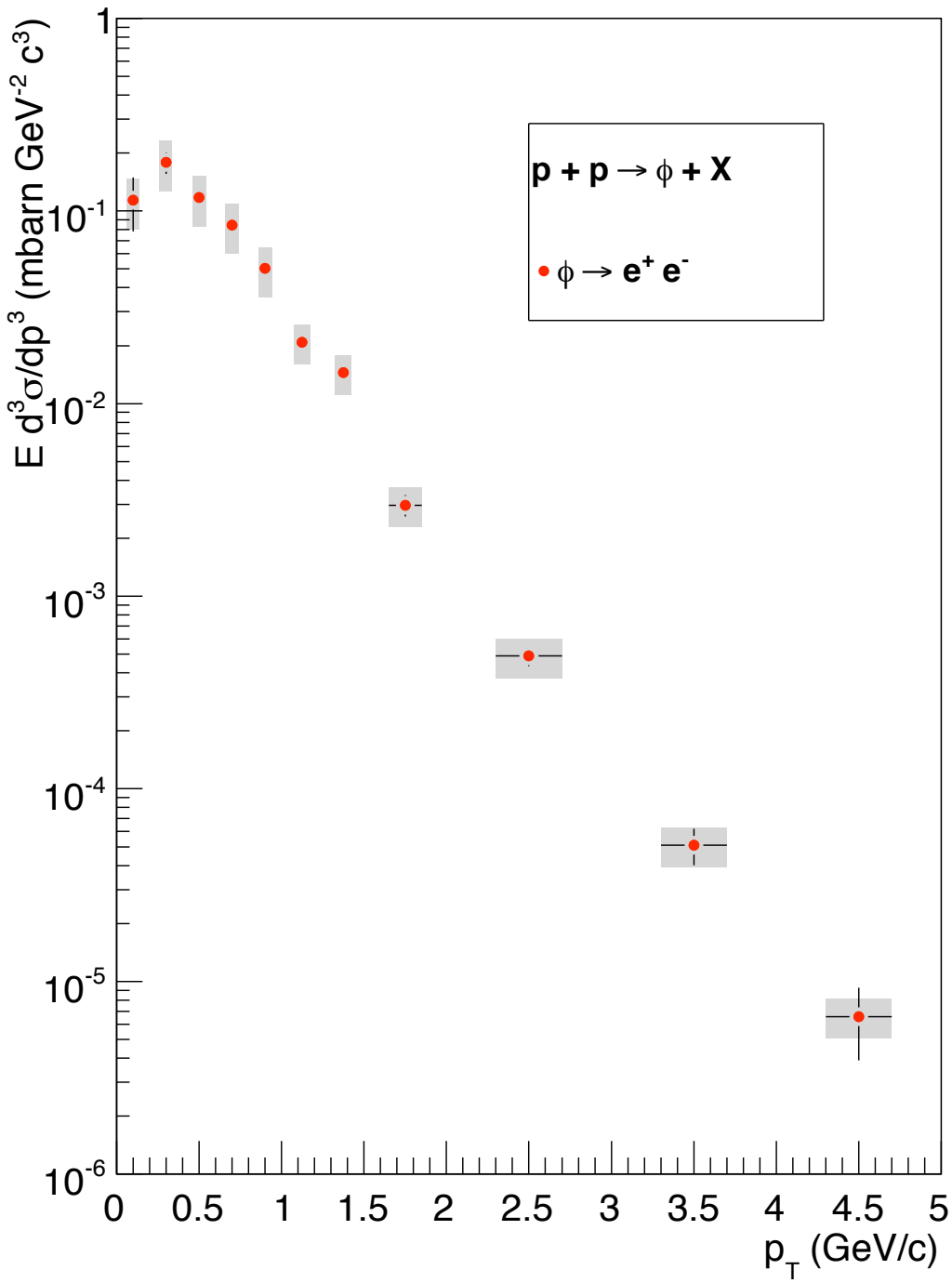

Figure 4.13: Invariant cross section of ϕ in $p+p$ collisions as function of p_T. The stat. errors are drawn as bars, the syst. uncertainties are represented with the gray boxes.

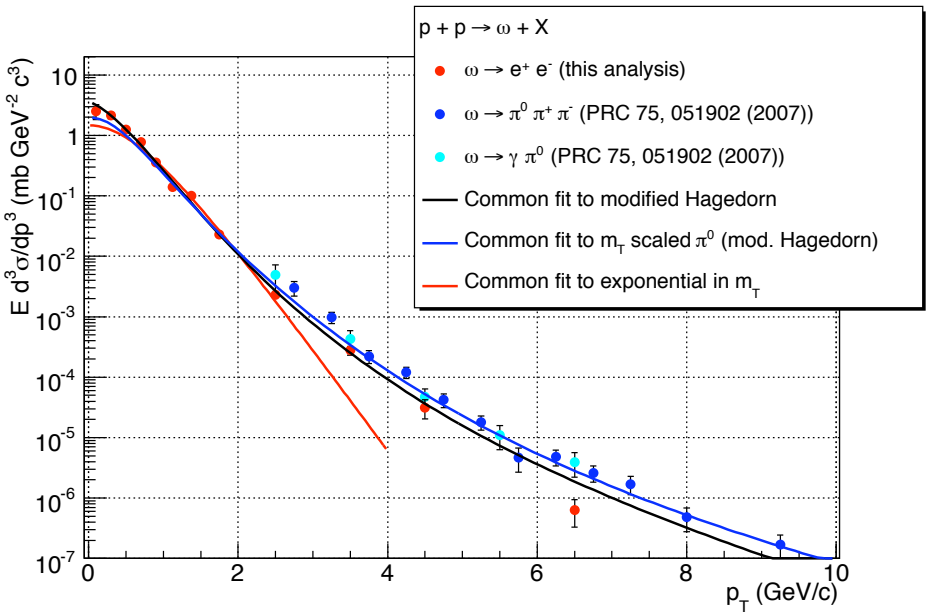

Figure 4.14: Invariant cross section of ω in $p + p$ collisions as function of p_T measured in electromagnetic and hadronic decay channels. The results are fitted to the pion parameterization (*blue*), a modified Hagedorn (*black*) and an exponential in m_T (*red*).

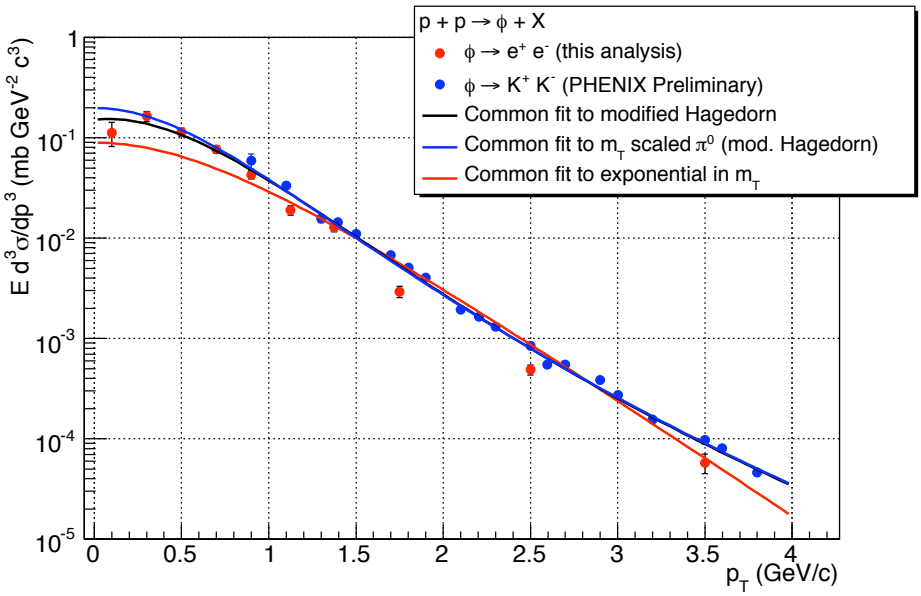

Figure 4.15: Invariant cross section of ϕ in $p + p$ collisions as function of p_T measured in electromagnetic and hadronic decay channels. The results are fitted to the pion parametrization (*blue*), a modified Hagedorn (*black*) and an exponential in m_T (*red*).

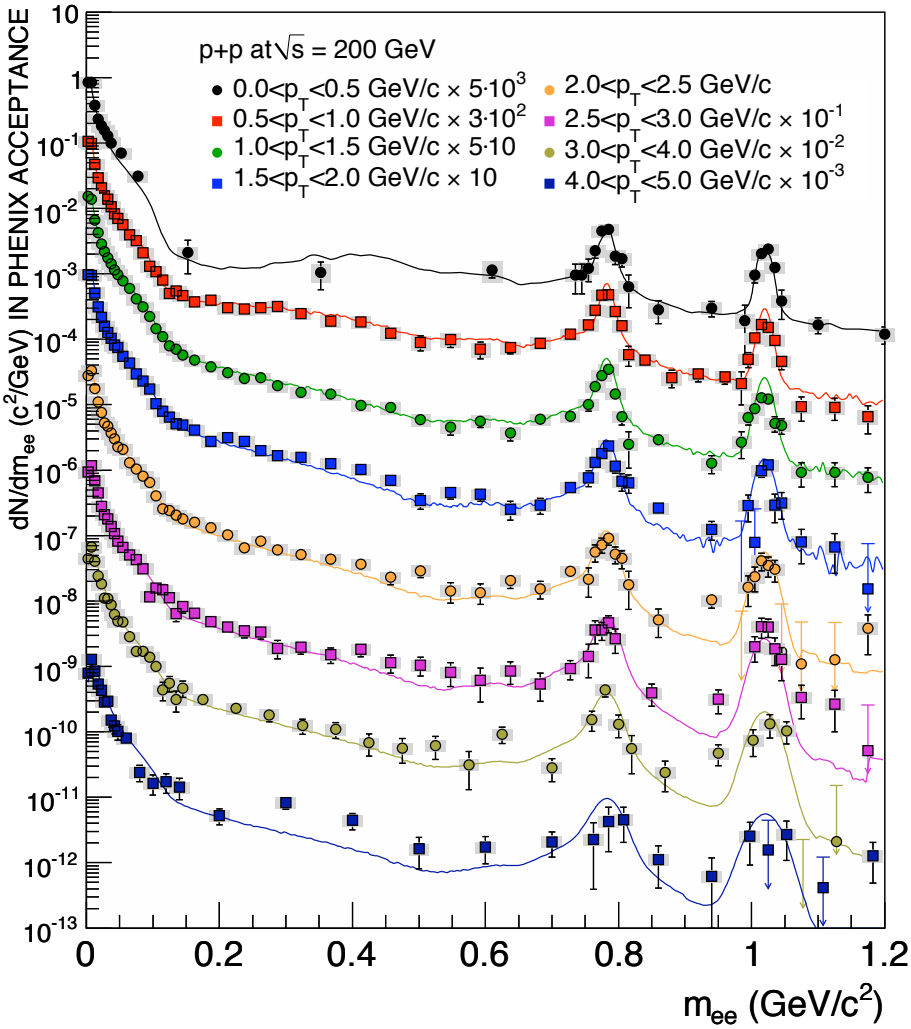

Figure 4.16: The e^+e^- pair invariant mass distributions in $p+p$ collisions. The p_T ranges are shown in the legend. The solid curves represent an estimate of hadronic sources.

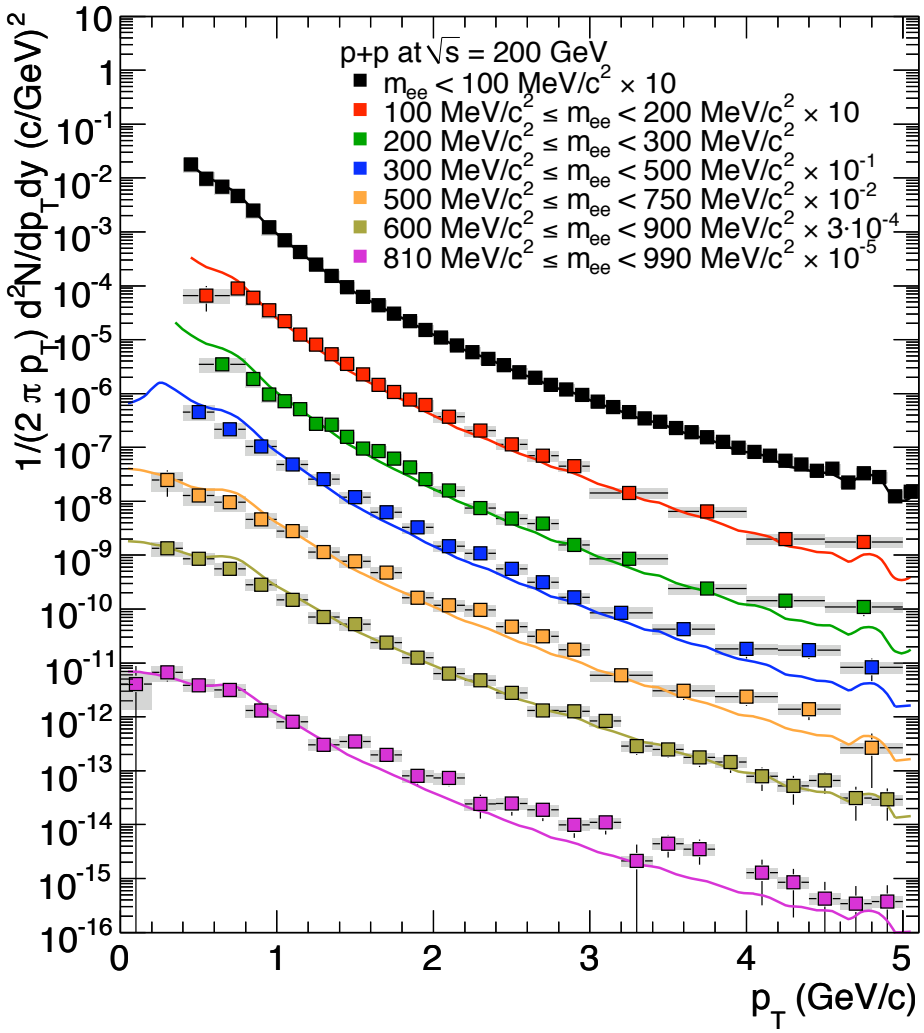

Figure 4.17: Shown is the invariant yield of e^+e^- pairs in different mass ranges in $p+p$ collisions. The mass ranges are defined in the legend.

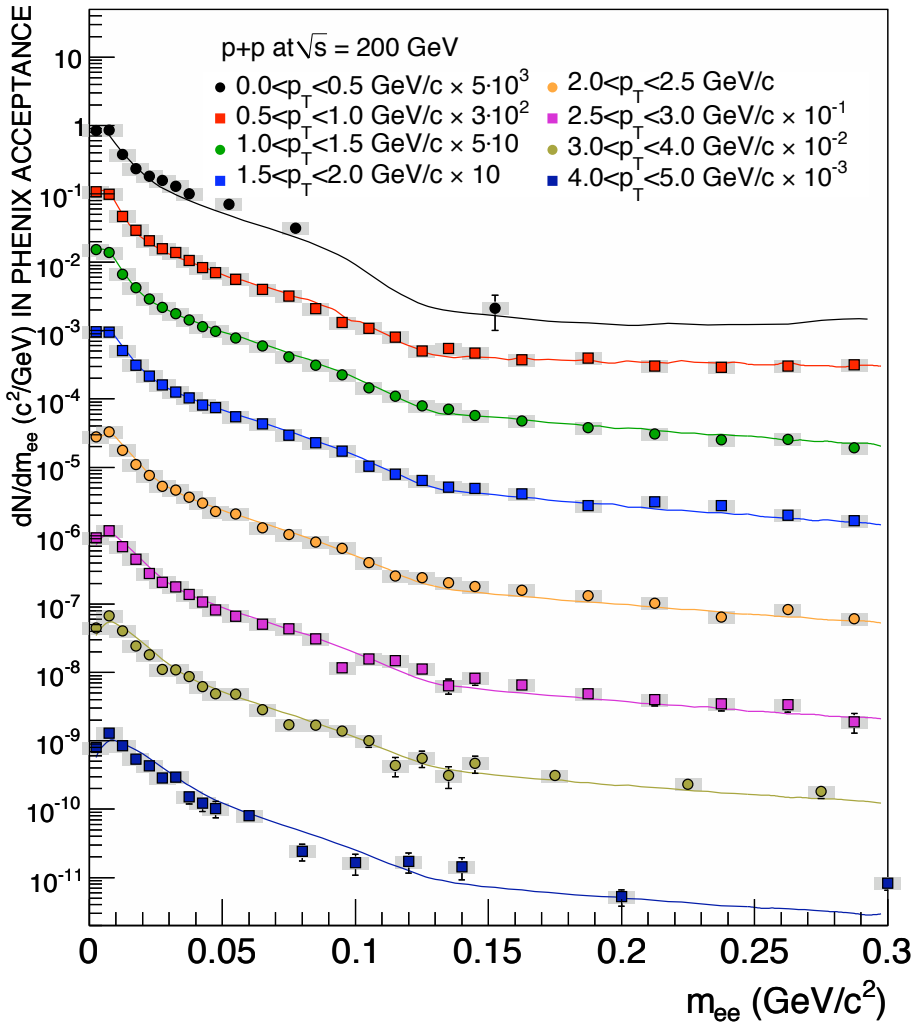

Figure 4.18: The e^+e^- pair invariant mass distributions in $p+p$ collisions. The p_T ranges are shown in the legend. The solid curves represent an estimate of hadronic sources. This is a zoomed version of Fig. 4.16.

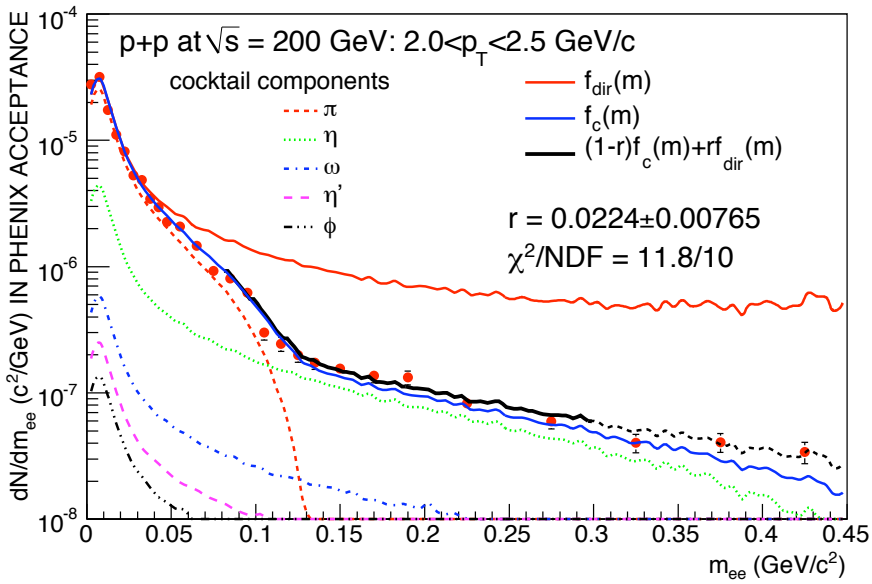

Figure 4.19: Invariant mass distribution of e^+e^- pairs in $p+p$ collisions with $2.0 < p_T < 2.5$ GeV/c. The fit with Eq. (4.3) in the range $80 < m_{ee} < 300$ MeV/c^2 is explained in the text. The *black dashed* curve shows $f(m_{ee})$ outside of the fit range.

in which the π^0 contribution is severely suppressed. The only fit parameter is the relative fraction of direct photons r:

$$f(m_{ee}) = (1-r)f_{\text{cocktail}}(m_{ee}) + r f_{\text{direct}}(m_{ee}). \tag{4.3}$$

As an example, the fit result is shown in Fig. 4.19 for e^+e^- pairs with $2.0 < p_T < 2.5$ GeV/c in $p+p$ collisions. The quality of the fit result (*e. g.*, $\chi^2/NDF = 11.8/10$ for the lowest p_T bin) indeed justifies the assumption that the observed excess is due to internal conversion of virtual photons. For each p_T bin, the fit is performed for several mass ranges $m_{\text{low}} < m_{ee} < 300$ MeV/c^2. It is assumed that the form factor $F(m_{ee}^2)$ for direct photons is 1 independent of mass. This may not be the case for direct photons from parton fragmentation or, in case of heavy ion collisions, direct photon radiation from a hadron gas. If the form factor of direct photons is arbitrarily set to the one of the η meson, the fraction of direct photons r would decrease by $\simeq 10\%$. The mass region above 300 MeV/c^2 is not used in the fits to avoid possible effects due to the form factor and to stay well within the region of $m_{ee} \ll p_T$, in which the approximation $S = 1$ is valid.

The largest uncertainty in the fit is the particle composition of the cocktail, in particular the η/π^0 ratio, which is 0.48 ± 0.03 at high p_T, based on PHENIX measurements [13, 115]. This corresponds to a 7% uncertainty in the $p+p$ cocktail for the mass range $100 < m_{ee} < 300$ MeV/c^2. Other sources cause only a few percent uncertainty in this mass range, once the normalization of the cocktail is fixed to the mass range $m_{ee} < 30$ MeV/c^2. As the η meson is the dominant hadronic source in this mass range the data has been fit with three components $f(m_{ee}) = (1-r-r_\eta)f_{\text{cocktail}}(m_{ee}) + r f_{\text{direct}}(m_{ee}) + r_\eta f_\eta(m_{ee})$, with a constrain on r_η such that the η/π^0 range is not changed beyond 0.48 ± 0.03. This alternative method results in values for r which are consistent within the statistical uncertainties.

The fraction of direct photons r is shown in the left panel of Fig. 4.28 for and compared to a NLO pQCD prediction [41, 138]. The curve shows the predicted direct photon cross section $d\sigma_\gamma^{\text{NLO}}(p_T)$ divided by the inclusive photon cross section $d\sigma_\gamma^{\text{incl}}$. The three curves which are shown correspond to three different choices of the momentum scale $\mu = 0.5p_T$, $1.0p_T$, $2.0p_T$. For a perturbative treatment, the covered p_T range of $1 < p_T \leq 5$ GeV/c is very low, and the theoretical uncertainties are quite large. Nevertheless, the NLO calculation seems in quite good agreement with the data.

The fraction of direct photons r can be converted into a cross section of direct photons by multiplying with the inclusive photon spectrum. The inclusive photon cross section is determined for each p_T bin by $d\sigma_\gamma^{\text{incl}} = \sigma_{pp}^{\text{inel}}\, dN_{ee}^{\text{data}} \times dN_\gamma^{\text{cocktail}}/dN_{ee}^{\text{cocktail}}$, where dN_{ee}^{data} and $dN_{ee}^{\text{cocktail}}$ are the yields of e^+e^- pairs in $m < 30$ MeV/c^2 for data and cocktail, respectively, and $dN_\gamma^{\text{cocktail}}$ is the yield of photons from the cocktail. The resulting direct photon spectrum for $p+p$ is shown in Fig. 4.29. The pQCD calculation is consistent with the $p+p$ data for $p_T > 2$ GeV/c within theoretical uncertainties. A similar good agreement is observed for π^0 production in $p+p$ [87]. The $p+p$ data can be well described by a modified power-law function:

$$E\frac{d\sigma^2}{dp^3} = A_{pp}\left(1 + \frac{p_T^2}{p_0}\right)^{-n} \tag{4.4}$$

as shown by the dashed line in Fig. 4.29.

In summary the dielectron continuum in $p+p$ collisions at $\sqrt{s} = 200$ GeV can be fully understood by known hadronic sources, correlated semi-leptonic decays of D and B mesons and direct photons produced in hard-scattering processes of the incoming partons. The measurement of "quasi-real" direct photons in a mass region in which π^0 Dalitz decays are suppressed has allowed the first measurement of direct photons at low p_T. These results will be crucial for the understanding and interpretation of the observed dielectron yields in

Au + Au collisions.

4.2 Comparison to Au + Au Collisions

The yield e^+e^- pairs in the PHENIX acceptance measured in min. bias Au + Au collisions at $\sqrt{s_{NN}} = 200$ GeV is shown in Fig. 4.20 as function of invariant mass. The yield is compared to the expected sources from hadron decays from EXODUS and open charm from PYTHIA. The open charm contribution is scaled to the measured charm cross section in $p + p$ ($\sigma_{c\bar{c}} = 567 \pm 57(\text{stat.}) \pm 193(\text{syst.})$ μb) [16] multiplied by the average number of binary collisions: $\langle N_{\text{coll}} \rangle = 257.8 \pm 25.4$ (see Tab. 3.1).

The data are well described by the cocktail of hadron decays in the mass region below 150 MeV/c^2. Due to the larger background to signal ratio the resonance peaks of ω and ϕ are not as well measured as in $p+p$ but within the systematic uncertainties in agreement with the expected yield. However, the yield of e^+e^- pairs in the mass range $150 < m_{ee} < 750$ MeV/c^2 is significantly enhanced above the expected cocktail yield. The enhancement factor in this mass range, defined by the ratio of the measured yield to the expected yield from hadronic sources, is $4.0 \pm 0.3(\text{stat.}) \pm 1.5(\text{syst.}) \pm 0.8(\text{model})$. Here the first uncertainty is the statistical error, the second the systematic uncertainty on the data, and the last error the uncertainty on the cocktail. The last two uncertainties are very conservative estimates and not equivalent to one standard deviation (1σ).

In a direct comparison to the measured dielectron continuum in $p + p$ the result of min. bias Au + Au is shown in Fig. 4.21a. The invariant mass spectra of Au + Au collisions in five centrality bins (0–10%, 10–20%, 20–40%, 40–60% and 60–92%, see Tab. 3.1) are shown in Fig. 4.21b and compared to the individual cocktail expectations. The low mass enhancement is concentrated in the 20% most central collisions and becomes less significant in more peripheral ones. The yield in the IMR is consistent with the PYTHIA calculation for all centrality bins. In the following the centrality dependence of the IMR and LMR are further investigated.

4.2.1 The Intermediate Mass Region

The intermediate mass region which served in the $p+p$ analysis as a window to extract the charm cross section is well described by the PYTHIA calculation of open charm pairs. This result is somewhat surprising as the measurement of single electron from semi-leptonic charm decays shows a strong modification of charm, *i. e.*, a suppression of high p_T electrons and a significant elliptic

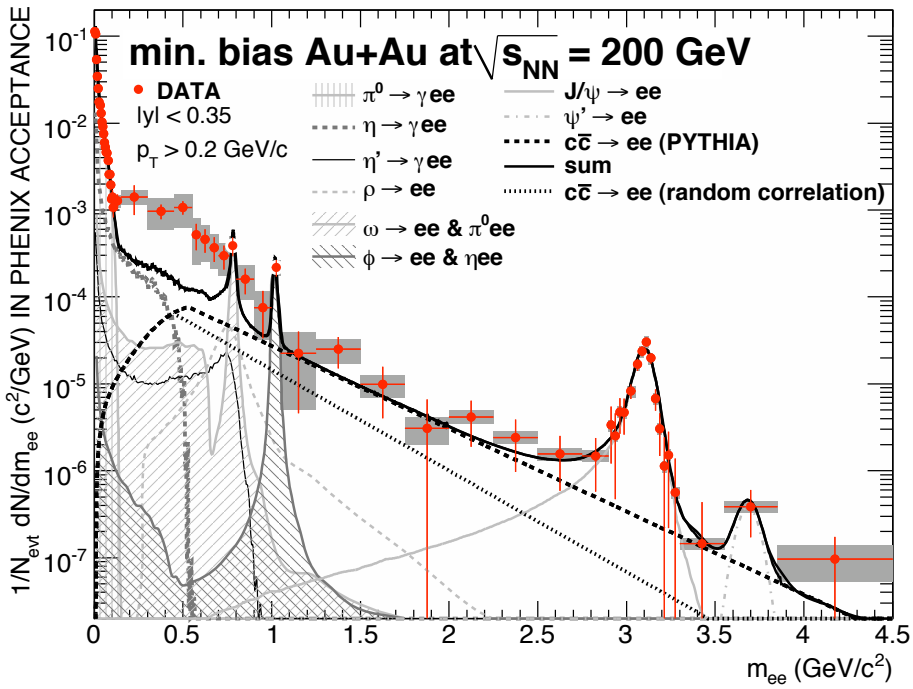

Figure 4.20: Electron-positron pair yield as function of pair mass. Data show statistical (bars) and systematic (shades) errors separately. The data are compared to a expected sources from the decays of light hadron and correlated charm decays [23]. The charm contribution expected if the dynamical correlation of the $c\bar{c}$ pair is broken, is shown separately. The systematic uncertainty on the cocktail is not shown.

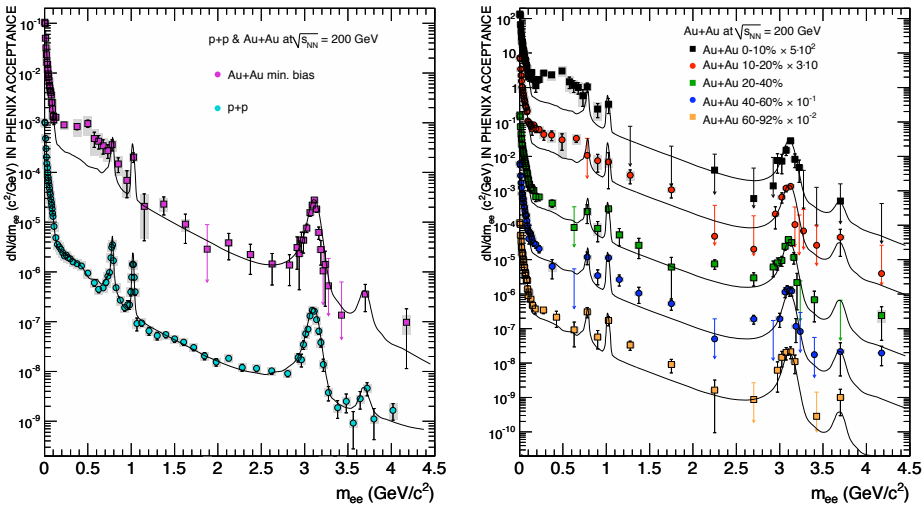

(a) (b)

Figure 4.21: (a) shows the invariant mass spectrum in $p+p$ and min. bias Au+Au collisions. (b) shows the invariant mass spectra of five centrality classes in Au + Au collisions. The data are shown with statistical (bars) and systematic (shades) errors separately. The data are compared to the expected sources from the decays of light hadron calculated with EXODUS and correlated charm decays based on PYTHIA.

flow [16]. Therefore, one would expect this modification to also influence the pair properties. An extreme scenario is shown in addition to the PYTHIA curve as dotted line in Fig. 4.20 assuming the initial correlation of the $c\bar{c}$ pair is completely broken, e^+e^- pairs are generated with a single p_T distribution following the measured spectrum of single electrons from semi-leptonic heavy-flavor decays [16], but a random azimuthal opening angle. This distribution is much softer, than the PYTHIA curve, which would leave room to other contributions such as thermal radiation via $q\bar{q}$ annihilation.

If the yield in the IMR is dominated by open charm, it is expected to increase proportional to the number of binary collisions. The yield per number of binary collision N_{coll} in the mass range $1.2 < m_{ee} < 2.8$ GeV/c^2 is shown as function of N_{part} in Fig. 4.22. The data show no significant centrality dependence and are consistent with the expected yield calculated with PYTHIA. But the apparent scaling with the number of binary collisions may be a coincidence of two counteracting effects: (i) the suppression of e^+e^- pairs from open charm in the IMR due to modifications of charm which increases with N_{part} and (ii) an additional contribution due to thermal radiation from $q\bar{q}$ annihilation which is expected to increase faster than proportional to N_{part}. As discussed in Section 1.3.3, such a coincidence may have been observed at the

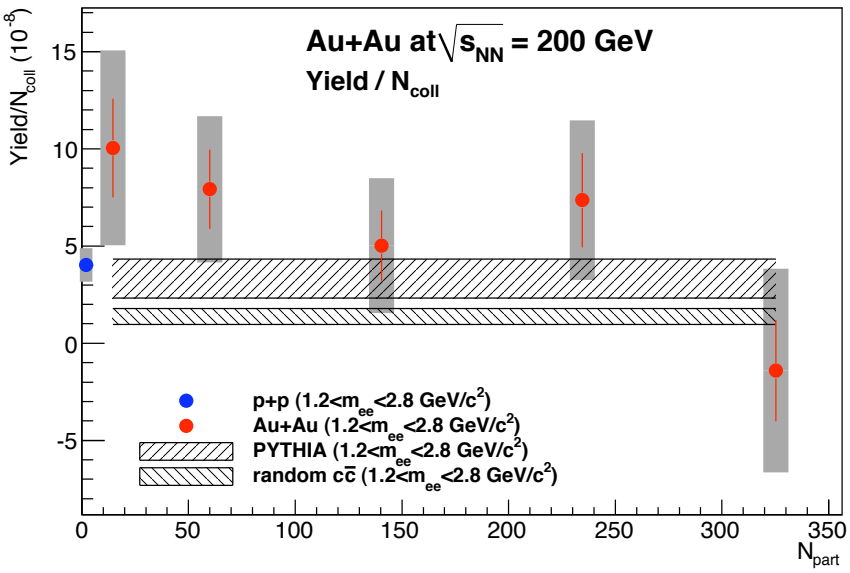

Figure 4.22: Dielectron yield per binary collision as function of N_{part} for the mass range $1.2 < m_{ee} < 2.8$ GeV/c^2. Statistical and systematic uncertainties are shown separately. Also shown are two bands corresponding to two different estimates of the contribution from charmed meson decays. The width of the bands reflect the uncertainties on the charm cross section only.

SPS [74], where a prompt component has been suggested by NA60 [75].

4.2.2 The Low Mass Enhancement

The centrality dependence of the yield in the low mass region has been studied more quantitatively. The first range, $m_{ee} < 100$ MeV/c^2, is dominated by π^0 Dalitz decays. As the π^0 multiplicity roughly scales with the number of participating nucleons, the yield in this range should scale linearly with N_{part}. Fig. 4.23 shows the yield in $m_{ee} < 100$ MeV/c^2 divided by the number of participating nucleon pairs ($N_{\text{part}}/2$) as function of N_{part}. The yields in all centrality bins as well as $p + p$ are in good agreement with the cocktail, and show the expected scaling.

The top panel of Fig. 4.23 shows the yield per participating nucleon pair for the mass region $150 < m_{ee} < 750$ MeV/c^2, in which the enhancement is observed. While the agreement with the cocktail is good for $p + p$ and the peripheral collisions, an increase of the yield is observed in the data above $N_{\text{part}} \approx 200$ that is stronger than linear. For the most central bin, the yield

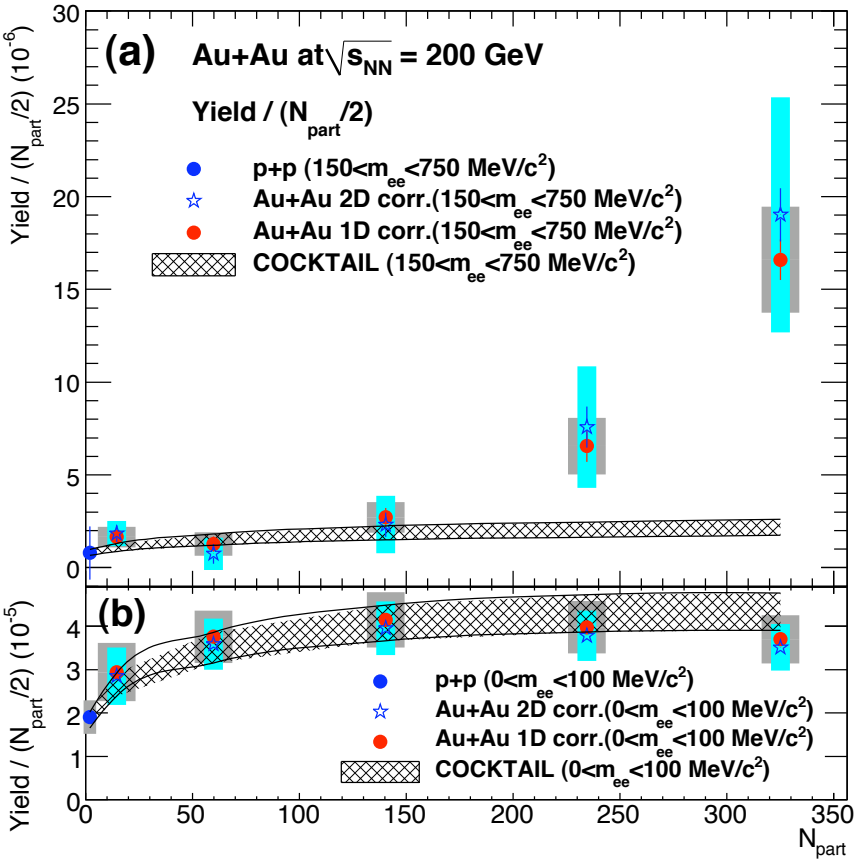

Figure 4.23: Dielectron yield per participating nucleon pair as function of N_{part} for the mass range $150 < m_{ee} < 750$ MeV/c^2 (a) and $m_{ee} < 100$ MeV/c^2 (b). Statistical and systematic uncertainties are shown separately. Also shown are the expected cocktail yields. The band reflects the systematic uncertainty on the cocktail

is a factor $7.6 \pm 0.5(\text{stat.}) \pm 1.5(\text{syst.}) \pm 1.5(\text{model})$ above the cocktail. This stronger than linear rise of the yield is qualitative understood with the notion of $q\overline{q}$ or $\pi\pi$ annihilation as source of the enhancement.

4.2.3 Direct Photons

In this chapter it is tested whether the excess observed in the low mass region is compatible with a source of virtual direct photons. The analysis has been performed with the same method as for $p+p$ which has been discussed in Section 4.1.4. Fig. 4.24 shows the yield of e^+e^- pairs as function mass below 1.2 GeV/c^2 for various p_T ranges in min. bias Au + Au collisions. The low mass enhancement is concentrated at low transverse momenta: $p_T < 1$ GeV/c. For $p_T > 1$ GeV/c the enhancement, although reduced, is still quite significant (a factor ≈ 2 above the expected yield), but is quite different in shape. The low p_T mass spectrum divided in finer p_T bins as shown in Fig. 4.26. While the low p_T enhancement has a "bump" like structure, the shape at higher p_T is consistent with the $1/m_{ee}$ shape expected from internal conversions of direct virtual photons.

Thus the excess of e^+e^- pairs for $p_T > 1$ GeV/c is treated as entirely due to internal conversions and as in $p+p$ the mass spectra are fitted with the sum of cocktail and a direct photon component with a $1/m_{ee}$ dependence. An example for $1.0 < p_T < 1.5$ GeV/c is shown in Fig. 4.27. The uncertainty on the η/π^0 ratio is a bit larger than in $p+p$, but the same central value is assumed: 0.48 ± 0.08, which is the more conservative approach, since the actual PHENIX measurement of the ratio Au + Au is ≈ 0.4 with an uncertainty of 11% [13, 115]. This leads to a 17% uncertainty due to the η contribution in the mass range $80 < m_{ee} < 300$ MeV/c^2. As in $p+p$ a fit with a variable η contribution within a η/π^0 ratio of 0.48 ± 0.08 gives consistent results within the statistical uncertainties.

The fraction of direct photons r in min. bias Au + Au is shown as function of p_T in the right panel of Fig. 4.28. It is compared to the NLO pQCD prediction of direct photons for $p+p$ divided by the inclusive photon yield and scaled by the nuclear overlap factor T_{AA} ($T_{AA}\, d\sigma_\gamma^{\text{NLO}}(p_T)/dN_\gamma^{\text{incl}}(p_T)$), which is also shown for the three theory scales $\mu = 0.5p_T$, $1.0p_T$, $2.0p_T$. While the fraction of direct photons measured in $p+p$ was consistent with the NLO prediction, the fraction measured in Au+Au is larger than than the calculation for $p_T < 4$ GeV/c.

As for $p+p$, the fraction of direct photons r is converted into a direct photon yield by multiplying with the inclusive photon yield. The inclusive photon yield is determined for each p_T bin by $dN_\gamma^{\text{incl}} = dN_{ee}^{\text{data}} \times dN_\gamma^{\text{cocktail}}/dN_{ee}^{\text{cocktail}}$, where dN_{ee}^{data} and $dN_{ee}^{\text{cocktail}}$ are the yields of e^+e^- pairs in $m < 30$ MeV/c^2

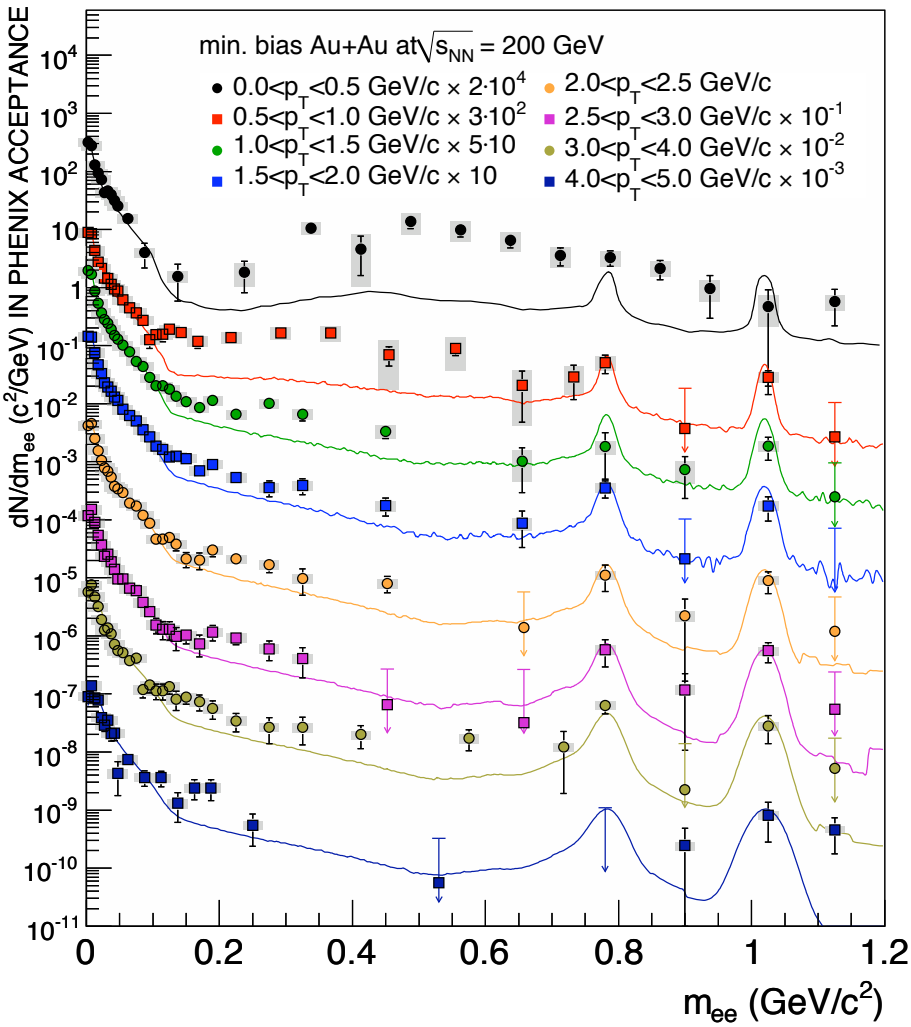

Figure 4.24: The e^+e^- pair invariant mass distributions in Au + Au collisions. The p_T ranges are shown in the legend. The solid curves represent an estimate of hadronic sources.

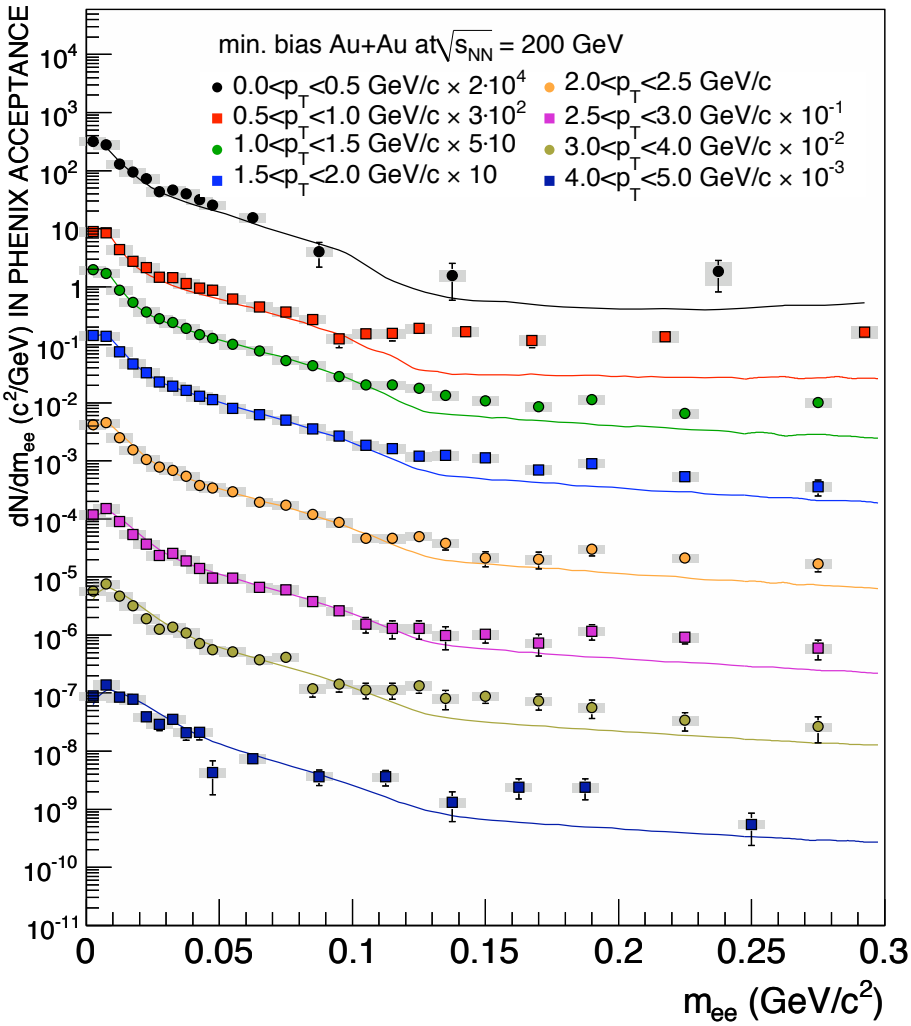

Figure 4.25: The e^+e^- pair invariant mass distributions in Au + Au collisions. The p_T ranges are shown in the legend. The solid curves represent an estimate of hadronic sources. This is a zoomed version of Fig. 4.24.

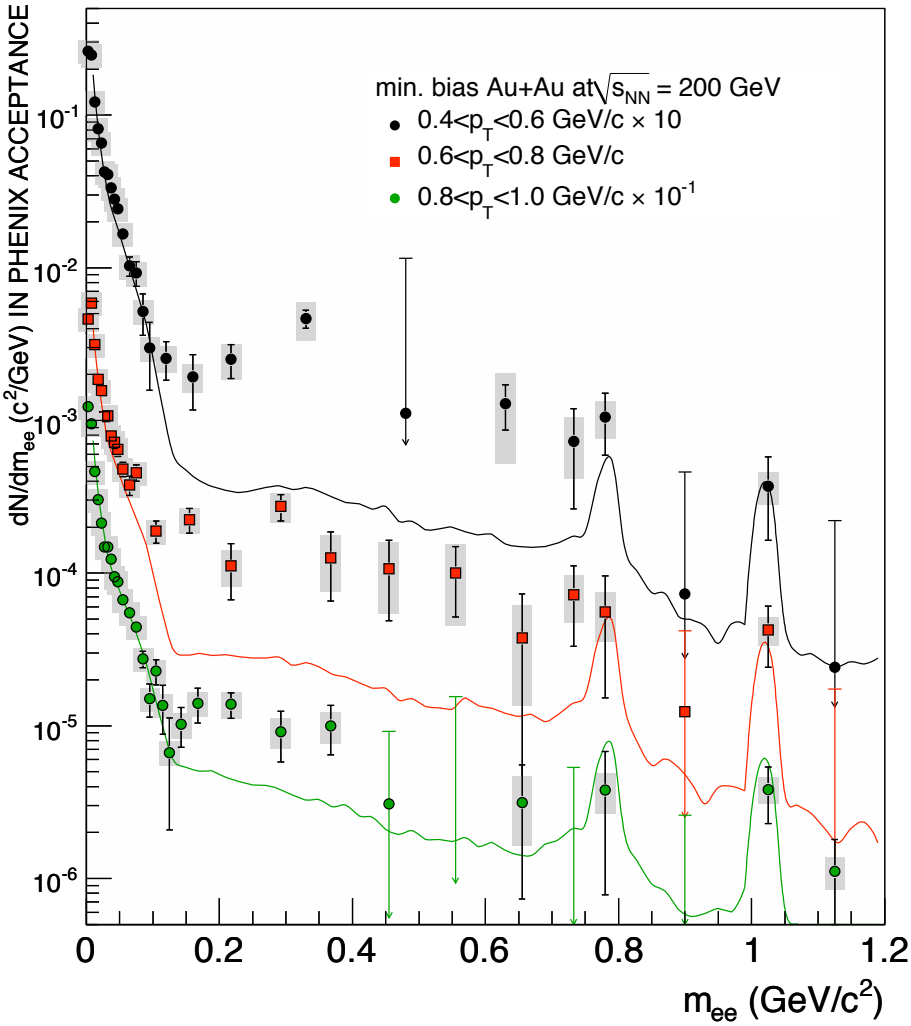

Figure 4.26: The e^+e^- pair invariant mass distributions in Au + Au collisions for the low p_T range. The solid curves represent an estimate of hadronic sources.

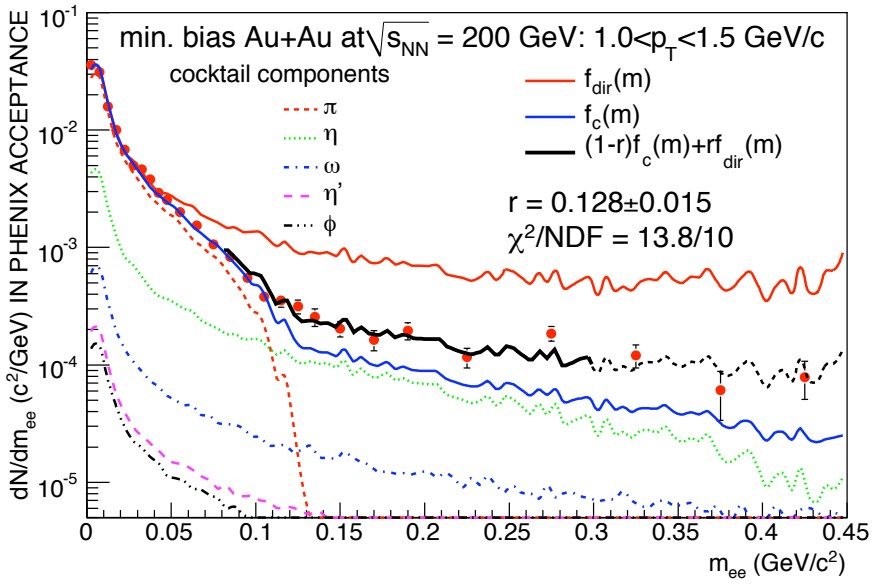

Figure 4.27: Invariant mass distribution of e^+e^- pairs in Au + Au collisions with $1.0 < p_T < 1.5$ GeV/c. The fit with Eq. (4.3) in the range $80 < m_{ee} < 300$ MeV/c^2 is explained in the text. The *black dashed* curve shows $f(m_{ee})$ outside of the fit range.

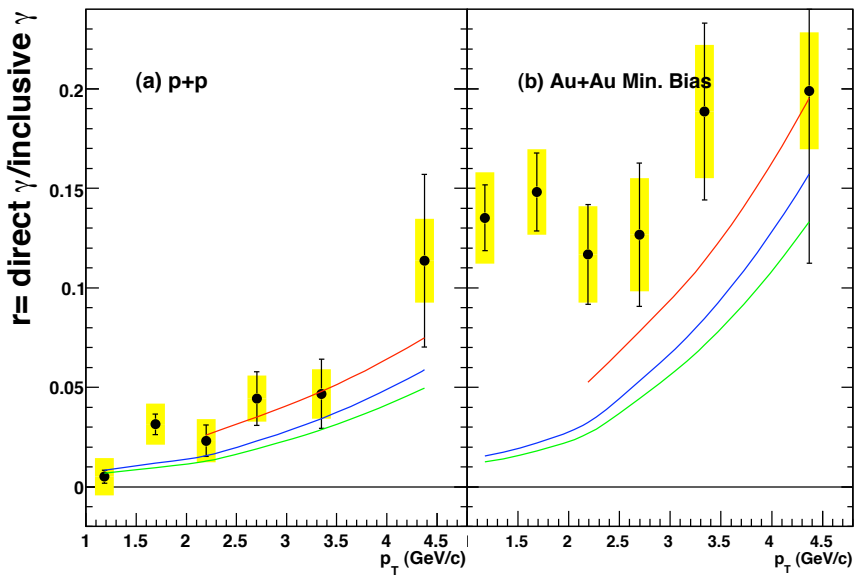

Figure 4.28: The fraction of direct photons as function of p_T in (a) $p + p$ and (b) Au + Au collisions. The error bars and the error band represent statistical and systematic uncertainties, respectively. The curves show the direct photon prediction of a NLO pQCD calculation.

Table 4.2: Summary of the fits with Eq. (4.5) to the direct photon spectra measured in Au + Au at $\sqrt{s_{NN}}$ = 200GeV. The first and second errors are statistical and systematical, respectively.

Centrality	$dN/dy(p_T > 1$ GeV$/c)$	T (MeV)	χ^2/DOF
0–20%	1.10 ± 0.20 ± 0.30	221 ± 23 ± 18	3.6/4
20–40%	0.52 ± 0.08 ± 0.14	214 ± 20 ± 15	5.2/3
MB	0.33 ± 0.04 ± 0.09	224 ± 16 ± 19	0.9/4

for data and cocktail, respectively, and $dN_\gamma^{\text{cocktail}}$ is the yield of photons from the cocktail. The resulting direct photon spectrum for 0–20%, 20–40% and minimum bias Au+Au collisions is shown in Fig. 4.29 together with the direct photon cross section measured in $p+p$ collisions. At high p_T the direct photon spectrum is extended by the EMCal measurement of direct photons [40, 45], which show good agreement with the NLO calculation. It is worth to point out the significant improvement of the systematic uncertainties by the internal conversion method with respect to the EMCal measurement

The measured direct photon yield in Au + Au is above the $p + p$ fit to Eq. (4.4) scaled by T_{AA} for $p_T < 2.5$ GeV$/c$, which indicates the the direct photon yield at low p_T increases faster than the binary scaled $p + p$ cross section. To quantify this excess, an exponential plus a modified power-law are fit to the Au + Au data. The power-law is fixed to the T_{AA} scaled $p + p$ fit:

$$\frac{1}{2\pi p_T}\frac{d^2N}{dp_T\,dy} = A\,\mathrm{e}^{-p_T/T} + T_{AA} \times A_{pp}\left(1 + \frac{p_T^2}{p_0}\right)^{-n} \tag{4.5}$$

The inverse slope of the exponential T and the A are the only free parameters. The systematic uncertainties of this fit are estimated by changing the $p + p$ fit parameters within the uncertainties. The results are summarized in Tab. 4.2, for which the fit result of A has been converted into a rapidity density $dN/dy(p_T > 1$ GeV$/c)$. For the most central collision an inverse slope of $T = 221 \pm 23 \pm 18$ MeV is found. If the direct photons in Au + Au collisions are of thermal origin, the inverse slop T is related to the initial temperature T_{init} of the dense matter. In thermal models, T_{init} is 1.5–3 times T due to the space-time evolution [143]. Comparisons to a few models are shown in Section 4.3.1.

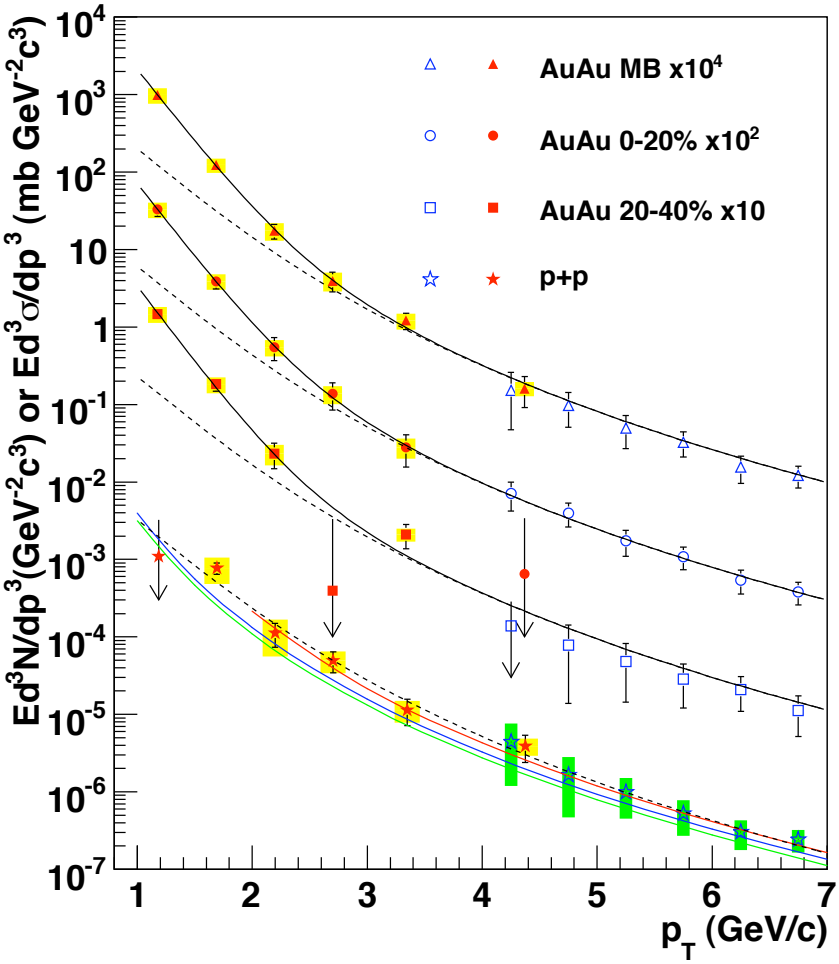

Figure 4.29: Invariant cross section ($p+p$) and invariant yield (Au + Au) of direct photons as function of p_T. The *filled* point are from this analysis and the *open* points are from [40, 45]. The three curves on the $p+p$ data represent the NLO pQCD calculation of direct photons, the *dashed* curves show a power-law fit to the $p+p$ data, scaled by T_{AA}. The *solid black* curves are exponential plus T_{AA} scaled $p+p$ fit.

4.2.4 p_T of the Low Mass Enhancement

As shown in Fig. 4.24, the dominant fraction of the low mass enhancement is localized at low p_T. Clearly, in this region the approximation $m_{ee} \ll p_T$ does not hold any longer, and consequently $S \neq 1$. Therefore, the excess in this mass and p_T range cannot be analyzed rigorously under the assumption of internal conversions of direct photons as done at high p_T in the previous chapter.

The invariant yield of e^+e^- pairs as function of p_T is calculated as defined in Eq. (3.24) and compared to the cocktail of hadronic and charmed meson decays for various mass ranges in Fig. 4.30. The systematic uncertainties are dominated by the background subtraction which contributes as $\sigma_S/S = 0.25\% B/S$. As the signal to background ratio improves towards high p_T, the systematic uncertainties decrease. For the mass ranges below 400 MeV/c^2 the data are cut at low p_T due to the single electron p_T cut at 200 MeV/c^2.

In the mass region $m_{ee} < 100$ MeV/c^2 the Au + Au data are in agreement with the cocktail, as expected. In the higher mass bins, the data show a large excess both at low and high p_T. At high p_T this excess has been interpreted as direct photons in the previous chapter. The p_T spectra of direct photons have been successfully described with the functional form given in Eq. (4.5) an the fit values in Tab. 4.2. The yield of direct photons can be converted into a yield of e^+e^- pairs in a mass range $m_1 < m_{ee} < m_2$ according to Eq. (1.23):

$$\begin{aligned}
\frac{1}{2\pi p_T}\frac{d^2N_{ee}}{dp_T\,dy} &= \frac{1}{2\pi p_T}\frac{d^2N_\gamma}{dp_T\,dy}\int_{m_1}^{m_2}\frac{2\alpha}{3\pi}\frac{1}{m_{ee}}\sqrt{1-\frac{4m_e^2}{m_{ee}^2}}\left(1+\frac{2m_e^2}{m_{ee}^2}\right)S\,dm_{ee} \\
&= A\,\mathrm{e}^{-p_T/T} + T_{AA}\times A_{pp}\left(1+\frac{p_T^2}{p_0}\right)^{-n} \\
&\quad\cdot\int_{m_1}^{m_2}\frac{2\alpha}{3\pi}\frac{1}{m_{ee}}\sqrt{1-\frac{4m_e^2}{m_{ee}^2}}\left(1+\frac{2m_e^2}{m_{ee}^2}\right)
\end{aligned} \tag{4.6}$$

As previously, the distributions of direct photons and cocktail are normalized to the data in the mass range $m_{ee} < 30$ MeV/c^2, where both have nearly identical shapes. The extension of the direct photon contribution to lower p_T is done using the suppression factor S for quark-gluon Compton scattering

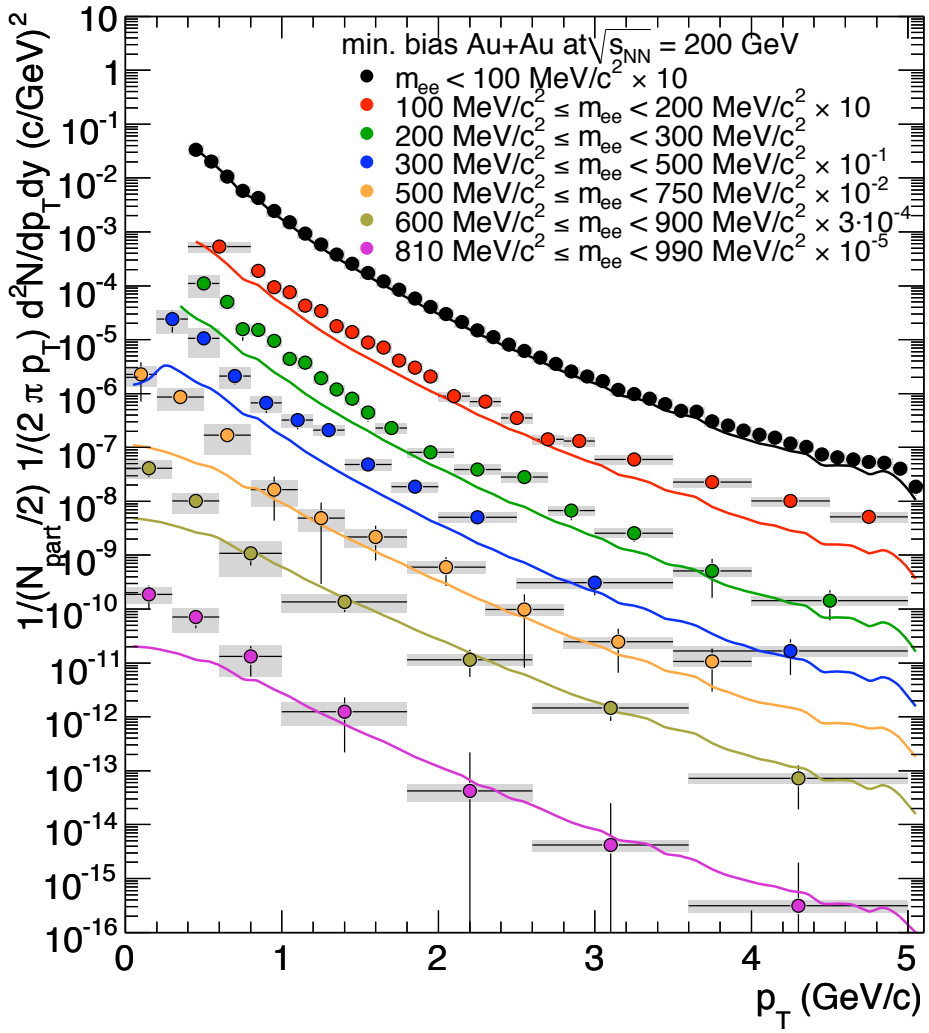

Figure 4.30: Shown is the invariant yield of e^+e^- pairs in different mass ranges in min. bias Au + Au collisions. The mass ranges are defined in the legend.

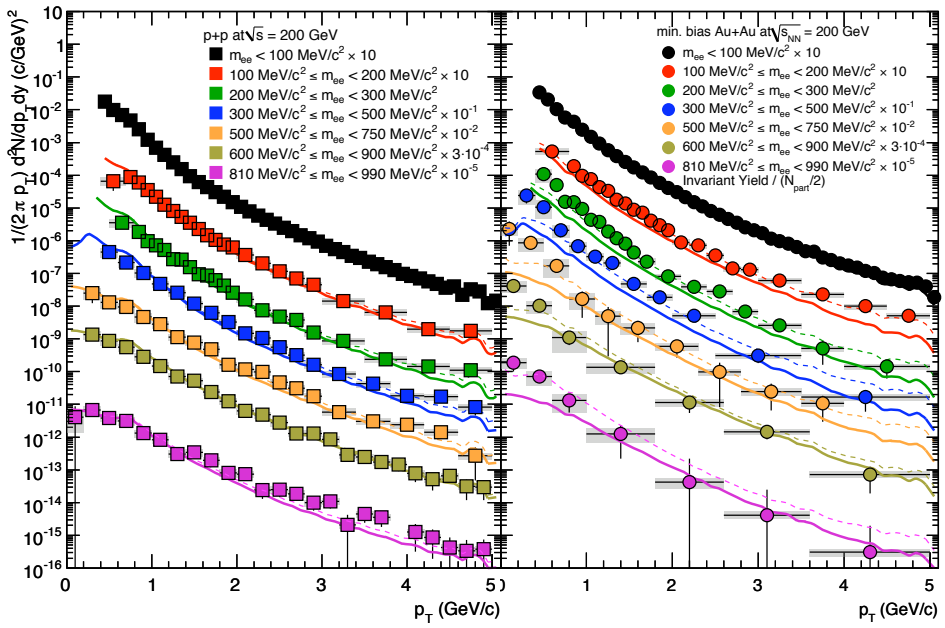

Figure 4.31: Shown is the invariant yield of e^+e^- pairs in different mass ranges in $p+p$ (left) min. bias Au + Au collisions (right). The mass ranges are defined in the legend. The data are compared to the cocktail from hadronic decays (*solid line*) and the sum of hadronic cocktail and direct photons (*dashed line*).

defined in Eq. (1.26):

$$\begin{aligned} S &= 1 + \frac{2u}{t^2+s^2} m_{ee}^2 \\ &= 1 - \frac{2x}{(x+\sqrt{1+x^2})(3x^2+1+2x\sqrt{1+x^2})} \end{aligned} \tag{1.26}$$

with $x = p_T/m_{ee}$. This contribution is added to the cocktail and the sum is shown as dashed line in Fig. 4.31, which shows the p_T spectra of e^+e^- pairs in both $p+p$ and Au+Au collisions. The excess at at $p_T \gtrsim 1$ GeV/c with respect to the hadronic cocktail agrees with the sum of cocktail and direct photons. For the mass range 100–300 MeV/c^2 this is of course redundant, as the excess in exactly this region of phase space had been used to measure this direct photon component, but also above 300 MeV/c^2 the excess at $p_T > 1$ GeV/c is in good agreement with a direct photon contribution.

At low p_T, however, a significant excess beyond the extrapolated direct photon contribution remains in the Au + Au data. This excess increases in strength towards low p_T, despite the restriction on the single electrons to have at least a transverse momentum of $p_T > 0.2$ GeV/c to be fall within

the PHENIX acceptance. This trend is quite remarkable and opposite to the behavior of the cocktail component. It is also reminiscent of the steepening of the m_T spectra of the dimuon excess yield measured by NA60 [78] (also see Section 1.3.3). To further study the low p_T excess, the spectra are combined to a one mass range of $300 < m_{ee} < 750$ MeV/c^2.

In Ref. [124] PHENIX has measured that the differential cross section of charged hadrons ($\pi^{\pm}$, $K^{\pm}$, p, and $\overline{p}$) in Au + Au collisions at $\sqrt{s_{NN}} = 200$ GeV can be described by an exponential in $m_T - m_0$, where m_0 is the particle mass, and $m_T = \sqrt{p_T^2 + m_0^2}$. This is also known from lower beam energies for $p+p$, $p+A$, and $A+A$ collisions. Such an exponential shape of the invariant yield can be parameterized as:

$$\frac{1}{2\pi m_T}\frac{d^2N}{dm_T\,dy} = \frac{1}{2\pi T(T_{\text{eff}} + m_0)}\,A\,\exp\left(-\frac{m_T - m_0}{T_{\text{eff}}}\right) \tag{4.7}$$

where T_{eff} denotes the inverse slope or effective temperature, and A is a normalization parameter which is related to the rapidity density dN/dy. It has been observed that the inverse slope increases with the particle mass, which is consistent with a hydrodynamical description of particle emission from a source with transverse flow [144–148]. Under such conditions the measured effective temperature T_{eff} is blue shifted with respected to the freeze out temperature T_{fo}:

$$T_{\text{eff}} = T_{\text{fo}} + m\langle\beta_T\rangle^2. \tag{4.8}$$

where $\langle\beta_T\rangle$ is a measure of the strength of the transverse flow. The inverse slopes measured for kaons are larger then 200 MeV for all centralities. Together with the effective temperatures measured for charged pions, protons, and antiprotons a centrality independent freeze out temperature of ≈ 180 MeV has been extracted [124].

Following this approach to characterize the low p_T excess, the p_T spectrum of e^+e^- pairs with $300 < m_{ee} < 750$ MeV/c^2 is fitted with the sum of hadronic cocktail, direct photons and an m_T exponential as defined in Eq. (4.7). The direct photon contribution to the cocktail at low p_T is 10% at $m_{ee} = 0$, which leads to equal contribution of cocktail and direct photon in the fitted mass range. The total contribution of cocktail and direct photons is fixed by the normalization to the data in $m_{ee} < 30$ MeV/c^2.

The p_T spectrum and the fit result are shown in Fig. 4.32, together with the individual components. The data are well reproduced by the fit which gives an inverse slope of $T_{\text{eff}} = 88 \pm 11(\text{stat.})^{+8}_{-13}(\text{syst.})$ MeV with a $\chi^2/DOF \approx 1$. The systematic uncertainty accounts for the uncertainty on the data and the uncertainty on the cocktail normalization (20%). The yield attributed to the

exponential accounts for more than 50% of the total e^+e^- yield.

If the source of this excess is due to thermal radiation from the fireball, which is dominated by $\pi\pi$ annihilation, the excess yield in the LMR should exhibit a similar mass dependent effective temperature due to transverse flow as the hadrons. The effective temperature is significantly lower than for any of the identified hadron spectra [124]. In particular the kaon, with a mass comparable to the average invariant mass of the e^+e^- pairs in the fitted mass region, has an effective temperature more than twice as large. This seems to advocate a source of dielectrons that does not exhibit the rise with mass typical for a radially expanding source. Also the temperature extracted from the direct photons at high p_T ($T_{\text{eff}} = 221 \pm 23(\text{stat.}) \pm 18(\text{syst.})$ MeV) is significantly larger than the one of the excess yield at low p_T.

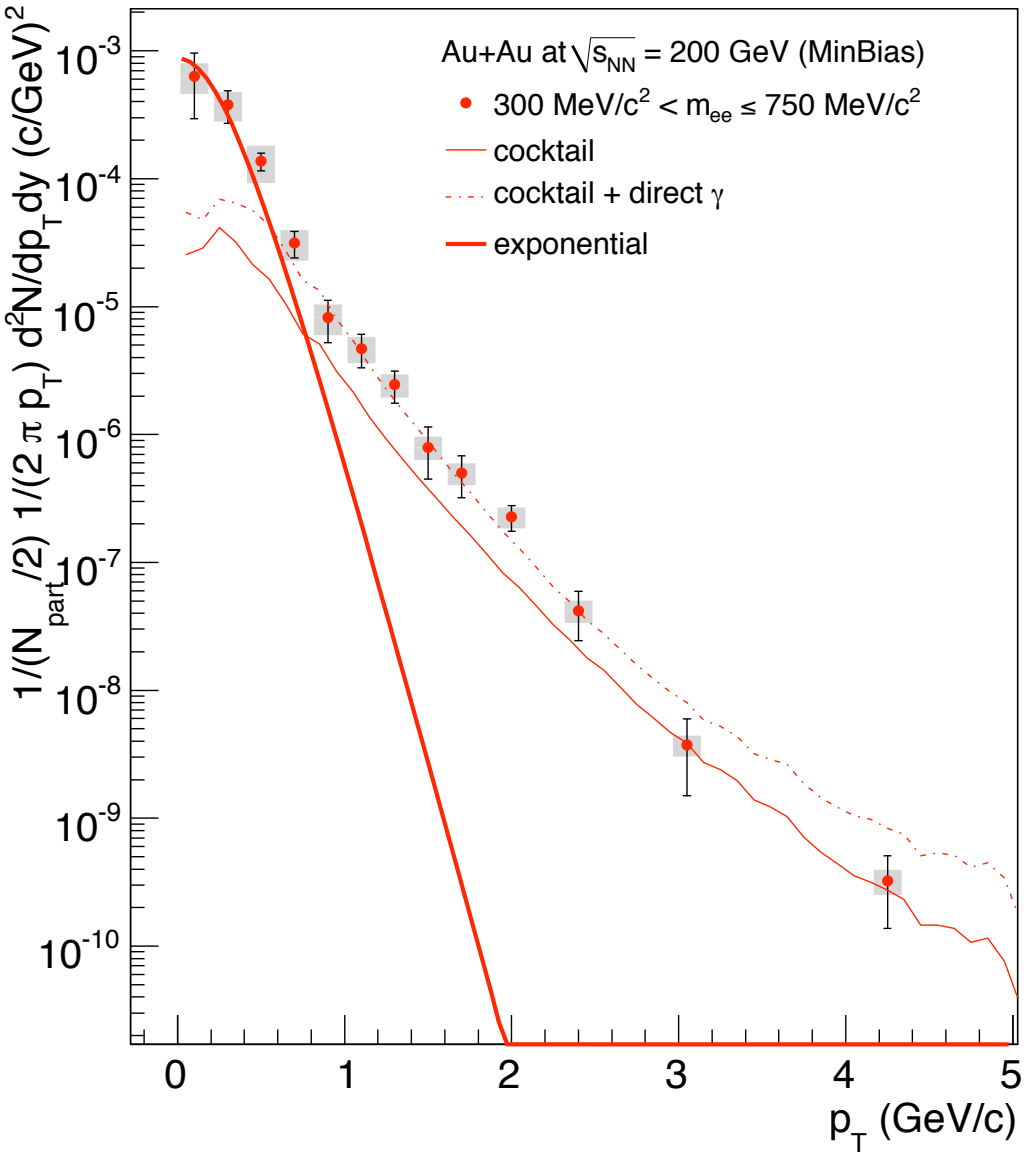

Figure 4.32: The figure shows p_T spectra for the mass range $300 < m_{ee} < 750$ MeV/c^2. The spectrum is fitted to the sum of the cocktail expectation (*thin line*), direct photons and an exponential function in m_T (*thick line*). The cocktail include contributions from charmed mesons. The *dashed line* shows the expectation from the cocktail plus the direct photon contribution. The exponential function is also shown.

Table 4.3: The initial Temperature T_{init} and formation time τ_0 for various models predictions of thermal photons in Au + Au collisions at $\sqrt{s_{NN}} = 200$ GeV.

	T_{init} (MeV)	τ_0 fm/c	notes
David d'Enterria *et al.*	590	0.15	[143]
Rasanen *et al.*	580	0.17	[149, 153]
Srivastava	450–600	0.2	[150, 154]
Turbide*et al.*	370	0.33	[48]
L. Liu *et al.*	370	0.6	[152]
J. Alam *et al.*	300	0.5	[151]

4.3 Model Comparisons

In this section the enhanced production of direct photons and the low mass enhancement of the dielectron continuum observed in Au + Au collisions are compared to theoretical models

4.3.1 Thermal Photons

In Fig. 4.33 the direct photon spectrum measured in 0–20% Au + Au collisions is compared to a number of hydrodynamical models [48, 143, 149–152]. All of these models are in good agreement with the data, and with each other within a factor of two. This fact is quiet remarkable as the initial temperature and formation times of these models vary in the range of $T_{\text{init}} = 300$ MeV, $\tau_0 = 0.6$ fm/c to $T_{\text{init}} = 600$, $\tau_0 = 0.6$ fm/c. Tab. 4.3 lists the initial conditions of all the models mentioned here. They are also shown as pairs of $(T_{\text{init}}, \tau_0)$ in Fig. 4.34, which illustrates the apparent anti-correlation between the formation time τ_0 and the initial temperature T_{init} which produces time averaged direct photon spectra all in agreement with the data.

The general good agreement of the hydrodynamical models with the data confirms that the p_T range of 1–3 GeV/c is dominated by thermal radiation. To disentangle the details of the initial condition and the hydrodynamic evolution of the system more detailed studies will be necessary.

4.3.2 Low mass dileptons

While the excess of direct photons produced in Au + Au collision in comparison to $p + p$ seems to be qualitatively explained by thermal radiation from a medium with temperatures of 300–600 MeV, the situation for the low mass

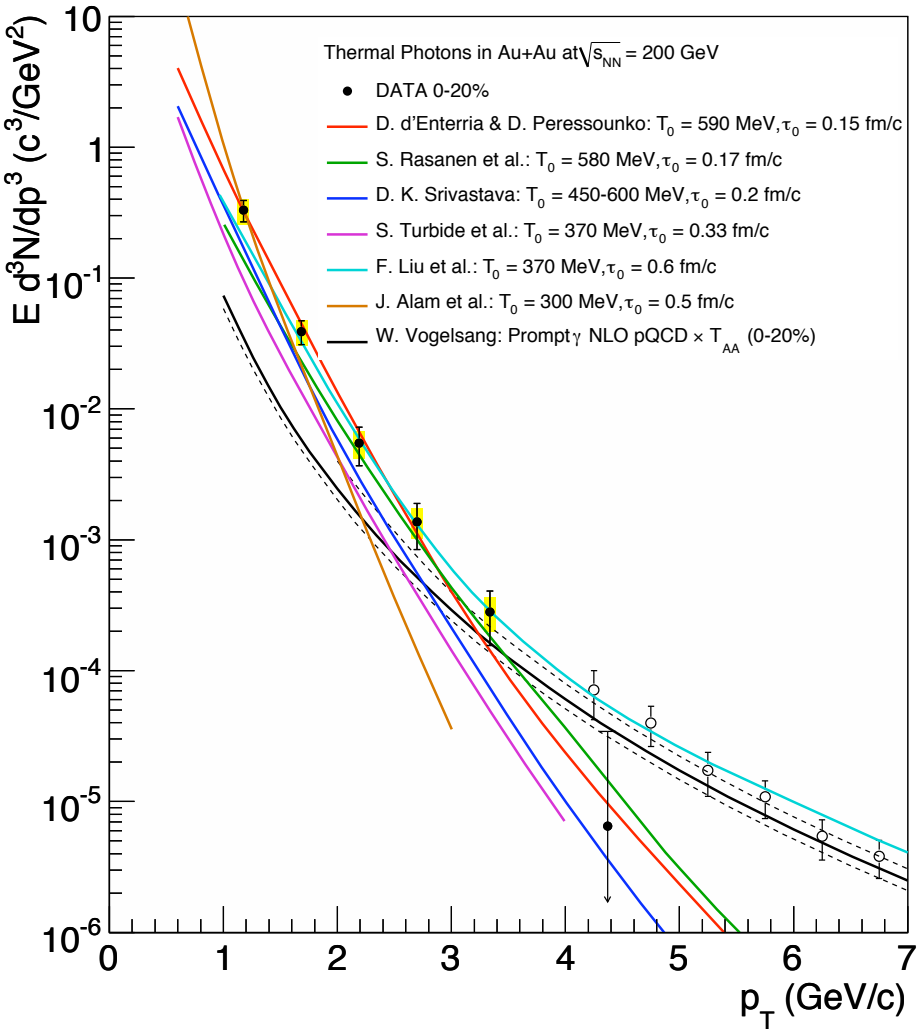

Figure 4.33: Comparison of direct photon yield Au + Au to theoretical predictions [48, 143, 149–152]. Note that the *cyan* curve by Liu *et al.* has a pQCD contribution included, while all other model curves only show the thermal contribution. For a comparison to the data above 3 GeV/c a pQCD contribution, *e. g.* the one shown by W. Vogelsang [41, 138] needs to be added.

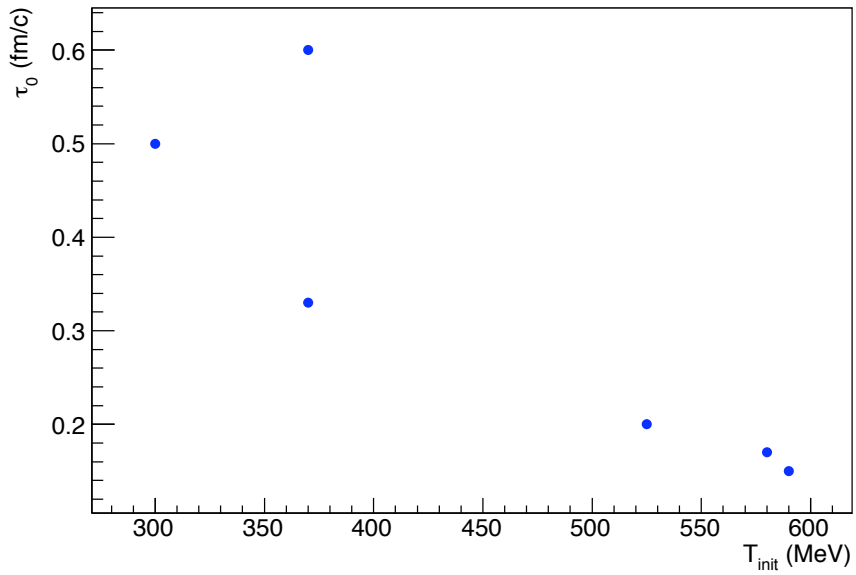

Figure 4.34: Comparison of formation time τ_0 and initial temperature T_{init} of the thermal photon predictions.

enhancement of dielectrons of the expected cocktail of hadron decays is quiet different.

In Fig. 4.35 the LMR of the dielectron continuum in min. bias Au + Au collision at $\sqrt{s_{NN}} = 200$ GeV is compared to a number of predictions involving different scenarios for in-medium modifications of the vector mesons by R. Rapp and H. van Hees [54], K. Dusling and I. Zahed [155], and E. L. Bratkovskaya and W. Cassing [156]. As discussed in Section 1.3, an expanding fireball model with a modified in-medium spectral function by R. Rapp successfully describes the dilepton spectra measured by CERES (see Fig. 1.24) and NA60 (see Fig. 1.26b) [80]. Also the other authors find good agreement of their models with NA60[156, 157]. Both, Rapp and Dusling include a contribution from $q\overline{q}$ annihilation during the QGP phase in their predictions which, however, is important only in the intermediate mass range.

Predictions for different ρ spectral functions (vacuum, dropping mass, and collisional broadening) are filtered into the PHENIX acceptance and added to the hadronic cocktail which beforehand has its vacuum ρ contribution subtracted as this is yield is part of the prediction. The results by R. Rapp [54] are shown as blue lines in Fig. 4.35, the vacuum rho is shown as *dashed*, the dropping ρ as *dotted* and the broadening scenario (for which the ρ spectral function was shown in Fig. 1.21) as *solid* line. The predictions are in agreement with the

data within the systematic uncertainties for $m_{ee} \gtrsim 0.5$ MeV/c^2, but clearly do not provide enough yield in the mass range $150 \lesssim m_{ee} \lesssim 0.5$ MeV/c^2 to describe the data. All three scenarios have in common a sharp drop of the ρ spectral function below $m_{ee} < 2m_\pi$, something that is not observed in data. In data the enhancement stays at an almost constant level down to $m_{ee} \approx 100$ MeV/c^2.

Also the hydrodynamic calculation by K. Dusling is able to describe the NA60 data [157] with dilepton rates following from a chiral virial expansion [158], does not describe the low mass enhancement below ≈ 600 MeV/c^2, as shown with the *red solid* line in Fig. 4.35.

The third theoretical calculation by E. L. Bratkovskaya [156] which is based on a microscopic HSD (Hadron String Dynamics) transport model [159] provides two scenarios, one is a collisional broadening of the ρ meson, the other includes in addition a drop of the ρ mass. They are shown in Fig. 4.35 as *solid* green and *dashed* green line, respectively. As the other model calculations, also this does not account for the enhancement observed below 600 MeV/c^2.

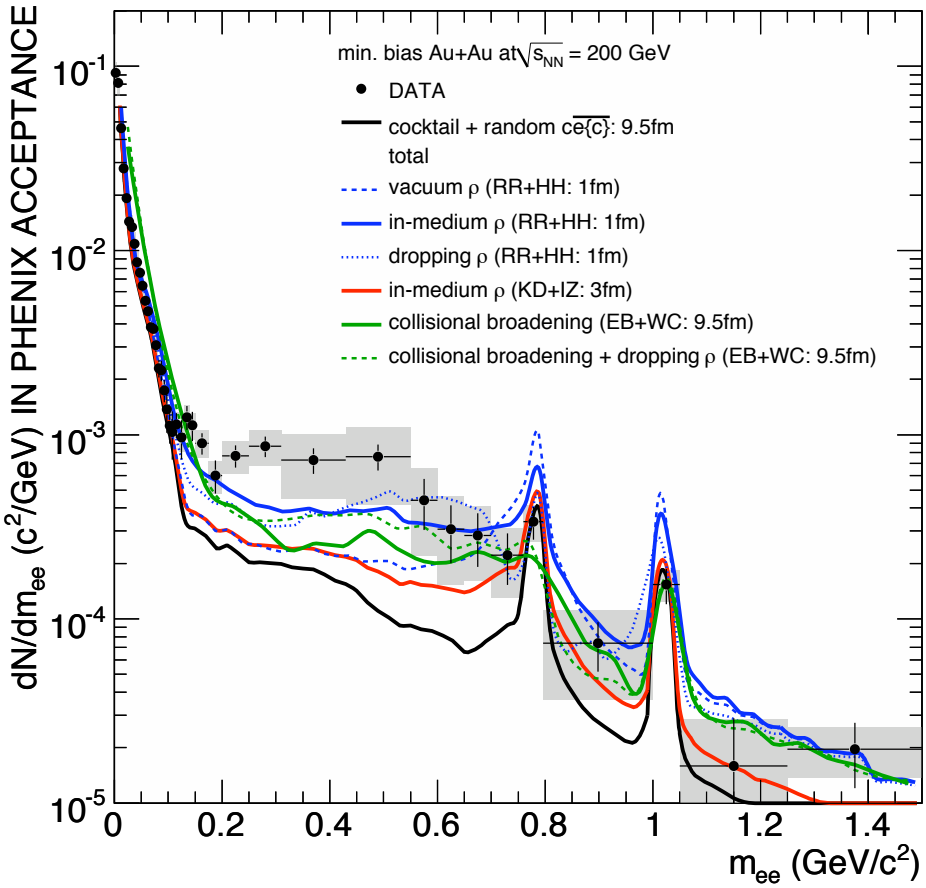

Figure 4.35: Invariant mass distribution of e^+e^- pairs in min. bias Au + Au collisions compared to theoretical predictions including dropping mass and broadening scenarios by Rapp and Hees [54], Dusling and Zahed [155], Bratkovskaya and Cassing [156].

Chapter 5

Summary and Outlook

This thesis has presented the analysis of the dielectron continuum in $p + p$ collisions at $\sqrt{s} = 200$ GeV which allowed to extract a variety of physics signals: The measurement of the total charm and bottom cross section in the intermediate and high mass region ($\sigma_{c\bar{c}} = 544 \pm 39(\text{stat.}) \pm 142(\text{syst.}) \pm 200(\text{model})$ μb and $\sigma_{b\bar{b}} = 3.9 \pm 2.4(\text{stat.})^{+3}_{-2}(\text{syst.})$ μb), the differential cross section measurement of ω and ϕ mesons and the p_T dependence of the low mass dielectron continuum. A detailed study of the spectral shape in the mass region $100 < m_{ee} < 300$ MeV/c^2 resulted in the measurement of direct photons via internal conversions in the p_T range of $1 < p_T < 5$ GeV/c which is consistent to NLO pQCD prediction.

These results provide an important baseline for any measurement of the dielectron continuum in heavy ion collisions. As part of this thesis a discussion of the dielectron continuum measured in Au + Au collisions has been given. The results can be summarized briefly as follows: a dielectron yield is observed in the mass range $150 < m_{ee} < 750$ which is enhanced by a factor of $4.0 \pm 0.3(\text{stat.}) \pm 1.5(\text{syst.}) \pm 0.8(\text{model})$ in min. bias Au + Au collisions with respect to the expected contribution from hadron decays and semi-leptonic charm decays. This enhancement is localized in central collisions and is absent in $p+p$ and peripheral collisions. It increases faster than linear with N_{part} and is moreover localized at low p_T. The p_T dependence of the enhancement has an inverse slope of $T_{\text{eff}} = 88 \pm 11(\text{stat.})^{+8}_{-13}(\text{syst.})$ MeV and does not show any signs of radial flow. The concentration of the enhancement at low p_T is qualitatively consistent with results from SPS experiments [70, 78], but the missing evidence for radial flow and the very small effective temperatures seem to indicate some differences to the observations at SPS. This becomes more evident when comparing the enhancement with current models of in-medium modifications to the ρ meson which are able to explain the SPS results with collisional broadening of the ρ [80, 156, 157], but fail to give a complete description of the

enhancement observed at RHIC. The measurement of direct photons via internal conversions at high p_T shows an excess compared to the $p+p$ measurement. This excess has an inverse slope of $T_{eff} = 221 \pm 23(\text{stat.}) \pm 18(\text{syst.})$ MeV in 0–20% most central collisions and can be described by hydrodynamical models with an initial temperature in the range of $300 \leq T_{\text{init}} \leq 600$ MeV at formation times of $0.12 \leq \tau_0 \leq 0.6$ fm/c as thermal radiation.

With upcoming data taking periods and the expected increases in luminosity, one of the most interesting regions, besides a more quantitative analysis of the low mass enhancement, will be the intermediate mass region. Currently, the statistics available in $\text{Au} + \text{Au}$ does not allow to distinguish thermal from open charm contributions, but with more statistics a study of the p_T dependence of the IMR may provide new opportunities. This is equally true for the study of $p + p$ collisions. The comparison of the measured p_T spectrum of the IMR and leading-order PYTHIA calculations suggests that higher order processes will need to be considered at high p_T and invariant masses. With more statistics to come the high mass region beyond the J/ψ will allow more precise measurements of the bottom cross section. The Silicon Vertex Detector (VTX) upgrade [160] will accurately measure the collision vertex as well as secondary decay vertices. This will tremendously improve the open heavy flavour measurement, as it will allow to differentiate between prompt decays and the off-vertex decays of charmed and bottom meson.

Returning to the low mass region, it may be possible (at least in $p + p$) to measure low momentum η via their Dalitz decays by combining e^+e^- pairs with $100 < m_{ee} < 500$ with photons measured in the calorimeter. This would be very analog to the beam pipe conversion analysis presented in Appendix B.2. A low momentum η measurement would significantly reduce the uncertainties on the hadronic cocktail and may, together with a good understanding of the open charm background, lead the way to a measurement of the ω form factor in $p + p$ collisions at $\sqrt{s_{NN}} = 200$ GeV.

The Hadron Blind Detector (HBD) upgrade [97] should significantly improve the signal-to-background ratio of any low mass dielectron analysis, by identifying e^+e^- pairs with small opening angle as originating from π^0 Dalitz decays and photon conversion in a magnetic field free region surrounding the beam pipe. The HBD is a windowless proximity-focusing Cherenkov detector with a radiator length of 50 cm operating in pure CF_4 as radiator and detector gas. Cherenkov photons emitted by electrons create photoelectrons in a CsI photocathode, which are avalanched by a triple stack of Gas Electron Multipliers (GEM) and read out by PCB boards. The operation in a reverse bias mode together with a shielding mesh above the photocathode makes the HBD blind to minimum ionizing particles, *i. e.* hadron blind, as their charge is

collected on the mesh. e^+e^- pairs from π^0 Dalitz decays or photon conversions with small opening angle will produce overlapping avalanches which could be identified by their signal height compared to avalanches from single electrons.

Bibliography

[1] E. V. Shuryak, *Quark-Gluon Plasma and Hadronic Production of Leptons, Photons and Psions*, Phys. Lett. **B78**, 150 (1978).

[2] F. Karsch, *Lectures on Quark Matter* (Springer, Berlin, Germany, 2002), vol. 583 of *Lecture Notes in Physics*, chap. Lattice QCD at high temperature and density, pp. 209–249, ISBN 978-3-540-43234-0, *Preprint* arXiv:hep-lat/0106019.

[3] R. Rapp and J. Wambach, *Adv. Nucl. Phys.* (Springer, New York, USA, 2000), vol. 25 of *Advances in Physics of Particles and Nuclei*, chap. Chiral Symmetry Restoration and Dileptons in Relativistic Heavy-Ion Collisions, pp. 1–205, ISBN 978-0-306-46440-9, and references therein, *Preprint* arXiv:hep-ph/9909229.

[4] P. Braun-Munzinger and J. Stachel, *Dynamics of ultra-relativistic nuclear collisions with heavy beams: An experimental overview*, Nucl. Phys. **A638**, 3c (1998), *Preprint* arXiv:nucl-ex/9803015.

[5] P. Braun-Munzinger, K. Redlich, and J. Stachel, *Particle production in heavy ion collisions* (2003), *Preprint* arXiv:nucl-th/0304013.

[6] P. Braun-Munzinger, J. Stachel, J. P. Wessels, and N. Xu, *Thermal and hadrochemical equilibration in nucleus-nucleus collisions at the SPS*, Phys. Lett. **B365**, 1 (1996), *Preprint* arXiv:nucl-th/9508020.

[7] P. Braun-Munzinger, D. Magestro, K. Redlich, and J. Stachel, *Hadron production in Au-Au collisions at RHIC*, Phys. Lett. **B518**, 41 (2001), *Preprint* arXiv:hep-ph/0105229.

[8] I. Arsene *et al.* (BRAHMS Collaboration), *Quark-gluon plasma and color glass condensate at RHIC? The perspective from the BRAHMS experiment*, Nucl. Phys. **A757**, 1 (2005), *Preprint* arXiv:nucl-ex/0410020.

[9] K. Adcox *et al.* (PHENIX Collaboration), *Formation of dense partonic matter in relativistic nucleus nucleus collisions at RHIC: Experimental evaluation by the PHENIX Collaboration*, Nucl. Phys. **A757**, 184 (2005), *Preprint* arXiv:nucl-ex/0410003.

[10] B. B. Back *et al.* (PHOBOS Collaboration), *The PHOBOS perspective on discoveries at RHIC*, Nucl. Phys. **A757**, 28 (2005), *Preprint* arXiv:nucl-ex/0410022.

[11] J. Adams *et al.* (STAR Collaboration), *Experimental and theoretical challenges in the search for the quark-gluon plasma: The STAR Collaboration's critical assessment of the evidence from RHIC collisions*, Nucl. Phys. **A757**, 102 (2005), *Preprint* arXiv:nucl-ex/0501009.

[12] K. Adcox *et al.* (PHENIX Collaboration), *Suppression of Hadrons with Large Transverse Momentum in Central Au + Au Collisions at* $\sqrt{s_{NN}}$ *= 130 GeV*, Phys. Rev. Lett. **88**, 022301 (2002), *Preprint* arXiv:nucl-ex/0109003.

[13] S. S. Adler *et al.* (PHENIX Collaboration), *Common Suppression Pattern of* η *and* π^0 *Mesons at High Transverse Momentum in Au + Au Collisions at* $sqrts_{NN}$ *= 200 GeV*, Phys. Rev. Lett. **96**, 202301 (2006), *Preprint* arXiv:nucl-ex/0601037.

[14] S. S. Adler *et al.* (PHENIX Collaboration), *Nuclear Modification of Electron Spectra and Implications for Heavy Quark Energy Loss in Au + Au Collisions at* $\sqrt{s_{NN}}$ *= 200 GeV*, Phys. Rev. Lett. **96**, 032301 (2006), *Preprint* arXiv:nucl-ex/0510047.

[15] A. Adare *et al.* (PHENIX Collaboration), *Energy Loss and Flow of Heavy Quarks in Au + Au Collisions at* $\sqrt{s_{NN}}$ *= 200 GeV*, Physical Review Letters **98**, 172301 (2007), *Preprint* arXiv:nucl-ex/0611018.

[16] A. Adare *et al.* (PHENIX Collaboration), *Measurement of high-*p_T *Single Electrons from Heavy-Flavor Decays in p+p Collisions at* $\sqrt{s}$ *= 200 GeV*, Phys. Rev. Lett. **97**, 252002 (2006).

[17] S. S. Adler *et al.* (PHENIX Collaboration), *Elliptic Flow of Identified Hadrons in Au + Au Collisions at* $\sqrt{s_{NN}}$ *= 200 GeV*, Phys. Rev. Lett. **91**, 182301 (2003), *Preprint* arXiv:nucl-ex/0305013.

[18] A. Adare *et al.* (PHENIX Collaboration), *Scaling Properties of Azimuthal Anisotropy in Au + Au and Cu + Cu Collisions at* $\sqrt{s_{NN}}$ =

200 GeV, Phys. Rev. Lett. **98**, 162301 (2007), *Preprint* arXiv:nucl-ex/0608033.

[19] S. Afanasiev *et al.* (PHENIX Collaboration), *Elliptic Flow for ϕ Mesons and (Anti)deuterons in $Au + Au$ Collisions at $\sqrt{s_{NN}} = 200$ GeV*, Phys. Rev. Lett. **99**, 052301 (2007), *Preprint* arXiv:nucl-ex/0703024.

[20] R. D. Pisarski, *Phenomenology of the chiral phase transition*, Phys. Lett. **B110**, 155 (1982).

[21] A. Adare *et al.* (PHENIX), *Dilepton mass spectra in $p + p$ collisions at $\sqrt{s} = 200$ GeV and the contribution from open charm* (2008), accepted for publication in Phys. Lett. B, *Preprint* arXiv:0802.0050.

[22] A. Adare *et al.* (PHENIX Collaboration), *Enhanced production of direct photons in $Au + Au$ collisions at $\sqrt{s_{NN}} = 200$ GeV* (2008), submitted to Phys. Rev. Lett, *Preprint* arXiv:0804.4168.

[23] S. Afanasiev *et al.* (PHENIX), *Enhancement of the dielectron continuum in $\sqrt{s_{NN}} = 200$ GeV $Au+Au$ collisions* (2007), submitted to Phys. Rev. Lett., *Preprint* arXiv:0706.3034.

[24] D. J. Gross and F. Wilczek, *Ultraviolet Behavior of Non-Abelian Gauge Theories*, Phys. Rev. Lett. **30**, 1343 (1973).

[25] H. D. Politzer, *Reliable Perturbative Results for Strong Interactions?*, Phys. Rev. Lett. **30**, 1346 (1973).

[26] D. J. Gross and F. Wilczek, *Asymptotically Free Gauge Theories. I*, Phys. Rev. D **8**, 3633 (1973).

[27] H. D. Politzer, *Asymptotic freedom: An approach to strong interactions*, Phys. Rep. **14**, 129 (1974).

[28] C. Itzykson and J. B. Zuber, *Quantum Field Theory*, International Series in Pure and Applied Physics (McGraw-Hill, New York, USA, 1980), 1st ed., ISBN 007-03-2071-3.

[29] W.-M. Yao *et al.*, *Review of Particle Physics*, J. Phys. **G33**, 1 (2006).

[30] J. Goldstone, *Field Theories with Superconductor Solutions*, Nuovo Cim. **19**, 154 (1961).

[31] V. Koch, *Aspects of chiral symmetry*, Int. J. Mod. Phys. **E6**, 203 (1997), *Preprint* arXiv:nucl-th/9706075.

[32] M. Gell-Mann, R. J. Oakes, and B. Renner, *Behavior of Current Divergences under $SU_3 \times SU_3$*, Phys. Rev. **175**, 2195 (1968).

[33] S. Klimt, M. Lutz, and W. Weise, *Chiral phase transition in the SU(3) Nambu and Jona- Lasinio model*, Phys. Lett. **B249**, 386 (1990).

[34] G. Hering, *Dielectron production in heavy ion collisions at 158 GeV/c per nucleon*, Ph.D. thesis, Technische Universität Darmstadt (2001), *Preprint* arXiv:nucl-ex/0203004.

[35] G. E. Brown and M. Rho, *Scaling effective lagrangians in a dense medium*, Phys. Rev. Lett. **66**, 2720 (1991).

[36] C.-Y. Wong, *Introduction to high-energy heavy-ion collisions* (World Scientific, Singapore, Singapore, 1994), 1st ed., ISBN 981-02-0263-6.

[37] D. Acosta *et al.* (CDF Collaboration), *Measurement of Prompt Charm Meson Production Cross Sections in $p\bar{p}$ Collisions at $\sqrt{s}$ = 1.96TeV*, Phys. Rev. Lett. **91**, 241804 (2003), *Preprint* arXiv:hep-ex/0307080.

[38] S. S. Adler *et al.* (PHENIX Collaboration), *Measurement of single muons at forward rapidity in $p+p$ collisions at $\sqrt{s}$ = 200 GeV and implications for charm production*, Phys. Rev. D **76**, 092002 (2007), *Preprint* arXiv:hep-ex/0609032.

[39] M. Cacciari, P. Nason, and R. Vogt, *QCD Predictions for Charm and Bottom Quark Production at RHIC*, Phys. Rev. Lett. **95**, 122001 (2005), *Preprint* arXiv:hep-ph/0502203.

[40] S. S. Adler *et al.* (PHENIX Collaboration), *Measurement of Direct Photon Production in $p+p$ Collisions at $\sqrt{s}$ = 200 GeV*, Phys. Rev. Lett. **98**, 012002 (2007), *Preprint* arXiv:hep-ex/0609031.

[41] L. E. Gordon and W. Vogelsang, *Polarized and unpolarized prompt photon production beyond the leading order*, Phys. Rev. D **48**, 3136 (1993).

[42] L. E. Gordon and W. Vogelsang, *Polarized and unpolarized isolated prompt photon production beyond the leading order*, Phys. Rev. D **50**, 1901 (1994).

[43] P. Aurenche *et al.*, *Prompt Photon Production at Large p(T) in QCD Beyond the Leading Order*, Phys. Lett. **B140**, 87 (1984).

[44] P. Aurenche, R. Baier, M. Fontannaz, and D. Schiff, *Prompt Photon Production at Large p(T) Scheme Invariant QCD Predictions and Comparison with Experiment*, Nucl. Phys. **B297**, 661 (1988).

[45] S. S. Adler *et al.* (PHENIX Collaboration), *Centrality Dependence of Direct Photon Production in $\sqrt{s_{NN}}$ = 200 GeV Au + Au Collisions*, Phys. Rev. Lett. **94**, 232301 (2005), *Preprint* arXiv:nucl-ex/0503003.

[46] S. S. Adler *et al.* (PHENIX Collaboration), *Suppressed π^0 Production at Large Transverse Momentum in Central Au + Au Collisions at $\sqrt{s_{NN}}$ = 200 GeV*, Phys. Rev. Lett. **91**, 072301 (2003), *Preprint* arXiv:nucl-ex/0304022.

[47] G. David, R. Rapp, and Z. Xu, *Electromagnetic probes at RHIC-II*, Phys. Rept. **462**, 176 (2008), *Preprint* arXiv:nucl-ex/0611009.

[48] S. Turbide, R. Rapp, and C. Gale, *Hadronic production of thermal photons*, Phys. Rev. C **69**, 014903 (2004), *Preprint* arXiv:hep-ph/0308085.

[49] H. Gong (PHENIX Collaboration), *Search for direct photons from $\sqrt{s_{NN}}$ = 200 GeV Au + Au collisions using a new π^0 tagging method in the PHENIX experiment at RHIC* (2007), *Preprint* arXiv:0705.1133.

[50] N. M. Kroll and W. Wada, *Internal Pair Production Associated with the Emission of High-Energy Gamma Rays*, Phys. Rev. **98**, 1355 (1955).

[51] L. G. Landsberg, *Electromagnetic decays of light mesons*, Phys. Rep. **128**, 301 (1985).

[52] Y. Akiba, T. Dahms, A. Toia, and Y. Yamaguchi, *Measurement of direct photon via internal conversions in Au+Au and p+p collisions at $\sqrt{s_{NN}}$ = 200 GeV (Final analysis note for PPG086)* (2008), PHENIX Internal Analysis Note 695.

[53] J. J. Sakurai, *Currents and Mesons* (University of Chicago Press, Chicago, USA, 1969), ISBN 978-0-226-73383-8.

[54] R. Rapp, *Thermal lepton production in heavy-ion collisions* (2002), *Preprint* arXiv:nucl-th/0204003.

[55] R. Rapp, *Signatures of thermal dilepton radiation at ultrarelativistic energies*, Phys. Rev. C **63**, 054907 (2001), *Preprint* arXiv:hep-ph/0010101.

[56] J.-e. Alam *et al.*, *Thermal photons and lepton pairs from quark gluon plasma and hot hadronic matter*, Ann. Phys. **286**, 159 (2001), *Preprint* arXiv:hep-ph/9909267.

[57] C. Gale and K. L. Haglin, *Electromagnetic radiation from relativistic nuclear collisions* (2003), *Preprint* arXiv:hep-ph/0306098.

[58] M. Harada and K. Yamawaki, *Hidden local symmetry at loop: A new perspective of composite gauge boson and chiral phase transition*, Phys. Rept. **381**, 1 (2003), *Preprint* arXiv:hep-ph/0302103.

[59] G. E. Brown and M. Rho, *Double Decimation and Sliding Vacua in the Nuclear Many- Body System*, Phys. Rept. **396**, 1 (2004), *Preprint* arXiv:nucl-th/0305089.

[60] A. Adare *et al.* (PHENIX Collaboration), *J/ψ Production versus Centrality, Transverse Momentum, and Rapidity in $Au + Au$ Collisions at $\sqrt{s_{NN}} = 200$ GeV*, Phys. Rev. Lett. **98**, 232301 (2007), *Preprint* arXiv:nucl-ex/0611020.

[61] G. Agakishiev *et al.* (HADES Collaboration), *Study of dielectron production in $C + C$ collisions at 1 AGeV*, Phys. Lett. **B663**, 43 (2008), *Preprint* arXiv:0711.4281.

[62] G. Agakichiev *et al.* (HADES Collaboration), *Dielectron Production in $^{12}C + {}^{12}C$ Collisions at 2 AGeV with the HADES Spectrometer*, Phys. Rev. Lett. **98**, 052302 (2007), *Preprint* arXiv:nucl-ex/0608031.

[63] R. J. Porter *et al.* (DLS Collaboration), *Dielectron cross section measurements in nucleus-nucleus reactions at* 1.0*a gev*, Phys. Rev. Lett. **79**, 1229 (1997).

[64] Y. C. Pachmayer (HADES Collaboration), *Dielectron Production in $C + C$ Collisions at 1 GeV/u and the Solution to the DLS Puzzle* (2008), *Preprint* arXiv:0804.3993.

[65] I. Fröhlich (HADES Collaboration), *Elementary Collisions with HADES* (2007), *Preprint* arXiv:0712.1505.

[66] L. P. Kaptari and B. Kämpfer, *Di-electron bremsstrahlung in intermediate-energy pn and Dp collisions*, Nucl. Phys. **A764**, 338 (2006), *Preprint* arXiv:nucl-th/0504072.

[67] E. L. Bratkovskaya and W. Cassing, *Dilepton production and off-shell transport dynamics at SIS energies*, Nucl. Phys. **A807**, 214 (2008), *Preprint* arXiv:0712.0635.

[68] G. Agakichiev *et al.* (CERES/NA45 Collaboration), *Enhanced Production of Low-Mass Electron Pairs in 200 GeV/Nucleon $S - Au$ Collisions at the CERN Super Proton Synchrotron*, Phys. Rev. Lett. **75**, 1272 (1995).

[69] D. Adamová *et al.* (CERES/NA45 Collaboration), *Enhanced production of low-mass electron-positron pairs in 40-agev pb-au collisions at the cern sps*, Phys. Rev. Lett. **91**, 042301 (2003), *Preprint* arXiv:nucl-ex/0209024.

[70] G. Agakichiev *et al.* (CERES/NA45 Collaboration), *e^+e^--pair production in $Pb - Au$ collisions at 158 GeV per nucleon*, Eur. Phys. J. **C41**, 475 (2005), *Preprint* arXiv:nucl-ex/0506002.

[71] G. E. Brown and M. Rho, *On the manifestation of chiral symmetry in nuclei and dense nuclear matter*, Phys. Rep. **363**, 85 (2002), *Preprint* arXiv:hep-ph/0103102.

[72] C. Baglin *et al.* (NA38 Collaboration), *The Production of J/ψ in 200-GeV/Nucleon Oxygen Uranium Interactions*, Phys. Lett. **B220**, 471 (1989).

[73] M. C. Abreu *et al.* (NA50 Collaboration), *J/ψ and Drell-Yan cross-sections in $Pb - Pb$ interactions at 158 GeV/c per nucleon*, Phys. Lett. **B410**, 327 (1997).

[74] M. C. Abreu *et al.* (NA38 and NA50 Collaborations), *Dimuon and charm production in nucleus-nucleus collisions at the CERN-SPS*, Eur. Phys. J **C14**, 443 (2000).

[75] R. Shahoyan (NA60 Collaboration), *NA60 results on charm and intermediate mass dimuons' production in $In - In$ 158 GeV A^{-1} collisions*, J. Phys. **G34**, S1029 (2007).

[76] S. Damjanovic (NA60 Collaboration), *Thermal dileptons at SPS energies* (2008), *Preprint* arXiv:0805.4153.

[77] R. Arnaldi *et al.* (NA60 Collaboration), *First Measurement of the ρ Spectral Function in High-Energy Nuclear Collisions*, Phys. Rev. Lett. **96**, 162302 (2006), *Preprint* arXiv:nucl-ex/0605007.

[78] R. Arnaldi *et al.* (NA60 Collaboration), *Evidence for Radial Flow of Thermal Dileptons in High-Energy Nuclear Collisions*, Phys. Rev. Lett. **100**, 022302 (2008), *Preprint* arXiv:0711.1816.

[79] T. Renk and J. Ruppert, *Dimuon transverse momentum spectra as a tool to characterize the emission region in heavy-ion collisions*, Phys. Rev. C **77**, 024907 (2008), *Preprint* arXiv:hep-ph/0612113.

[80] H. van Hees and R. Rapp, *Comprehensive Interpretation of Thermal Dileptons Measured at the CERN Super Proton Synchrotron*, Phys. Rev. Lett. **97**, 102301 (2006), *Preprint* arXiv:hep-ph/0603084.

[81] M. M. Aggarwal *et al.* (WA98 Collaboration), *Observation of Direct Photons in Central 158 $AGeV$ $^{208}Pb+$ ^{208}Pb Collisions*, Phys. Rev. Lett. **85**, 3595 (2000), *Preprint* arXiv:nucl-ex/0006008.

[82] M. M. Aggarwal *et al.* (WA98 Collaboration), *Interferometry of Direct Photons in Central $^{208}Pb+$ ^{208}Pb Collisions at 158 $AGeV$*, Phys. Rev. Lett. **93**, 022301 (2004), *Preprint* arXiv:nucl-ex/0310022.

[83] R. Hanbury Brown and R. Q. Twiss, *A Test of a New Type of Stellar Interferometer on Sirius*, Nature **178**, 1046 (1956).

[84] R. Hanbury Brown and R. Q. Twiss, *A New Type Of Interferometer For Use In Radio Astronomy*, Phil. Mag. **45**, 663 (1954).

[85] D. K. Srivastava, *Intensity interferometry of thermal photons from relativistic heavy-ion collisions*, Phys. Rev. C **71**, 034905 (2005), *Preprint* arXiv:nucl-th/0411041.

[86] W. Liu and R. Rapp, *Low-energy thermal photons from meson-meson bremsstrahlung*, Nucl. Phys. **A796**, 101 (2007), *Preprint* arXiv:nucl-th/0604031.

[87] A. Adare *et al.* (PHENIX Collaboration), *Inclusive cross section and double helicity asymmetry for π^0 production in $p+p$ collisions at $\sqrt{s}$ = 200 GeV: Implications for the polarized gluon distribution in the proton*, Phys. Rev. D **76**, 051106 (2007), *Preprint* arXiv:0704.3599.

[88] K. Adcox *et al.* (PHENIX Collaboration), *PHENIX detector overview*, Nucl. Instr. and Meth. A **499**, 469 (2003).

[89] K. Adcox *et al.* (PHENIX Collaboration), *PHENIX central arm tracking detectors*, Nucl. Instr. and Meth. A **499**, 489 (2003).

[90] M. Aizawa *et al.* (PHENIX Collaboration), *PHENIX central arm particle ID detectors*, Nucl. Instr. and Meth. A **499**, 508 (2003).

[91] H. Akikawa *et al.* (PHENIX Collaboration), *PHENIX Muon Arms*, Nucl. Instr. and Meth. A **499**, 537 (2003).

[92] M. Allen *et al.* (PHENIX Collaboration), *PHENIX inner detectors*, Nucl. Instr. and Meth. A **499**, 549 (2003).

[93] K. Ikematsu *et al.*, *A start-timing detector for the collider experiment PHENIX at RHIC-BNL*, Nucl. Instr. and Meth. A **411**, 238 (1998), *Preprint* arXiv:physics/9802024.

[94] C. Adler *et al.*, *The RHIC zero degree calorimeters*, Nucl. Instr. and Meth. A **470**, 488 (2001).

[95] S. H. Aronson *et al.* (PHENIX Collaboration), *PHENIX magnet system*, Nucl. Instr. and Meth. A **499**, 480 (2003).

[96] A. Kozlov *et al.*, *Development of a triple GEM UV-photon detector operated in pure CF_4 for the PHENIX experiment*, Nucl. Instr. Meth. A **523**, 345 (2004), *Preprint* arXiv:physics/0309013.

[97] Z. Fraenkel *et al.*, *A hadron blind detector for the PHENIX experiment at RHIC*, Nucl. Instr. Meth. A **546**, 466 (2005), *Preprint* arXiv:physics/0502008.

[98] L. Aphecetche *et al.* (PHENIX Collaboration), *PHENIX calorimeter*, Nucl. Instr. and Meth. A **499**, 521 (2003).

[99] K. Reygers, *Glauber Monte-Carlo Calculations for Au + Au Collisions at $\sqrt{s_{NN}}$ = 200 GeV* (2003), PHENIX Internal Analysis Note 169.

[100] S. C. Johnson, *Three-Dimensional Track Finding in the PHENIX Drift Chamber by a Combinatorial Hough Transform Method*, in *Proc. of Int. Conf. on Computing in High-Energy Physics (CHEP '98)* (Chicago, IL, USA, 1998).

[101] Y. Akiba and T. Hachiya, *Analysis Note on electron analysis Part II* (2001), PHENIX Internal Analysis Note 44.

[102] T. Sjöstrand *et al.*, *High-energy-physics event generation with PYTHIA 6.1*, Comput. Phys. Commun. **135**, 238 (2001), *Preprint* arXiv:hep-ph/0010017.

[103] T. Sjöstrand, L. Lonnblad, and S. Mrenna, *Pythia 6.2: Physics and manual* (2001), *Preprint* arXiv:hep-ph/0108264.

[104] T. Sjöstrand, *High-energy physics event generation with PYTHIA 5.7 and JETSET 7.4*, Comput. Phys. Commun. **82**, 74 (1994).

[105] B. Andersson, G. Gustafson, G. Ingelman, and T. Sjöstrand, *Parton Fragmentation and String Dynamics*, Phys. Rept. **97**, 31 (1983).

[106] H. L. Lai *et al.*, *Global QCD analysis of parton structure of the nucleon: CTEQ5 parton distributions*, Eur. Phys. J **12**, 375 (2000), *Preprint* arXiv:hep-ph/9903282.

[107] A. Adare *et al.* (PHENIX Collaboration), *Dihadron azimuthal correlations in Au + Au collisions at* $\sqrt{s_{NN}}$ *= 200 GeV*, Phys. Rev. C **78**, 014901 (2008), *Preprint* arXiv:0801.4545.

[108] *GEANT 3.15 User's Guide*, CERN Program Library (1993).

[109] A. Lebedev *et al.*, *Electron acceptance/efficiency calculation in RUN-2 data* (2002), PHENIX Internal Analysis Note 137.

[110] I. G. Bearden *et al.* (BRAHMS Collaboration), *Rapidity Dependence of Charged Antihadron to Hadron Ratios in Au + Au Collisions at* $\sqrt{s_{NN}}$ *= 200 GeV*, Phys. Rev. Lett. **90**, 102301 (2003).

[111] D. Ivanishchev, A. Milov, V. Riabov, and Y. Riabov, *Hadron decay of* η'*-mesons in run5* $p + p$ (2008), PHENIX Internal Analysis Note 692.

[112] R. Gavai *et al.*, *Quarkonium production in hadronic collisions*, Int. J. Mod. Phys. **A10**, 3043 (1995), *Preprint* arXiv:hep-ph/9502270.

[113] M. Donadelli, M. Rosati, and C. L. Silva, *Charmonium Production in Run 6* $p + p$ *Collisions at* $\sqrt{s}$ *= 200 GeV* (2008), PHENIX Internal Analysis Note 722.

[114] S. S. Adler *et al.* (PHENIX Collaboration), *Nuclear effects on hadron production in* $d + Au$ *collisions at* $\sqrt{s_{NN}}$ *= 200 GeV revealed by comparison with* $p + p$ *data*, Phys. Rev. C **74**, 024904 (2006).

[115] S. S. Adler *et al.* (PHENIX Collaboration), *High transverse momentum* η *meson production in* p+p*,* d+Au*, and* Au+Au *collisions at* $\sqrt{s_{NN}}$ *= 200 GeV*, Phys. Rev. C **75**, 024909 (2007), *Preprint* arXiv:nucl-ex/0611006.

[116] T. Dahms, A. Drees, and A. Toia, *Measurement of ω & $\phi \to e^+e^-$ in $p+p$ collisions at $\sqrt{s}$ = 200 GeV (Run5)* (2007), PHENIX Internal Analysis Note 614.

[117] K. M. Kijima, K. Ozawa, K. Shigaki, and Y. Tsutimoto, *$\omega, \phi \to e^+e^-$ in Run5 $p+p$ collisions at $\sqrt{s}$ = 200 GeV* (2007), PHENIX Internal Analysis Note 610.

[118] D. Sharma *et al.*, *Run 5 $p+p$ $\omega, \phi \to e^+e^-$* (2007), PHENIX Internal Analysis Note 618.

[119] S. S. Adler *et al.* (PHENIX Collaboration), *Production of ω mesons at large transverse momenta in $p+p$ and $d+Au$ collisions at $\sqrt{s_{NN}}$ = 200 GeV*, Phys. Rev. C **75**, 051902 (2007), *Preprint* arXiv:nucl-ex/0611031.

[120] Y. Riabov (PHENIX Collaboration), *Measurement of leptonic and hadronic decays of ω- and ϕ-mesons at RHIC by PHENIX*, J. Phys. **G34**, S925 (2007).

[121] D. Ivanishchev, A. Milov, V. Riabov, and Y. Riabov, *Hadron decay of omega and K_s^0 - mesons in Run5 $p+p$* (2006), PHENIX Internal Analysis Note 535.

[122] D. Ivanishchev *et al.*, *$\phi \to K^+K^-$ measurement in Run5 $p+p$ and Run3 $d+Au$ with no PID* (2006), PHENIX Internal Analysis Note 600.

[123] A. Adare *et al.* (PHENIX Collaboration), *J/ψ Production versus Transverse Momentum and Rapidity in $p+p$ Collisions at $\sqrt{s}$ = 200 GeV*, Phys. Rev. Lett. **98**, 232002 (2007).

[124] S. S. Adler *et al.* (PHENIX Collaboration), *Identified charged particle spectra and yields in $Au+Au$ collisions at $\sqrt{s_{NN}}$ = 200 GeV*, Phys. Rev. C **69**, 034909 (2004), *Preprint* arXiv:nucl-ex/0307022.

[125] S. S. Adler *et al.* (PHENIX Collaboration), *Production of ϕ mesons at midrapidity in $\sqrt{s_{NN}}$ = 200 GeV $Au+Au$ collisions at relativistic energies*, Phys. Rev. C **72**, 014903 (2005), *Preprint* arXiv:nucl-ex/0410012.

[126] R. I. Dzhelyadin *et al.*, *Study of the electromagnetic transition form-factor in $\omega \to \pi^0\mu^+\mu^-$ decay*, Phys. Lett. **B102**, 296 (1981).

[127] G. J. Gounaris and J. J. Sakurai, *Finite-Width Corrections to the Vector-Meson-Dominance Prediction for $\rho \to e^+e^-$*, Phys. Rev. Lett. **21**, 244 (1968).

[128] S. A. Butsyk, *Study of Open Charm Production in $p+p$ Collisions at $\sqrt{s}$ = 200 GeV*, Ph.D. thesis, Stony Brok University, Department of Physics and Astronomy, Stony Brook, NY 11794-3800, USA (2004), *Preprint* arXiv:hep-ex/0511048.

[129] K. Adcox *et al.*, *Measurement of Single Electrons and Implications for Charm Production in Au + Au Collisions at $\sqrt{s_{NN}}$ =130 GeV*, Phys. Rev. Lett. **88**, 192303 (2002), *Preprint* arXiv:nucl-ex/0202002.

[130] C. H. Jaroschek, *A study of bottom production with the PYTHIA event generator*, Master's thesis, Stony Brok University, Department of Physics and Astronomy, Stony Brook, NY 11794-3800, USA (2001), the bottom cross section was obtained by tuning PYTHIA to experimental data and interpolating to $\sqrt{s} = 200$ GeV.

[131] S. Gavin *et al.*, *Production of Drell-Yan pairs in high-energy nucleon-nucleon collisions*, Int. J. Mod. Phys. **A10**, 2961 (1995), *Preprint* arXiv:hep-ph/9502372.

[132] B. I. Abelev *et al.* (STAR Collaboration), *Transverse Momentum and Centrality Dependence of High-p_T Nonphotonic Electron Suppression in Au+Au Collisions at sqrts_{NN} = 200 GeV*, Phys. Rev. Lett. **98**, 192301 (2007), *Preprint* arXiv:nucl-ex/0607012.

[133] J. Adams *et al.* (STAR Collaboration), *Open Charm Yields in d + Au Collisions at $\sqrt{s_{NN}}$ = 200 GeV*, Phys. Rev. Lett. **94**, 062301 (2005), *Preprint* arXiv:nucl-ex/0407006.

[134] H. L. Lai *et al.*, *Improved parton distributions from global analysis of recent deep inelastic scattering and inclusive jet data*, Phys. Rev. D **55**, 1280 (1997).

[135] M. Glück, E. Reya, and A. Vogt, *Dynamical parton distributions of the proton and small x physics*, Z. Phys. **C67**, 433 (1995).

[136] M. Glück, E. Reya, and A. Vogt, *Dynamical parton distributions revisited*, Eur. Phys. J. **C5**, 461 (1998), *Preprint* arXiv:hep-ph/9806404.

[137] A. D. Martin, R. G. Roberts, W. J. Stirling, and R. S. Thorne, *Parton distributions: A new global analysis*, Eur. Phys. J. **C4**, 463 (1998), *Preprint* arXiv:hep-ph/9803445.

[138] W. Vogelsang (2008), private communication.

[139] J. Pumplin *et al.*, *New Generation of Parton Distributions with Uncertainties from Global QCD Analysis*, J. High Energy Phys. **07**, 012 (2002), *Preprint* arXiv:hep-ph/0201195.

[140] Y. Morino (PHENIX Collaboration), *Measurement of charm and bottom production in $p+p$ collisions at $\sqrt{s}$ = 200 GeV at RHIC-PHENIX* (2008), *Preprint* arXiv:0805.3871.

[141] R. Vogt, *The total charm cross section*, Eur. Phys. J. ST **155**, 213 (2008), *Preprint* arXiv:0709.2531.

[142] M. Bedjidian *et al.*, *Hard probes in heavy ion collisions at the LHC: Heavy flavour physics* (2004), *Preprint* arXiv:hep-ph/0311048.

[143] D. G. d'Enterria and D. Peressounko, *Probing the QCD equation of state with thermal photons in nucleus nucleus collisions at RHIC*, Eur. Phys. J. **C46**, 451 (2006), *Preprint* arXiv:nucl-th/0503054.

[144] E. Schnedermann, J. Sollfrank, and U. Heinz, *Thermal phenomenology of hadrons from 200 AGeV $S+S$ collisions*, Phys. Rev. C **48**, 2462 (1993), *Preprint* arXiv:nucl-th/9307020.

[145] T. Csörgő and B. Lörstad, *Bose-Einstein correlations for three-dimensionally expanding, cylindrically symmetric, finite systems*, Phys. Rev. C **54**, 1390 (1996), *Preprint* arXiv:hep-ph/9509213.

[146] T. Csörgő *et al.*, *Observables and initial conditions for self-similar ellipsoidal flows*, Phys. Rev. C **67**, 034904 (2003), *Preprint* arXiv:hep-ph/0108067.

[147] D. Teaney, J. Lauret, and E. V. Shuryak, *Flow at the SPS and RHIC as a Quark-Gluon Plasma Signature*, Phys. Rev. Lett. **86**, 4783 (2001), *Preprint* arXiv:nucl-th/0011058.

[148] D. Teaney, J. Lauret, and E. V. Shuryak, *A hydrodynamic description of heavy ion collisions at the SPS and RHIC* (2001), *Preprint* arXiv:nucl-th/0110037.

[149] P. Huovinen, P. V. Ruuskanen, and S. S. Räsänen, *Photon emission in heavy ion collisions at the CERN SPS*, Phys. Lett. **B535**, 109 (2002), *Preprint* arXiv:nucl-th/0111052.

[150] D. K. Srivastava and B. Sinha, *Radiation of single photons from $pb+pb$ collisions at relativistic energies and the quark-hadron phase transition*, Phys. Rev. C **64**, 034902 (2001), *Preprint* arXiv:nucl-th/0006018.

[151] J.-e. Alam *et al.*, *Photons from Pb-Pb collisions at ultrarelativistic energies*, Phys. Rev. C **63**, 021901 (2001), *Preprint* arXiv:hep-ph/0008074.

[152] F.-M. Liu *et al.*, *Centrality-dependent direct photon pt spectra in Au+Au collisions at RHIC* (2008), *Preprint* arXiv:0807.4771.

[153] S. S. Räsänen, *On hydrodynamical description of thermal photons*, Nucl. Phys. **A715**, 717 (2003), *Preprint* arXiv:nucl-th/0210007.

[154] D. K. Srivastava, *Single photons, dileptons and hadrons from relativistic heavy ion collisions and quark hadron phase transition*, Pramana **57**, 235 (2001).

[155] K. Dusling and I. Zahed, *Low mass dilepton radiation at RHIC* (2007), *Preprint* arXiv:0712.1982.

[156] E. L. Bratkovskaya, W. Cassing, and O. Linnyk, *Low mass dilepton production at ultrarelativistic energies* (2008), *Preprint* arXiv:0805.3177.

[157] K. Dusling, D. Teaney, and I. Zahed, *Thermal dimuon yields: Comparison with NA60 results at 158 GeV/nucleon*, Phys. Rev. C **75**, 024908 (2007), *Preprint* arXiv:nucl-th/0604071.

[158] J. V. Steele, H. Yamagishi, and I. Zahed, *Dilepton and photon emission rates from a hadronic gas. II*, Phys. Rev. D **56**, 5605 (1997), *Preprint* arXiv:hep-ph/9704414.

[159] W. Ehehalt and W. Cassing, *Relativistic transport approach for nucleus nucleus collisions from SIS to SPS energies*, Nucl. Phys. **A602**, 449 (1996).

[160] J. M. Heuser (PHENIX), *Vertex detector upgrade plans for the PHENIX experiment at RHIC*, Nucl. Instr. Meth. A **511**, 210 (2003).

[161] T. Isobe, *Systematic study of high-p_T direct photon production with the PHENIX experiment at RHIC*, J. Phys. **G34**, S1015 (2007), *Preprint* arXiv:nucl-ex/0701040.

Appendix A

Background Normalization

A.1 Pairing of electrons and positrons

In the following it is assumed that positrons and electrons are always produced in pairs. Let N pairs be produced in a particular event and N is given by a probability distribution $P(N)$. Of the N pairs only a fraction p is reconstructed, and then the number of reconstructed pairs n_p is given by a binomial distribution B sampling out of N "events" with a probability ε_p.

- Probability to get n_p pairs from N true pairs: $\omega(n_p) = B(n_p, N, \varepsilon_p)$
- with an average: $\langle n_p \rangle = \varepsilon_p N$
- and variance: $\sigma_p^2 = \varepsilon_p N(1 - \varepsilon_p)$

Of the remaining pairs one track is reconstructed with a probability ε_+ or ε_-. For a given N and n_p the number of additional single positive tracks n_+ and negative tracks n_- follow a multinomial distribution M with possible three possible outcomes for each of the $N - n_p$ unreconstructed pairs: no track, one + track or one − track.

The probability to get n_+ and n_- single tracks from N true pairs with n_p reconstructed pairs, *i. e.*, from $N' = (N - n_p)$ not fully reconstructed pairs is: $\omega(n_+, n_-) = M(n_+, n_-; N', \varepsilon_+, \varepsilon_-)$

- with average: $\langle n_\pm \rangle = \varepsilon_\pm N'$
- variance: $\sigma_\pm^2 = \varepsilon_\pm N'(1 - \varepsilon_\pm)$
- and covariance: $\mathrm{cov(n_+, n_-)} = -\mathrm{N'}\varepsilon_+\varepsilon_-$

In this case the number of unlike-sign pairs for a given N and n_p is:

$$\begin{aligned}
\langle n_{+-}\rangle &= n_p^2 + n_p \sum_{+} n_+\omega(n_+) + n_p \sum_{-} n_-\omega(n_-) + \sum_{+}^{N-n_p}\sum_{-}^{N-n_p} n_+ n_-\omega(n_+, n_-) \\
&= n_p^2 + n_p\varepsilon_+(N-n_p) + n_p\varepsilon_-(N-n_p) + \langle n_+ n_-\rangle \\
&= n_p^2 + n_p\varepsilon_+(N-n_p) + n_p\varepsilon_-(N-n_p) + \varepsilon_+\varepsilon_-(N-n_p)^2 \\
&\quad - \varepsilon_+\varepsilon_-(N-n_p) \\
&= n_p^2 + \varepsilon_+ N n_p - \varepsilon_+ n_p^2 + \varepsilon_- N n_p - \varepsilon_- n_p^2 + \varepsilon_+\varepsilon_- N^2 - 2\varepsilon_+\varepsilon_- N n_p \\
&\quad + \varepsilon_+\varepsilon_- n_p^2 - \varepsilon_+\varepsilon_- N + \varepsilon_+\varepsilon_- n_p \\
&= \left(n_p + \varepsilon_+\left(N-n_p\right)\right)\left(n_p + \varepsilon_-\left(N-n_p\right)\right) - \varepsilon_+\varepsilon_-(N-n_p). \qquad \text{(A.1)}
\end{aligned}$$

Similarly one can calculate the number of like-sign pairs:

$$\begin{aligned}
2\langle n_{++}\rangle &= \sum_{+}(n_p + n_+)(n_p + n_+ - 1)\omega(n_+) \\
&= n_p^2 - n_p + \langle n_+^2\rangle - \langle n_+\rangle + 2n_p\langle n_+\rangle \\
&= n_p^2 - n_p + \varepsilon_+^2(N-n_p)^2 + \varepsilon_+(1-\varepsilon_+)(N-n_p) - \varepsilon_+(N-n_p) \\
&\quad + 2\varepsilon_+ n_p(N-n_p) \\
&= n_p^2 - n_p + \varepsilon_+^2(N-n_p)^2 - \varepsilon_+^2(N-n_p) + 2\varepsilon_+ n_p(N-n_p) \qquad \text{(A.2)}
\end{aligned}$$

and

$$2\langle n_{--}\rangle = n_p^2 - n_p + \varepsilon_-^2(N-n_p)^2 - \varepsilon_-^2(N-n_p) + 2\varepsilon_- n_p(N-n_p). \qquad \text{(A.3)}$$

To obtain the expected number of like- and unlike-sign pairs for a fixed number of real pairs N it is averaged over all possible reconstructed pairs n_p:

$$\begin{aligned}
\langle N_{+-}\rangle &= \sum_{n_p}\langle n_{+-}\rangle B(n_p) \\
&= (1 - \varepsilon_+ - \varepsilon_- + \varepsilon_+\varepsilon_-)\langle n_p^2\rangle + (\varepsilon_+ N + \varepsilon_- N - 2\varepsilon_+\varepsilon_- N + \varepsilon_+\varepsilon_-)\langle n_p\rangle \\
&\quad + \varepsilon_+\varepsilon_- N^2 - \varepsilon_+\varepsilon_- N \\
&= (1 - \varepsilon_+ - \varepsilon_- + \varepsilon_+\varepsilon_-)(\varepsilon_p^2 N^2 + \varepsilon_p(1-\varepsilon_p)N) \\
&\quad + (\varepsilon_+ N + \varepsilon_- N - 2\varepsilon_+\varepsilon_- N + \varepsilon_+\varepsilon_-)\varepsilon_p N + \varepsilon_+\varepsilon_- N^2 - \varepsilon_+\varepsilon_- N \\
&= (\varepsilon_p^2 - \varepsilon_p^2\varepsilon_+ - \varepsilon_p^2\varepsilon_- + \varepsilon_p^2\varepsilon_+\varepsilon_- + \varepsilon_p\varepsilon_+ + \varepsilon_p\varepsilon_- - 2\varepsilon_p\varepsilon_+\varepsilon_- + \varepsilon_+\varepsilon_-) \\
&\quad \cdot (N^2 - N) + \varepsilon_p N \\
&= (\varepsilon_p + \varepsilon_+(1-\varepsilon_p))(\varepsilon_p + \varepsilon_-(1-\varepsilon_p))(N^2 - N) + \varepsilon_p N. \qquad \text{(A.4)}
\end{aligned}$$

Now the like-sign background is calculated:

$$
\begin{aligned}
2\langle N_{++}\rangle &= \sum_{n_p} 2\langle n_{++}\rangle B(n_p) \\
&= \varepsilon_p^2 N^2 + \varepsilon_p(1-\varepsilon_p)N - \varepsilon_p N + \varepsilon_p^2\varepsilon_+^2 N^2 + \varepsilon_+^2\varepsilon_p(1-\varepsilon_p)N - 2\varepsilon_+^2\varepsilon_p N^2 \\
&\quad + \varepsilon_+^2 N^2 - \varepsilon_+^2 N + \varepsilon_+^2\varepsilon_p N + 2\varepsilon_+\varepsilon_p N^2 - 2\varepsilon_+\varepsilon_p^2 N^2 - 2\varepsilon_+\varepsilon_p(1-\varepsilon_p)N \\
&= \varepsilon_p^2(N^2-N) + \varepsilon_+^2\varepsilon_p^2(N^2-N) + \varepsilon_+^2\varepsilon_p N - 2\varepsilon_+^2\varepsilon_p N^2 + \varepsilon_+^2(N^2-N) \\
&\quad + \varepsilon_+^2\varepsilon_p N + 2\varepsilon_+\varepsilon_p N^2 - 2\varepsilon_+\varepsilon_P^2 N^2 - 2\varepsilon_+\varepsilon_p N + 2\varepsilon_+\varepsilon_p^2 N \\
&= (\varepsilon_p^2 + \varepsilon_+^2 + \varepsilon_+^2\varepsilon_p^2)(N^2-N) - 2\varepsilon_+^2\varepsilon_p(N^2-N) + 2\varepsilon_+\varepsilon_p(N^2-N) \\
&\quad - 2\varepsilon_+\varepsilon_p^2(N^2-N) \\
\langle N_{++}\rangle &= \frac{1}{2}(\varepsilon_p + \varepsilon_+(1-\varepsilon_p))^2(N^2-N) \qquad \text{(A.5)}
\end{aligned}
$$

and

$$
\langle N_{--}\rangle = \frac{1}{2}(\varepsilon_p + \varepsilon_-(1-\varepsilon_p))^2(N^2-N). \qquad \text{(A.6)}
$$

Finally, it is averaged over all N to get the foreground unlike-sign pairs:

$$
\begin{aligned}
\langle FG_{+-}\rangle &= \sum_N \langle N_{+-}\rangle P(N) \\
&= (\varepsilon_p + \varepsilon_+(1-\varepsilon_p))(\varepsilon_p + \varepsilon_-(1-\varepsilon_p))(\langle N^2\rangle - \langle N\rangle) + \varepsilon_p\langle N\rangle \\
&= \langle BG_{+-}\rangle + \langle S\rangle. \qquad \text{(A.7)}
\end{aligned}
$$

The unlike-sign foreground FG_{+-} consists of the sum of the unlike-sign background BG_{+-} and the signal $S = \varepsilon_p\langle N\rangle$. Similarly the like-sign foreground is calculated as:

$$
\begin{aligned}
\langle FG_{++}\rangle &= \sum_N \langle N_{++}\rangle P(N) \\
&= \frac{1}{2}(\varepsilon_p + \varepsilon_+(1-\varepsilon_p))^2(\langle N^2\rangle - \langle N\rangle) \\
&= \langle BG_{++}\rangle \qquad \text{(A.8)}
\end{aligned}
$$

and

$$
\langle FG_{--}\rangle = \langle BG_{--}\rangle. \qquad \text{(A.9)}
$$

The like-sign foreground contains no signal.

So due to the fact that electrons and positrons are always created in pairs, the unlike-sign background is the geometric mean of the like-sign backgrounds, independent of the primary multiplicity distribution.

$$\langle BG_{+-}\rangle = 2\sqrt{\langle BG_{++}\rangle\langle BG_{--}\rangle} \tag{A.10}$$

Comparing the background to the product of the average track multiplicities one gets for a fixed n_p:

$$\begin{aligned}\langle n_+\rangle &= \sum_+ (n_p + n_+)\omega(n_+) \\ &= n_p + \langle n_+\rangle \\ &= n_p + \varepsilon_+(N - n_p)\end{aligned} \tag{A.11}$$

averaged over all possible n_p:

$$\begin{aligned}\langle N_+\rangle &= \sum_{n_p} \langle n_+\rangle\omega(n_p) \\ &= \varepsilon_p N + \varepsilon_+ N - \varepsilon_+\varepsilon_p N \\ &= (\varepsilon_p + \varepsilon_+(1-\varepsilon_p))N\end{aligned} \tag{A.12}$$

or averaged over all possible N:

$$\begin{aligned}\langle FG_+\rangle &= \sum_N \langle N_+\rangle P(N) \\ &= (\varepsilon_p + \varepsilon_+(1-\varepsilon_p))\langle N\rangle\end{aligned} \tag{A.13}$$

and thus:

$$\langle FG_+\rangle\langle FG_+\rangle = (\varepsilon_p + \varepsilon_+(1-\varepsilon_p))(\varepsilon_p + \varepsilon_-(1-\varepsilon_p))\langle N\rangle^2 \tag{A.14}$$

or

$$\frac{\langle BG_{+-}\rangle}{\langle FG_+\rangle\langle FG_-\rangle} = 1 + \frac{\sigma^2 - \langle N\rangle}{\langle N\rangle^2}. \tag{A.15}$$

So in general $\langle BG_{+-}\rangle \neq \langle FG_+\rangle\langle FG_-\rangle$, except for the special case that $P(N)$ is a Poisson distribution. Note this is the opposite conclusion one derives in the case that the sources of $+$ and $-$ tracks are independent, *i. e.*, $+$ and $-$ tracks are produced as singles and not as pairs like they are for muons. In

that case $\langle FG_+\rangle\langle FG_-\rangle$ is the correct background normalization.

Appendix B

Beam Pipe Conversions

B.1 Introduction

In this Appendix another approach to measure direct photons at low p_T is presented. It is the measurement of real photons which convert externally in the beam pipe, surrounding the collision vertex at a radius of 4 cm. These are the pairs which are removed with the ϕ_V cut in the regular dielectron continuum and internal conversion analysis. The basic idea is to identify e^+e^- pairs from beam pipe conversions and to combine these with photons in the EMCal to tag conversion photons from π^0 decays. It is certainly not as strong as the virtual photon analysis but is nevertheless an interesting approach.

B.2 Analysis

To identify e^+e^- pairs from photon conversions, a single electron identification cut is applied, which requires signals from at least two phototubes in the Ring Imaging Cherenkov Detector (RICH) matching to a reconstructed charged track in the Drift Chamber (DC). No further electron identification cuts were applied since the pair cuts (see Section B.2.1) to separate conversion photons from other e^+e^- pairs are more efficient and powerful enough to provide a very clean photon conversion sample.

The extracted photon conversions are tagged with photons reconstructed in the EMC to determine the contribution from $\pi^0 \rightarrow \gamma\gamma$ decays (see Section B.2.2).

All yields are measured as a function of p_T of the $\mathrm{e^+e^-}$–pair, which makes a direct comparison of the inclusive photon yield, N_γ^{incl}, and the tagged photon

yield, $N_\gamma^{\pi^0\mathrm{tag}}$, possible:

$$N_\gamma^{\mathrm{incl}}\left(p_T\right) = \epsilon_{e^+e^-}\ a_{e^+e^-}\ \gamma^{\mathrm{incl}}\left(p_T\right) \tag{B.1}$$

$$N_\gamma^{\pi^0\mathrm{tag}}\left(p_T\right) = \epsilon_{e^+e^-}\ a_{e^+e^-}\ \epsilon_\gamma\left(p_T\right)\ f\ \gamma^{\pi^0}\left(p_T\right) \tag{B.2}$$

The measured yield of inclusive photons depends on the reconstruction efficiency $\epsilon_{e^+e^-}$ and the PHENIX acceptance $a_{e^+e^-}$ of the conversion e^+e^- pair. The tagged photon yield depends in addition on the efficiency to reconstruct the second photon in the EMC $\epsilon_\gamma(p_T)$ and on the conditional probability f to find it in the EMC acceptance, given that the e^+e^- pair has been reconstructed already. Here, $\epsilon_\gamma(p_T)$ is weighted with the p_T distribution of the e^+e^- pair. In the ratio $N_\gamma^{incl}/N_\gamma^{\pi^0 tag}$ the e^+e^- pair reconstruction efficiency and acceptance correction factor cancel.

A ratio of the hadronic decay photon yield, N_γ^{hadr}, and the tagged photon yield from π^0 decays, $N_\gamma^{\pi^0\mathrm{tag}}$, is calculated with simulations.

$$N_\gamma^{\pi^0\mathrm{tag}}\left(p_T\right) = f\ N_\gamma^{\pi^0}\left(p_T\right) \tag{B.3}$$

The comparison of the ratio in data and in simulations in a double ratio leads to an expression that is equivalent to the ratio of inclusive and decay photons as shown in Eq. (B.4).

$$\frac{\gamma^{\mathrm{incl}}\left(p_T\right)}{\gamma^{\mathrm{hadr}}\left(p_T\right)} = \frac{\epsilon_\gamma\left(p_T\right)\cdot\left(\frac{N_\gamma^{\mathrm{incl}}(p_T)}{N_\gamma^{\pi^0\mathrm{tag}}(p_T)}\right)_{\mathrm{Data}}}{\left(\frac{N_\gamma^{\mathrm{hadr}}(p_T)}{f\ N_\gamma^{\pi^0}(p_T)}\right)_{\mathrm{Sim}}} \tag{B.4}$$

The only remaining factors are the reconstruction efficiency of the photon in the EMC, $\epsilon_\gamma(p_T)$, and the conditional acceptance f in the simulation part of the double ratio, which have both been determined with Monte Carlo simulations (see Section B.2.3).

B.2.1 Photon Conversions

Since the PHENIX tracking algorithm assumes the track to originate from the collision vertex, off-vertex conversion pairs are reconstructed with an artificial opening angle which leads to an invariant mass that is proportional to the radius at which the conversion occurs.

Therefore, photon conversions that occur in the beam pipe material (Be, 0.3 % radiation length) at a radius of 4 cm are reconstructed with an invariant mass of ~ 20 MeV/c^2. Fig. B.1 shows an invariant mass spectrum of e^+e^- pairs

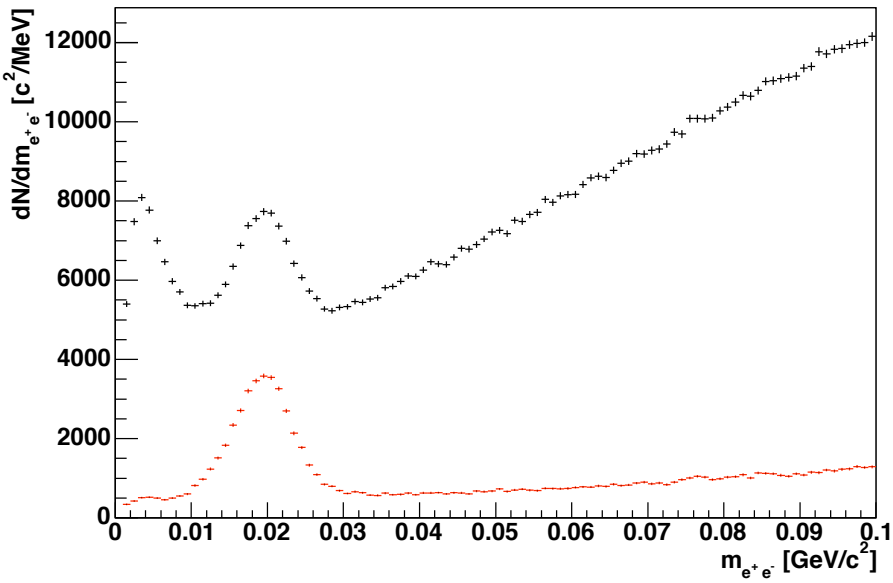

Figure B.1: Invariant mass of e^+e^- pairs before (black) and after (red) applying cuts on the orientation of the e^+e^- pair in the magnetic field.

in the range 0–0.1 GeV/c^2. The peak from photon conversions in the beam pipe at 20 MeV/c^2 can be clearly separated from Dalitz decays $\pi^0 \to \gamma e^+e^-$, which dominate the spectrum below 10 MeV/c^2, and combinatorial background pairs, whose contribution increases toward higher invariant masses.

The photon conversion pairs, which have no intrinsic opening angle, can be distinguished from Dalitz decays and purely combinatorial pairs by cutting on the orientation of the e^+e^- pair in the magnetic field.

Fig. B.1 shows the invariant mass spectra of e^+e^- pairs before (black) and after (red) applying these pair cuts. The yield from integrating the mass region < 35 MeV/c^2 of the conversion peak is corrected for the remaining p_T dependent contamination of $\sim 15.0 \pm 2.0$ (syst) % due to combinatorial e^+e^- pairs which has been determined with mixed events.

B.2.2 Tagging of Decay Photons

To reveal which of these conversion photons come from $\pi^0 \to \gamma\gamma$ decays, the e^+e^- pairs in the conversion peak are combined with photons which have been measured in the EMC, under loose cuts based on the time of flight and the shower profile for photons with a minimum p_T of 0.3 GeV/c, and their invariant mass is calculated (see Fig. B.2).

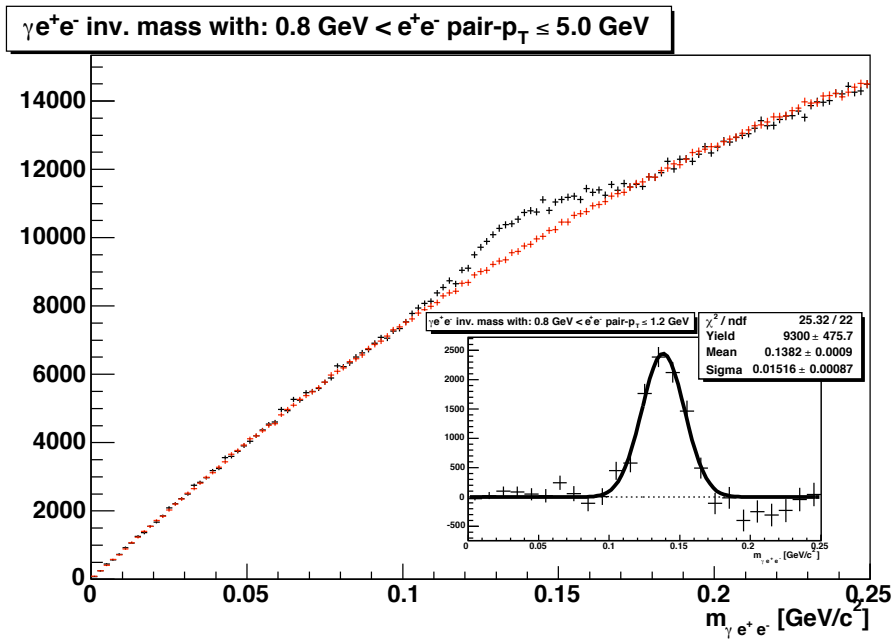

Figure B.2: Invariant mass of γe^+e^- triplets in same events (black) and normalized mixed events (red) for e^+e^- pairs with $0.8 < p_T \leq 5.0$ GeV/c. The insert shows the invariant mass of γe^+e^- triplets after background subtraction for e^+e^- pairs with $0.8 < p_T \leq 1.2$ GeV/c. A fit with a Gaussian is drawn and the resulting parameters shown in the box in the upper right of the graph.

The reconstruction efficiency $\epsilon_\gamma(p_T)$ of the loose photon has been estimated with a full GEANT simulation which embed simulated photons into real EMC data, therefore providing a combined information on the photon identification efficiency and occupancy effects. The overall efficiency is determined to be $82 \pm 1\,\%$ independent of p_T beyond the minimum p_T cut off.

Conversion photons that are identified as decay products of π^0 can be tagged as $N_\gamma^{\pi^0\mathrm{tag}}$. This signal has a large combinatorial background due to the high photon multiplicity in Au + Au collisions.

The combinatorial background is reproduced with an event mixing method, which creates uncorrelated pairs of photons and e^+e^- pairs from different events. The mixed event spectrum is normalized to the same event spectrum well outside the π^0 mass region (0–100 MeV/c^2, 170–250 MeV/c^2) and subtracted.

The statistical error on the normalization factor is on the order of $0.2\,\%$ and depends only on the statistics in the same event spectrum in the normalization region. As an example, the resulting π^0 signal for e^+e^- pairs with $0.8 < p_T \leq 1.2$ GeV/c is shown as insert in Fig. B.2.

Mean and σ are determined by a fit of the background subtracted data with a Gaussian. The data are also fitted to the sum of a second order polynomial and a Gaussian, to take into account the possibility that the shape is not completely described by the mixed event spectrum. The difference in the resulting mean and σ is negligible. The mean and σ obtained by the fit are then used to integrate the data in a region $\pm 1.5\ \sigma$ around the mean, chosen to optimize the signal to background ratio.

The statistical error on the extracted π^0 signal is given by:

$$\sigma_S^2 = \sum_i FG(i) + \alpha \sum_i BG'(i) + \left(\frac{\sigma_\alpha}{\alpha} \sum_i BG'(i) \right)^2 \tag{B.5}$$

With $FG(i)$ and $BG'(i)$ being the yields in bin i of invariant mass spectrum in same events and normalized mixed events, respectively, the summations are performed over the integration region. It is important to note that the last term in Eq. (B.5), is the square of the sum over the normalized background, and therefore, depends on the integration region and is not bin independent. Different integration regions have been used. Variations in the resulting yield have been used to set a systematic uncertainty on the yield extraction of 2.5 % independent of p_T.

The loss of $N_\gamma^{\pi^0\mathrm{tag}}$ due to the external conversion of the second photon is corrected by a factor $1 - p_{conv} = 94 \pm 2\,\%$. In this factor p_{conv} is the conversion probability due to the material budget between the vertex and the Pad Chamber 3 (PC3) in front of the EMC.

B.2.3 Simulations

The contribution of hadronic decays has been determined with a fast Monte Carlo simulation of π^0 and η Dalitz decays. A parameterization of the π^0 spectrum measured by PHENIX [46] has been used as input. The η distribution has been generated assuming m_T scaling ($p_T \rightarrow \sqrt{p_T^2 + m_\eta^2 - m_{\pi^0}^2}$) of the π^0 spectral shape and a normalization at high p_T to $\eta/\pi^0 = 0.45 \pm 0.04$, according to PHENIX data [13]. The relative error of 9 % on the η/π^0 ratio is reduced by the branching ratio of the two photon decay and results in a 3 % error in the ratio $N_\gamma^{\mathrm{hadr}}/N_\gamma^{\pi^0}$.

The contamination due to neutral Kaons which decay before the beam pipe has been found negligible ($\sim 1\,\%$) and has been folded into the systematic error on the simulations.

The conditional probability f that the photon is reconstructed in the EMC once the e^+e^- pair is reconstructed already was calculated with a fast Monte

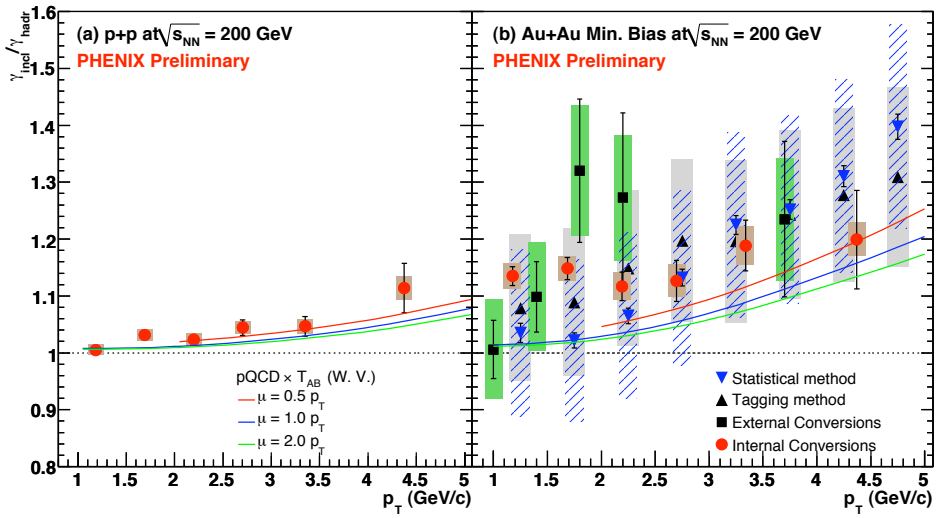

Figure B.3: Direct photon excess. (a) The fraction of the direct photon component as a function of p_T in p+p. (b) Au+Au (min. bias) compared to other measurements of direct photons as described in the legend. The curves are from a NLO pQCD calculation [41, 138].

Carlo simulation of $\pi^0 \to \gamma e^+e^-$. The use of Dalitz decays is justified by the fact that the p_T spectra of photons from $\pi^0 \to \gamma\gamma$ are essentially identical to the e^+e^- pair p_T spectrum from $\pi^0 \to \gamma e^+e^-$.

After the e^+e^- pair has been filtered in the detector acceptance, the conditional acceptance f for the second photon has been calculated taking dead areas of the detector into account. Uncertainties in calculating f are found to be 5 %, which is the largest source of systematic errors. The limited energy resolution of the EMC of $\sigma_E/E = 5\,\% \oplus 9\,\%/\sqrt{E}$ introduced an additional systematic error of $\sim 1\,\%$ due to the p_T cut at 0.3 GeV/c.

B.3 Conclusions

The right panel of Fig. B.3 shows the preliminary result for the double ratio $\gamma^{\rm incl}(p_T)/\gamma^{\rm hadr}(p_T)$ as in Eq. (B.4) for Minimum Bias Au + Au collisions at $\sqrt{s_{NN}} = 200$ GeV. The main sources of systematic errors arise from the uncertainties in the description of the detector active areas, in the peak extraction and in the assumptions of the π^0 shape and give a final systematic error on the double ratio of $\sim 7\,\%$. The result is compared to the conventional statistical subtraction of hadronic decay photons [161], and a result [49] which is based on the same tagging method, but instead of photons coming from conversions

in the beam pipe, the clean photon sample is determined by selecting EMC clusters with very strict photon identification cuts.

In addition the result of the internal conversion analysis is shown as $1+r \approx \gamma_{\mathrm{incl}}/\gamma_{\mathrm{hadr}}$ in the right panel for $\mathrm{Au}+\mathrm{Au}$ and in the left of Fig. B.3 for $p+p$ collisions. While all results agree within their uncertainties, the improvement in statistical and systematic uncertainties with the internal conversion analysis is quite significant. Also the NLO pQCD predictions of W. Vogelsang [41, 138] are shown..

Appendix C

Data Tables

Table C.1: ω and ϕ yields.

p_T (GeV/c)	N_ω (0.740–0.815 GeV/c^2)	N_ϕ (0.965–1.065 GeV/c^2)
0.10	33.6 ± 9.0	30.4 ± 9.5
0.30	153 ± 19	141 ± 18
0.50	372 ± 28	185 ± 19
0.70	508 ± 29	223 ± 20
0.90	358 ± 24	193 ± 18
1.10	261 ± 20	140 ± 15
1.30	182 ± 16	93 ± 12
1.50	134 ± 13	57.6 ± 9.2
1.70	68.3 ± 9.3	40.5 ± 7.4
1.90	65.3 ± 8.9	28.4 ± 6.2
2.50	142 ± 13	91 ± 10
4.00	51.4 ± 7.4	31.2 ± 5.8
5.50	3.8 ± 2.0	0.9 ± 1.0

Table C.2: Fit results of ω yield extraction.

	Yield			
p_T (GeV/c)	Gauss	Gauss + Pol0	Gauss + Pol1	Gauss + Pol2
0.10	34.3 ± 9.7	47 ± 12	41 ± 12	45 ± 16
0.30	145 ± 21	126 ± 23	125 ± 23	116 ± 26
0.50	247 ± 26	212 ± 29	210 ± 29	186 ± 38
0.70	484 ± 37	359 ± 33	363 ± 33	299 ± 34
0.90	487 ± 35	330 ± 32	340 ± 33	289 ± 35
1.10	301 ± 23	230 ± 22	234 ± 22	215 ± 24
1.30	215 ± 19	164 ± 19	166 ± 20	141 ± 20
1.50	171 ± 20	10 ± 14	104 ± 15	85 ± 15
1.70	140 ± 16	83 ± 15	85 ± 15	78 ± 19
1.90	59.6 ± 8.8	51.2 ± 9.0	49.6 ± 9.1	43.4 ± 9.2
2.50	178 ± 15	137 ± 15	139 ± 15	117 ± 16
4.00	47.9 ± 7.4	50.6 ± 7.7	43.0 ± 7.6	52 ± 10

	Sigma (MeV/c^2)			
p_T (GeV/c)	Gauss	Gauss + Pol0	Gauss + Pol1	Gauss + Pol2
0.10	17.6 ± 5.4	22.5 ± 6.2	20.2 ± 6.0	21.6 ± 6.9
0.30	8.2 ± 1.6	7.2 ± 1.6	7.1 ± 1.6	6.7 ± 1.7
0.50	16.7 ± 2.4	14.3 ± 2.7	14.1 ± 2.7	12.2 ± 3.6
0.70	10.2 ± 1.5	6.89 ± 0.78	7.00 ± 0.81	5.92 ± 0.71
0.90	25.7 ± 3.3	16.1 ± 1.8	16.6 ± 1.9	14.5 ± 1.9
1.10	15.6 ± 1.7	11.7 ± 1.3	11.9 ± 1.3	11.1 ± 1.3
1.30	20.6 ± 3.0	14.7 ± 2.1	15.0 ± 2.2	13.0 ± 2.0
1.50	35.1 ± 9.4	11.4 ± 2.3	12.0 ± 2.4	9.3 ± 2.5
1.70	43.5 ± 9.7	21.2 ± 4.2	21.8 ± 4.5	20.4 ± 4.9
1.90	14.4 ± 2.6	12.4 ± 2.3	12.1 ± 2.2	10.9 ± 2.3
2.50	20.6 ± 2.9	14.7 ± 1.7	15.0 ± 1.7	13.1 ± 1.6
4.00	21.2 ± 2.2	22.8 ± 2.5	20.5 ± 2.9	24.7 ± 4.2

Continued on next page

Table C.2: (continued)

p_T (GeV/c)	χ^2/ndf Gauss	Gauss + Pol0	Gauss + Pol1	Gauss + Pol2
0.10	25.51/28	19.02/27	16.98/26	16.72/25
0.30	34.32/28	32.22/27	31.84/26	31.47/25
0.50	52.24/28	46.99/27	46.30/26	45.18/25
0.70	87.42/28	48.89/27	44.51/26	32.96/25
0.90	86.84/28	37.16/27	31.66/26	26.28/25
1.10	94.51/28	38.00/27	31.98/26	28.46/25
1.30	67.84/28	42.57/27	40.62/26	34.94/25
1.50	90.59/28	51.59/27	45.66/26	38.84/25
1.70	43.87/28	26.07/27	25.52/26	25.22/25
1.90	39.52/28	31.76/27	30.16/26	26.10/25
2.50	89.68/28	42.62/27	37.99/26	27.94/25
4.00	47.46/28	44.28/27	26.22/26	18.73/25

Table C.3: Fit results of ϕ yield extraction.

	Yield			
p_T (GeV/c)	Gauss	Gauss + Pol0	Gauss + Pol1	Gauss + Pol2
0.10	29.1 ± 7.9	32.4 ± 8.8	29.8 ± 8.7	27.7 ± 8.7
0.30	139 ± 16	120 ± 16	119 ± 16	124 ± 17
0.50	159 ± 17	134 ± 17	132 ± 18	130 ± 18
0.70	169 ± 18	150 ± 18	139 ± 18	134 ± 18
0.90	206 ± 18	181 ± 19	168 ± 19	188 ± 21
1.10	151 ± 16	139 ± 18	138 ± 18	142 ± 21
1.30	117 ± 15	103 ± 16	101 ± 17	97 ± 19
1.50	67 ± 10	71 ± 12	75 ± 13	100 ± 31
1.70	25.4 ± 5.7	30.4 ± 5.9	28.2 ± 6.0	29 ± 6.0
1.90	28.4 ± 6.0	35.1 ± 6.5	27.3 ± 6.1	27.3 ± 6.2
2.50	86.5 ± 9.9	96 ± 10	83 ± 10	84 ± 10
4.00	20.4 ± 4.9	25.8 ± 5.1	23.2 ± 5.5	21.4 ± 5.6

	Sigma (MeV/c^2)			
p_T (GeV/c)	Gauss	Gauss + Pol0	Gauss + Pol1	Gauss + Pol2
0.10	9.1 ± 3.8	10.4 ± 4.2	9.4 ± 4.1	8.6 ± 5.2
0.30	5.48 ± 0.72	4.79 ± 0.68	4.77 ± 0.68	4.92 ± 0.71
0.50	13.1 ± 1.3	11.8 ± 1.3	11.7 ± 1.3	11.6 ± 1.3
0.70	6.55 ± 0.76	5.97 ± 0.71	5.66 ± 0.68	5.54 ± 0.68
0.90	15.9 ± 1.4	14.4 ± 1.4	13.7 ± 1.4	14.8 ± 1.6
1.10	19.4 ± 2.4	18.0 ± 2.4	18.0 ± 2.5	18.4 ± 2.7
1.30	23.7 ± 3.6	21.2 ± 3.5	20.8 ± 3.6	20.3 ± 3.8
1.50	18.4 ± 4.0	19.5 ± 4.7	21.0 ± 5.2	29.5 ± 9.4
1.70	5.5 ± 1.9	7.0 ± 1.4	6.4 ± 1.7	6.5 ± 1.6
1.90	8.7 ± 2.6	16.5 ± 7.5	8.3 ± 2.5	8.3 ± 2.6
2.50	14.3 ± 2.0	16.9 ± 3.2	13.6 ± 1.9	13.8 ± 1.9
4.00	21.2 ± 2.6	26.8 ± 2.4	24.9 ± 3.1	25.0 ± 3.7

Continued on next page

Table C.3: (continued)

	χ^2/ndf			
p_T (GeV/c)	Gauss	Gauss + Pol0	Gauss + Pol1	Gauss + Pol2
0.10	18.57/28	17.03/27	15.78/26	15.13/25
0.30	49.46/28	33.43/27	33.37/26	32.19/25
0.50	51.69/28	33.32/27	33.23/26	32.99/25
0.70	27.39/28	17.95/27	12.29/26	11.45/25
0.90	60.09/28	47.10/27	41.32/26	31.12/25
1.10	32.43/28	29.74/27	29.73/26	29.56/25
1.30	19.12/28	16.33/27	16.06/26	15.94/25
1.50	52.02/28	51.64/27	48.58/26	46.97/25
1.70	133.5/28	65.33/27	61.16/26	60.53/25
1.90	80.72/28	51.22/27	36.73/26	36.72/25
2.50	111.4/28	79.21/27	60.80/26	50.34/25
4.00	57.31/28	24.48/27	23.07/26	20.02/25

Table C.4: Invariant Cross Section of ω.

p_T (GeV/c)	$Ed^3\sigma/dp^3$ (mbarn GeV$^{-2}/c^3$)	stat. error	syst. error
0.10	2.91	7.7×10^{-1}	7.4×10^{-1}
0.30	2.12	2.7×10^{-1}	5.4×10^{-1}
0.50	1.39	1.0×10^{-1}	3.5×10^{-1}
0.70	8.56×10^{-1}	5.0×10^{-2}	2.2×10^{-1}
0.90	3.67×10^{-1}	2.4×10^{-2}	9.3×10^{-2}
1.12	1.49×10^{-1}	1.1×10^{-2}	3.8×10^{-2}
1.38	1.049×10^{-1}	7.6×10^{-3}	2.6×10^{-2}
1.75	2.20×10^{-2}	1.8×10^{-3}	5.5×10^{-3}
2.50	2.15×10^{-3}	2.0×10^{-4}	5.4×10^{-4}
3.50	2.50×10^{-4}	4.0×10^{-5}	6.3×10^{-5}
4.50	3.1×10^{-5}	1.1×10^{-5}	7.7×10^{-6}
6.50	3.7×10^{-7}	2.0×10^{-7}	2.0×10^{-7}

Table C.5: Invariant Cross Section of ϕ.

p_T (GeV/c)	$Ed^3\sigma/dp^3$ (mbarn GeV$^{-2}/c^3$)	stat. error	syst. error
0.10	1.14×10^{-1}	3.5×10^{-2}	3.4×10^{-2}
0.30	1.79×10^{-1}	2.2×10^{-2}	5.2×10^{-2}
0.50	1.17×10^{-1}	1.2×10^{-2}	3.4×10^{-2}
0.70	8.47×10^{-2}	7.6×10^{-3}	2.5×10^{-2}
0.90	5.03×10^{-2}	4.7×10^{-3}	1.5×10^{-2}
1.12	2.09×10^{-2}	2.3×10^{-3}	4.9×10^{-3}
1.38	1.45×10^{-2}	1.5×10^{-3}	3.4×10^{-3}
1.75	2.97×10^{-3}	3.8×10^{-4}	6.9×10^{-4}
2.50	4.90×10^{-4}	5.7×10^{-5}	1.1×10^{-4}
3.50	5.1×10^{-5}	1.1×10^{-5}	1.2×10^{-5}
4.50	6.6×10^{-6}	2.7×10^{-6}	1.5×10^{-6}
6.50	1.9×10^{-8}	3.9×10^{-8}	4.0×10^{-8}